



Università degli Studi di Cagliari

**DOTTORATO DI RICERCA**  
in Scienze e Tecnologie Chimiche  
Ciclo XXIX  
UniCa

**Sustainability in cultural heritage: from diagnosis to the  
development of innovative systems for monitoring and  
understanding corrosion inside ancient brass wind  
instruments**

CHIM/01 Chimica Analitica

Presentata da:	Federica Cocco
Coordinatore Dottorato:	Prof. Stefano Enzo
Supervisor:	Prof.ssa Antonella Rossi Prof. Bernhard Elsener

Esame finale anno accademico 2015/2016  
Tesi discussa nella sessione d'esame marzo – aprile 2017





Università degli Studi di Cagliari

Università degli Studi di Sassari

**DOTTORATO DI RICERCA**  
in Scienze e Tecnologie Chimiche  
Ciclo XXIX  
UniCa – UniSS

**Sustainability in cultural heritage: from diagnosis to the  
development of innovative systems for monitoring and  
understanding corrosion inside ancient brass wind  
instruments**

CHIM/01 Chimica Analitica

Presentata da: Federica Cocco  
Coordinatore Dottorato: Prof. Stefano Enzo  
Supervisor: Prof.ssa Antonella Rossi  
Prof. Bernhard Elsener

Esame finale anno accademico 2015/2016





# *Abstract*

In the context of the project “Brass instruments of the 19<sup>th</sup> and early 20<sup>th</sup> centuries between long-term conservation and use in historically informed performance practice” an interdisciplinary methodology is being developed for the evaluation and monitoring of the corrosion state inside historical brass wind instruments before and after being played. A protocol has been established in order to prevent corrosion damage of the instruments and the efficiency of this treatment has to be monitored. In situ, non-destructive and portable techniques have to be used to evaluate the actual corrosion state inside the ancient instruments.

In a first part the focus is on the development of a non-destructive electrochemical sensor for the in-situ determination of the corrosion state (corrosion potential) and rate (polarization resistance) inside historical brass wind instruments, allowing also insight into the degradation mechanism which affects the artifacts. The electrochemical sensor consists of a combined Ag/AgCl solid-state reference electrode and a small platinum grid as counter electrode, both embedded in a thin sponge soaked with a diluted phosphate buffer solution, pH 7, with  $10^{-3}$  M chlorides. XPS surface analysis has shown that the test solution does not alter the surface composition of the brass alloys during the maximum 10 min of contact. To test the sensor, electrochemical measurements were performed on different brass model alloys with different surface treatments. The calibration of the sensor was achieved carrying out the same measurements in a traditional three-electrode cell using the same test solution on the same samples. The electrochemical response of the sensor was in agreement with the results obtained with the traditional cell.

For a correct interpretation, the electrochemical measurements with the sensor have to be related to surface state, requiring surface analysis of the brass alloys. This is challenging, because for both the alloy components, copper and zinc, the chemical state identification based on the binding energy values of Cu2p and Zn2p photoelectron signals is not possible: the chemical shifts between Zn(II) and Zn(0) in the Zn2p photoelectron signal and between Cu(I) and Cu(0) in the Cu2p photoelectron signal are very small.

Thus, in the second part of the thesis, a novel analytical strategy has been proposed for the identification and the quantification of copper and zinc when different chemical states are simultaneously present in thin-layered systems. The chemical state identification is based on the x-ray excited Auger signals (XAES) and on the determination of the multicomponent signals of copper and zinc metal and oxides on reference compounds. The intensities obtained from curve fitting the XAES spectra had to be converted to XPS photoelectron signals. This analytical approach has been tested on the Cu37Zn model brass alloy; the approach has proven to be successful. As a result it was applied for the identification and characterization of brass model alloys with different surface states.

In the third part of the thesis the electrochemical and corrosion behavior of brass model alloys after aging in two neutral solutions, a phosphate buffer solution pH 7 and an artificial saliva solution (pH 7.4), were studied by means of open circuit (OCP), linear polarization ( $R_p$ ) and Electrochemical Impedance Spectroscopy (EIS) measurements. In the phosphate buffer solution the effect of immersion time (ageing) was small and the EIS data indicated a charge transfer control. In artificial saliva both the potential and the polarization resistance increased markedly and the EIS data indicated a resistive control by a surface film. Indeed, surface analysis by X-ray photoelectron spectroscopy (XPS) and X-ray induced Auger electron spectroscopy (XAES) clearly showed the formation of a thick, protective film composed of CuSCN and  $Zn_3(PO_4)_2$  on brass alloys in artificial saliva. In buffer solution only a very thin  $Cu(OH)_2/CuO/ZnO$  film was formed. Thus it was possible to correlate the electrochemical and corrosion data with the surface composition of the aged brass alloys. A mechanistic explanation based on the oxygen reduction current that is catalysed in presence of  $Cu(OH)_2/CuO$  couple on the surface could be given and explain the much higher corrosion rates in the phosphate buffer solution.

Finally, the electrochemical sensor was used on samples from ancient brass instruments and inside the tuning slides of brass wind instruments of the 19<sup>th</sup> century to check the efficiency of the preventive conservation protocol. A plot of logarithm of polarization resistance ( $R_p$ ) versus the open circuit potential (OCP) allowed to compare all the results obtained on the brass model alloys, brass from ancient instruments and brass alloys exposed to solutions. Knowing the surface state (composition, film thickness, oxidation state) from the XPS/XAES surface analysis, the electrochemical results could be correlated to the surface state of the brass samples studied. So, the condensed representation of the electrochemical results showing distinct groups of  $\log(R_p)$  vs OCP data can be used both for diagnostic purpose and for mechanistic interpretation. The interdisciplinary approach combining electrochemical and surface analytical techniques at the forefront of research allowed reaching successfully the research goal.

# *Table of contents*

---

<b>Abstract</b> .....	<b>I</b>
<b>Abbreviations and symbols</b> .....	<b>VII</b>
<b>List of tables</b> .....	<b>VIII</b>
<b>List of figures</b> .....	<b>XI</b>
<b>Chapter 1</b> .....	<b>1</b>
<b>Introduction</b> .....	<b>1</b>
1.1    Introduction .....	2
1.2    Scope and outline of the thesis.....	4
References .....	6
<b>Chapter 2</b> .....	<b>7</b>
<b>Literature Review</b> .....	<b>7</b>
2.1    Properties of brass.....	8
2.1.1    Phase diagram of brass .....	8
2.1.2    Influence of alloying elements.....	9
2.2    Corrosion of brass alloys – dezincification.....	9
2.2.1    Corrosion in aqueous solution .....	10
2.2.2    Atmospheric corrosion.....	10
2.2.3    Effect of mechanical polishing .....	11
2.3    Development of brass production methods.....	11
2.4    Chemical composition of brass musical instrument over time.....	12
References .....	14
<b>Chapter 3</b> .....	<b>17</b>
<b>Investigation methods</b> .....	<b>17</b>
3.1.    Corrosion reactions.....	18
3.2.    Fundamentals.....	18
3.2.1.    Thermodynamic of corrosion [1 – 2].....	18
3.2.2.    Corrosion kinetics.....	20
3.3.    Electrochemical measurements.....	21
3.3.1.    Open circuit potential measurements.....	21
3.3.2.    Polarization curves.....	21
3.3.3.    Polarization resistance .....	22
3.3.4.    Electrochemical Impedance Spectroscopy.....	23
3.3.4.1.    Electrical Circuit Elements.....	25
3.4.    X-ray Photoelectron Spectroscopy (XPS).....	29
3.5.    X-ray Fluorescence (XRF).....	32
3.6.    Scanning Electron Microscopy (SEM) .....	33
3.7.    Atomic Force Microscopy (AFM) .....	34
<b>Chapter 4</b> .....	<b>37</b>
<b>Experimental</b> .....	<b>37</b>
4.1.    Materials and solutions .....	38
4.1.1.    Reference materials .....	38
4.1.2.    Brass model alloys.....	38
4.1.4.    Chemical etching .....	39

4.2.	Solutions .....	39
4.3.	Microscopy.....	39
4.3.1.	Optical microscopy (OM) .....	39
4.3.2.	Scanning Electron Microscopy (SEM).....	40
4.3.3.	Atomic Force Microscopy (AFM).....	40
4.4.	X-ray Fluorescence (XRF).....	40
4.5.	Electrochemical methods .....	41
4.5.1.	Electrochemical cell.....	41
4.5.2.	Open circuit potential.....	42
4.5.3.	Cathodic and anodic polarization curves.....	42
4.5.4.	Electrochemical Impedance Spectroscopy (EIS).....	42
4.6.	X-ray Photoelectron Spectroscopy (XPS).....	42
4.6.1.	Theta Probe .....	43
4.6.2.	ULVAC - PHI Quantera <sup>SXM</sup> .....	44
4.6.3.	Data processing and quantitative analysis .....	44
	References .....	48
<b>Chapter 5.....</b>		<b>49</b>
<b>Characterization of surface films on brass alloys by XPS/XAES analysis.....</b>		<b>49</b>
5.1	Introduction.....	50
5.2	Experimental .....	53
5.2.1	Materials and surface preparation .....	53
5.2.2	Characterization Method.....	53
5.3	Results.....	53
5.3.1	Metallographic analysis.....	53
5.3.2	Optical microscopy and atomic force microscopy .....	54
5.3.3	Scanning electron microscopy.....	55
5.3.4	X-ray photoelectron spectroscopy results.....	57
5.3.4.1	Reference materials.....	57
	Cu <sub>37</sub> Zn brass model alloy.....	61
5.3.5	As received brass alloys .....	67
5.3.6	Mechanically polished brass alloys .....	71
5.3.7	Angle resolved spectra .....	75
5.3.7.1	As received brass alloys .....	75
5.4	Discussion.....	79
5.4.1	Curve fitting of X-ray induced Auger spectra .....	79
5.4.1.1	Cu <sub>37</sub> Zn model brass alloy compared to reference compounds.....	79
5.4.1.2	Cu <sub>18</sub> Zn, Cu <sub>28</sub> Zn, Cu <sub>35</sub> Zn <sub>1</sub> Pb, Cu <sub>38</sub> Zn <sub>2</sub> Pb model brass alloy compared to reference compounds.....	80
5.4.2	Chemical state plot.....	81
5.4.3	Development of analytical strategy for simultaneous quantification of copper and zinc in complex nanostructured systems .....	87
5.4.4	Testing the analytical strategy on a model system: Cu <sub>37</sub> Zn model brass alloy.....	90
5.4.5	Application of the analytical strategy: brass alloys with thin oxide film.....	91
5.4.5.1	Cu <sub>37</sub> Zn mechanically polished.....	91
5.4.5.2	Mechanically polished Cu <sub>18</sub> Zn, Cu <sub>28</sub> Zn, Cu <sub>35</sub> Zn <sub>1</sub> Pb and Cu <sub>38</sub> Zn <sub>2</sub> Pb brass alloys .....	92
5.4.5.3	Thickness and composition of the oxide layer .....	93
5.5	Conclusions.....	95
	References.....	96



<b>Chapter 6 .....</b>	<b>99</b>
<b>Development of an in-situ and non-destructive electrochemical sensor for the determination of the corrosion rate inside historical brass wind instruments .....</b>	<b>99</b>
6.1 Introduction .....	100
6.2 Experimental.....	101
6.2.1 Development of the electrochemical sensor .....	101
6.2.2 Materials and solutions .....	102
6.2.3 Electrochemical measurements.....	102
6.2.4 Surface characterization.....	103
6.3 Results .....	103
6.3.1 Measurements in the electrochemical cell .....	103
6.3.2 Measurements with the electrochemical sensor .....	104
6.3.3 XPS surface characterization .....	106
6.4 Discussion.....	109
6.4.1 Working characteristics and calibration of the sensor.....	109
6.4.2 Alteration of the surface state .....	110
6.4.3 Efficiency of preventative conservation measures .....	112
6.5 Conclusions .....	114
References .....	115
<b>Chapter 7 .....</b>	<b>117</b>
<b>XPS and EIS studies on the protective films formed on Cu-Zn alloys after aging in neutral solutions .....</b>	<b>117</b>
7.1 Introduction .....	118
7.2 Experimental.....	119
7.2.1 Materials and surface preparation.....	119
7.2.2 Solutions .....	119
7.2.3 Electrochemical tests .....	119
7.2.4 Characterization methods .....	120
7.3 Results .....	120
7.3.1 Electrochemical Results.....	120
7.3.1.1 Open circuit potential measurements.....	120
7.3.1.2 Polarization resistance measurements – corrosion rate.....	123
7.3.1.3 Polarization curves .....	124
7.3.1.4 Impedance spectroscopy.....	125
7.3.2 Results of XPS – XAES surface analysis – buffer solutions.....	128
Cu18Zn alloy exposed to buffer solutions.....	128
Cu37Zn alloy exposed to buffer solutions.....	133
Cu38Zn2Pb alloy exposed to buffer solutions.....	137
7.3.3 Results of XPS – XAES surface analysis – artificial saliva solutions.....	141
Cu18Zn alloy exposed to artificial saliva solutions .....	141
Cu37Zn alloy exposed to artificial saliva solutions .....	145
Cu38Zn 2pb alloy exposed to artificial saliva solutions .....	148
7.3.4 Scanning electron microscopy .....	153
7.4 Discussion.....	158
7.4.1 Influence of the zinc content in brass alloys .....	158
7.4.2 Influence of exposure time .....	159
7.4.3 Mechanism of brass dissolution – influence of surface films .....	160
7.4.4 Influence of the surface film .....	161

7.5	Conclusions.....	163
	References.....	164
<b>Chapter 8.....</b>	<b>.....</b>	<b>166</b>
<b>Application of the in situ electrochemical sensor to monitor corrosion on ancient brass musical artifacts.....</b>	<b>.....</b>	<b>166</b>
8.1	Introduction.....	167
8.2	Experimental.....	167
8.2.1	Materials.....	167
8.2.2	In-situ measurements with the sensor.....	169
8.2.3	Electrochemical measurements with the sensor.....	169
8.3	Results.....	169
8.3.1	X-ray fluorescence results.....	169
8.3.2	Optical microscopy (OM).....	170
8.3.3	X-ray Photoelectron Spectroscopy analysis.....	171
8.3.4	Electrochemical measurements.....	172
8.4	Discussion.....	173
8.4.1	Electrochemical measurements - correlation between OCP and Rp.....	173
8.4.2	Mechanistic interpretation.....	175
8.4.3	Further application - inside the tuning slides.....	176
8.4.4	Instantaneous corrosion rate.....	176
8.5	Conclusions.....	177
	References.....	179
<b>Chapter 9.....</b>	<b>.....</b>	<b>180</b>
<b>Conclusions and Outlook.....</b>	<b>.....</b>	<b>180</b>
<b>Appendix.....</b>	<b>.....</b>	<b>183</b>
<b>Acknowledgments.....</b>	<b>.....</b>	<b>196</b>
<b>Curriculum vitae.....</b>	<b>.....</b>	<b>198</b>

# *Abbreviations and symbols*

---

§	Chapter – Section
AFM	Atomic Force Microscopy
ARXPS	Angle Resolved X-ray Photoelectron Spectroscopy
at %	Atomic percentage
BE	Binding energy
CPE	Constant Phase Element
EIS	Electrochemical Impedance Spectroscopy
FWHM	Full Width at Half Maximum
HIP	Historically Informed Performance Practice
IMFP	Inelastic Mean free path
ISO	International Organization for Standardization
KE	Kinetic energy
LP	Linear polarization
LPR	Linear Polarization Resistance
NHE	Normal Hydrogen Electrode
NIST	National Institute of Standards and Tecnology
OCP	Open Circuit Potential
OM	Optical Microscopy
RH	Relative Humidity
SCE	Saturated Calomel Electrode
<i>SEM</i>	Scanning Electron Microscopy
WHO	World Health Organisation
wt.%	Weight percentage
XAES	X-ray induced Auger Electron Spectroscopy
XPS	X-ray Photoelectron Spectroscopy
XRF	X-ray Fluorescence

# List of Tables

---

Table 3. 1: Impedance of a resistor, capacitor and inductance. ....	26
Table 3. 2: A and B values for the equation 3.31.....	30
Table 3. 1: Impedance of a resistor, capacitor and inductance. ....	26
Table 3. 2: A and B values for the equation 3.31.....	30
Table 4. 1: Nominal composition of model brass alloys used in this work. ....	38
Table 4. 2: Parameters of the mechanical polishing procedure. After each polishing step the samples were cleaned in ethanol in the ultrasonic bath once for 5 minutes. ....	39
Table 4. 3: List of regions and relative energy ranges as well as the parameters used for experiments. ....	43
Table 5. 1: Peak fitting parameters for the photoelectron and Auger spectra of the sputtered metallic copper and zinc. Spectra were acquired using the Thetaprobe.....	58
Table 5. 2: Peak fitting parameters for the high-resolution Cu 2p <sub>3/2</sub> , Cu L <sub>3</sub> M <sub>45</sub> M <sub>45</sub> , spectra of CuO and Cu <sub>2</sub> O and for the Zn 2p <sub>3/2</sub> and Zn L <sub>3</sub> M <sub>45</sub> M <sub>45</sub> of ZnO. Spectra were acquired using the Thetaprobe: beam size 400 μm. Standard deviations were calculated over three independent measurements. ....	62
Table 5. 3: Peak parameters for fitting the O1s, Cu 2p <sub>3/2</sub> , Zn 2p <sub>3/2</sub> , Cu L <sub>3</sub> M <sub>45</sub> M <sub>45</sub> and Zn L <sub>3</sub> M <sub>45</sub> M <sub>45</sub> spectra of an as received Cu37Zn sample. ....	64
Table 5. 4: Peak parameters for fitting the O1s, Cu 2p <sub>3/2</sub> , Zn 2p <sub>3/2</sub> , Cu L <sub>3</sub> M <sub>45</sub> M <sub>45</sub> and Zn L <sub>3</sub> M <sub>45</sub> M <sub>45</sub> spectra of a sputtered Cu37Zn. Spectra were acquired using the Quantera <sup>SXM</sup> .....	65
Table 5. 5: Peak parameters for fitting the O1s, Cu 2p <sub>3/2</sub> , Zn 2p <sub>3/2</sub> , Cu L <sub>3</sub> M <sub>45</sub> M <sub>45</sub> and Zn L <sub>3</sub> M <sub>45</sub> M <sub>45</sub> spectra of a Cu37Zn sample following mechanical polishing. Spectra were acquired using the Thetaprobe.....	66
Table 5. 6: Peak parameters for fitting the O 1s, Cu 2p <sub>3/2</sub> , Zn 2p <sub>3/2</sub> , Cu L <sub>3</sub> M <sub>45</sub> M <sub>45</sub> and Zn L <sub>3</sub> M <sub>45</sub> M <sub>45</sub> spectra of Cu18Zn, Cu28Zn, Cu35Zn1Pb and Cu38Zn2Pb samples in the as received state. ....	69
Table 5. 7: Peak parameters for fitting the O 1s, Cu 2p <sub>3/2</sub> , Zn 2p <sub>3/2</sub> , Cu L <sub>3</sub> M <sub>45</sub> M <sub>45</sub> and Zn L <sub>3</sub> M <sub>45</sub> M <sub>45</sub> spectra of Cu18Zn, Cu28Zn, Cu35Zn1Pb and Cu38Zn2Pb samples following mechanical polishing. ....	74
Table 5. 8: Column 2 and 3 reports the BEs of the Cu 2p <sub>3/2</sub> and KEs of the Cu L <sub>3</sub> M <sub>45</sub> M <sub>45</sub> signals of the analysed materials (column 1). In column 4 the Auger parameters calculated using the different components for the XAES signals. Mean values and standard deviations were calculated over at least three independent measurements. ...	83
Table 5. 9: in column 2 and 3 are listed the BEs of the Zn 2p <sub>3/2</sub> and KEs of the Zn L <sub>3</sub> M <sub>45</sub> M <sub>45</sub> signals of the analysed compounds (column 1). In column 4 the Auger parameters calculated using the different components for the XAES signals. (standard deviations are reported in brackets) .....	85
Table 5. 10: Ratio of the intensity of Cu 2p <sub>3/2</sub> and Cu L <sub>3</sub> M <sub>45</sub> M <sub>45</sub> and of Zn 2p <sub>3/2</sub> and Zn L <sub>3</sub> M <sub>45</sub> M <sub>45</sub> ; the correction factor $k = R_{ox}/R_{met}$ for copper and zinc compounds is also reported: spectra were acquired with two spectrometers and areas were corrected for the geometry of the instruments.....	88

Table 5. 11: Input parameters and results of calculations to determine the metallic and oxide intensity in the (unresolved) 2p photoelectron peak of copper and zinc in the case of the Cu <sub>37</sub> Zn mechanically polished sample. ....	89
Table 5. 12: Quantitative analysis results of Cu <sub>37</sub> Zn sputtered model brass alloy (wt.%). ....	90
Table 5. 13: Quantitative analysis results of the oxide film on the “as received” Cu <sub>37</sub> Zn model brass alloy .....	91
Table 5. 14: Quantitative analysis results of the oxide film and the alloy beneath the oxide film formed on Cu <sub>37</sub> Zn brass model alloy after mechanical polishing are reported. The thickness of the oxide layer and the contamination film are also listed in the table. ....	92
Table 5. 15: Quantitative results obtained for mechanically polished Cu <sub>18</sub> Zn, Cu <sub>28</sub> Zn, Cu <sub>35</sub> Zn <sub>1</sub> Pb and Cu <sub>38</sub> Zn <sub>2</sub> Pb brass model alloys. ....	92
Table 5. 16: Quantitative results of as received Cu <sub>18</sub> Zn, Cu <sub>28</sub> Zn, Cu <sub>35</sub> Zn <sub>1</sub> Pb and Cu <sub>38</sub> Zn <sub>2</sub> Pb brass model alloys. ....	93
Table 5. 18: In table are reported the thickness values obtained by eq (5). Standard deviations are reported in brackets.....	95
Table 6. 1: Open circuit potential (OCP) and Polarization resistance measurements (Rp) obtained on brass alloys using the traditional electrochemical cell and the sensor. Electrolyte: pH = 7 phosphate buffer solution containing 10 <sup>-2</sup> , 10 <sup>-3</sup> and 10 <sup>-4</sup> M NaCl. OCP are given vs Ag/AgCl saturated electrode.....	105
Table 6.3 BE and KE values of Cu 2p <sub>3/2</sub> , Zn 2p <sub>3/2</sub> , Cu L <sub>3</sub> M <sub>4,5</sub> M <sub>4,5</sub> , Zn L <sub>3</sub> M <sub>4,5</sub> M <sub>4,5</sub> and P 2p signals of the mechanically polished Cu <sub>37</sub> Zn after the measurement with the sensor. Electrolyte: buffer phosphate at pH 7 + 10 <sup>-2</sup> , 10 <sup>-3</sup> and 10 <sup>-4</sup> M NaCl.....	108
Table 6.4: Surface composition (wt%) determined by XPS analysis; in brackets the standard deviation .....	108
Table 6. 5: Results of the OCP, Rp, i <sub>corr</sub> and of estimated instantaneous corrosion rates for brass alloys in the as received and mechanically polished states. ....	112
Table 7. 1: Average of the initial (E <sub>0</sub> ) and final (E <sub>1,3,16h</sub> ) open circuit potential values (mV vs SCE) of copper and brass samples exposed to artificial saliva for 1, 3 and 16 h. Standard deviations are given in parentheses. ....	121
Table 7. 2: Average and standard deviation of the initial (E <sub>0</sub> ) and final (E <sub>1,3,16h</sub> ) open circuit potentials (mV vs SCE) of copper and brass samples exposed to phosphate buffer pH 7 for 1, 3 and 16 h.....	122
Table 7. 3: Average polarization resistance Rp (kΩ cm <sup>2</sup> ) of copper and brass samples exposed to artificial saliva for 1, 3 and 16 h. The standard deviations are given in parentheses. ....	124
Table 7. 4: Average polarization resistance Rp (kΩ cm <sup>2</sup> ) of copper and brass samples exposed to pH = 7 phosphate buffer for 1, 3 and 16 h. The standard deviations are given in parentheses.....	124
Table 7. 5: Calculated fitting parameters for brass alloys after 1 hour of immersion in phosphate buffer solution (standard deviation percentage is reported in brackets).....	127
Table 7. 6: Calculated fitting parameters for brass alloys after 3 hours of immersion in phosphate buffer solution (standard deviation percentage is reported in brackets).....	127
Table 7. 7: Calculated fitting parameters for brass alloys after 3 hours of immersion in artificial saliva solution (standard deviation percentage is reported in brackets).....	127

Table 7.8a: Binding energy (BE) and FWHM of the most intense peaks of the elements detected on the Cu18Zn samples after contact with the phosphate buffer solution for 1, 3 and 16 hours. Standard deviations are given in parentheses.....	130
Table 7.9: Quantitative analysis results for the Cu18Zn after 1, 3 and 16hours of immersion in the neutral phosphate buffer solution. Standard deviations are reported in brackets. ....	132
Table 7. 10a: Average binding energy (BE) and FWHM of the most intense peaks of the elements detected on the Cu37Zn samples after contact with the phosphate buffer solution. Standard deviations are given in parentheses.....	135
Table 7. 11: Results of the quantitative analysis for the Cu37Zn after 1, 3 and 16hours of immersion in neutral phosphate buffer solution. Standard deviations are reported in brackets. ....	136
Table 7. 12a: Average binding energy (BE) and FWHM of the most intense peaks of the elements detected on the Cu38Zn2Pb after exposure to the phosphate buffer solution. Standard deviations are given in parentheses. ....	139
Table 7. 13: Results of the quantitative analysis for the Cu38Zn 2pb after 1, 3 and 16hours of immersion in neutral phosphate buffer solution. Standard deviations are reported in brackets. ....	140
Table 7. 14: Average kinetic energy (KE) and FWHM of the most intense peaks of the elements detected on the Cu18Zn after contact with the saliva solution. Standard deviations are given in parentheses.....	144
Table 7. 15: Results of the quantitative analysis (average at%) for the Cu18Zn after 1, 3 and 16 hours of immersion in artificial saliva solution. Standard deviations are reported in brackets. ....	144
Table 7. 16: Average kinetic energy (KE) and FWHM of the most intense peaks of the elements detected on the Cu37Zn after contact with the saliva solution. Standard deviations are given in parentheses.....	147
Table 7. 17: Results of the quantitative analysis (average at%) for the Cu37Zn after 1, 3 and 16 hours of immersion in artificial saliva solution. Standard deviations are reported in brackets.....	148
Table 7. 18: Average kinetic energy (KE) and FWHM of the most intense peaks of the elements detected on the Cu38Zn2Pb after contact with the saliva solution. Standard deviations are given in parentheses.....	149
Table 7. 19: Results of the quantitative analysis (average at%) for the Cu18Zn after 1, 3 and 16hours of immersion in artificial saliva solution. Standard deviations are reported in brackets.....	152
Table 8. 1: Samples of historical brass musical instruments analyzed in this work. ....	168
Table 8. 2: Composition of the reference and ancient brass samples obtained by XRF. ....	169
Table 8. 3: Polarization resistance Rp measured on ancient samples listed in tables 8.1. ....	172

# List of Figures

---

Figure 2. 1: Copper – zinc phase diagram [1]. .....	8
Figure 3. 1: Pourbaix diagram for the system copper – water at 25°C. ....	19
Figure 3. 2: Total current/voltage diagram of a metal electrode corroding under H <sub>2</sub> formation. Dotted curve (----) indicates partial current density (eq. 3.7, 3.8); the solid line (___) indicates the total current density. ....	20
Figure 3. 3: Scheme of anodic and cathodic polarization curve showing Tafel lines. ....	22
Figure 3. 4: Current vs Voltage curve showing a pseudo – linear system. ....	24
Figure 3. 5: Lissajous figure .....	24
Figure 3. 7: Graphical representation of the impedance as a) Nyquist and b,c) Bode plots. ....	25
Figure 3. 7: Electrochemical system where a polarizable electrode is in contact with an electrolyte. ....	28
Figure 3. 8: Randles circuit used to describe the system in Fig. 3.7. ....	28
Figure 3. 9: Schematic diagram of the photoemission process of a 1s electron, followed by the relaxation of the ionized atom and the emission of a KL <sub>2,3</sub> L <sub>2,3</sub> Auger electron. ....	30
Figure 4. 1: The handled XRF spectrometer a) used direct on the sample and b) using the docking station. ....	40
Figure 4. 2: Scheme of the electrochemical cell. ....	41
Figure 4. 3: Schematic representation of a non-homogeneous sample where there is the presence of an outer contamination layer and an oxide layer between the bulk and the contamination layer. ....	46
Figure 5.1: Photomicrography of a) Cu18Zn, b) Cu28Zn, c) Cu37Zn, d) Cu35Zn1Pb and e) Cu38Zn2Pb after chemical etching with an ammonium solution. (x200). ....	54
Figure 5.2: Morphology obtained by OM and AFM of Cu28Zn, Cu37Zn and Cu38Zn1Pb brass samples, after mechanical polishing. ....	55
Figure 5. 3: Scanning electron microscopy images of the mirror polished Cu18Zn, Cu28Zn, Cu37Zn, Cu35Zn1Pb and Cu38Zn2Pb after mechanical polishing. ....	56
Figure 5. 4: High-resolution spectra a) Cu 2p <sub>3/2</sub> and b) Cu L <sub>3</sub> M <sub>4,5</sub> M <sub>4,5</sub> of pure sputtered copper. ....	58
Figure 5. 5: High-resolution spectra a) Zn 2p <sub>3/2</sub> and b) Zn L <sub>3</sub> M <sub>4,5</sub> M <sub>4,5</sub> of pure sputtered zinc. ....	58
Figure 5. 6: High-resolution spectra a) Cu 2p <sub>3/2</sub> and b) Cu L <sub>3</sub> M <sub>4,5</sub> M <sub>4,5</sub> c) O 1s of pure CuO. ....	60
Figure 5. 7: High resolution spectra a) Cu 2p <sub>3/2</sub> and b) Cu L <sub>3</sub> M <sub>4,5</sub> M <sub>4,5</sub> c) O 1s of pure Cu <sub>2</sub> O. ....	60
Figure 5. 8: High-resolution spectra a) Zn 2p <sub>3/2</sub> and b) Zn L <sub>3</sub> M <sub>4,5</sub> M <sub>4,5</sub> c) O 1s of pure ZnO. ....	61
Figure 5. 9: The a) Cu 2p <sub>3/2</sub> , b) Cu L <sub>3</sub> M <sub>4,5</sub> M <sub>4,5</sub> , c) Zn 2p <sub>3/2</sub> , d) Zn L <sub>3</sub> M <sub>4,5</sub> M <sub>4,5</sub> high-resolution spectra of Cu37Zn in the as received state. ....	63

Figure 5. 10: Peak fitting for the O1s, Cu 2p <sub>3/2</sub> , Zn 2p <sub>3/2</sub> , Cu L <sub>3</sub> M <sub>4,5</sub> M <sub>4,5</sub> and Zn L <sub>3</sub> M <sub>4,5</sub> M <sub>4,5</sub> spectra of the sputter-cleaned alloy Cu37Zn .....	65
Figure 5. 11: The a) Cu 2p <sub>3/2</sub> , b) Cu L <sub>3</sub> M <sub>4,5</sub> M <sub>4,5</sub> , c) Zn 2p <sub>3/2</sub> , d) Zn L <sub>3</sub> M <sub>4,5</sub> M <sub>4,5</sub> high-resolution spectra of the mirror - like polished Cu37Zn sample. ....	67
Figure 5. 12: The a) Cu 2p <sub>3/2</sub> , b) Cu L <sub>3</sub> M <sub>4,5</sub> M <sub>4,5</sub> , c) Zn 2p <sub>3/2</sub> , d) Zn L <sub>3</sub> M <sub>4,5</sub> M <sub>4,5</sub> high-resolution spectra of the as received Cu18Zn alloy.....	69
Figure 5. 13: High-resolution a) Cu 2p <sub>3/2</sub> , b) Cu L <sub>3</sub> M <sub>4,5</sub> M <sub>4,5</sub> , c) Zn 2p <sub>3/2</sub> , d) Zn L <sub>3</sub> M <sub>4,5</sub> M <sub>4,5</sub> spectra of the as received Cu28Zn alloy.....	70
Figure 5. 14: High-resolution a) Cu 2p <sub>3/2</sub> , b) Cu L <sub>3</sub> M <sub>4,5</sub> M <sub>4,5</sub> , c) Zn 2p <sub>3/2</sub> , d) Zn L <sub>3</sub> M <sub>4,5</sub> M <sub>4,5</sub> spectra of the as received Cu35Zn1Pb alloy.....	70
Figure 5. 15: High-resolution a) Cu 2p <sub>3/2</sub> , b) Cu L <sub>3</sub> M <sub>4,5</sub> M <sub>4,5</sub> , c) Zn 2p <sub>3/2</sub> , d) Zn L <sub>3</sub> M <sub>4,5</sub> M <sub>4,5</sub> spectra of the as received Cu35Zn2Pb .....	71
Figure 5. 16: High-resolution spectra of a) Cu 2p <sub>3/2</sub> , b) Cu L <sub>3</sub> M <sub>4,5</sub> M <sub>4,5</sub> , c) Zn 2p <sub>3/2</sub> , d) Zn L <sub>3</sub> M <sub>4,5</sub> M <sub>4,5</sub> of the mirror polished Cu18Zn.....	72
Figure 5. 17: High-resolution spectra of a) Cu 2p <sub>3/2</sub> , b) Cu L <sub>3</sub> M <sub>4,5</sub> M <sub>4,5</sub> , c) Zn 2p <sub>3/2</sub> , d) Zn L <sub>3</sub> M <sub>4,5</sub> M <sub>4,5</sub> of the mirror polished Cu28Zn.....	73
Figure 5. 18: High-resolution spectra of a) Cu 2p <sub>3/2</sub> , b) Cu L <sub>3</sub> M <sub>4,5</sub> M <sub>4,5</sub> , c) Zn 2p <sub>3/2</sub> , d) Zn L <sub>3</sub> M <sub>4,5</sub> M <sub>4,5</sub> acquired on the mirror-like polished Cu35Zn1Pb alloy .....	73
Figure 5. 19: High-resolution spectra of a) Cu 2p <sub>3/2</sub> , b) Cu L <sub>3</sub> M <sub>4,5</sub> M <sub>4,5</sub> , c) Zn 2p <sub>3/2</sub> , d) Zn L <sub>3</sub> M <sub>4,5</sub> M <sub>4,5</sub> acquired on the mirror-like polished Cu38Zn2Pb alloy. ....	74
Figure 5. 20: Angle resolved high-resolution C 1s (a), O 1s (b), Cu 2p (c) and Zn 2p (d) spectra of the as received Cu18Zn acquired at different emission angles. ....	75
Figure 5. 21: Angle resolved high-resolution C 1s (a), O 1s (b), Cu 2p (c) and Zn 2p (d) spectra of the as received Cu37Zn acquired at different emission angles. ....	76
Figure 5. 22: Angle resolved results acquired on mechanically polished Cu18Zn. Mean and standard deviations were calculated over three independent measurements. ....	77
Figure 5. 23: Angle resolved results acquired on mechanically polished Cu28Zn. Mean and standard deviations were calculated over three independent measurements. ....	77
Figure 5. 24: Angle resolved results acquired on mechanically polished Cu37Zn alloy. Mean and standard deviation were calculated over three independent measurements. ....	77
Figure 5. 25: Angle resolved results obtained on mechanically polished Cu35Zn1Pb. Only the alloy elements are shown. Copper and zinc are shown as total amount of metal and oxidized components.....	78
Figure 5. 26: Angle resolved results acquired on mechanically polished Cu38Zn2Pb. Only alloy elements are shown. Copper and zinc apparent concentrations were calculated using the Cu 2p <sub>3/2</sub> and Zn 2p <sub>3/2</sub> signals.....	79
Figure 5. 27: Copper chemical state plot using data listed in Table 5.8. ....	84
Figure 5. 28: Zinc chemical state plot using data listed in Table 5.9.....	86
Figure 5. 29: Percentage of oxidized component in the 2p signal vs percentage of the oxidized component in the LMM signal for copper and zinc .....	89
Figure 5. 30: CuLMM high-resolution spectra of a) Cu18Zn, b) Cu28Zn, c) Cu35Zn1Pb and d) Cu38Zn2Pb acquired at two different emission angles, $\theta$ : 28.6° and 66.1° respectively.....	94



Figure 6. 1: a) Schematic drawing of the newly developed sensor for in-situ electrochemical measurements. The sponge is ca. 1.5 x 1.5 cm (area 2 cm <sup>2</sup> ), b) the photograph of the first developed sensor. ....	101
Figure 6.3: Open circuit potentials (OCP) versus contact time with the pH = 7 phosphate buffer solution containing NaCl (10 <sup>-4</sup> , 10 <sup>-3</sup> and 10 <sup>-2</sup> M) measured using the electrochemical cell for the (a) Cu18Zn and (b) Cu37Zn after mechanically polishing procedure.....	103
Figure 6.4: Open circuit potentials (OCP) versus contact time with the pH = 7 phosphate buffer solution containing NaCl (10 <sup>-4</sup> , 10 <sup>-3</sup> and 10 <sup>-2</sup> M) measured using the electrochemical sensor for the (a) Cu18Zn and (b) Cu37Zn after mechanically polishing procedure.....	104
Figure 6.5: Examples of polarization resistance measurements: brass alloys in pH = 7 phosphate buffer solution containing 10 <sup>-2</sup> , 10 <sup>-3</sup> and 10 <sup>-4</sup> M NaCl performed with the sensor (red line; Area = 2 cm <sup>2</sup> ) and in the electrochemical cell (green line; area = 0.78 cm <sup>2</sup> ). (a) CuZn18 as received, (b) Cu37Zn mechanically polished .....	105
Figure 6.6: XPS spectra of the sample Cu37Zn mechanically polished before and after the electrochemical tests performed with the sensor using phosphate buffer solution at pH 7 with different chloride concentrations. (a) Survey spectrum, (b) magnification of the region from 300 to 100 eV.....	106
Figure 6.7: XPS high resolution spectra of Cu 2p <sub>3/2</sub> , Zn 2p <sub>3/2</sub> , Cu L <sub>3</sub> M <sub>4,5</sub> M <sub>4,5</sub> , Zn L <sub>3</sub> M <sub>4,5</sub> M <sub>4,5</sub> and P 2p of the sample mechanically polished Cu37Zn before the electrochemical tests performed with the sensor using phosphate buffer solution at pH 7 with different chloride concentrations.....	107
Figure 6. 8: The specific polarization resistance, R <sub>p</sub> , measured by the sensor versus the specific R <sub>p</sub> measured using the electrochemical cell for the Cu18Zn and Cu37Zn in as received and mechanically polished states in the different test solutions. The dotted lines differ for ± 10%.....	110
Figure 6.9: Optical micrographs of the mirror polished Cu37Zn before (a, b) and after (c, d) the 7 minutes measurement with the sensor at two magnification: x100 (a, c) and x200 (b, d). ....	111
Figure 6.10: Diagram log R <sub>p</sub> versus OCP of CuZn18, Cu28Zn, Cu37Zn, Cu35Zn1Pb and Cu38Zn2Pb brass alloys in the as received state and after mechanical polishing. The measurements were carried out with the sensor after 5 minutes of contact with the pH = 7 buffer solution containing different NaCl concentration. ....	113
Figure 7. 1: Open circuit potential versus time curves for a) Cu18Zn, b) Cu37Zn, c) Cu28Zn, d) Cu35Zn1Pb, e) Cu38Zn 2pb and f) pure copper following mechanical polishing and exposure to artificial saliva. Inserts show OCP vs time for the first three hours. ....	122
Figure 7. 2: Open circuit potential versus time curves for mechanically polished a) Cu18Zn, b) Cu37Zn, c) Cu28Zn, d) Cu35Zn1Pb, e) Cu38Zn 2pb and f) pure copper in pH = 7 phosphate buffer. Inserts show OCP vs time for the first three hours. ....	123
Figure 7. 3: Potentiodynamic polarization curves of brass alloys after 1h of contact with (a) the artificial saliva solution and (b) the phosphate buffer solution. ....	125
Figure 7. 4: Nyquist (a) and Bode (b) plots of the five different brass alloys after 1 h immersion in a naturally aerated pH = 7 buffer solution (copper is also shown). ....	125
Figure 7. 5: Nyquist (a) and Bode (b) plots of the five different brass alloys after 3 h immersion in a naturally aerated pH = 7 buffer solution (copper is also shown). ....	126
Figure 7. 6: Nyquist (a) and Bode (b) plots of the five different brass alloys after 3 h immersion in a naturally aerated saliva solution (copper is also shown). ....	126
Figure 7. 7: Equivalent circuits used to analyse the impedance spectra. a) in phosphate buffer solution, b) in saliva solution.....	126

Figure 7. 8: Cu 2p <sub>3/2</sub> (a), Cu L <sub>3</sub> M <sub>45</sub> M <sub>45</sub> (b), Zn 2p <sub>3/2</sub> (c), Zn L <sub>3</sub> M <sub>45</sub> M <sub>45</sub> (d), O 1s (e), P 2p (f) signals for the Cu18Zn alloy after 1 hours of contact with the phosphate buffer solution. ....	128
Figure 7. 9: Cu 2p <sub>3/2</sub> (a), Cu L <sub>3</sub> M <sub>45</sub> M <sub>45</sub> (b), Zn 2p <sub>3/2</sub> (c), Zn L <sub>3</sub> M <sub>45</sub> M <sub>45</sub> (d), O 1s (e), P 2p (f) signals for the Cu18Zn alloy after 3 hours of contact with the phosphate buffer solution. ....	129
Figure 7. 10: Cu 2p <sub>3/2</sub> (a), Cu L <sub>3</sub> M <sub>45</sub> M <sub>45</sub> (b), Zn 2p <sub>3/2</sub> (c), Zn L <sub>3</sub> M <sub>45</sub> M <sub>45</sub> (d), O 1s (e), P 2p (f) signals for the Cu18Zn alloy after 16 hours of contact with the phosphate buffer solution. ....	129
Figure 7. 11: Apparent composition (at%) vs emission angle from ARXPS data for Cu18Zn after 1, 3 and 16 hours of contact with the phosphate solution. ....	132
Figure 7. 12: Cu 2p <sub>3/2</sub> (a), Cu L <sub>3</sub> M <sub>45</sub> M <sub>45</sub> (b), Zn 2p <sub>3/2</sub> (c), Zn L <sub>3</sub> M <sub>45</sub> M <sub>45</sub> (d), O 1s (e), P 2p (f) signals for the Cu37Zn alloy after 1 hours of contact with the phosphate buffer solution. ....	133
Figure 7. 13: Cu 2p <sub>3/2</sub> (a), Cu L <sub>3</sub> M <sub>45</sub> M <sub>45</sub> (b), Zn 2p <sub>3/2</sub> (c), Zn L <sub>3</sub> M <sub>45</sub> M <sub>45</sub> (d), O 1s (e), P 2p (f) signals for the Cu37Zn alloy after 3 hours of contact with the phosphate buffer solution. ....	133
Figure 7. 14: Cu 2p <sub>3/2</sub> (a), Cu L <sub>3</sub> M <sub>45</sub> M <sub>45</sub> (b), Zn 2p <sub>3/2</sub> (c), Zn L <sub>3</sub> M <sub>45</sub> M <sub>45</sub> (d), O 1s (e), P 2p (f) signals for the Cu37Zn alloy after 16 hours of contact with the phosphate buffer solution. ....	134
Figure 7. 15: Apparent composition (at%) vs emission angle from ARXPS data for Cu37Zn after 1, 3 and 16 hours of contact with the phosphate solution. ....	136
Figure 7. 16: Cu 2p <sub>3/2</sub> (a), Cu L <sub>3</sub> M <sub>45</sub> M <sub>45</sub> (b), Zn 2p <sub>3/2</sub> (c), Zn L <sub>3</sub> M <sub>45</sub> M <sub>45</sub> (d), O 1s (e), P 2p (f) signals for the Cu38Zn2Pb after 1 hours of contact with the phosphate buffer solution. ....	137
Figure 7. 17: Cu 2p <sub>3/2</sub> (a), Cu L <sub>3</sub> M <sub>45</sub> M <sub>45</sub> (b), Zn 2p <sub>3/2</sub> (c), Zn L <sub>3</sub> M <sub>45</sub> M <sub>45</sub> (d), O 1s (e), P 2p (f) signals for the Cu38Zn2Pb after 3 hours of exposure to the phosphate buffer solution. ....	137
Figure 7. 18: Cu 2p <sub>3/2</sub> (a), Cu L <sub>3</sub> M <sub>45</sub> M <sub>45</sub> (b), Zn 2p <sub>3/2</sub> (c), Zn L <sub>3</sub> M <sub>45</sub> M <sub>45</sub> (d), O 1s (e), P 2p (f) signals for the Cu38Zn2Pb after 16 hours of exposure to the phosphate buffer solution. ....	138
Figure 7. 19: Apparent composition (at%) vs emission angle from ARXPS data for Cu38Zn2Pb after 1, 3 and 16 hours of contact with the phosphate solution. ....	140
Figure 7. 20: High resolution spectra of Cu 2p <sub>3/2</sub> (a), Zn 2p <sub>3/2</sub> (b), O 1s (c), Cu L <sub>3</sub> M <sub>45</sub> M <sub>45</sub> (d), Zn L <sub>3</sub> M <sub>45</sub> M <sub>45</sub> (e), P 2p (f), N 1s (g), and S 2p (h) for the Cu18Zn after 1 hour of contact with the saliva solution. ....	141
Figure 7. 21: High resolution spectra Cu 2p <sub>3/2</sub> (a), Zn 2p <sub>3/2</sub> (b), O 1s (c), Cu L <sub>3</sub> M <sub>45</sub> M <sub>45</sub> (d), Zn L <sub>3</sub> M <sub>45</sub> M <sub>45</sub> (e), P 2p (f), N 1s (g), and S 2p (h) for the Cu18Zn after 3 hours of contact with the saliva solution. ....	142
Figure 7. 22: High resolution spectra Cu 2p <sub>3/2</sub> (a), Zn 2p <sub>3/2</sub> (b), O 1s (c), Cu L <sub>3</sub> M <sub>45</sub> M <sub>45</sub> (d), Zn L <sub>3</sub> M <sub>45</sub> M <sub>45</sub> (e), P 2p (f), N 1s (g), and S 2p (h) for the Cu18Zn after 16 hours of contact with the saliva solution. ....	143
Figure 7. 23: Cu 2p <sub>3/2</sub> (a), Cu L <sub>3</sub> M <sub>45</sub> M <sub>45</sub> (b), Zn 2p <sub>3/2</sub> (c), Zn L <sub>3</sub> M <sub>45</sub> M <sub>45</sub> (b), O 1s (e), P 2p (f), N 1s (g) and S 2p (g) signals of the Cu37Zn sample after 1 hours of contact with the saliva solution. ....	145
Figure 7. 24: Cu 2p <sub>3/2</sub> (a), Cu L <sub>3</sub> M <sub>45</sub> M <sub>45</sub> (b), Zn 2p <sub>3/2</sub> (c), Zn L <sub>3</sub> M <sub>45</sub> M <sub>45</sub> (b), O 1s (e), P 2p (f), N 1s (g) and S 2p (g) signals of the Cu37Zn sample after 3 hours of contact with the saliva solution. ....	146
Figure 7. 25: Cu 2p <sub>3/2</sub> (a), Cu L <sub>3</sub> M <sub>45</sub> M <sub>45</sub> (b), Zn 2p <sub>3/2</sub> (c), Zn L <sub>3</sub> M <sub>45</sub> M <sub>45</sub> (b), O 1s (e), P 2p (f), N 1s (g) and S 2p (g) signals of the Cu37Zn sample after 16 hours of contact with the saliva solution. ....	147
Figure 7. 26: The Cu 2p <sub>3/2</sub> (a), Cu L <sub>3</sub> M <sub>45</sub> M <sub>45</sub> (b), Zn 2p <sub>3/2</sub> (c), Zn L <sub>3</sub> M <sub>45</sub> M <sub>45</sub> (b), O 1s (e), Pb 4f together with P 2p (f), N 1s (g) and S 2p (g) for the Cu38Zn 2pb after 1 hours of contact with the saliva solution are shown. ..	149
Figure 7. 27: Cu 2p <sub>3/2</sub> (a), Cu L <sub>3</sub> M <sub>45</sub> M <sub>45</sub> (b), Zn 2p <sub>3/2</sub> (c), Zn L <sub>3</sub> M <sub>45</sub> M <sub>45</sub> (b), O 1s (e), Pb 4f together with P 2p (f), N 1s (g) and S 2p (g) signals of the Cu38Zn2Pb sample after 3 hours of contact with the saliva solution. ....	150

Figure 7. 28: Cu 2p <sub>3/2</sub> (a), Cu L <sub>3</sub> M <sub>45</sub> M <sub>45</sub> (b), Zn 2p <sub>3/2</sub> (c), Zn L <sub>3</sub> M <sub>45</sub> M <sub>45</sub> (b), O 1s (e), Pb 4f together with P 2p (f), N 1s (g) and S 2p (g) signals of the Cu38Zn2Pb sample after 16 hours of contact with the saliva solution. ....	151
Figure 7. 29: Cu L <sub>3</sub> M <sub>45</sub> M <sub>45</sub> Auger signals of Cu37Zn after mechanical polishing, after 16 hours of contact with the buffer solution and after 1, 3 and 16 h of contact with the saliva solution. ....	153
Figure 7. 30: SEM images acquired on the Cu18Zn alloy after the mechanical polishing procedure, after 16 hours of exposure to the phosphate buffer solution and to the artificial saliva solution. ....	154
Figure 7. 31: SEM images acquired on the Cu37Zn alloy after the mechanical polishing, after 16 hours of exposure to the phosphate buffer solution and to the artificial saliva solution. ....	155
Figure 7. 32: SEM images acquired on the Cu38Zn2Pb alloy after the mechanical polishing, after 16 hours of exposure to the phosphate buffer solution and to the artificial saliva solution. ....	156
Figure 7. 33: SEM images acquired on the pure copper after the exposure to the saliva solution. ....	157
Figure 7. 34: SEM images acquired on the Cu18Zn alloy after the contact with the KSCN solution. ....	157
Figure 7. 35: SEM images acquired on the Cu37Zn alloy after the contact with the KSCN solution. ....	157
Figure 7. 36: Influence of the zinc content on the open circuit potentials measured after 1h, 3h and 16 h of immersion in a) artificial saliva, b) phosphate buffer. ....	158
Figure 7. 37: Variation of the specific polarization resistance R <sub>p</sub> with time of immersion for the different brass alloys in a) artificial saliva, b) phosphate buffer pH 7. ....	158
Figure 7. 38: Variation of the metal ion content in the surface film formed after exposure to the solutions. a) artificial saliva and b) phosphate buffer. ....	159
Figure 7. 39: Diagram log R <sub>p</sub> vs OCP for brass alloys (18 – 37 wt% Zn) exposed for 1, 3 and 16 hours in a) artificial saliva, b) diluted buffer solution pH 7. Same potential axes are used in order to facilitate the comparison of the two sets of data. ....	160
Figure 7. 40: Wagner chemical state plots of copper (a) and zinc (b). The BE and KE of the photoelectron and Auger signals are compared with the literature. ....	161
Figure 7. 41: Log (R <sub>p</sub> ) vs OCP diagram as diagnostic plot showing the different evolution of brass alloys in artificial saliva and in buffer solution. Other data on brass wind instruments are reported in Chapter 6. ....	162
Figure 8. 1: Micrographs acquired under optical microscope (10x and 20x of magnification) of the OO1 and OO2 samples. ....	170
Figure 8. 2: Survey spectra, Cu 2p <sub>3/2</sub> , Zn 2p <sub>3/2</sub> and Pb 4f on OO4 ancient brass samples. ....	171
Figure 8. 3: Relation between specific polarization resistance R <sub>p</sub> and open circuit potential of the samples reported in table 8.1. Data obtained brass model alloys immersed for 1, 3 and 16 h in artificial saliva in the pH = 7 buffer solution are included in the plot. ....	173
Figure 8. 4: Relation between open circuit potential and corrosion current of the samples reported in table 8.1. Data obtained on brass model alloys immersed for 1, 3 and 16 h in artificial saliva in pH = 7 buffer solution (Chapter 7) and data obtained on the as received and mechanically polished samples measured by the sensor (Chapter 6) are included in the plot. ....	175
Figure 8.5: Relation between open circuit potential and corrosion rate of the samples reported in table 8.1. The data obtained on brass model alloys immersed for 1, 3 and 16 h in artificial saliva in the pH = 7 buffer solution (Chapter 7) and the data acquired on the as received and mechanically polished samples measured by the sensor (Chapter 6) are included in the plot. ....	177



# *Chapter 1*

## *Introduction*

*This chapter presents a brief overview about the ancient brass musical instruments and the corrosion phenomena related to informed practice in the field of the new musical movement called historically informed performance practice. In Section 1.2 the scope and outline of this thesis are presented.*

## 1.1 Introduction

Copper and copper alloys are used in many industrial fields due to their physical and mechanical properties and to their good corrosion resistance [1]. Brass is a copper and zinc alloy which is malleable, ductile, durable, solderable and not thermosetting, easy to cast and has good corrosion resistance. The zinc content can be varied to produce a wide range of brasses with different properties. Brasses with a low zinc content (< 38 wt.%) can be cold worked and have good corrosion resistance; the increase of zinc improves the strength and ductility of these alloys while the electrical and thermal conductivities are reduced. Brasses with a high zinc content e.g. between 46 – 50 wt.%, can be hot worked; instead brasses with zinc content between 38 – 40 wt.% have notable properties, as they can be both hot and cold worked. Some other elements including lead, tin, aluminium may be added to the alloy in a range of 0.1 – 5 wt.% to enhance for example corrosion resistance or machinability properties [2].

Due to the good properties described above brass alloys have attracted great consideration over the years in various technological and artistic applications. Brass has been used to make pipes, tubes, condensers and heat exchangers, radiators, taps, and for its good corrosion resistance and the golden – yellow looking aspect it has also found applications in jewellery.

Furthermore, brass has been used since the Middle Ages as a material for the construction of lip vibrated musical instruments and since the 16<sup>th</sup> century brass has been exploited for the fabrication of wind musical instruments due to its good corrosion resistance, the ease of manufacturing of the instruments as well as its very good acoustic properties. Brass alloys used for historical instruments had a chemical composition that changed upon time due to the various production technologies of brasses. Before 1840s the Zn amount in the alloy was variable and lower than 30 wt.%: early instruments contained 70-90 wt.% copper and 10-30 wt.% zinc and 1-5 wt.% lead. Afterwards the zinc content was between 30 and 35 wt.% while the amount of lead was lower. It is worth to note that brass instruments usually do not show a homogeneous composition because the manufacturer used different alloy compositions for the fabrication of the various parts [3].

There is a musical movement called ‘historically informed performance practice’ (HIP) which started in the 1970s and proposes to play a music re-creating the same conditions of the past including the use of instruments corresponding to the period of the piece being firstly played. This movement became a dominant trend in contemporary musical practice since the performances are considered more authentic than those during which modern instruments are played. The instruments are called ‘period instruments’: they are either restored instruments or their copies for which the music was originally written. Musical instruments have changed a lot over time due to employment of new materials and techniques. For example, old wooden flutes have been replaced by nickel flutes and strings gut were

replaced by metals strings. The changes that have occurred over the years had an effect on the sound of the instruments and clearly, old instruments sound different from the way of today's instruments. Hence, through HIP movement, people have the occasion to hear the unique textures afforded by period instruments and orchestras.

Whereas, about the music before the 19<sup>th</sup> century the use of extant copies of old instruments has become established since it is complicated to find well conserved ones, for the music of the 19<sup>th</sup> and early 20<sup>th</sup> centuries it is fairly normal to play on original wind instruments. Historical wind musical instruments generally are conserved and well maintained in private or public collections in museums. For example the Burri Museum in Bern consists of more than 1200 brass wind instruments mainly of the 19<sup>th</sup> century [4].

As a matter of fact playing of historic instruments could involve a deterioration caused by for example corrosion processes taking place during the musical performance. Corrosion could alter the appearance but also the acoustic and mechanical properties. In fact, the main concern of museums and conservators besides mechanical damage is the corrosion of the brass instruments due to the high humidity inside the instruments during and after playing.

In a recent study [5] the humidity conditions were assessed on different historical brass instruments before, during and after being played. Measurements have shown that the internal relative humidity (RH) reaches very high levels (90%) in a few minutes of the musical performance and it takes several days to reach ambient RH (about 45%) again. Regularly played instruments have constantly a high level of internal relative humidity, which results in an increase of the risk of metal corrosion and susceptibility to stress damage.

In the field of museology and archaeology, preventive conservation is defined as “all measures and actions aimed at avoiding or minimizing future deterioration and loss.” [ICOM-CC 2008:2]. Understanding the mechanism of corrosion is thus the starting point in order to propose preventive approaches able to control the conditions that might cause corrosion and to prevent further damages.

An interdisciplinary research project entitled “*Brass instruments of the 19<sup>th</sup> and early 20<sup>th</sup> centuries between long-term conservation and use in historically informed performance practice*” has a clearly defined object of research, the brass instruments used in a Parisian theatre orchestra on a specific evening in May 1913 – for the world première of Igor Stravinsky's "Le sacre du printemps". This project was integrated with the one financially supported by the Italian Ministry of Research “Sustainability in Cultural Heritage” (SICH PRIN 2010/2011)

The project concerns the examination of the corrosion phenomena in historical instruments currently being used, and the proposal of an appropriate set of recommendations for the conservation and usage of historic instruments [6].

An interdisciplinary methodology is being developed for the evaluation and monitoring of the corrosion state inside historical brass instruments before and after being played and to establish the efficiency of preventive conservation measures.

## 1.2 Scope and outline of the thesis

The scope of the thesis is the development of innovative systems for monitoring and understanding corrosion inside ancient brass wind instruments of the 19<sup>th</sup> and 20<sup>th</sup> centuries to be used for diagnosis of the degradation mechanism that affects the artifacts.

According to the Conservation Committee of the International Council of Museums non-destructive, non-invasive and *in-situ* techniques should be developed to assess the conservation state of the ancient brass wind instruments. In-situ measurements are very important tools for conservators to obtain the relevant information on the corrosion state and rate and to control the efficiency of preventive conservation measures.

Since corrosion is an electrochemical process, electrochemical techniques provide an immediate access to the corrosion rate. The first objective of this work was to develop a small non-destructive and non-invasive electrochemical sensor for in-situ measurements inside ancient brass instruments to measure the corrosion potential and corrosion rate.

The electrochemical measurements do not provide any direct chemical information. Therefore, to correlate the measured potentials and the related corrosion rates with the corrosion state of the instruments, surface characterization was exploited to get information about the composition of the surface. Model brass alloys, produced so to have similar metallurgical structure as found in wind instruments from the 19<sup>th</sup> century, were used to perform the tests in the development phase of the method in order to preserve the state of ancient samples.

Pursuing this idea, this thesis is structured as follows:

- *Characterization of brass model alloys before the electrochemical test.* It is important to know the metallographic structure, the morphology and the surface roughness of the alloys together with their composition so to be able to correlate the corrosion potential values and the corrosion rates with the surface of the material under investigation. The chemical state identification and thus also the quantification based on the results of the curve fitting of the X-ray photoelectron spectra and the X-ray induced Auger electron spectra is challenging for copper and zinc compounds. In fact it is difficult to distinguish between Zn (II) and Zn (0) as between Cu (I) and Cu (0) using only their photoelectron signals. In the first part of this work a novel analytical strategy has been proposed for the identification and the quantification of the corrosion products formed on brass alloys.

*Electrochemical behaviour surface analytical study of brass model alloys after aging in neutral solutions.* The evaluation of the stability of the brass model alloys in neutral solutions



that simulate those that might be encountered inside the brass instrument during playing the music is a necessary step for understanding the results of the measurements carried out in the instruments. This aim was achieved by performing the corrosion tests using a phosphate buffer solution at pH 7 and an artificial saliva solution (pH 7.4). Open circuit potential, linear polarization, cathodic and anodic polarization measurements were measured. The corrosion potential, corrosion resistance and corrosion rate were monitored upon time. Moreover, electrochemical impedance spectroscopy (EIS) has been used to gain information about the mechanism of the corrosion processes. Surface morphology alterations were detected by optical and scanning electron microscopy and the patinas were characterized by XPS/XAES. These results enable the correlation between the electrochemical measurements and the surface properties.

*The development of a non-destructive electrochemical sensor for the in-situ determination of the corrosion rate inside historical brass wind instruments.* This aim was achieved and the sensor was tested on brass model alloys and then applied to the historical brass instruments.

A relevant outcome of this thesis concerns the influence of the surface composition on the corrosion resistance of the brass alloys in contact with saliva: the presence of  $\text{Cu}_2\text{O}$  and of  $\text{Cu}(\text{OH})_2$  catalyses the reaction of the oxygen reduction and it thus accelerates the anodic dissolution of the alloy. The brass alloys, exploited as model systems, demonstrate to be a powerful analytical tool for the understanding and clarifying the electrochemical mechanism of brass corrosion. The combined analytical approach based on surface chemistry and electrochemistry has demonstrated to be very useful for correlating the measurements inside the instruments with the surface status.

## References

1. Joseph R. Davis, Copper and Copper Alloys – ASM Specialty Handbook, ed. ASM International, USA (2001)
2. B. Tavasci, Tecnologia dei Materiali e Chimica Applicata, 2a parte, Tamburini Editore – Milano (1966)
3. M. Senn, H.J. Leber, M. Tuchschnid, N. Rizvic, Blechblasinstrumentenbau in Frankreich im 19. Jh.: Analysen von Legierung und Struktur des Messings zugunsten eines historisch informierten Instrumentenbaus, Proc. Symp. Romantic Brass II: Französische Hornpraxis und historischer Blechblasinstrumentenbau, Bern, Argus, Schliengen, 2012 (Edition, in press)
4. A. von Steiger, Die Instrumentensammlung Burri, Hintergründe und Herausforderungen, Bern. Eigenverlag, 2013
5. M. Ledergerber, E. Cornet, E. Hildbrand, Humidity in brass instruments and the prevention of corrosion, accepted to the International Conference Vienna Talk 2015, on Music Acoustics “Bridging the Gaps” [http://viennatalk2015.mdw.ac.at/?page\\_id=1000](http://viennatalk2015.mdw.ac.at/?page_id=1000)
6. Web site of the project “Brass instruments of the 19<sup>th</sup> and early 20<sup>th</sup> centuries between long-term conservation and use in historically informed performance practice” see <http://p3.snf.ch/Project-146330>.

## *Chapter 2*

### *Literature Review*

*In this Chapter a general description on the brass is presented. Firstly the different phases of brass and their different properties are described on the basis of the zinc content, followed by the effect that alloying elements have on the properties of brasses. Successively an overview on the corrosion of brass alloys is presented. The latest two paragraphs regard the development of production methods from the cementation to the distillation processes that allowed producing brass from copper and zinc. Processes that influenced the composition of the alloys and thus a brief description of the chemical composition of brass musical instruments before and after the 19<sup>th</sup> century is reported.*

## 2.1 Properties of brass

Brass is a copper and zinc alloy that is ductile, can easily be cold-worked, welded and cast and has good corrosion resistance. Brass is used in various technological and artistic applications including electrical equipments, tubes, condenser and heat exchanger, radiators, pipes, taps, cartridge cases, as well as decorative fixture and jewelry applications. Due to its very good acoustic properties, brass has been used for centuries for the construction of musical instruments.

### 2.1.1 Phase diagram of brass

The copper and zinc content can be varied to produce a wide range of brasses with different properties. The phase diagram of brass, reported in figure 2.1, shows the existence of three different phases:  $\alpha$ ,  $\beta$ ,  $\gamma$ . The most common alloys have a Zn content ranging between 28 – 42% [1] and can be formed by casting, rolling, drawing extruding and forging techniques [2]. The properties of brass mainly depend on the zinc content.

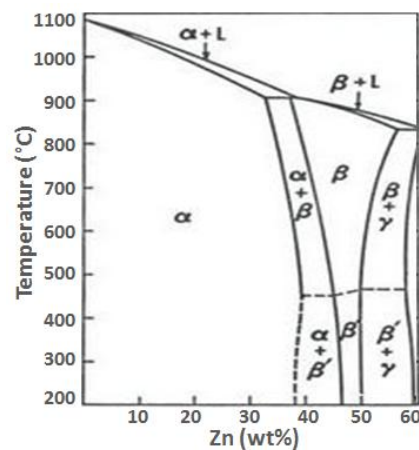


Figure 2. 1: Copper – zinc phase diagram [1].

The  $\alpha$  phase contains up to 37 % of zinc. It has a close packed cubic face centered lattice as pure copper. The lattice parameter changes from 3.608 Å for pure copper to 3.6849 Å for a brass with 34.9% of Zn [3], this increase is due to the larger size of the zinc atom ( $a_{Zn} = 1.25$  Å;  $a_{Cu} = 1.179$  Å) [4]. The  $\alpha$  brasses are further divided in two groups: red brasses (5 – 20% Zn) and gilding metals (20 – 36% Zn) used for the decorative brass fixtures, jewelry and for architectural applications. These types of brasses have good strength and ductility and are easily cold worked [1].

The  $\beta$  type of brass has a Zn content between 46 – 50 wt.%, showing a body centered cubic lattice. An allotropic transition is observed at about 460 °C quickly passing during cooling from a disordered to an ordered bcc structure where the copper is found in edges and zinc at the centre [5,6]. The  $\beta$  crystals are hard and they increase the strength but lower the ductility of the brass [7].

The ( $\alpha + \beta$ ) duplex phase structure, a mixture of  $\alpha$  and  $\beta$  crystals [1], appears at Zn contents of about 40%. The duplex brasses are cheaper and easier to produce than  $\alpha$  brasses [8]. The most important alloy belonging this group is the Muntz Metal, CuZn40 (40% of Zn) that has high strength and good cold workability. It is used mainly in shipbuilding industry [5].

### **2.1.2 Influence of alloying elements**

Brass alloys are made of copper and zinc, minor quantities of other alloying elements such as Pb, Sn, As, P, Sb can be added to enhance the properties of brasses such as workability and corrosion resistance, mainly to inhibit the process of dezincification (selective leaching of Zn from the alloy). The addition of tin (Sn) improves the corrosion resistance, increases the tensile strength and the hardness of brass [8]. The addition of a small amount of As, Ar or P can reduce the dezincification of  $\alpha$  brass. Also brass alloys containing aluminum, iron or manganese seem to possess a better resistance to corrosion [8].

The addition of lead at a concentration comprised between 1 and 3% by weight improves the workability [8 – 10]. Lead is insoluble in the alloy due to its very large atomic radius, it segregates and is found at grain boundaries reducing the brass shear strength [9]. Machinability is improved if lead is added in a range between 1 and 3%; a lead content higher than 3% does not provide significant improvement [10, 11].

Unfortunately, lead is a toxic metal with the most deleterious effects on the hemopoietic, nervous, reproductive systems and the urinary tract [12]. Severe regulations for the allowable lead levels released in drinking water and at the foundry provided the impetus for the development of lead-free brasses [13]. The release of lead in tap water causes serious problems to human health, for example, renal failure, hypertension and mental retardation in children. The maximum allowable concentration suggested by the WHO is 10 mg/dm<sup>3</sup>, while the US-EPA has proposed a value of 5mg/dm<sup>3</sup> [3, 14]. It has been reported that the brass fixtures are an important source of lead in drinking water in which the amount of lead released can exceed 50 mg/dm<sup>3</sup>.

Nowadays lead is being replaced by bismuth and selenium [15, 16]. Bi does not have the adverse health effect of lead and it can be expected to play the same of lead in the alloy. Lower Bi concentrations are allowed because Se enhances its effect [13].

## **2.2 Corrosion of brass alloys – dezincification**

Corrosion is defined as the deterioration of a material by reaction with its environment [17]. As the majority of metals, brass alloys sufferer of corrosion. Corrosion of metals in aqueous electrolytes or exposed to the atmosphere occurs by electrochemical reactions. In the literature, there are many

studies on the brass corrosion in aqueous environments at different pH levels both in the absence and in the presence of chloride ions [18, 19]. Most of the studies are referred to the dezincification process. Dezincification is a specific form of de-alloying, the selective leaching of the less noble metal (zinc) from the alloy. Three different hypotheses were proposed to define the mechanism of dezincification. The first hypothesis is based on the preferential dissolution of zinc [20 – 22], the second one assumes the simultaneous dissolution of copper and zinc from the alloy followed by a subsequent re-deposition of copper at the brass surface [23 – 25], the third hypothesis is based on a combination of the two above proposed mechanisms [26].

### **2.2.1 Corrosion in aqueous solution**

The corrosion behavior of brass alloys with a Zn content ranging from 5.5 to 38.0 wt.% and the behavior of leaded Cu38ZnPb alloy with different Pb contents (1.0 – 3.4 wt.%) was studied in neutral sulfate solutions in a concentration range from 0.01 M to 1 M Na<sub>2</sub>SO<sub>4</sub> [27]. The authors reported that the corrosion rate of brass increases with increasing zinc content and decreases with prolonged immersion due to the formation of a protective surface layer. The corrosion mechanism proposed is a dezincification process, starting with selective dissolution of zinc and continuing by simultaneously dissolution of zinc and copper, followed by a re-deposition of copper. Moreover Pb increases the corrosion resistance of the brass alloys studied due to the formation of a PbSO<sub>4</sub> that reduces the corrosion rates.

The corrosion behavior of brass alloys was investigated in aqueous solutions for different pH values. As an example, some authors [28] reported the results obtained after the exposure of three different brass alloys to an aqueous solution (buffer solution) of different pH values from acid to basic media. The results showed that the brass alloys underwent passivation after longer immersion time. In neutral and basic solutions the surface was covered by a Cu(I) oxide film. Instead, the corrosion rate was higher a pH 2 for all the electrodes that could be imputable to the presence of Cr<sub>2</sub>O<sub>7</sub><sup>2-</sup> in the acid medium which enhances the oxidation of the Cu(I) passive film into the soluble Cu(II) compound, leading to the increase of the corrosion rate [28].

### **2.2.2 Atmospheric corrosion**

Various literature studies report the corrosion behavior of brass under outdoor exposure [30 – 33]. Kleber and coworkers [34] reported a study in which the atmospheric corrosion of brasses (CuZn15 and CuZn20) in non-sheltered field exposure was investigated over years. In the first six months of exposure, a dezincification process dissolved zinc preferentially, but after about 12 months, the released went to more constant level. The results showed some zinc rich phases co-existed with

predominantly copper-rich phases to a higher extent for CuZn15. This effect could be explained based on two mechanisms reaction, firstly an initial selective dissolution of zinc followed by a simultaneous dissolution of copper and zinc and subsequent re-deposition of copper on a porous layer [34]. Cuprite  $\text{Cu}_2\text{O}$  was the predominantly phase revealed at the surface together with basic copper sulphates (Posnjakite and Brochantite). In addition, zinc carbonate, sulphate and crystalline (ZnO) zinc-rich corrosion products covered a large portion of the brass surfaces due to the outdoor-polluted site [34]. In a previous work [35] it was analyzed with XPS the surface of  $\alpha$  brass alloy with different Zn content (35 – 20 wt.%) after exposure to air at room temperature (moderate humidity). The authors reported that at first there is the formation of a ZnO film (about 10 nm) with Cu(0) trapped in the film. Subsequently a  $\text{Cu}_2\text{O}$  film formation followed the ZnO. This films are covered by a terminal thin layer (about 0.5 nm) mainly composed by Cu(II) species such as CuO and  $\text{Cu}(\text{OH})_2$ .

### **2.2.3 Effect of mechanical polishing**

The effect of the mechanical pretreatment on the surface of brass alloys was studied in the literature. T.M.H. Saber and A.A. El Warraky [36] compared the effect of dry and wet mechanical polishing procedure on the CuZn30 using SiC paper of grades from 150 to 100. Argon ion sputtering and a cleaning treatment with acetone were also investigated. Dry cleaning results showed the removal of both components of the alloy during cleaning, moreover promoting preferential diffusion of zinc to the alloy surface, probably due to the increase of the temperature induced by the grinding procedure.

## **2.3 Development of brass production methods**

Brass is a copper-zinc alloy and its production started in Asia Minor after the first millennium BC but a few examples of prehistoric copper alloys containing zinc were found [38]. By the 1st century BC the Romans used copper-zinc alloys for coinage but also for decorative metalwork replacing bronze. By the 3<sup>rd</sup> century AC an alloy of copper with a little amount of lead, zinc and tin called as modern leaded gunmetal was regularly used [38].

By the 1<sup>st</sup> century BC [38] before the intentional production of zinc metal through distillation processes (16<sup>th</sup> century AC [39, 40]) the cementation process was used for producing brass until the middle of 19<sup>th</sup> century when zinc distillation was developed in Europe at the industrial scale [40, 41]. The cementation process is a method in which brass is produced directly by zinc ore heated with charcoal and pieces of metallic copper in a sealed crucible [39 – 42]. The zinc ore was heated to about 1000°C in order to vaporize the zinc, the presence of charcoal provides the reducing atmosphere to reduce zinc ore to zinc. The zinc vapor was forced to diffuse into the solid copper (sealed crucible) and to form brass [38, 39, 42, 43]. After this process, the temperature was raised and the melted brass was stirred to form a uniform alloy [38]. Zinc ore was mainly composed by smithsonite,  $\text{ZnCO}_3$ , and herminophite,  $2\text{ZnO}\cdot\text{SiO}_2\cdot\text{H}_2\text{O}$  both referred as calamine ore found in association with copper and

lead ores [38, 43]. The adsorption of zinc in copper metal during the cementation process was dependent on the purity of copper and zinc. Lead and tin reduce notably the solubility of zinc in the copper-zinc alloy and for example 2% of lead would adsorb 4% less of zinc [43], this could be due to the fact that metals soluble in the alpha-phase brass may replace zinc in the proportions 1:2 for tin and 1:4 for lead [38]. However if the lead content is more than 5% the lead was most likely added on purpose since it lowered the temperature of the process [38]. After the 16<sup>th</sup> century, metallic zinc has been started to be imported in Europe from the East with the name of *zinken*. India was the chief source of metallic zinc in Europe [45]. The direct method to make brass from metallic zinc and copper appeared to be well established from the middle of the 19<sup>th</sup> century [40] and by the 1801 in several part of Europe [44].

## 2.4 Chemical composition of brass musical instrument over time

Brass is a suitable material for the construction of wind instruments due to its good mechanical, physical and acoustic properties. These properties are affected primarily by the amount of zinc present in the material [46]. The chemical composition of the alloy, and especially the ratio of zinc to copper, is thus an extremely significant parameter in the manufacturing process [46]. Brasses produced in the sixteenth until the middle of the 19<sup>th</sup> -century showed an inhomogeneous composition that includes several trace elements. Lead is the most abundant trace elements as it had been added to improve the mechanicability property.

In a study reported in literature [46] the authors analyzed more than 500 brass artefacts from the 1600s or earlier to the 1900s by X-ray Fluorescence (XRF). The results presented showed that brasses from the 17<sup>th</sup> century had a Zn content ranging between 15 to 23 wt.% and Pb, Sn, Al, Fe, Ni, P, Si and As were also found. The presence of aluminum and silica was hypothesized derived either from dust or from a cleaning product.

In another study, the authors analyzed brass wind instrument of the 19<sup>th</sup> century by *Energy-Dispersive-X-Ray-Fluorescence analysis (ED-XRF)* results. Also in these brass wind instruments Cu, Zn, Pb, Sn, Sb, Ni, Fe, Co, Si, Al were detected. Silicon and aluminium are not alloying elements but can be related to corrosion products or impurities of the raw materials used to produce the alloy.

As reported in the work of Senn et al. [47], the chemical composition of French musical instruments of the nineteenth century showed some variability in the copper and zinc content. In fact the amount of copper could range between 64% and 72% and that of zinc between 21% and 38%. Instead, the content of Pb was generally comprised between <0.05 and 3.5%, while the Sn content was between <0.05 and 0.7%. Lead and tin were added to improve the machinability of the brasses during the manufacture. Iron (0.05% - 0.5%), nickel (<0.05% - 0.3%) and antimony (<0.05 and 0.1%) were also detected.



The difference in composition between a contemporary brass alloy Cu37Zn and a brass of the 19<sup>th</sup> or earlier influences their physical properties and has a direct effect on structural vibrations [46, 47]. In recent studies, advanced numerical techniques have been extensively used in the study of structural vibrations and in particular in the study of the influence of material composition on wall vibration in brass wind instruments [46, 49].

## References

1. J.R.Davis, Copper and CopperAlloys, ed. Asm International(2001)
2. K. Hewitt, T. Wall, The zinc industry, ed. Woodhead Publishing Limited – Cambridge, England (2000)
3. P.Atkins, L.Jones, Principi di Chimica, ed. Zanichelli (2012)
4. B.H. Mahan, Chimica Generale e Inorganica, Ambrosiana (1971)
5. A. Cigada, T. Pastore, Struttura e proprietà dei materiali metallici, ed. McGraw-Hill (2012)
6. P. Haasen, Physical Metallurgy, ed. Cambridge University press (1996)
7. A.C. Davis, The Science and Practice of Welding, ed. Cambridge University press (1963)
8. Lytle, D.A., Schock, M.R., stagnation time, composition, pH, and orthophosphate effects on Qmetal leaching from brass, US Environmental Protection Agency (EPA), p.172
9. C. Nobel, F. Klocke, D. Lung, S. Wolf, Procedia CIRP 14 ( 2014 ) 95 – 100
10. C. Vilarinho, J.P. Davimb, D. Soares, F. Castro, J. Barbosa, Journal of Materials Processing Technology 170 (2005) 441–447
11. M.A. Taha, N.A. El-Mahallawy, R.M. Hammouda, T.M. Moussa, M.H. Gheith, A. Shams Engineering Journal 3 (2012) 383–392
12. N.C. Papanikolaou, E.G. Hatzidaki, S. Belivanis, G.N Tzanakakis, A.M Tsatsakis, A. La Fontaine, V.J. Keast, Materials Characterization 57 (2006) 424–429
13. D. Zivkovic, E. Begovic, A. Kostov, S. Ekinovi, Journal of Environmental Protection and Ecology 13 (2012) 1914–1920
14. S. Kumar, T.S.N. Sankara Narayanan, A.Manimaran, M. Suresh Kumar, Materials Chemistry and Physics, 106 (2007) 143 – 141
15. D.T. Peters, Modern Casting, 87 (1997) 57–9.
16. H.T. Michels, Advanced Materials and Processes 160 (2002) 75
17. G.E. Totten, H. Liang Mechanical Tribology: Materials, Characterization, and applications, ed. Marcel Dekker, Inc. (2004)
18. K.Isamail, R. Elsherif, W. Badawy, 49 (2004) 5151 – 5160
19. W.A. Badawy, F. Al-Kharafi, CORROSION Nace 55 (1999) 268 – 277
20. E.P. Polubkin, M. Shuldner, TAIME, 161 (1945) 214
21. E.E. Langenegger, F.P.A. Robinson, Corrosion 25 (1968) 59
22. C. H. Stiwell, E. C. Turniseed, Industrial and Engineer Chemistry, 26 (1934) 740
23. U.R. Evans, The corrosion of Oxidation of Metals, ed. Edward Arnold, London (1960)
24. S. Selvaraj, S. Ponmariappan, M. Natesan, N. Palaniswamy, Corrosion Reviews, 21 (2003) 41- 74
25. H. Sugawara, H. Ebiko Corrosion Science, 1967 (1967) 513 – 523
26. R. W. FINK, Transactions of the American Electrochemical Society, 75 (1939) 441

27. K.M. Ismail, S.S. El-Egamy, M. Abdelfata, *Journal of Applied Electrochemistry*, 31 (2001) 663–670
28. W. A. Badawy, F. Al-Kharafi, *Corrosion Nace* 55 (1999) 268 – 277
29. A. Krätschmer, I. O. Wallinder, C. Leygraf, *Corrosion Science* 44 2002, 425–450
30. R. Holm, E. Mattsson, *ASTM STP 767* (1982) 85-105.
31. G. Herting, S. Goidanich, I.O. Wallinder, C. Leygraf, *Environmental Monitoring and Assessment* 144 (2008) 455–61.
32. J.P. Franey, *ASTM STP 964* (1988) 306–15.
33. S. Goidanich, J. Brunk, G. Herting, M.A. Arenas, I. Odnevall Wallinder, *Science of The Total Environment*, 412–413 (2011) 46–57
34. C. Kleber, M. Schreiner, *Corrosion Science* 45 (2003) 2851–66.
35. T.L. Barr, J.J. Hackenberg, *Applications of Surface Science* 10 (1982) 523 – 545
36. T.M. Saber, A.ElWarraky, *Br. Corr. J.* 26 (1991) 279
37. D.A. Scott, *Copper and Bronze in Art: Corrosion, Colorants, Conservation*, Ed. Getty Trust Publications: Getty Conservation Institute (2002)
38. Paul T. Craddock, *Journal of Archeological Science* 5 (1978) 1 – 16
39. P.T. Craddock, K. Eckstein, *Production of brass in Antiquity by direct reduction*, *Mining and Metal Production through the ages*, ed. P.Craddock and J.Lang (2003)
40. D. Bougarit, F. Bauchau, *Journal of the Minerals, Metals and Materials Society*, 62 (2010) 27–33
41. J. Day, *Brass and Zinc in Europe from the Middle Ages until the Mid-nineteenth Century*, 200 years of Zinc and Brasses, ed. P.T. Craddock, 1988
42. P.T. Craddock, *Archeometry* 27 (1985) 17 – 41
43. C.P. Thornton. “Of brass and bronze in prehistoric Southwest Asia.” In *Metals and Mines: Studies in Archaeometallurgy* by S. La Niece, D. Hook, P. Craddock, ed. London: Archetype Publications (2007)
44. A.L. Bacon, *A technical study of the alloy composition brass wind musical instrument (1951 – 1867) utilizing non-destructive X-ray Fluorescence – volume 1*, PhD thesis in Archeometallurgy (2003)
45. A.K. Biswas, *Indina Journal of Science* 41 (2006) 159 – 174
46. Hannes W. Vereecke, Bernadette Frühmann, and Manfred Schreiner, *Historic Brass Society Journal* 24 (2012) 61-77
47. M. Senn, H.J. Leber, M. Tuchschnid, N. Rizvic, *Blechblasinstrumente aus dem Frankreich des 19. Jh, Legierung und Struktur des Messings in Romantic Brass II – Symposium HSK Bern“*, Autunno 2013

48. V. Chatziioannou, W. Kausel, T. Moore, "The Effect of Wall Vibrations on the Air Column Inside Trumpet Bells," in Proceedings of the Acoustics 2012 Nantes Conference (Nantes, France), 2243–48
49. W. Kausel, D.W. Zielow, T.R. Moore, Journal of the Acoustical Society of America 128/5 (2010) 3161–3173

## *Chapter 3*

### *Investigation methods*

*In this Chapter an introduction to the fundamentals of the characterisation techniques used in this work is given. In the first Section the principles of the electrochemical methods, in particular the electrochemical impedance spectroscopy (EIS), and of X-ray photoelectron spectroscopy (XPS) will be presented. In the following paragraphs a short description of the X-ray fluorescence (XRF), scanning electron microscopy (SEM) and atomic force microscopy (AFM) is also provided.*

### 3.1. Corrosion reactions

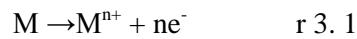
Corrosion is a natural process that occurs when a metal reacts with the environment forming oxides. This reaction causing the deterioration of metals can be classified in two categories: dry and wet corrosion. The first one usually occurs at high temperatures and does not require the presence of moisture or water. Wet corrosion occurs when a metal is in contact with an aqueous electrolyte: at the metal-solution interface oxidation – reduction reactions can take place causing the dissolution of the metal and the reduction of oxygen. As a result the metal ions can be dissolved in the electrolyte or form a new compound (oxide).

Corrosion processes are electrochemical reactions that obey the laws of thermodynamics and kinetics and can be studied by electrochemical techniques.

### 3.2. Fundamentals

#### 3.2.1. Thermodynamic of corrosion [1 – 2]

The generic corrosion process can be described as the sum of an anodic and a cathodic reaction. The anodic reaction is the oxidation of the metal involving loss of electrons:

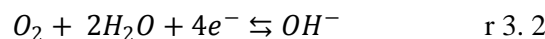


According to Nernst's law the equilibrium potential  $E$  is for the (r 3.1):

$$E_{\text{anod}} = E^0 + \frac{RT}{nF} \ln a_M^{n+} \quad \text{eq 3. 1}$$

Where  $E^0$  is the standard potential (V),  $T$  is the absolute temperature (K),  $F$  is the Faraday constant (96486 C/mol),  $R$  is the universal gas constant (8.314 JK<sup>-1</sup>mol) and  $n$  is the number of exchanged electrons.

The cathodic reaction is a reduction reaction that involves a gain of electrons. In natural environments the cathodic reaction are reduction of oxygen (r 3.2) and reduction of protons (r 3.3). Both reduction reactions depend on the pH, thus in neutral or alkaline solution, the cathodic reaction is the reduction of oxygen:

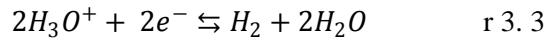


$$E_{O_2} = E^0 + \frac{RT}{4F} \ln \frac{P_{O_2}}{a_{OH^{-}}^4} \quad \text{eq 3. 2}$$

For oxygen partial pressure  $P_{O_2} = 1$  atm and with  $E^0 = 1.23$  V the equation becomes

$$E_{O_2} = 1.23 - 0.059 \text{ pH} \quad \text{eq 3. 3}$$

In acidic environments the hydrogen reduction occurs according to the following reaction:



$$E_{H^+} = E^0 + \frac{RT}{2F} \ln \frac{a_{H^+}^2}{P_{H_2}} \quad \text{eq 3. 4}$$

For hydrogen partial pressure  $P_{H_2} = 1 \text{ atm}$  and with  $E^0 = 0 \text{ V}$  the equation becomes

$$E_{H^+} = -0.059 \text{ pH} \quad \text{eq 3. 5}$$

From a thermodynamic point of view the change in Gibbs free energy ( $\Delta G$ ) predicts whether or not a (corrosion) reaction takes place spontaneously. If  $\Delta G < 0$  a reaction occurs spontaneously. Since,  $\Delta G = -nF\Delta E$  and  $\Delta E = (E_{\text{cathod}} - E_{\text{anod}})$ , consequently a metal can corrode if:

$$E_{\text{cathod}} > E_{\text{anod}} \quad \text{eq 3. 6}$$

The Pourbaix diagram, also known as potential – pH equilibrium diagram, indicates the possible stable phases of an aqueous electrochemical system. The diagram refers to equilibrium conditions and presents the stability regions of the metal (immunity), its ions and its oxidized compounds. Figure 3.1 shows the Pourbaix diagram of copper – water system at 25°C [3]. Note that the potentials of the two cathodic reactions, hydrogen (eq. 3.3) and oxygen reduction (eq. 3.5) are plotted in the diagram as line a and b respectively.

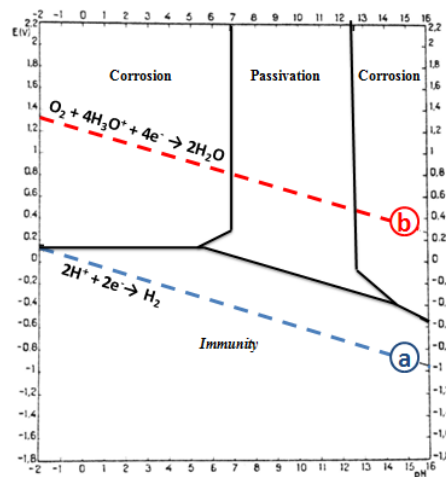


Figure 3. 1: Pourbaix diagram for the system copper – water at 25°C.

According to the diagram and eq. 3.6, copper is found to be immune at any pH value in oxygen-free environments, meaning that the metal cannot corrode in these conditions. Passivity stable state is found between pH 6 to 13 and above the line shifted about 0.4 V from line a. In this region copper is passivated by the formation of an oxide layer consisting of copper oxides. The corrosion regions are

those were the copper dissolution is occurring: in this situation reaction products such as  $\text{Cu}^{2+}$ ,  $\text{CuO}_2^{2-}$  and  $\text{HCuO}_2^-$  are soluble and thus no protection of the metal from further dissolution is present [3].

### 3.2.2. Corrosion kinetics

Thermodynamic predicts whether corrosion can occur, but the rate at which corrosion processes occur depends on the reaction kinetics.

Corrosion process involves an electron exchange between an anodic and cathodic reaction, causing a current flow. The current flow causes an electrode polarization, that is a shift of the electrode potential  $E$  away from its equilibrium value. The electrode polarization is measured experimentally as overpotential,  $\eta$ . According to Tafel's law  $\eta$  is defined as:

$$\eta_c = E_c - E_{eq,c} = -\beta_c \ln \frac{i_c}{i_{0,c}} \quad (\text{cathode}) \quad \text{eq 3.7}$$

$$\eta_a = E_a - E_{eq,a} = -\beta_a \ln \frac{i_a}{i_{0,a}} \quad (\text{anode}) \quad \text{eq 3.8}$$

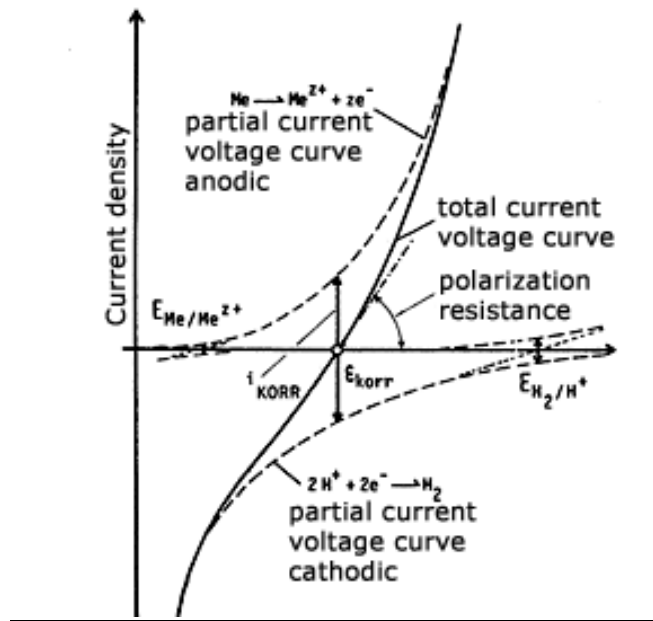


Figure 3. 2: Total current/voltage diagram of a metal electrode corroding under  $\text{H}_2$  formation. Dotted curve (-----) indicates partial current density (eq. 3.7, 3.8); the solid line (\_\_\_) indicates the total current density.

Where  $E_{c,a}$  are the actual potentials,  $E_{eq,c,a}$  are the electrode equilibrium potentials,  $\beta_{c,a}$  are the Tafel constants (volts/decade),  $i_{c,a}$  are the current densities and  $i_{0,c,a}$  are the exchange current densities referring to cathode and anode reactions (Fig.3.2).

As the electrons released by the anodic reaction (r 3.1) have to be consumed immediately by a cathodic reaction (r 3.2 or r 3.3), anodic and cathodic current have to be identical. Thus the corrosion potential  $E_{corr}$  (or open circuit potential) is determined by the electroneutrality condition between the anodic and cathodic reactions, being the corrosion current  $i_{corr} = i_a = |i_c|$ . As anodic and cathodic



current have the same magnitude, no net current can be measured. A corrosion system can thus be considered as a short-circuited battery.

### 3.3. Electrochemical measurements

#### 3.3.1. Open circuit potential measurements

The open circuit potential  $E_{\text{corr}}$  depends on the kinetics of the metal dissolution (eq. 3.7) and the reduction reaction (eq. 3.8) of the environment, thus it characterizes a metal – solution system.

$E_{\text{corr}}$  of a metal – solution system is experimentally measured as the potential difference between the metal under test and a *reference electrode* (an electrode system with defined and constant potential, e.g. Ag/AgCl) in the test solution with a high impedance voltmeter (or a potentiostat). Thus by measuring  $E_{\text{corr}}$  and comparing with the Pourbaix diagram it is possible to get a first indication if a metal is the active or in the, passive state. Important information can be obtained from the variation upon time: if a corrosion process is taking place  $E_{\text{corr}}$  usually decreases with time, while if a passive layer is forming at the surface of the metal sample  $E_{\text{corr}}$  increases with time to more positive values [4].

#### 3.3.2. Polarization curves

From polarization curves or current density/potential curves (see Fig. 3.3) information about the corrosion mechanism and the corrosion rate can be obtained. The principle of additivity of Wagner and Traud and the exponential potential dependence of electrochemical reactions (eq. 3.7, eq. 3.8) lead to the equation for the total current density/potential curve. The total current  $i_s$  for a system with metal dissolution and hydrogen evolution is given by:

$$i_s = i_{\text{corr}} \left( \exp\left(\frac{E - E_{\text{corr}}}{\beta_{a,Me}}\right) - \exp\left(\frac{E_{\text{corr}} - E}{\beta_{c,H}}\right) \right) \quad \text{eq 3.9}$$

When the electrode potential  $E$  lies far from the corrosion potential, the cathodic resp. anodic partial current can be neglected (see Fig. 3.3) and the experimentally measured total current density  $i_s$  equals exactly the anodic resp. cathodic partial current density (eq 3.10):

$$i_{s,a} = i_{\text{corr}} \exp\left(\frac{E - E_{\text{corr}}}{\beta_{a,Me}}\right); \quad i_{s,c} = i_{\text{corr}} \exp\left(\frac{E_{\text{corr}} - E}{\beta_{c,H}}\right) \quad \text{eq 3.10}$$

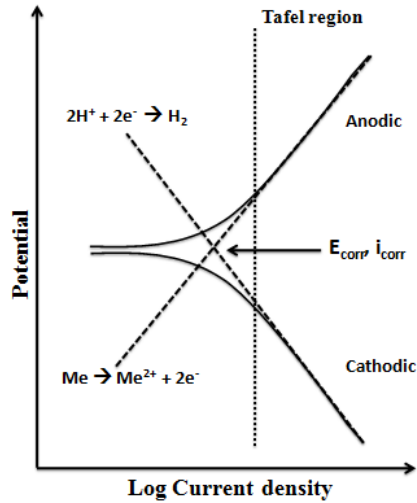


Figure 3. 3: Scheme of anodic and cathodic polarization curve showing Tafel lines.

With these two equations, the *kinetics* of the anodic and cathodic partial reactions can be studied. The Tafel equation can be written as straight lines (the so-called *Tafel lines*) sees Fig. 3.3 and thus transferring to the logarithmic scale, the equations result in:

$$(E-E_{\text{corr}}) = a + \beta'_{\text{Me}} * \ln i_s \quad \text{natural logarithm} \quad \text{eq 3. 11}$$

$$(E-E_{\text{corr}}) = a + \beta_{\text{Me}} * \log i \quad \text{decadic logarithm} \quad \text{eq 3. 12}$$

where  $a$  and  $\beta$  are constants. From the slope, the *Tafel constant*  $\beta$  can be determined and allows conclusions about the mechanism of the electrochemical reactions.

$$\frac{\Delta\eta}{\Delta \ln i} = \beta_{\text{Me}} = \frac{RTn}{F(1-\beta)} \quad \text{eq 3. 13}$$

Where  $\beta'_{\text{Me}} = 2.3 \beta_{\text{Me}}$ .

Further on, the (extrapolated) anodic and cathodic Tafel regions intersect at the corrosion potential, the current at this point is the corrosion current density  $i_{\text{corr}}$ . Thus from polarization curves the corrosion rate can be determined.

### 3.3.3. Polarization resistance

When the electrode potential  $E$  is *very close to the corrosion potential*  $E_{\text{corr}}$ ,  $(E - E_{\text{corr}}) \cong dE$  and the exponential functions can be approximated as

$$\exp^x (x \rightarrow 0) = x \quad \text{eq 3. 14}$$

The equation for the total current density/potential curve results in

$$i_s(dE) = i_{\text{corr}} (E - E_{\text{corr}}) \cdot \left( \frac{1}{\beta_{\text{Me}}} - \frac{1}{\beta_{\text{H}}} \right) \quad \text{eq 3. 15}$$

This results in a straight line with the slope that is the inverse to the polarization resistance  $R_p$  of the system

$$\frac{di_s}{dE} = i_{corr} \cdot \left( \frac{1}{\beta_{Me}} - \frac{1}{\beta_H} \right) = \frac{1}{R_p} \quad \text{eq 3. 16}$$

The corrosion current density,  $i_{corr}$ , (often termed as corrosion rate) cannot be measured, but it can be determined indirectly by linear polarization measurement. The working electrode is slightly ( $\pm 10$  mV) polarized away from its open circuit potential value and the current needed is measured. This is obtained through a potential scan from higher to lower values than the OCP. The scheme of the processes is shown in figure 3.2.

The metal polarization induces a current flow and the corrosion resistance can be found by taking the slope of the applied potential versus current density curve:

$$\frac{1}{R_p} = \frac{\Delta i}{\Delta E} = \frac{2.303 (\beta_a + \beta_c)}{\beta_a \beta_c} i_{corr} \quad \text{eq 3. 17}$$

Where  $\beta_c$  and  $\beta_a$  are the anodic and cathodic constants which are the slope of the polarization curve also called Tafel slopes determined by scanning the potential over a range of about  $\pm 250$  mV from the OCP. The Tafel slope are related to the kinetics of the oxidation – reduction reactions involved during the corrosion reaction. Figure 3.3 shows schematically both the anodic dissolution of metal and the cathodic reduction of hydrogen ions in acid solutions [5].

From the polarization resistance the corrosion rate  $i_{corr}$  for uniform corrosion can be calculated (eq. 3.17). The Tafel constants of the anodic partial reaction can be assumed to be equal to 60 mV, the one for the cathodic partial reaction can be assumed to be 120 mV.

Using Faraday's law the corrosion rate  $v_{corr}$  ( $\mu\text{m}/\text{year}$ ) can be calculated:

$$v_{corr} = \frac{M}{nFd} \cdot i_{corr} \quad \text{eq 3. 18}$$

Where  $M$  is the molar mass of the corroding metal,  $d$  is the density,  $n$  is the number of electrons exchanged during the reaction and  $F$  is the Faraday constant.

### 3.3.4. Electrochemical Impedance Spectroscopy

Electrochemical impedance spectroscopy (EIS) is a powerful tool for the study of the electric properties of materials and of the processes taking place at the electrode – solution interface. EIS is a non-destructive electrochemical method for the evaluation of a wide range of materials, including organic coatings, anodized films and corrosion inhibitors. Corrosion rate, electrochemical mechanisms, reaction kinetics, detection of localized corrosion might be determined from the EIS data [6]. The processes involved in the transport of mass and charge can be represent by elements of a model circuit. During an EIS experiment the system under investigation is perturbed by a small amplitude ac signal and the output signal is recorded so the cell's response is pseudo – linear.

Impedance analysis of linear circuits is easier than analysis of non-linear ones. A linear system possesses the important property of superposition. If the input consists of the weighted sum of numerous signals, then the output is simply the superposition, that is, the weighted sum, of the responses of the system to each of the signals [7]. Electrochemical reactions are non-linear as it can be seen from the graph current versus voltage (figure 3.4). A pseudo linear system can be achieved using a small amplitude signals thus the output signal is recorded at the same frequency as the input but shifted in phase [7].

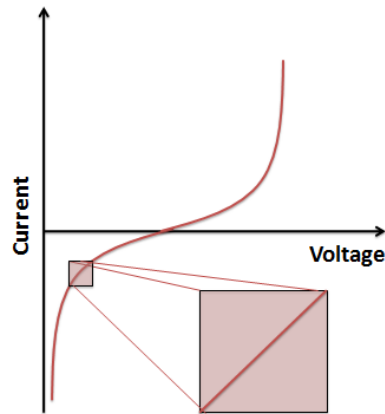


Figure 3. 4: Current vs Voltage curve showing a pseudo – linear system

In a first approximation, as the perturbation *signal* is small, the current response will be a linear response as well. If the applied sinusoidal signal is plotted on the x-axis of a graph and the output sinusoidal signal on the y-axis, an oval is obtained called a Lissajous figure (figure 3.5).

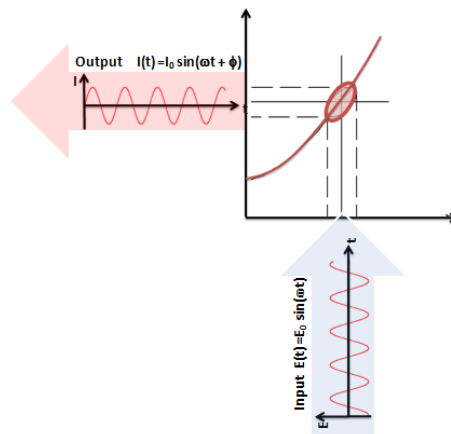


Figure 3. 5: Lissajous figure

The input potential excitation signal with small AC amplitude can be expressed in the time domain in Cartesian and polar variables as :

$$E(t) = E_0 \sin(\omega t) = E_0 \exp(j\omega t) \quad \text{eq 3. 19}$$

Where  $E(t)$  is the potential at time  $t$ ,  $E_0$  is the amplitude of the excitation signal,  $\omega$  is the angular frequency and  $j$  is the imaginary number ( $j = \sqrt{-1}$ ).

The output current signal,  $I(t)$ , can be expressed as:

$$I(t) = I_0 \sin(\omega t + \phi) = I_0 \sin(j\omega t + \phi) \quad \text{eq 3. 20}$$

Where  $I_0$  is the amplitude of the output signal and  $\phi$  is the phase shift. The impedance of the system can be calculated from an expression analogous to Ohm's law:

$$Z(\omega) = \frac{E(t)}{I(t)} = Z_0 \exp(j\phi) = Z_0(\cos\phi + j\sin\phi) = Z_{re} + jZ_{im} \quad \text{eq 3. 21}$$

Where  $Z_{re}$  and  $Z_{im}$  are the real and imaginary part of the impedance respectively.

### Data presentation

EIS data may be presented as a Nyquist or Bode Plot. The Nyquist or complex plan plot (Fig. 3.6a) is obtained plotting the imaginary part of the impedance  $-Z_{im}$  versus the real part  $Z_{re}$ . Each point of the Nyquist plot corresponds to the impedance at a given frequency value. The frequency increases to the right to the left of x – axis. In the Nyquist plot the impedance  $Z$  can be represented as a vector of  $|Z|$  magnitude at a phase angle  $\phi$  (angle between this vector and the x-axis). The Nyquist plot is very useful and popular because its shape yields (as a kind of fingerprint) insight into possible reaction mechanism and the kinetics governing interfacial processes [7]. A perfect semicircle is characteristic of a single time constant while multiple semicircles can be related to the presence of more than one time constant. A depressed semicircle indicates that a more detailed model is required [7].

Since no indication of frequency is shown from a Nyquist plot a further impedance representation is the Bode plot (figure 3.6 b,c). Bode plot clearly shows frequency information. The impedance is plotted with log frequency on the x-axis and both the absolute value of the impedance,  $|Z|$  (Fig.3.7a) and phase-shift on the y-axis (Fig.3.7b).

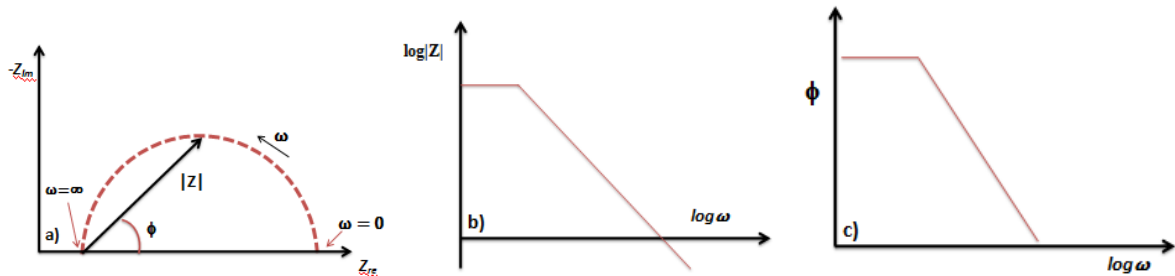


Figure 3. 6: Graphical representation of the impedance as a) Nyquist and b,c) Bode plots.

### 3.3.4.1. Electrical Circuit Elements

Data obtained by EIS measurements are usually analyzed by fitting the data to an equivalent electrical circuit model. Most of the circuit elements are common electrical elements such as resistors,

capacitors, inductors and their impedance; they are listed in Table 3.1. *Note that all model circuit elements must be based on a physical equivalent circuit in the electrochemical system under study.*

Table 3. 1: Impedance of a resistor, capacitor and inductance.

Element	Impedance	Note
Resistor R	$Z = R$	No imaginary part of impedance
Capacitance C	$Z = \frac{j}{j\omega C}$	No real part of impedance
Inductance L	$Z = j\omega L$	No real part of impedance

The single elements of electrical circuits are described below.

**Resistor, R.** The impedance of a resistor is independent of frequency and has no imaginary component (no phase shift). With only a real impedance component, the current through a resistor stays in phase with the voltage across the resistor.

$$Z_R = \frac{E(t)}{I(t)} = \frac{E_0 \sin(\omega t)}{I_0 \sin(\omega t)} = R \quad \text{eq 3. 22}$$

The equivalent circuit element R could be associated to the electrolyte resistance, the polarization resistance or the charge-transfer resistance. In the Nyquist plot a resistor is represented by a point on the  $Z_{re}$  – axis, its position depends on the R value [7 – 9].

**Capacitor, C.** The current flow in a capacitor is defined by the following equation:

$$I(t) = C \frac{dE(t)}{dt} \quad \text{eq 3. 23}$$

Thus the impedance of a capacitor C is described by the relation:

$$Z_C = \frac{E(t)}{I(t)} = \frac{E_0 \sin(\omega t)}{I_0 \sin(\omega t + \phi)} = \frac{1}{jC\omega} \quad \text{eq 3. 24}$$

The impedance of capacitor  $Z_c$  decreases as the frequency of the excitation signal is increased. Ideal capacitors have only an imaginary impedance component. The current through a capacitor is phase shifted by  $90^\circ$  respect to the voltage. As a result a capacitor is represented in the Nyquist plot by a series of points falling on a line perpendicular to the x-axis. The capacitor in an equivalent circuit could be associated to the electrical double layer existing at the interface between an electrode and its surrounding electrolyte, formed as the ions from the solution adsorb onto the electrode. Thus a non-polarizable metal in contact with the solution could behave like a capacitor. The double layer capacitance  $c_d$  depends on the temperature, ionic concentrations, surface state, electrode potential, roughness, and many other factors [6 – 9]. In addition, organic coatings behave as a capacitance.

**Inductor, L.** The current that flows through an inductor is defined by the following equation:

$$Z_i = \frac{E(t)}{I(t)} = \frac{E_0 \sin(\omega t)}{I_0 \sin(\omega t + \phi)} = j\omega L \quad \text{eq 3. 25}$$

Unlike the capacitor, the inductor impedance increases with increasing frequency  $\omega$  and the current through an inductor is phase-shifted -90 degrees with respect to the voltage. In general, in an electrical cell the inductor is related to the adsorption onto the electrode surface, for example the adsorption of CO at the anode of a fuel cell or the adsorption of hydrogen in the active corrosion of iron. As in the case of the capacitor, the Nyquist plot of an inductor shows a series of points each for a different  $\omega$  on the  $Z_{im} -$  axis [6 – 9].

**Warburg Element, W.** When diffusion phenomena occur in an electrochemical process the Warburg element is used. The Warburg impedance ( $Z_w$ ) depends on the frequency of the input signal. At high frequencies, the  $Z_w$  is small since diffusing reactants do not have to move very far. At low frequencies, the reactants have to diffuse farther, increasing the Warburg impedance [10]. The  $Z_w$  of semi – infinite diffusion layer can be described as: [8]

$$Z_W = \frac{E(t)}{I(t)} = \frac{1}{q (j\omega)^{0.5}} \quad \text{eq 3. 26}$$

Where  $q$  is the Warburg coefficient.  $Z_w$  is characterized by having identical real and imaginary contributions, resulting in a phase angle of  $45^\circ$ ; on a Nyquist plot this can be identify by a diagonal line with a slope of  $45^\circ$ . Instead, for a finite layer thickness  $Z_w$  is modeled by:

$$Z_W = \frac{1}{q} \tanh(B (j\omega)^{0.5}) \quad \text{eq 3. 27}$$

Where  $B$  represents the diffusion layer thickness.

**Constant Phase Element, CPE.** Capacitors often do not behave ideally, e.g. the double layer capacitance on a rough surface often is distributed around a mean value. This distribution of reactivity is represented as a constant phase element (CPE) in equivalent circuits. A CPE results in a depressed semi-circle in the Nyquist plot. The CPE impedance can be expressed as:

$$Z_{CPE} = \frac{E(t)}{I(t)} = \frac{1}{q (j\omega)^n} \quad \text{eq 3. 28}$$

Where  $q$  and  $n$  are CPE parameters. Depending on the  $n$  value a CPE behaves as a capacitor ( $n=1$ ), a resistor ( $n=0$ ), an inductor ( $n= - 1$ ) and a Warburg element ( $n=0.5$ ).

#### ***A simple electrochemical system - Randles Circuit***

A metal / solution interface with corrosion reaction (Fig. 3.7) can be described by the ohmic resistance of the solution, the double-layer capacitance at the interface and electrochemical reactions that occurs on the electrode [6].

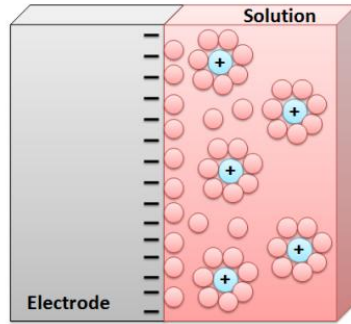


Figure 3. 7: Electrochemical system where a polarizable electrode is in contact with an electrolyte.

The most common and simple model that represents a polarizable electrode assuming that diffusion limitation does not exist and that a single step electrochemical reaction occur on the polarizable electrode is the so-called Randles circuit (Fig. 3.8). This equivalent circuit includes a resistor  $R_2$  in parallel to a capacitor  $C_{dl}$  and a second resistor  $R_1$  in series.

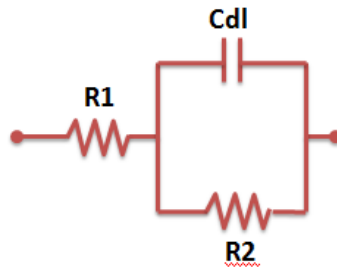


Figure 3. 8: Randles circuit used to describe the system in Fig. 3.7

$R_1$  represents the solution resistance or ohmic resistance,  $R_s$ ; the capacitance is associated to the double layer capacitance at the metal – solution interface,  $C_{dl}$ , and  $R_2$  represents the charge transfer resistance,  $R_{ct}$ , describing the process of electron transfer from the electrode to the solution. The impedance  $Z$  of this cell is given by the following equation:

$$Z(\omega) = R_s + \frac{1}{\frac{1}{R_2} + i\omega C} \quad \text{eq 3. 29}$$

The graphical representation of the impedance of the Randles circuit is a semicircle on the x-axis of the Nyquist diagram (Fig. 3.6a). At high frequencies the impedance of the capacitance  $C_{dl}$ ,  $Z_C$ , tends to zero and the impedance becomes  $Z(\omega \rightarrow \infty) = R_1$  (solution resistance). At very low frequencies the impedance becomes  $Z(\omega \rightarrow 0) = R_1 + R_2$  thus the sum of the ohmic resistance and the charge transfer (or polarization) resistance.

The Randles circuit can describe many electrochemical systems where corrosion reactions are occurring. More complicated systems, e.g. with formation of a protective film, require more complicated electrical equivalent circuits. It should be kept in mind that any circuit element must have physical/electrochemical significance in the system being analyzed.



### 3.4. X-ray Photoelectron Spectroscopy (XPS)

The interaction between solid materials and the surroundings occur thorough their surfaces, which determine the nature of the interactions, the corrosion rates, adhesive properties, contact potential and wettability. Moreover, the surface influences important properties of solid materials [11]. Hence, the knowledge of the surface chemistry is very useful to understand the interaction between a material and its surrounding. During this work, X-ray photoelectron spectroscopy (XPS) was exploited to characterize brass samples hence to identify the elements present on the surface, to determine their chemical state and to calculate the concentration and the spatial distribution. Furthermore, an insight on the thickness and the composition of the oxide layer, which might be formed at the surface of the samples, can be gained.

XPS is an analytical technique based on the photoelectric effect. The photoelectric effect is involved in the ejection of an electron from a core level by adsorption of a suitable X-ray photon of energy  $h\nu$ . The kinetic energy of the photoemitted electrons is then measured by the spectrometer. The kinetic energy is not an intrinsic property of the material being under study since it is dependent on the X-rays employed. Instead, the electron energy is a parameter that identifies a specific electron in terms of its parent element. The kinetic energy (KE) is related to the binding energy (BE) by the relationship:

$$BE = h\nu - KE - \phi \quad \text{eq 3. 30}$$

Where  $h\nu$  is the photon energy and  $\phi$  is the spectrometer's work function. The quantities on the right – hand side are known, so it is possible calculate the BE of the ejected electrons [12]. The photoemission is possible if the energy of the incident photon is greater than the BE of the electron. Moreover, the photon energy must be high enough to allow the electron photoemission of almost all elements. The most common x-ray sources employed in a XPS spectrometer are the  $AlK\alpha$  (1486.6 eV) and the  $MgK\alpha$  (1253.6 eV). The choice of the x-ray source determines the energy of the x-ray transition generated [12]. H and He are not detectable by XPS using neither  $AlK\alpha$  nor  $MgK\alpha$  radiations because their cross sections are too small being respectively: 0.0002 H and 0.0082 He [13]. Once the electrons are ejected from the surface of the sample under investigation the analyzer allows to discriminate electrons on the basis of their KE and the detector counts the number of photoelectrons emitted with a particular KE value that reach it per unit time and unit area.

Electrons could be ejected from a valence level or from a core level, which are those involved in a XPS experiment. The BE values differ from an element to element and thus the elemental analysis is straightforward.

Once an electron has been ejected, a vacancy is generated and the ion, which is in an excited state from energetic point of view, has to relax. The atom may relax following two mechanisms: by the emission of an X-ray photon (X-ray fluorescence) or by the ejection of an Auger secondary electron as shown in figure 3.9 For elements with atomic numbers greater than 33 the Auger emission can be the

dominant relaxation process, for higher-energy excitation X-ray fluorescence is the primary relaxation process.

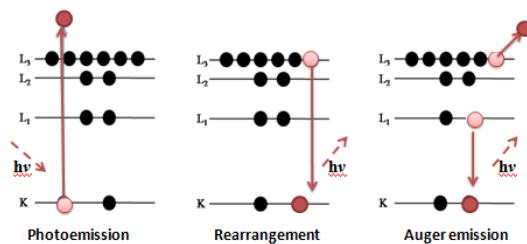


Figure 3. 9: Schematic diagram of the photoemission process of a 1s electron, followed by the relaxation of the ionized atom and the emission of a  $KL_{2,3}L_{2,3}$  Auger electron.

Auger electrons can yield valuable chemical information about the atom from where they are photoemitted. Unlike the photoelectrons, the Auger electrons are independent from the x-ray energy source since are dependent on the transition energy involved when an electron from a higher level falls to fill the hole core level. The sampling depth of the XP-spectroscopy varies with the kinetic energy of the electrons under consideration. The attenuation length ( $\Lambda$ ) is the quantity that determines the sampling depth. This parameter is related to the inelastic mean free path ( $\lambda$ , IMFP). IMFP is defined as the average distance that an electron travels between successive inelastic collision as reported in [12] and depends on the kinetic energy of the electrons ejected, the density of the solid being passed through by the electrons and on the take-off angle. According to the ASTM E 673 – 97 the take-off angle is defined as the angle at which particles leave a specimen measured relative to the plane of the specimen surface. Many approaches can be proposed for the IMFP calculation, the simplest one was proposed by Seah and Dench in 1979 [14]:

$$\lambda = \frac{A}{E^2} + B\sqrt{E} \text{ eq 3. 31}$$

Where A and B are parameters that depend on the type of the materials and are given in Table 3.2.

Table 3. 2: A and B values for the equation 3.31

	<b>A</b>	<b>B</b>
<b>Element</b>	143	0.054
<b>Organic compounds</b>	31	0.087
<b>Inorganic compounds</b>	641	0.096

Tanuma, Powell and Penn [14] suggested another approach, known as TPP-2M, for the calculation of the IMFPs in different materials. The TPP-2M equation considers the density of the material, the number of valence electrons, the atomic or molecule mass and the band gap energy [12].

The 95% of the information obtained by the XPS is originated from within three times the attenuation length ( $3\Lambda$ ). This distance is called sampling depth [11]. Although the X-ray can penetrate deep into

the solid, only electrons arising from about 10 nm can be detected without loss of energy. In fact the electrons generated deeper lose their energy on the way to go out by anelastic collisions with other atoms [15]. This is the reason why XPS is considered a surface technique.

The elemental characterization of the surface chemistry of a specimen is achieved by taking a survey spectrum, which is recorded over a wide range of energy (0 – 1400 eV). From a wide scan spectrum is possible the identification of the elements by comparing BEs experimentally obtained with the energy reference tables. Subsequently high-resolution spectra of each element of interest are acquired. The high-resolution spectra need a curve fitting procedure to obtain chemical information on the specimen. Curve fitting routine of these spectra allows resolving peak overlap thus providing chemical information on the specimen and making quantitative analysis possible. Generally the first step of the curve fitting procedure is the background subtraction then a model is created from a set of Gaussian/Lorentzian line-shape. After the curve fitting procedure, it is possible a chemical state evaluation based on the BEs of the different components. In fact, the BE of an electron depends not only on the level from which the electron is ejected, but also on the oxidation state of the atom and its surroundings. Hence, variations from the elemental states generate small shifts of the peaks in the spectrum, and this effect is called chemical shift. The chemical shift variation can vary from a fraction up to several eVs [16].

Chemical information can be achieved by analyzing other spectra features such as spin – orbit coupling, shake-up and shake-off satellites, multiplet splitting and Auger electrons peaks.

The spin-orbit coupling is responsible of the split of peaks originated from orbitals whose angular momentum quantum number is greater than zero. The peak is split into two components as a consequence of the interaction of the spin angular momentum ( $s = \pm \frac{1}{2}$ ) and the orbital angular momentum ( $l$ ). The two resulting states have a different total angular momentum. The relative intensity of the doublets formed is dependent on their relative populations. The spacing between the doublet components depends upon the strength of the spin orbit coupling.

Shake-up and shake-off are due to electronic rearrangement effects after the photoemission process. Shake-up satellites appear when a valence electron is excited to a higher level by the energy relaxation of the core hole level; shake-off satellites are originated when the photo-ionization is followed by the excitation of an electron to a free level state. Such features are not very common but their presence can give further details for the chemical investigation as in the case of copper compounds. A well-defined satellite structure appears at the high binding energy side from the main peak of Cu (II) in the CuO compound which is associated with the  $d^9$  configuration characteristics of Cu(II) compounds ( $3d^9$ ). These two satellites appeared as two overlapping peaks shifted about 7.7 eV from the main peak according to literature. Unlike the Cu (II) compounds, Cu (I) and Cu (0) do not show a satellite structure. A differentiation between Cu (0), Cu (I) and Cu (II) can be achievable on the basis of both chemical shift and the characteristic satellites structure. This point will be well detailed in Chapter 5.

Multiplet splitting may occur in compounds, which have unpaired electrons in the valence band, and arises from different spin distribution of the electrons band structure [11]. This results in a doublet of core level peak and it is observed for several transition metals.

In cases where XP spectra lines overlap showing the same BE values for different chemical state other features in the spectra could be useful to an unambiguous differentiation of the species such as Auger peak. The most well known example is the case of the copper as well as the zinc. In fact on the basis on their photoelectron signals is not possible distinguish between Cu(I) and Cu(0) and between Zn(0) and Zn(II) since they show a very small chemical shift. Only on the basis of the Auger signals is possible an unambiguous identification of the species. Combining the information obtained by the Auger and the XP spectra, thus using the Chemical state plot, it is possible an unambiguous differentiation of the species. This is a crucial point regarding this work, which will be detailed in the Chapter 5 of the thesis.

In Chapter 4 data processing and quantitative analysis of the XPS experiment will be detailed.

### **3.5. X-ray Fluorescence (XRF)**

The elemental composition of brass alloys was determined by a handled X-ray fluorescence (XRF) spectrometer. XRF is a technique used for routine chemical analyses of rocks, minerals, sediments, metals and fluids. It has been employed in archeological analysis as its remarkable combination of practical and economic advantages. In fact is a non-destructive technique utilized directly on the artifacts without destroy the samples and at ambient temperature and pressure. Little or minimal preparation is needed to carry out the experiment.

During the experiment, a specimen is excited by a primary high-energy X-ray source and the secondary fluorescence x-ray emitted is measured. The characteristic fluorescence x-ray produced is unique for a particular element and the intensity of the resulting peak is indicative of the element concentration.

X-ray fluorescence is based on the photoelectron process. A sample is irradiated by a primary high energy X-ray beam. If the beam energy is greater than the binding energy of an inner shell electron, an electron from an inner shell is photo emitted and a vacancy is created leaving an electron hole. An electron from an outer shell falls to fill the inner shell vacancy as the atom regains stability and relaxes to the ground state [17]. The electron falls to lower energy level state emitting a fluorescence radiation that is characteristic in its energy distribution for a particular material. The X-ray line spectrum consisting of a series of discrete energies with intensities related to the probability that a particular transition will occur [18]. Transitions from the L and M level to the K level where there is the shell vacancy produce  $K\alpha$  and  $K\beta$  spectral lines. Each element will have many characteristic lines since a distinct X-ray will be emitted for each type of level transition [18]. The XRF spectrum shows on the x-

axis the element-characteristic fluorescent energies, and on y-axis the counts or pulses. Higher intensity of the peak means more counts of that particular energy were detected.

The quantitative analysis is performed by calculating the areas of measured spectrum peaks. The instruments compare the spectral intensities of unknown samples to those of known elemental composition. The quantification is achieved with the fundamental parameters model (FPM) which is based on the theoretical expression of XRF intensity as a function of sample composition [19].

Since it is a standardless instrument, to be able to calculate all information from the spectrum without any standards, the FP model needs to include all phenomena that can occur, when the X-rays interact with the sample such as approximation on attenuation and enhancement in the sample, production of secondary X-rays, attenuation in the air, tube spectra, scattering processes [19].

### **3.6. Scanning Electron Microscopy (SEM)**

The observation and the characterization of heterogeneous organic and inorganic materials on a nanometre to a micrometre scale is possible by scanning electron microscopy (SEM) [20]. It is one of the most versatile instruments and it is used widely in metallurgy, geology, biology, medicine, archaeology and many others. The area to be analysed is scanned in a raster pattern with a finally focused electron beam [21]. Several types of signals are produced when an electron beam impinges on a specimen surface including backscattered, secondary and Auger electron, in addition X ray fluorescence photons and other photons of different energies [21]. These different signals can be very useful to examine many characteristics of the material under analysis such as composition, surface topography and crystallography [20 – 22]. Backscattered and secondary electrons are the signals of greatest interest in SEM analysis, since this kind of signals varies according to differences in surface topography [20]. Characteristic x-rays are also emitted from the sample which can yields both qualitative and quantitative elemental information.

The basic principle of such a microscope is the following: electrons are produced at the top of a column and they are accelerated down and a combination of electromagnetic lenses and apertures produces a focused beam of electrons which impinges the surface of the sample. The electron beam is moved in different position by a scan coils situated above the lens. The microscope is designed to operate at high vacuums ( $10^{-5}$  to  $10^{-6}$  mbar) by a combination of pumps. As a result of the electron-sample interaction, a number of signals are produced. These electrons signals are then collected by suitable detectors.

Two of the main signals relating to topography come from the elastically backscattered electrons (BSE) and the secondary electrons (SE). The SEs are inelastically scattered [23]. SE signals come mostly from the outermost layer of the sample and partly depend on the sample orientation respect to the electron beam, which makes it highly sensitive to topographical changes [23]. In the SE image the surface inclination contrasts are important to the formation of the image thus surfaces inclined turned away from the detector are darker than those inclined towards the detector. BS electrons have high-

energy electrons. BSEs are originated in the electron beam, that are reflected or backscattered out of the specimen interaction volume by interactions with specimen atoms. BSE give information about the elemental composition of the surface since the measured intensity depends on the element and the BSE increase with increasing the atomic number. The lighter elements reveal a lighter backscattering, so that the corresponding areas appear darker in the BSE image, whereas heavier elements appear brighter. The characteristic X-rays were employed in SEM analysis to distinguish the element composition [24]. SEM combine with Energy Dispersive Spectroscopy (EDS) allows one to identify and quantify particular elements.

### **3.7. Atomic Force Microscopy (AFM)**

The atomic force microscope (AFM) is a high-lateral resolution technique that provides local information at the nanometre scale. The AFM is a very powerful technique widely used in materials science and in biological sciences for evaluating the chemical and atomic orientations of polymers, crystals and other structures, to study biological samples structures such as cells, viruses, and DNA [25 – 27]. Unlike the light or electron microscopes, the AFM measures the forces (such as Van der Waals, hydration forces and electrostatic forces depending on the sample and the situation) between atoms and the tip [25, 30]. The force probe of AFM technique could remain stationary while the sample is moving or could move over a stationary sample [24]. As a result a tridimensional mapping of the shape surface is detailed from the atomic and molecular scale up to 125  $\mu\text{m}$  [26]. The AFM operation relies on a sharp tip supported at the end of a microcantilever. Little deflections of the cantilever can be monitored. The heart of the instrument is a tip mounted at the end of the microcantilever with a known spring constant. The tip is positioned at a certain distance from the sample surface and the cantilever will deflect toward the surface by a certain amount due to attractive interaction forces between the tip and the substrate [28]. The small deflection can be approximated in terms of Hook's law which calculate an upward restoring force proportional to the cantilever deflection [28]. A laser beam is focused in the cantilever and the reflected light is directed onto a four-segment photo-detector that allows the detection of both lateral and normal deflection of the cantilever [27]. The AF microscope can operate in different modes such as contact mode and non-contact mode (also known as tapping or dynamic mode). The contact mode is achieved when a tip is raster scanned across the surface and is always touching the sample and it can be either constant force or height mode [28]. The non-contact mode is preferred for investigating soft material and in this case the tip is quite close to the sample and does not touch the surface. In not-contact mode the tip is driven sinusoidally at a frequency close to its mechanical resonance and by measuring the change in amplitude of the oscillation at a constant frequency or by measuring the change in resonant frequency a 3-dimensional topographic map is obtainable [28 – 29].

## References

1. G. Bianchi, F. Mazza, *Fondamenti di corrosione e protezione dei metalli*, ed. Masson (1989)
2. J. O'M Bockris, A.K.N. Reddy, *Modern Electrochemistry*, ed. A Plenum/Rosetta (1977)
3. M. Pourbaix, *Atlas of Electrochemical Equilibria in aqueous solution*, ed. Pergamon Press (1966)
4. application note corr-1 princeton applied research
5. M. Stern and A.L. Geary, *Electrochemical Polarization*, *Journal of the Electrochemical Society*, 104 (1957) p.56
6. A. S. Hamdy, E. El-Shenawy, T. El-Bitar, *Int. J. Electrochem. Sci.*, 1(2006)171-180
7. X-Z. Yuan, C. Song, H. Wang, J. Zhang, *Electrochemical Impedance Spectroscopy in PEM fuel cells* Ed. Springer (2010)
8. V.F. Lvovich, *Impedance Spectroscopy – Applications to Electrochemical and Dielectric Phenomena*, ed. Wiley (2012)
9. M. E. Orazem, B. Tribollet, *Electrochemical Impedance Spectroscopy*, ed. Wiley (2008)
10. *Electrochemical Impedance Spectroscopy (EIS) for the in-situ analysis of metallic heritage artefacts*, Ed. Woodhead Publishing Limited, Philadelphia – USA (2013)
11. J.F.Watts, J. Wolstenholme, *An Introduction to Surface Analysis by XPS and AES*, ed. Wiley (2003)
12. D.Briggs, J.T. Grant, *Surface Analysis by Auger and X-ray Spectroscopy*, ed. IMPublications (2003)
13. J.H. Scofield, *Journal of Electron Spectroscopy and Related Phenomena* , 8 (1976) 129 – 137
14. M. P. Seah and W. A. Dench, *Surface and Interface Analysis*(1979) 1: 2–11.
15. S. Tanuma, C. J. Powell, D. R. Penn: *Surf. Interf. Anal.*, Vol. 21, 165 (1994)
16. J. C. Vikerma, *Surface Analysis – The Principal Techniques*, Wiley (1997)
17. P.J. Plotts, M. West, *Portable X-ray Fluorescence Spectrometry – Capabilities for in situ Analysis*, ed. RSC publishing
18. D. J. Kalnicky a, R. Singhvi, *Journal of Hazardous Materials* 83 (2001) 93–122
19. P. Jalas, J.P. Ruottinen, S. Hemminki, *Gold Technology* 35 Summer 2002.
20. J. Goldstein, D.E. Newbury, D.C. Joy, C.E. Lyman ,P. Echlin, E. Lifshin, L. Sawyer, J. Michael, *Scanning Electron Microscopy and X-ray Microanalysis*, ed. Springer Science + Business Media New York (2007)
21. J. Goldstein, D.E. Newbury, P. Echlin, D.C. Joy, A.D. Romig Jr., C.E. Lyman, C. Fiori, E. Lifshin, *Scanning Electron Microscopy and X-Ray Microanalysis: A Text for Biologists, material scientists and Geologist – 2nd edition – ed Plenum Press New York and London* (1992)
22. S. J. B. Reed, *Electron Microprobe Analysis and Scanning Electron Microscopy in Geology*, – 2nd edition – ed Cambridge University (2005)

23. J.V. Koleske, Paint and Coating Testing Manual 14th edition of the Gardner-Sward Handbook, ASTM Manual series (1995)
24. R.F. Egerton, Physical Principles of Electron Microscopy: An Introduction to TEM, SEM, and AEM – 2nd edition, ed. Springer
25. G. Haugstad, Atomic Force Microscopy: Understanding Basic Modes and Advanced Applications, ed. Wiley – A John Wiley & Sons, Inc., Publication (2012)
26. P.C. Braga, D. Ricci, Atomic Force Microscopy: Biomedical Methods and Applications, e. Humana Press Inc. (2004)
27. S. Morita, F.J. Giessibl, E. Meyer, R. Wiesendanger, Noncontact Atomic Force Microscopy, Volume 3, e. Springer (2015)
28. R. Reifenberger, Fundamentals of Atomic Force Microscopy: Part I: Foundations, ed. World Scientific (2016)
29. P. Eaton, P. West, Atomic Force Microscopy, ed. Oxford University press (2010)
30. K.S. Birdi, Scanning Probe Microscopes: Applications in Science and Technology, Ed. CRC Press (2003)



# Chapter 4

## Experimental

*The first part of the Chapter describes the materials and the solutions used during this work: details about the reference materials, the brass alloys and the solutions used for the electrochemical test are presented. In the second part of the Chapter the experimental conditions for all the techniques used in this work are reported: Section 4.3 concerns the morphological characterization by microscopy techniques; Section 4.4 reports the experimental details on the atomic force microscopy; Section 4.5 describes the conditions applied for the X-ray fluoresce measurements. Sections 4.6 and 4.7 are dedicated to the electrochemical techniques and to the X-ray photoelectron spectroscopy and X-ray induced Auger electron spectroscopy respectively.*

*This Chapter is based on my personal work: scanning electron microscopy measurements and atomic force microscopy images for the morphological characterization of the model brass alloys were carried out with the help of Cristiana Passiu at LSST ETH Zurich.*

## 4.1. Materials and solutions

### 4.1.1. Reference materials

Reference materials employed throughout this work were pure copper and zinc metal foils (purity > 99.9%, supplied by Goodfellow Cambridge Limited, UK) and copper and zinc oxides: CuO (99.999% Sigma Aldrich), Cu<sub>2</sub>O (≥ 99.99% anhydrous, purity Sigma Aldrich) and ZnO (≥ 99.0% Sigma Aldrich). Moreover a model brass alloy with a zinc content of 37 wt.%, Cu37Zn (Goodfellow Cambridge Limited, UK) was analyzed after different surface pre-treatments to test the analytical approach detailed in Chapter 5. The model brass alloy was analyzed “as received”, after mechanical polishing and after mechanical polishing and Ar<sup>+</sup> sputtering.

### 4.1.2. Brass model alloys

The model brass alloys used in this work were produced as thin sheets order with compositions similar as found in the brass musical instruments from the 19<sup>th</sup> century (Egger Intrumentenbau, Bern, Switzerland). The alloys have the nominal composition reported in Table 4.1.

Table 4. 1: Nominal composition of model brass alloys used in this work.

	<b>Cu wt.%</b>	<b>Zn wt.%</b>	<b>Pb wt.%</b>
<b>Cu18Zn</b>	<b>82</b>	<b>18</b>	<b>-</b>
<b>Cu28Zn</b>	<b>72</b>	<b>28</b>	<b>-</b>
<b>Cu37Zn</b>	<b>63</b>	<b>37</b>	<b>-</b>
<b>Cu35Zn1Pb</b>	<b>64</b>	<b>35</b>	<b>1</b>
<b>Cu38Zn2Pb</b>	<b>60</b>	<b>38</b>	<b>2</b>

### 4.1.3. Mechanical polishing procedure

Before the immersion in the test solutions, the brass alloys were mechanically polished to ensure reproducible starting conditions for the electrochemical tests and to remove the contamination and the oxide film, which is naturally present at the surface of the samples. The mechanical polishing procedure was performed according to Struers online Metalog guide [[www.struers.com](http://www.struers.com)]. Table 4.2 reports the sample preparation procedure.

The samples were mechanically ground with emery papers: silicon carbide paper of 2400 mesh and then of 4000 mesh (Struers) on a rotating polishing wheel. Ethanol of analytical grade was used as cooling liquid and as lubricant. Samples were ultrasonically cleaned in ethanol for 5 minutes at the end of the grinding.

Table 4. 2: Parameters of the mechanical polishing procedure. After each polishing step the samples were cleaned in ethanol in the ultrasonic bath once for 5 minutes.

Step	Surface	Time (min)
Grinding	2400 SiC paper	5
	4000 SiC paper	5
Polishing	DP Dur cloth with 1 $\mu\text{m}$ diamond paste	5
	DP Dur cloth with 0.25 $\mu\text{m}$ diamond paste	5

After the grinding procedure the surface was polished with a DP DUR cloth with 1  $\mu\text{m}$  polycrystalline diamond paste spray supplied by Struers GmbH (Ballerup Denmark), cleaned with ethanol and polished with 0.25  $\mu\text{m}$  polycrystalline diamond paste spray. Finally the surface was cleaned with ethanol and dried under an argon stream.

#### 4.1.4. Chemical etching

The microstructure of the brass alloys was investigated after chemical etching. Hence, the mechanically polished samples were chemically etched using an ammonium chloride solution, embedded in resin and then the microstructure was observed with a metallographic microscope.

## 4.2. Solutions

In order to simulate the solutions that could be present inside the brass wind instruments during playing, the experiments were performed in a diluted phosphate buffer solution pH 7 (1 : 10) and in the artificial saliva solution prepared according to Tani-Zucchi [1] with pH 7.2 – 7.8. This solution contains: KSCN 0.515 g dm<sup>-3</sup>, NaHCO<sub>3</sub> 1.264 g dm<sup>-3</sup>, KCl 1.490 g dm<sup>-3</sup>, NaH<sub>2</sub>PO<sub>4</sub> 0.123 g dm<sup>-3</sup>, CH<sub>4</sub>N<sub>2</sub>O (urea) 0.100 g dm<sup>-3</sup>,  $\alpha$ -Amilase 0.9687 g dm<sup>-3</sup>. All compounds were supplied by Sigma Aldrich (Sigma-Aldrich S.r.l. Milan, Italy). All reagents were of at least ACS grade and the solutions were prepared with distilled water with conductivity of 0.8  $\mu\text{S/cm}$ .

The normal pH of human saliva is between 6.2 and 7.6 and it can vary during the day [3]. Saliva varies in composition that can be affected by the type and intensity of stimulation, diet, age, time of day, diseases and pharmacological agents. Hence, an exact replica of human saliva is quite impossible. In literature different formulations have been developed for different purposes. The Tani-Zucchi artificial saliva has been chosen because its composition is very close to the actual conditions existent in a cavity media [3]. Microscopy

### 4.2.1. Optical microscopy (OM)

Optical microscopy images of the brass alloys surfaces, before and after mechanical polishing, after chemical etching and after the immersion into the test solutions, were taken using an Axiolab A (Zeiss, Oberkochen, Germany) microscope equipped with a charge-coupled device (CCD).

### 4.2.2. Scanning Electron Microscopy (SEM)

The Scanning Electron Microscope used was a Zeiss Ultra-55 (Carl Zeiss, Feldbach, Switzerland) equipped with InLens, SE2 (Everhart-Thornley Secondary Electron) and EsB (Energy Selective Backscattered) detectors but only the InLens and SE2 detectors were used in this work.

### 4.2.3. Atomic Force Microscopy (AFM)

The AFM images were acquired using a Dimension 3100 Atomic Force Microscope (Veeco, Santa Barbara, CA). The cantilevers employed were silicon cantilevers (Olympus, Japan): resonance frequency 300 kHz, spring constant 26 N/m and scan rate 0.7 Hz. Images were processed with the NanoScope Analysis v1.50 software.

## 4.3. X-ray Fluorescence (XRF)

In this work a hand-held EDXRF was used: EDXRF SPECTRO xSORT EDXRF (Ametek Italia Srl – MI) working in atmospheric pressure. The instrument can be used either directly on the sample using the protective plate (figure 4.1a) to prevent the scattered radiation from reaching the user or using the docking station as in figure 4.1b. The instrument is equipped with a miniaturized X-ray tube with a Rh anode; an acceleration voltage of 50 kV, with a maximum current intensity of 50 mA was used for carrying out the measurements presented in this thesis. It is also equipped with a high silicon drift detector (SDD).

The XRF beam can be collimated down to 3mm. The EDXRF is under computer control by the xSORT software (Ametek). An optical integrated video camera is available for precise spot testing. A simplified software featuring touch screen interface can be used directly on the XRF gun.

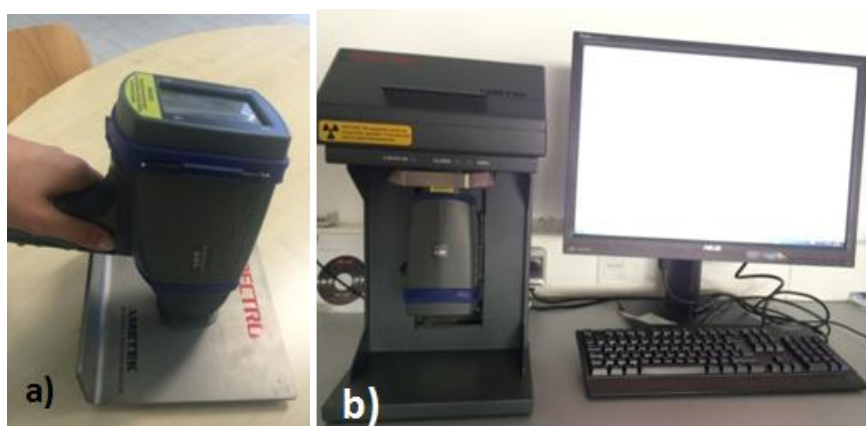


Figure 4. 1: The handled XRF spectrometer a) used direct on the sample and b) using the docking station.

The instrument calibration is carried out by the instrument and it is based on the ICAL algorithm that determines the current detector resolution, calculates the spectrum-energy-correlation and furthermore the X-ray intensity. This calibration is needed in order to perform accurate analyses. On each sample from 3 up to 10 different areas were analyzed depending on the sample size. The measurements were repeated three times per points. Each measurement takes up to 60s. The accuracy was tested on the

model brass alloy Cu<sub>37</sub>Zn and it was estimated to be lower than 1 wt.% for both copper and zinc in these experimental conditions.

#### 4.4. Electrochemical methods

A VersaSTAT 4 Model 400 potentiostat/galvanostat (Ametek Inc. PAR, USA) was used to perform the electrochemical measurements under computer control (USB port, software Versa Studio v2). The measurements performed in this investigation were: open circuit potential, linear polarization, potentiodynamic polarization curves and electrochemical impedance spectroscopy. All measurements were carried out at room temperature (25°C) in naturally aerated solutions. Each experiment was executed in a freshly prepared solution and with a freshly polished electrode surface.

The electrochemical measurements performed in this work can be divided in two steps: first open circuit potential, linear polarization and potentiodynamic polarization curves were performed. In the second step electrochemical impedance (EIS) spectra were acquired.

##### 4.4.1. Electrochemical cell

The electrochemical cell used to carry out the experiments was made of plexiglass and the cylinder had a volume of about 200 cm<sup>3</sup>, with a 0.785 cm<sup>2</sup> lateral porthole close to the base. The metal samples were pressed against the o-ring sealing of the hole. The cell was filled with an approximately 200 cm<sup>3</sup> of the test solutions. The cell was closed with a cell lid, which has two openings for the insertion of the counter electrode and the reference electrode. The scheme of the cell is shown in figure 4.2.

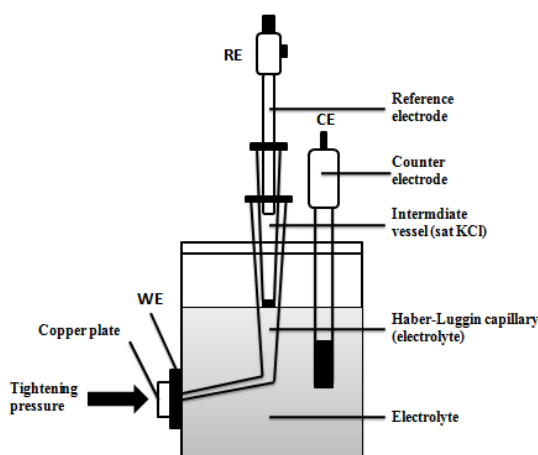


Figure 4. 2: Scheme of the electrochemical cell.

The reference electrode used in this work was a saturated calomel electrode (SCE):



The reference electrode was placed into an intermediate vessel filled with a saturated KCl solution and inserted into a Haber-Luggin capillary filled with the test solution. The distance between capillary and

sample was 3 mm. This set-up was necessary to prevent the SCE from undergoing ion exchange with the test solutions.

#### **4.4.2. Open circuit potential**

Samples were immersed for 1, 3 and 16 hours in the electrolytes to monitor the behaviour of the corrosion potential with time. At the end of the exposure period the polarization resistance was measured. A small polarization of  $\pm 20$  mV vs open circuit potential (OCP) was imposed on the sample and the resulting current measured. The scan rate was 0.167 mV/s.

The measurements were replicated at least three times and the data obtained were processed using OriginPro 9.0. The corrosion potential ( $E_{\text{corr}}$ ) obtained by the OCP measurements was plotted against the exposure time (min). During the linear polarization measurements, the current density ( $\text{mA}/\text{cm}^2$ ) is measured versus the applied potential (mV). The resulting plot is a curve characterized by a linear region. It was possible determining the polarization resistance ( $R_p$ ) by calculating the slope of the linear region.

#### **4.4.3. Cathodic and anodic polarization curves**

Cathodic and anodic polarization curves were performed at a scan rate of 0.167 mV/s following one-hour immersion time at the open circuit potential. The scan was started in the cathodic region at -0.25 V vs. OCP and run in the anodic direction to +0.25 V vs. OCP.

The cathodic and anodic polarization curves were recorded to extrapolate the anodic ( $\beta_a$ ) and cathodic ( $\beta_c$ ) constants from the anodic and cathodic linear regions using the software Versa Studio.

#### **4.4.4. Electrochemical Impedance Spectroscopy (EIS)**

The electrochemical impedance spectroscopy (EIS) measurements were carried out over a frequency domain from 10 kHz to 0.01 Hz by 7 points per decade using an ac voltage of 5 mV. The EIS spectra were acquired after 20 min, 3 and 16 hours exposure to the test solutions.

The electrochemical impedance spectroscopy (EIS) data were processed using the Z-view software [SCRIBNER ASSOCIATES INC., North Carolina, USA] and the obtained data were presented as Nyquist and Bode plots detailed in Chapter 3.

### **4.5. X-ray Photoelectron Spectroscopy (XPS)**

The reference materials employed throughout this work such as pure copper and zinc metal foils, CuO, Cu<sub>2</sub>O and ZnO, Cu<sub>37</sub>Zn and the model brass alloys samples before and after the immersion in the test solutions were characterized by XPS. The XPS analyses were performed using two different instruments: a Theta Probe spectrophotometer (Thermo Fisher Scientific, East Grinstead, UK) and a PHI Quantera<sup>SXM</sup> spectrometer (ULVAC-PHI, Chanhassen, MN, USA).

### 4.5.1. Theta Probe

The part of the instrument, where the XPS analysis is carried out, is the main chamber where the residual pressure is usually maintained between  $10^{-7}$  and  $10^{-8}$  Pa thanks to the titanium sublimation and turbo-molecular pumps that ensure a well maintained ultra high vacuum (UHV). The samples are introduced in the main chamber through a fast entry air lock where the residual pressure is maintained at  $10^{-8}$  Pa by a turbomolecular pump. The spectrometer is equipped with a monochromatic  $AlK\alpha$  (energy = 1486.6 eV) micro focused source whose beam size ranges from 20  $\mu\text{m}$  to 400 $\mu\text{m}$ . The beam spot sizes used in this work were 300 and 400 $\mu\text{m}$ . The beam was operated for the 300 $\mu\text{m}$  at 4.7 mA and 15kV (70 W) and for the 400 $\mu\text{m}$  at 6.7 mA and 15kV (100 W )

The instrument is equipped with an argon ion gun. For sputtering experiments an acceleration voltage of 3 kV and an ion current of 1  $\mu\text{A}$  were used in this work. The sputtered was 3\*3  $\text{mm}^2$ . The residual pressure in the main chamber during the data acquisition was lower than  $10^{-7}$  Pa. The average emission angle is  $53^\circ$  while the angle between the source and the analyser axis is  $67.38^\circ$ . Spectra were collected in fixed analyser transmission mode (FAT) setting the pass energy equal to 200 eV for the survey spectra and to 100 eV for high-resolution spectra, respectively selecting the standard lens mode. Step-size was 1 eV and 0.05 eV, respectively. The list of the regions collected in standard mode is given in Table 4.3.

Table 4. 3: List of regions and relative energy ranges as well as the parameters used for experiments.

Element	Standard mode, BE (eV)	ARXPS, BE (eV)	Step size (eV)	Pass Energy, (eV)
Survey	0 – 1400		1	200
Cu 2p	925 – 975	928 – 940	0.05	100
Cu LMM	555 – 585	562 – 576	0.05	100
Cu 3s	98 – 148	-	0.05	100
Cu 3p	52 – 105	-	0.05	100
Zn 2p	1010 – 1060	1017 – 1027	0.05	100
Zn LMM	480 – 515	490 – 505	0.05	100
Zn 3s	120 – 150	-	0.05	100
Zn 3p	65 – 115	-	0.05	100
C 1s	275 – 295	281 – 293	0.05	100
O 1s	520 – 550	528 – 540	0.05	100
P 2p	120 – 140	128 – 140	0.05	100
N 1s	390 – 410	390 – 405	0.05	100
S 2p	155 – 175	155 – 170	0.05	100
Pb 4f	120 – 150	132 – 146	0.05	100
Pb 4d	400 – 450	-	0.05	100
VB	-5 – 50	-	0.05	100

Moreover, high-resolution spectra were acquired in angle resolved lens mode at 16 emission angles, ranging from  $24.88$ – $83.13^\circ$ . Emission angle is defined as the angle formed by the direction of the photo-emitted electrons and the normal to the sample surface. The list of the regions collected in angle

resolved mode is given in Table 4.3. The spectrometer was calibrated according to the instructions of the manufacturer and the linearity of the binding energy scale was periodically checked according to ISO 15472:2013.

#### 4.5.2. ULVAC - PHI Quantera<sup>SXM</sup>

The PHI Quantera<sup>SXM</sup> used in this work is installed at the Department of Material Science - Laboratory of Surface Science Materials at the ETH Zurich (Switzerland). The instrument is equipped with a focused and scanned AlK $\alpha$  (energy = 1486.6 eV) source. The beam diameter was 100  $\mu\text{m}$  and it was operated at 4 mA and 15 kV (60 W). The instrument is equipped with an argon ion gun. Argon ion sputtering was performed on 3x3 mm<sup>2</sup> area, applying an acceleration voltage of 3 kV and measuring an ion current of 15 mA. The emission angle is 45° and the angle between the source and the analyser axis is 45°. Survey and high-resolution spectra were acquired in fixed analyser transmission mode (FAT) setting the pass energy equal to 280 eV and to 69 eV respectively. Step-size was 1 eV and 0.125 eV, respectively. The full width at half-maximum (FWHM) of the peak height for the silver, Ag3d<sub>5/2</sub>, signal acquired using the conditions for the acquisition of the high-resolution spectra, was 0.79 eV. The spectrometer was calibrated according to ISO 15472:2013. The accuracy was found to be equal to  $\pm 0.1$  eV.

#### 4.5.3. Data processing and quantitative analysis

High-resolution spectra were processed using CASAXPS software [v2.3.16, Casa Software Ltd., Wilmslow, Cheshire, UK]. An interactive Shirley-Sherwood background subtraction routine [4] was applied before the curve fitting procedure. This background subtraction routine was selected since this model is the most popular in practical surface analysis. It is worth to emphasise that Tougaard's background was also applied to the sputtered cleaned alloy and the calculated composition was in excellent agreement with the one obtained by Shirley's background subtraction. The Gaussian and Lorentzian (GL) product functions were used for curve fitting.

##### *First principle model*

The quantitative analysis of the reference compounds was performed on the basis of the integrated intensity using the first-principle approach [5] assuming the sample homogeneity. The atomic concentrations of the samples were calculated using the equation:

$$x_j = \frac{\frac{I_{ij}}{S_{ij}}}{\sum_j \frac{I_{ij}}{S_{ij}}} \quad \text{eq 4. 2}$$



where I is the measured peak area in Cps\*eV and S is the sensitivity factor of the peak i of the element j. The sensitivity factor is calculated for each element, using the formula:

$$S_i = \sigma_i L_i(\gamma) Q_i(\text{KE}) \Lambda_i \quad \text{eq 4. 3}$$

Where:

$\sigma_i$  is the photoemission cross-section; in this work are used the Scofield's photoionization cross-section [6]

$L_i(\gamma)$  is the asymmetry function:

$$L_i(\gamma) = 1 + \frac{1}{2} \beta_i \left( \frac{3}{2} \sin^2 \gamma - 1 \right) \quad \text{eq 4. 4}$$

$\beta$  is the asymmetric parameter and it can be found in the tables of Reilman [7]

$\gamma$  is the angle between the X-ray source and the lens axis (67.38° for the Theta Probe and 45° for the PHI Quantera)

$Q(\text{KE})$  is the analyser transmission function  $T(E_i)$  of the instrument [8]

$\Lambda_i$  is the attenuation length:

$$\Lambda_i = \lambda_i \cos \theta \quad \text{eq 4. 5}$$

$\lambda_i$  is the inelastic mean free paths (IMFP). The IMFP was calculated using the equation proposed by Tanuma et al [9].

$\theta$  is the emission angle (53° for the Theta Probe and 45° for the PHI Quantera)

The quantitative analysis of the brass surfaces and the thickness of the thin oxide film that covered the surface (e.g. after mechanical polishing where the metallic component beneath the oxide layer is still detectable) were performed according to the three-layer model [10]. This model assumes the presence of an outer layer with a thickness,  $l_c$  (e.g. contamination layer), an intermediate layer,  $t$  (e.g. oxide layer) and an inner layer at the interface film/alloy as reported in figure 4.3

#### *Quantitative analysis with the Three layer model*

This model assumes the absence of concentration gradients and the lateral homogeneity of each layer. The photo-emitted electrons coming from the bulk are exponentially attenuated by the oxide and the contamination layer, while the electrons emitted in the oxide layer are attenuated by the contamination layer.

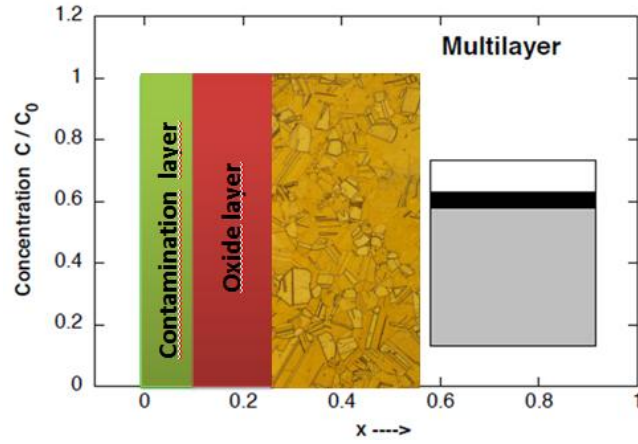


Figure 4. 3: Schematic representation of a non-homogeneous sample where there is the presence of an outer contamination layer and an oxide layer between the bulk and the contamination layer.

Thus the equations according to these assumptions are:

$$I_i^{ox} = \frac{g_i \sigma_i^{ox} C_i^{ox} \Lambda_i^{ox}}{A_i} \cdot \left( 1 - e^{-\frac{t}{\Lambda_i^{ox}}} \right) \cdot e^{-\frac{lc}{\Lambda_i^{ox}}} \quad \text{eq 4. 6}$$

$$I_j^m = \frac{g_j \sigma_j^m C_j^m \Lambda_j}{A_j} \cdot e^{-\frac{t}{\Lambda_j^{ox}}} \cdot e^{-\frac{lc}{\Lambda_j^{con}}} \quad \text{eq 4. 7}$$

Where A is the atomic weight, g is the transmission function of the spectrometer, t is oxide film thickness, lc is the thickness of the contamination layer and  $\rho$  is the density ( $\text{g/cm}^3$ ). Equations 4.6 and 4.7 must be written for each element present in the system being analyzed. t and lc can be calculated as follows:

Equations 4.6 and 4.7 must be written for each element present in the system being analyzed. t and lc can be calculated as follows:

$$f_1(t, lc) = \left( \frac{\rho^m}{\rho^{ox}} \Sigma I_j^m k_j^m e^{-\frac{t}{\Lambda_j^{ox}}} \cdot e^{-\frac{lc}{\Lambda_j^{con}}} \right) - \Sigma^{ox} \quad \text{eq 4. 8}$$

$$f_2(t, lc) = \left( \frac{l_c^{con} k_c \rho^{ox}}{1 - e^{-\frac{lc}{\Lambda^{con}}}} \right) - \Sigma^{ox} \quad \text{eq 4. 9}$$

Where k are calculated as:

$$k_j^m = \frac{g_o \sigma_o \Lambda_o A_j}{g_j \sigma_j \Lambda_j^m A_o} \quad \text{eq 4. 10}$$

$$k_j^{ox} = \frac{g_o \sigma_o \Lambda_o A_j}{g_j \sigma_j \Lambda_j^{ox} A_o} \quad \text{eq 4. 11}$$

$$k_c = \frac{g_o \sigma_o \Lambda_o A_j}{g_c \sigma_c \Lambda_c^{ox} A_o} \quad \text{eq 4. 12}$$

$$\Sigma^{ox} = \frac{\Sigma I_j^{ox} k_j^{ox} e^{-\frac{lc}{\Lambda^{con}}}}{1 - e^{-\frac{t}{\Lambda_j^{ox}}}} \quad \text{eq 4. 13}$$

The film and the interface compositions as well as the film thickness  $t$  and  $l_c$  are calculated simultaneously.

Alternatively, the thickness of the nanometric layer covering the brass samples can be estimated from ARXPS measurements based on the intensity of metallic component still detectable beneath the oxide layer at two different emission angles, using the equation [5]:

$$\frac{I_m(\theta_1)}{I_m(\theta_2)} = \exp\left[\frac{t^*}{\lambda_{ox}} \left(\frac{1}{\cos\theta_2} - \frac{1}{\cos\theta_1}\right)\right] \quad \text{eq 4. 14}$$

Where:

$\theta_{1,2}$  are two different emission angles

$I_m(\theta_{1,2})$  is the intensity of the metallic component at two different emission angles

$t^*$  is the total thickness of the oxide and contamination layers

$\lambda_i$  is the IMFP through the oxide layer

## References

1. G.Tani, F. Zucchi, *Minerva Stomatologica*, 16 (1967) 710 – 713
2. S. Baliga, S. Muglikar, R. Kale, *Journal of Indian Society of Periodontology*, 17 (2013) 461–465.
3. I. Demetrescu , B. Popescu , D. Ionita , I. Rau, R. Gavrilă, *Journal of Molecular Crystals and Liquid Crystals* 418 (2004) 271 – 284
4. D. A. Shirley, *Physical Review B: Solid State*, 5 (1972) 4709–4714.
5. D. Briggs and J. T. Grant, *Surface Analysis by Auger and X-ray Photoelectron Spectroscopy*, IM Publications and Surface Publication Data, West Sussex, 2003.
6. J. H. Scofield, *Journal of Electron Spectroscopy and Related Phenomena*, 8 (1976) 129–137.
7. R.F.Reilman, A.Msezane, S.T.Manson, *Journal of Electron Spectroscopy and Related Phenomena*, 8 (1976) 389-394
8. M. Fantauzzi, A. Pacella, J. Fournier, A. Gianfagna, G. B. Andreozzi and A. Rossi, *Analytical and Bioanalytical Chemistry*, 404 (2012) 821–833
9. S. Tanuma, C. J. Powell and D. R. Penn, *Surface and Interface Analysis*, 35 (2003) 268–275.
10. A. Rossi, B. Elsener, *Surface and Interface Analyses*, 18(1992) 499–504

# Chapter 5

## Characterization of surface films on brass alloys by XPS/XAES analysis

*This Chapter concerns the qualitative and quantitative analysis of copper, zinc and their alloys by means of X-ray Photoelectron Spectroscopy. In fact for copper and zinc compounds the chemical state identification based solely on the binding energy is challenging as the chemical shifts between Zn(II) and Zn(0) in the Zn2p signal and between Cu(I) and Cu(0) in the Cu 2p signal are very small. An analytical strategy for the chemical state identification and quantification of copper and zinc when different chemical states are simultaneously present in nanometre thick-layered systems is here proposed. It is shown that the different copper and zinc compounds can clearly be distinguished by means of their X-ray excited Auger spectra Cu L<sub>3</sub>M<sub>4,5</sub> M<sub>4,5</sub> and Zn L<sub>3</sub>M<sub>4,5</sub> M<sub>4,5</sub>. The multicomponent Auger spectra were fitted on the basis of copper and zinc reference oxides from which the intensity ratio  $R$  between photoelectron  $I_{2p}$  and Auger intensity  $I_{LMM}$  was calculated. Moreover the ratio between metallic components was obtained using pure metals and sputtered brass alloy: Cu<sub>37</sub>Zn. Hence, the ratio between the oxide and metallic components, which is shown to be independent of the instrument employed for the measurements, was exploited to transfer the experimental Auger intensity ratio into the photoelectron intensity ratio, which is required for the quantitative analysis by XPS. The analytical approach has been tested on the Cu<sub>37</sub>Zn model brass alloy after different surface pre-treatments. This approach has proven to be successful and it was followed for the characterization of different brass samples following the various surface treatments and the results are shown in the following Chapter.*

*Part of this Chapter have been published in RSC Advances [F.Cocco, B.Elsener, M. Fantauzzi, D. Atzei, A. Rossi, RSC Advances 6 (2016) 31277 - 31289] according to the journal policy it was not necessary to ask for the permission to report in thesis. The major part of the work outlined in this section was carried out by myself. Cristiana Passiu (PhD student at the ETH Zurich – Department of Material Science - Laboratory of Surface Science Materials) kindly performed the SEM and AFM analysis. Prof. A. Rossi, Prof. B. Elsener and Dr M. Fantauzzi supported the work with discussions and thorough revisions of the results.*

## 5.1 Introduction

X-ray photoelectron spectroscopy is a powerful surface analytical technique that allows the identification of elements and the determination of their chemical state by means of the binding energy values of their photoelectron and/or Auger signals. Curve fitting applied to these signals provides not only more detailed chemical information, but also allows the calculation of the composition when the elements are present in a layered structure.

Almost all elements in the periodic table exhibit a chemical shift defined as the change in peak energy arising from a change in the chemical environment of the atom [ISO 18115-1:2010]. The chemical shift can vary from a fraction of an electron volt up to several eVs [1].

The binding energy shift is a consequence of either initial state or final state effects. Initial state effects are mainly due to the formal electrical charge and to the contribution of the charge of all other atoms in the compound, related to the Madelung's potential. Moreover final state effects can contribute to the chemical shift of the core level. These effects can be related to the response of the local electronic structure to the presence of a core hole after the photoemission process. The atom is left with a core hole and it is thus an ion with a net positive charge will polarize the surrounding atoms. There will be a relaxation energy that will lower the binding energy values. The relaxation can be divided in an atomic contribution,  $R^a$ , that depends on the atomic number and on the core orbital involved in the photoemission process and an extra-atomic contribution,  $R^{ea}$ , that is related with the rest of the system, that is with the flow of electron density from the surrounding toward the core-ionized atom [2].

For example Cu  $2p_{3/2}$  in copper (II) oxide is shifted of about 1.3 eV relative to the Cu (0) and the chemical shift is found to be of maximum 4.4 eV depending on the different oxidation states, different bonds involved, various atoms with different electronic structure surrounding the atom emitting the electron.

While there is a chemical shift of the Cu  $2p_{3/2}$  signal in Cu (II) and Cu (0) the chemical shift of the copper (I) signal is very small in respect of the Cu(0) so that it cannot be revealed under the usual acquisition conditions exclusively on the basis of their photoelectron lines. The binding energy of Cu  $2p$  of Cu (0) is found to be at 932.61 eV (std. dev. = 0.21 eV) whereas the binding energy of copper (I) oxide is reported at 932.43 eV (std. dev. = 0.24 eV). Thus statistically the same BE is found for the two different chemical states. A similar situation is reported in the case of zinc since Zn  $2p_{3/2}$  in the metallic zinc has a BE of 1021.7 eV (std. dev. = 0.2 eV) while in zinc oxide ZnO, the BE value is equal to 1021.9 eV (std. dev. = 0.4 eV). These values are referred to the **NIST Standard Reference Database [3]**

When the lines contributing to a spectrum overlap because signals obtained from different compounds are very close to each other, other features in the photoelectron spectrum could be useful for an unambiguous differentiation of the species [2].

A close examination of the X-ray induced Auger signals Cu L<sub>3</sub>M<sub>4,5</sub>M<sub>4,5</sub> and Zn L<sub>3</sub>M<sub>4,5</sub>M<sub>4</sub> has showed different shape and kinetic energy values that could allowed us to distinguish between Cu (0) and Cu (I), and Zn (0) and Zn (II). In such cases the calculation of the Auger parameter and the Wagner Plot greatly improve the assignment of the chemical state in several works for both copper [4 - 8] and zinc compounds [8 - 11].

C. Wagner introduced the Auger parameter in the 1971 for the univocal identification of the elemental chemical state and it was found very useful when analysing insulators and semiconductors because it is independent of static charge referencing. The equation proposed for the Auger parameter is:

$$E_b (C) + E_k (CC'C'') = \text{const} + 2R^{\text{ea}} \text{ [11] (Eq.1)}$$

Where  $E_b (C)$  is the binding energy of the core level C in the free atom,  $E_k (CC'C'')$  is the kinetic energy of the Auger transition involving electrons from C', C'' and C''' core levels C and  $R^{\text{ea}}$  is the extra-atomic relaxation. The left part of the equation is called Auger parameter,  $\alpha'$  [12 - 13]. It is evident that for the same element in different compounds the shifts in the Auger parameter,  $\Delta\alpha'$ , are related to differences in the relaxation energies and thus to final state effects due to the neighbour atoms [8].

The Auger parameter still remains a one-dimensional parameter. A very helpful representation is the so –called chemical state plot or Wagner plot which shows on the x-axis the photoelectron energy of the peak maximum and on the y-axis the kinetic energy of the Auger spectrum [8].

In its first versions, which became very popular in the photoelectron spectroscopy community, the peak position of the most intense photoelectron and Auger lines, were reported in the two-dimensional plot. This representation is very useful whenever only one compound of a given element is present on the surface of the sample under investigation and it put the basis for a new approach to chemical state identification. In this representation, the Auger parameter is the intercept of the linear relationship  $E_k$  (Auger) vs.  $E_b$  (photoemission) to be read directly on the straight lines with slope – 1 [8] It has to be emphasized that the position of different chemical states depends on both initial and final state effects. It is apparent that the situation is more difficult, from the analytical point of view, when more than a chemical state of the same element is contributing to the Auger signal. In fact, it would be not correct to report on the plot the peak centroid that might be influenced by the presence of the various peak contributions. It is worth noting that the need to distinguish between the contributions to the Auger signal is also dictated by the need of the quantification of the species present in the outer layers of the sample. This is the case of copper and zinc: different compounds might be simultaneously present and

the chemical state identification as well as the quantification is made difficult by the presence of a large number of signals.

In few studies the quantification based on the x-ray excited Auger signals have been undertaken: a first attempt of curve fitting of the x-ray induced Auger signals of Cu and Cu<sub>2</sub>O was reported in 1988 [14]. The same group [15] reported Cu L<sub>3</sub>MM spectra of Cu, Cu<sub>2</sub>O, Cu(OH)<sub>2</sub> and CuO with an empirically-based curve fitting of the Auger signals. The ratio between Cu 2p and Cu L<sub>3</sub>MM intensity was discussed and a cross section  $\sigma_{L_3MM}$  for the Auger signals identical for oxidized and metallic compounds was experimentally deduced. A later work [16] on copper-zinc alloys in borate buffer solutions exploited the same approach to fit Cu L<sub>3</sub>M<sub>4,5</sub>M<sub>4,5</sub> and Zn L<sub>3</sub>M<sub>4,5</sub>M<sub>4,5</sub> Auger spectra of Cu, Zn, Cu<sub>2</sub>O and ZnO. The assumption of a constant  $\sigma_{L_3MM}$  was maintained and no complex Auger spectra with simultaneous presence of metal and oxide components (e.g. Cu<sub>2</sub>O on Cu, ZnO on Zn) were reported so that also the quantitative results are provided for a simple system.

In this Chapter an analytical strategy for simultaneous chemical state identification and full quantification of copper and zinc compounds, when occurring in complex nanostructured systems such as brass alloys with thin oxide - hydroxide surface films or patinas, is presented.

The starting point has been the curve fitting of Cu L<sub>3</sub>M<sub>4,5</sub>M<sub>4,5</sub> and Zn L<sub>3</sub>M<sub>4,5</sub>M<sub>4,5</sub> Auger signals based on theoretical descriptions. This procedure has allowed determining the intensity (abundance) of the metallic and oxidized copper and/or zinc components. This abundance, after the correction for the intensity ratio 2p/LMM calculated on reference materials such as pure zinc and copper metal and zinc and copper oxides, is then used for converting them to the areas of Cu 2p<sub>3/2</sub> or Zn 2p<sub>3/2</sub> signals that are at the basis of the subsequent quantification.

The strategy has been tested on a brass model alloy with zinc content of 37 wt.% (Cu37Zn) after different surface pre-treatments and has proven to be successful.

Subsequently the approach has been employed for the identification and quantification of other different brasses.

This approach has been developed in the framework of a wide research project detailed in Chapter 1 aiming to control the conditions that might cause damage on historical brass musical instruments and represents the starting point to relate non-destructive electrochemical tests to their surface chemistry.



## **5.2 Experimental**

### **5.2.1 Materials and surface preparation**

The reference materials employed throughout this work were pure copper and zinc metal foils, copper and zinc oxides details are reported in Chapter 4 .

A model brass alloy with a zinc content of 37 wt.%, Cu37Zn (Goodfellow Cambridge Limited, UK) was analyzed in the “as received” state, after mechanical polishing and after Ar<sup>+</sup> sputtering to test the analytical approach.

Furthermore, brass alloys with a zinc content of 18 and 37% Zn (Cu18Zn, Cu28Zn, Cu35Zn1Pb and Cu38Zn2Pb) produced as thin sheets with similar metallurgical structure as found in the artefacts from the 19<sup>th</sup> century, were analyzed.

The mechanical polishing procedure was performed according to the electronic manual published online by Struers (see Chapter 4 Section 4.1.3).

The surface of pure copper and zinc metals and the brass sample (Cu37Zn) were ion sputter etched by using an argon beam with an acceleration voltage of 3 kV and an ion current of 1  $\mu$ A for a maximum of 300 s. This condition was chosen in order to remove the contamination and oxidized layers until the complete disappearance of C 1s and O 1s signals.

More details about the materials are reported in Chapter 4.

### **5.2.2 Characterization Method**

In this work the reference materials and the brass alloys were characterized using the following technique: the metallographic optical microscopy (OM), the scanning electron microscopy (SEM) equipped with energy dispersive x-ray spectroscopy (EDX) and the X-ray Photoelectron Spectroscopy. Details about techniques, instruments and data processing are provided in Chapters 3 and 4.

## **5.3 Results**

### **5.3.1 Metallographic analysis**

The mechanically polished brasses were chemically etched using an ammonium chloride solution, embedded in resin. The microstructure was observed by a metallographic microscope.

The Cu18Zn, Cu28Zn and Cu37Zn (Fig. 5.1a, b, c) alloys showed after the chemical etching a monocrystalline microstructure where homogeneous twinned  $\alpha$  grains are visible; they might be due to cold working process followed by the annealing one. This causes the presence of twin  $\alpha$  grains with parallel and regular grain boundaries. The microstructure revealed a FCC lattice as could be found in the pure copper.

The Cu35Zn1Pb revealed the presence of twinned  $\alpha$  grains with regular grain boundaries and some black spots were visible. These black spots are lead inclusions. Dispersed particles were localized between the  $\alpha$  grain boundaries since at the solidification temperature of the alloy the lead is still liquid because its low melting point ( $T_{m,Pb} = 327.5^{\circ}\text{C}$ ,  $T_{m,Brass} = 900 - 1000^{\circ}\text{C}$ ). The Pb content appears to be higher than the nominal composition.

On the contrary, the Cu38Zn2Pb showed worked-deformed and smaller grains showing bent twins and strain lines. The presence of a duplex microstructure indicates the presence of  $\alpha + \beta$  brass. Lead inclusions were smaller and rare than in the case of Cu38Zn2Pb.

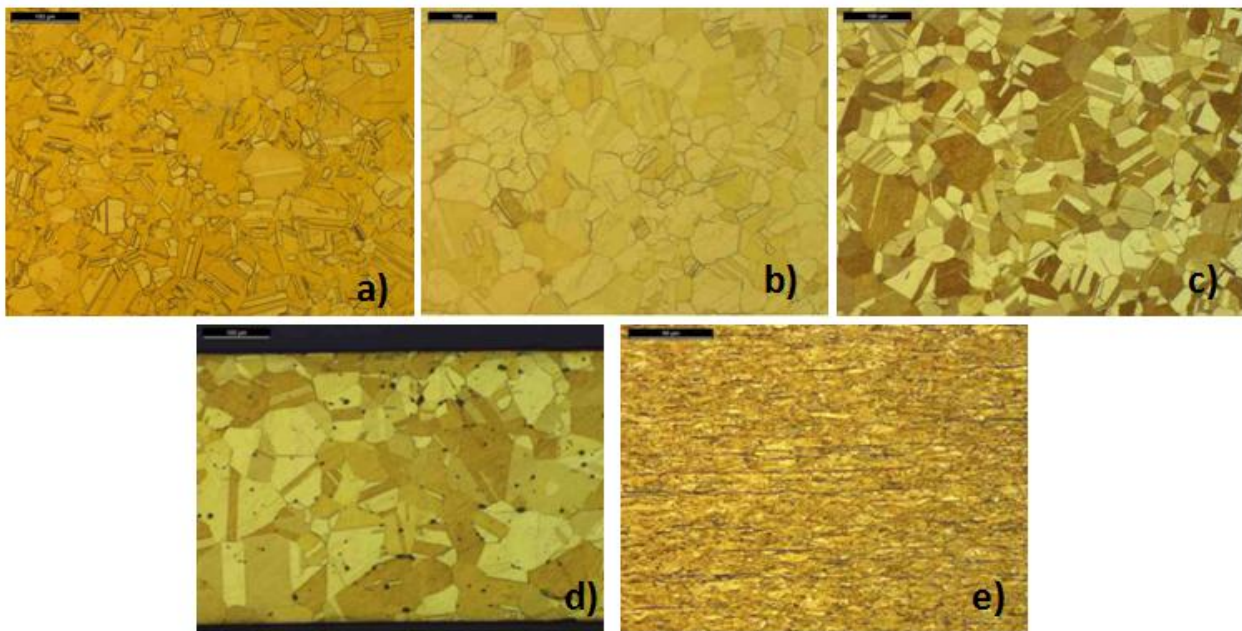


Figure 5.1: Photomicrography of a) Cu18Zn, b) Cu28Zn, c) Cu37Zn, d) Cu35Zn1Pb and e) Cu38Zn2Pb after chemical etching with an ammonium solution. (x200)

### 5.3.2 Optical microscopy and atomic force microscopy

The surface of brass alloys after mechanical polishing was observed by optical microscopy (OM) and Atomic Force Microscopy (AFM). The OM and AFM help to quantify the quality of the polishing method. In figure 5.2 are shown the OM and AFM images of Cu28Zn, Cu37Zn and Cu35Zn1Pb1. The polished surface shown shallow scratches for all the samples analyzed as reported in figure 5.2. Polishing defects are visible. The white spots may be due to small diamond paste inclusions used in the last step of the polishing procedure. The roughness of the mechanically polished samples was measured by Atomic Force Microscopy (AFM) and it was found to be:  $6.5 \pm 0.6$  nm for the Cu28Zn,  $5.2 \pm 0.5$  nm for the Cu37Zn and  $6.3 \pm 0.4$  nm for the Cu35Zn1Pb.

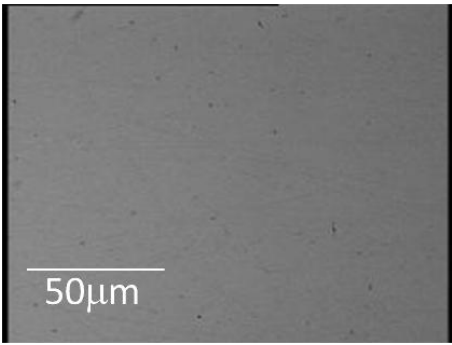
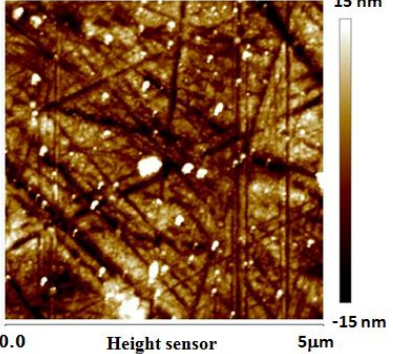
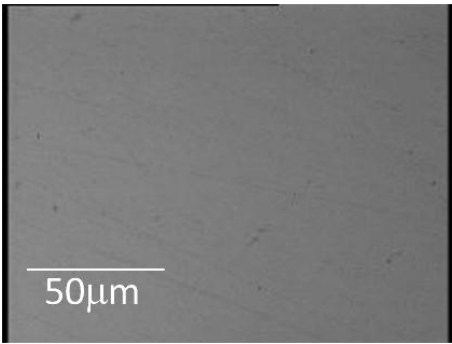
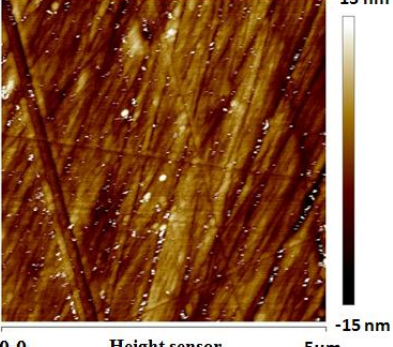
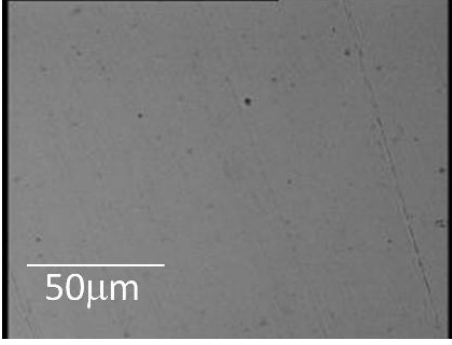
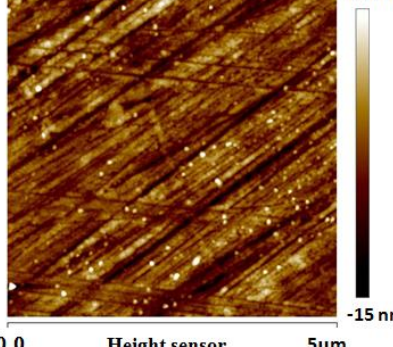
Sample	Optical Miscope	Atomic Force Microscopy
Cu28Zn		
Cu37Zn		
Cu38Zn1Pb1		

Figure 5.2: Morphology obtained by OM and AFM of Cu28Zn, Cu37Zn and Cu38Zn1Pb brass samples, after mechanical polishing.

### 5.3.3 Scanning electron microscopy

The morphology of the mechanically polished samples were investigated by scanning electron microscopy. Figure 5.3 shows the micrographs of the Cu18Zn, Cu28Zn, Cu37Zn, Cu35Zn1Pb and Cu38Zn2Pb samples. The mirror-like surfaces showed submicrometre-scratches uniformly present at the surface. Black spots become visible on the surface of the lead – containing brasses with the higher lead content. They might be due to lead inclusions similar to those also observed after the chemical etching procedure (see Section 5.3.1).

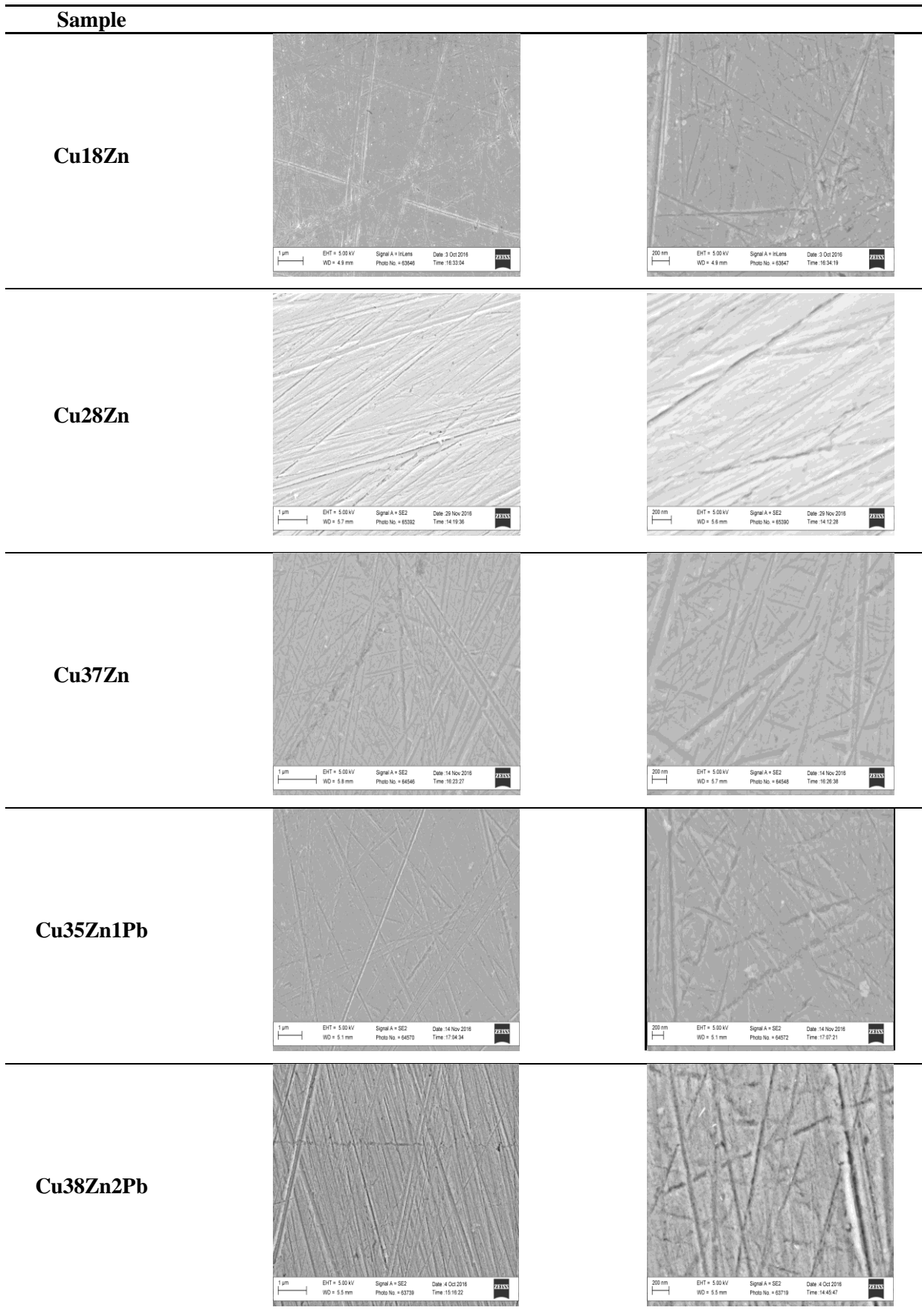


Figure 5. 3: Scanning electron microscopy images of the mirror polished Cu18Zn, Cu28Zn, Cu37Zn, Cu35Zn1Pb and Cu38Zn2Pb after mechanical polishing.

### 5.3.4 X-ray photoelectron spectroscopy results

Firstly the results concerning the reference materials are described, followed by the XP-spectra acquired on the Cu<sub>37</sub>Zn brass model alloy and by those obtained on Cu<sub>18</sub>Zn, Cu<sub>28</sub>Zn, Cu<sub>35</sub>Zn<sub>1</sub>Pb and Cu<sub>38</sub>Zn<sub>2</sub>Pb brass alloys. The high-resolution spectra were processed using CASAXPS software [17]. The background was subtracted according to the Shirley-Sherwood background subtraction routine [18] before curve fitting. This background subtraction routine was selected within those available since it is the most popular in practical surface analysis. It is worth to emphasize that Tougaard's background was also applied to the sputtered cleaned alloy and the composition of the alloy was in excellent agreement with the one obtained by Shirley's background subtraction and with expected value. Gaussian and Lorentzian (GL) product functions were used for curve fitting the signals. Quantitative analysis of "as received" and sputter cleaned brass surfaces were performed on the basis of the integrated intensity using the first-principles model (Chapter 4) assuming the sample homogeneity. The quantitative analyses of the mechanically polished samples were performed on the basis of the three layer model [19].

#### 5.3.4.1 Reference materials

In this section the high-resolution photoelectron spectra and X-ray induced electron spectra of reference compounds such as pure Cu and Zn metals, Cu<sub>2</sub>O, CuO and ZnO are presented.

*Copper and zinc metals.* In order to obtain the curve-fitting parameters of the pure metals, copper and zinc foils were analyzed as reference materials by XPS. The Cu 2p<sub>3/2</sub>, Cu L<sub>3</sub>M<sub>45</sub>M<sub>45</sub>, Zn 2p<sub>3/2</sub> and Zn L<sub>3</sub>M<sub>45</sub>M<sub>45</sub> high-resolution spectra were acquired for copper and zinc respectively.

The sputtering procedure with Ar<sup>+</sup> ions was necessary before acquiring the spectra so to remove the contamination and the oxide layer naturally grown on the surfaces under investigation as consequence of the exposure to the atmosphere. Then survey spectra (not shown) of both metals showed only signals from Cu and Zn. No oxygen and carbon signals were revealed.

*Pure copper:* The Cu 2p<sub>3/2</sub> region is shown in Fig. 5.4a: the peak maximum was found at BE 932.5 (0.1) eV in agreement with literature [8, 14 – 16, 20]. The fit parameters are listed in Tab. 5.1. The Cu L<sub>3</sub>M<sub>45</sub>M<sub>45</sub> Auger signal (Fig.5.4b) showed a complex fine structure due to different possible final states. The <sup>1</sup>S, <sup>3</sup>P, <sup>1</sup>D, <sup>3</sup>F and <sup>1</sup>G final states could be identified in agreement with literature [21 - 23]. The most intense peak of the Auger signal was found at KE 918.6 eV (0.1) (peak labeled with A); it is due to the <sup>1</sup>G multiplet of the two-localized-hole d<sup>8</sup> final state [21, 23], which splits in various multiplet states corresponding to structures seen in Fig. 5.4(b).

The peaks assigned to the <sup>3</sup>P and <sup>1</sup>D final state transitions were not resolved and contributed to one signal at KE 919.8 (0.1) eV (peak labeled with D) in agreement with literature [22, 24, 25]. A further peak detected at KE 916.5 (0.1) eV could not be explained on the basis of theoretical calculations

carried out on the structure of the copper Auger multiple signals but according to some authors might be assigned to the presence of satellites [26, 27]. Their origin is still debated but this topic is behind the scope of this investigation.

The fit parameters are listed in Table 5.1.

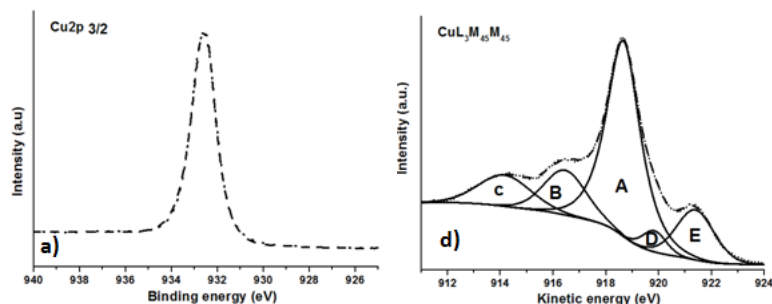


Figure 5. 4: High-resolution spectra a) Cu  $2p_{3/2}$  and b) Cu  $L_3M_{4,5}M_{4,5}$  of pure sputtered copper.

*Pure zinc:* The Zn  $2p_{3/2}$  and the Zn  $L_3M_{4,5}M_{4,5}$  Auger signal are shown in Figures 5.5a and 5.5b. The Zn  $2p_{3/2}$  signal was found at of BE 1021.6 (0.1) eV, the fit parameters are listed in Table 5.1.

Also for pure copper as for pure zinc, the Auger signal showed complex fine structure and the signals related to  $^1S$ ,  $^3P$ ,  $^1D$ ,  $^3F$  and  $^1G$  final states were identified. The most intense peak was ascribed to  $^1G$  final state transition (KE 992.1 (0.1) eV), which is the most probable transition [22]. The  $^3P$  and  $^1D$  final state transitions produce a signal at KE 993.5 (0.1) eV.

A further peak is present between  $^1G$  and  $^1S$  signals an additional peak (KE 989.6 (0.1) eV) although it could not be explained on the basis of theoretical calculations carried out on the structure of the zinc Auger signals and also in this case might be tentatively assigned to the satellite structure [26].

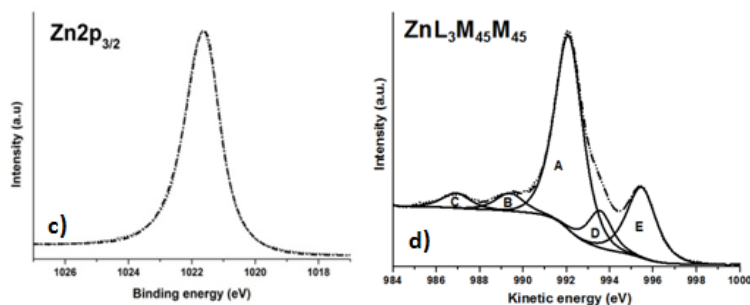


Figure 5. 5: High-resolution spectra a) Zn  $2p_{3/2}$  and b) Zn  $L_3M_{4,5}M_{4,5}$  of pure sputtered zinc.

Table 5. 1: Peak fitting parameters for the photoelectron and Auger spectra of the sputtered metallic copper and zinc. Spectra were acquired using the Thetaprobe.

Pure copper metal					
	BE (eV ± 0.1)	FWHM (eV ± 0.1)	Line Shape		
Cu 2p <sub>3/2</sub>	932.5	1.1	GL(85)T(2.5)		
	KE (eV ± 0.1)	Assignment	Intensity ratio	FWHM (eV ± 0.1)	Line Shape
Cu L <sub>3</sub> M <sub>4,5</sub> M <sub>4,5</sub> A	918.6	<sup>1</sup> G	1	1.5	GL(80)
Cu L <sub>3</sub> M <sub>4,5</sub> M <sub>4,5</sub> B	916.5		0.3	1.9	GL(30)
Cu L <sub>3</sub> M <sub>4,5</sub> M <sub>4,5</sub> C	914.1	<sup>1</sup> S	0.2	2.3	GL(30)
Cu L <sub>3</sub> M <sub>4,5</sub> M <sub>4,5</sub> D	919.8	<sup>3</sup> P/ <sup>1</sup> D	0.1	1.1	GL(30)
Cu L <sub>3</sub> M <sub>4,5</sub> M <sub>4,5</sub> E	921.4	<sup>3</sup> F	0.3	1.7	GL(30)
Pure zinc metal					
	BE (eV ± 0.1)	FWHM (eV ± 0.1)	Line Shape		
Zn 2p <sub>3/2</sub>	1021.6	1.1	GL(92)T(2)		
	KE (eV ± 0.1)	Assignment	Intensity ratio	FWHM (eV ± 0.1)	Line Shape
Zn L <sub>3</sub> M <sub>4,5</sub> M <sub>4,5</sub> A	992.1	<sup>1</sup> G	1	1.4	GL(70)
Zn L <sub>3</sub> M <sub>4,5</sub> M <sub>4,5</sub> B	989.6		0.1	2.4	GL(70)
Zn L <sub>3</sub> M <sub>4,5</sub> M <sub>4,5</sub> C	986.8	<sup>1</sup> S	0.1	1.9	GL(70)
Zn L <sub>3</sub> M <sub>4,5</sub> M <sub>4,5</sub> D	993.5	<sup>3</sup> P/ <sup>1</sup> D	0.2	1.5	GL(70)
Zn L <sub>3</sub> M <sub>4,5</sub> M <sub>4,5</sub> E	995.5	<sup>3</sup> F	0.4	1.5	GL(70)

**Copper and zinc oxides.** The high-resolution photoelectron and Auger spectra were also acquired on copper and zinc oxides reference materials.

**Copper (II) oxide, CuO.** The Cu 2p<sub>3/2</sub> photoelectron signal (Fig.5.6a) of CuO showed different shape and binding energy in comparison with the pure copper metal. The most intense peak was found at 933.8 eV (0.1) shifted 1.3 eV above the pure copper metal, that permits an unambiguous differentiation of Cu(II) in CuO from Cu (0). Additionally a well-defined satellite structure appeared at the high binding energy side of the main peak. The satellites structure is associated with the d<sup>9</sup> configuration characteristics of Cu(II) compounds (3d<sup>9</sup>) [21, 26, 27]. These two satellites appeared as two overlapping peaks shifted about 7.7 eV from the main peak in agreement with the literature [4, 15]. As the chemical shift, the characteristic satellites structure permits a differentiation between Cu (0) and Cu(II) when present in CuO. The Cu L<sub>3</sub>M<sub>4,5</sub>M<sub>4,5</sub> Auger spectra (Fig. 5.6b) showed a slightly different complex fine structure in comparison with that found for Cu. This is due to the differences in the ground state, d<sup>9</sup> for Cu (II) and d<sup>10</sup> for Cu (0) and to the presence of the oxygen in the structure. As a consequence a chemical shift of about -0.8 eV and a broadening of the peaks were found in respect to the metallic copper. The KE values and all parameters used to fitting the spectra are reported in Table 5.2. The main peak of the O 1s (Fig. 5.6c) signal was found at 530.1 (0.1) eV; furthermore a

signal ascribable to the presence of hydroxides on the surface was found above 1.6 eV the main signal in accordance with the literature [28].

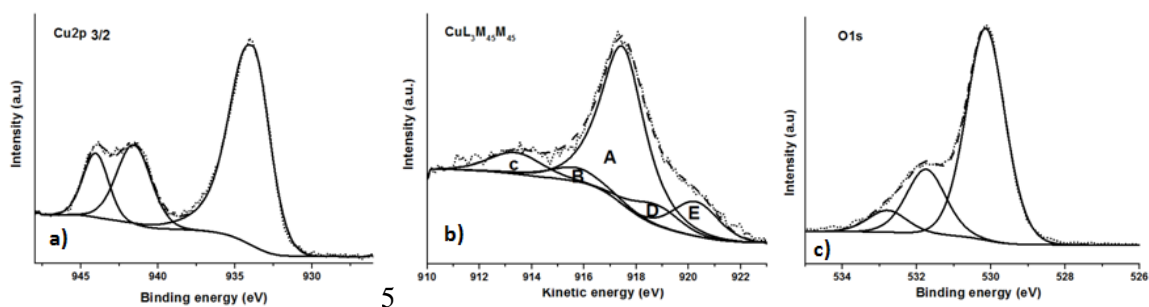


Figure 5. 6: High-resolution spectra a) Cu  $2p_{3/2}$  and b) Cu  $L_3M_{4.5}M_{4.5}$  c) O 1s of pure CuO.

**Copper (I) oxide,  $Cu_2O$ .** The Cu  $2p_{3/2}$  photoelectron signal (Fig. 5.7a) was found at 932.4 (0.1) eV as for the Cu(0). Unlike CuO, the  $Cu_2O$  peak is narrower and did not show a satellite structure. The Cu  $L_3M_{4.5}M_{4.5}$  Auger signal (Fig. 5.7b) exhibited a complex shape as a result of different final states and showed four peaks instead of five as in the case of Cu(0) and Cu(II). The main peak was found at KE 916.8 (0.1) eV. The centroid of the O 1s signal (Fig. 5.7c) was situated at about 530 eV. The fit resulted to be the convolution of three components: the most intense one at 530.3 (0.1) eV due to the  $Cu_2O$  and the other two components, which might be related to the presence of an organic contamination layer and to adsorbed water in the outer part of the sample surface. The energy values and all parameters used for fitting the spectra are reported in Table 5.2

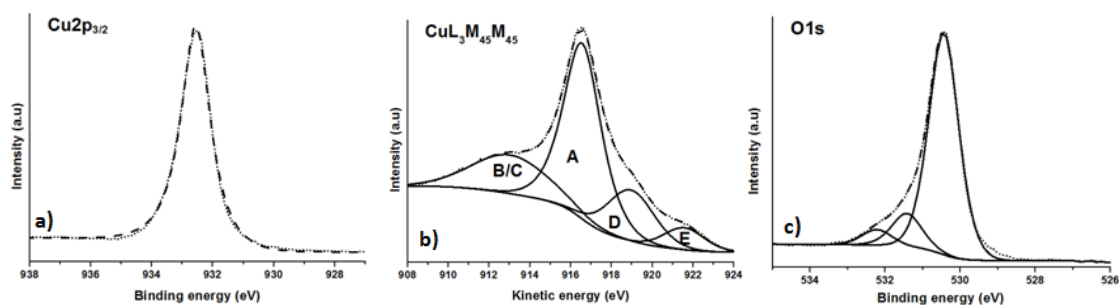


Figure 5. 7: High resolution spectra a) Cu  $2p_{3/2}$  and b) Cu  $L_3M_{4.5}M_{4.5}$  c) O 1s of pure  $Cu_2O$ .

**Zinc (II) oxide,  $ZnO$ .** The Zn  $2p_{3/2}$  signal was found at 1021.6 (0.1) eV (Fig. 5.8a), no chemical shift was detected between Zn(II) and Zn(0) under these experimental conditions. The Zn  $L_3M_{4.5}M_{4.5}$  Auger



peak (Fig. 5.8b) showed a general broadening and the satellite structure at low KE was less pronounced than in the metallic state, in agreement with [8, 9]. The oxygen, O 1s, signal of ZnO (Fig. 5.8c) showed three peaks. The curve-fitting parameters and the energy values of the analyzed signals are given in Table 5.2.

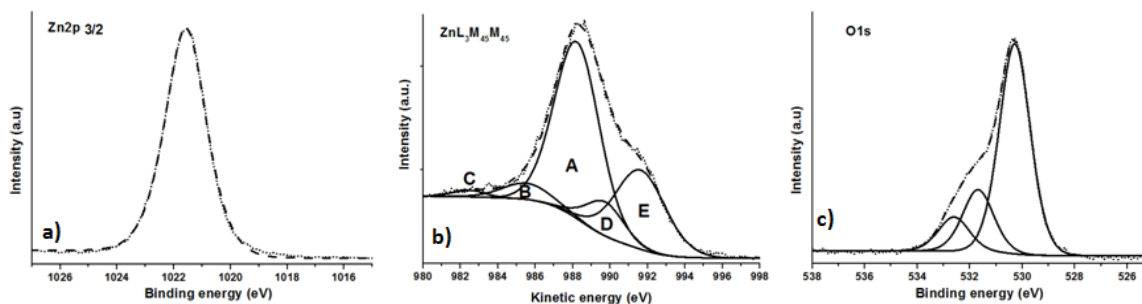


Figure 5. 8: High-resolution spectra a) Zn  $2p_{3/2}$  and b) Zn  $L_3M_{4,5}M_{4,5}$  c) O 1s of pure ZnO

### **Cu37Zn brass model alloy.**

High-resolution spectra of Cu37Zn brass model alloy were fitted using the parameters obtained on reference materials. Differences in kinetic energies and area ratios of the individual XAES signals were constrained, so XAES envelopes characterized by the KE and the intensity of the main peak could be used in curve fitting of more complex systems where two or more species are simultaneously present. The brass model alloys were analyzed in the as received state, after sputtering with  $Ar^+$  ions and after mechanical polishing procedure.

### **“As received” Cu37Zn brass model alloy.**

The survey spectra of the as received alloy showed together with peaks of copper and zinc, also the oxygen signals and an intense peak of carbon. BE values were corrected by referencing aliphatic C to 285.0 eV. The C1s (not shown) appeared to be a three component signal: the main component at 285.0 eV was assigned to aliphatic carbon, the second one shifted 1.6 eV above the main signal was assigned to  $-COH$  or  $-COC$  bonds, while the third component at higher BE (289.1 (0.1) eV) could be ascribed to carbon atoms in  $COO$  functional groups or to carbonates.

As in the case of CuO (Fig 5.6a) the Cu  $2p_{3/2}$  spectrum (Fig 5.9a) showed at higher BE of the main peak the characteristic shake-up satellites of  $Cu^{2+}$  compound. The reason for this might be attributed to the presence of copper (II) hydroxide in agreement with other authors [8, 15, 28, 29]. The Cu  $L_3M_{4,5}M_{4,5}$  Auger spectrum (Fig 5.9b) showed five components but it is different from the one obtained fitting the CuO Auger signal. In fact the spectrum is noisier and the components are broader

(higher FWHM). Furthermore, the KE of the main peak (A - Fig 5.9b) is shifted 1.6 eV to lower values compared to CuO. The Zn 2p<sub>3/2</sub> photoelectron signal (Fig 5.9c) was found at 1022.4 (0.1) eV shifted 0.8 eV to more positive BE of the pure ZnO (Table 5.2); this might be also due to the presence of zinc hydroxide as reported by Refs. 3 and 30.

Table 5. 2: Peak fitting parameters for the high-resolution Cu 2p<sub>3/2</sub>, Cu L<sub>3</sub>M<sub>4,5</sub>M<sub>4,5</sub>, spectra of CuO and Cu<sub>2</sub>O and for the Zn 2p<sub>3/2</sub> and Zn L<sub>3</sub>M<sub>4,5</sub>M<sub>4,5</sub> of ZnO. Spectra were acquired using the Thetaprobe: beam size 400 μm. Standard deviations were calculated over three independent measurements.

<b>Copper (II) Oxide, CuO</b>				
<b>Peak</b>	<b>BE (eV ± 0.1)</b>	<b>FWHM (eV ± 0.1)</b>	<b>Line Shape</b>	
<b>Cu 2p<sub>3/2</sub></b>	933.8	2.4	GL(70)T(1.5)	
<b>Sat 1</b>	941.6	2.6	GL(30)	
<b>Sat 2</b>	944.1	1.9	GL(30)	
<b>O 1s</b>	530.1	1.2	GL(40)	
<b>O 1s</b>	531.7	1.2	GL(40)	
<b>O 1s</b>	532.8	1.2	GL(40)	
	<b>KE (eV ± 0.1)</b>	<b>Attribution</b>	<b>Intensity ratio</b>	<b>FWHM (eV ± 0.1)</b>
<b>Cu L<sub>3</sub>M<sub>4,5</sub>M<sub>4,5</sub> A</b>	917.8	<sup>1</sup> G	1	1.8
<b>Cu L<sub>3</sub>M<sub>4,5</sub>M<sub>4,5</sub> B</b>	916.0		0.1	2.4
<b>Cu L<sub>3</sub>M<sub>4,5</sub>M<sub>4,5</sub> C</b>	913.3	<sup>1</sup> S	0.2	2.4
<b>Cu L<sub>3</sub>M<sub>4,5</sub>M<sub>4,5</sub> D</b>	919.1	<sup>3</sup> P/ <sup>1</sup> D	0.1	1.8
<b>Cu L<sub>3</sub>M<sub>4,5</sub>M<sub>4,5</sub> E</b>	920.6	<sup>3</sup> F	0.2	1.9
<b>Copper (I) Oxide, Cu<sub>2</sub>O</b>				
<b>Peak</b>	<b>BE (eV ± 0.1)</b>	<b>FWHM (eV ± 0.1)</b>	<b>Line Shape</b>	
<b>Cu 2p<sub>3/2</sub></b>	932.4	1.1	GL(90)	
<b>O 1s</b>	530.3	0.9	GL(50)	
<b>O 1s</b>	531.3	0.9	GL(50)	
<b>O 1s</b>	532.1	0.9	GL(50)	
	<b>KE (eV ± 0.1)</b>	<b>Assignment</b>	<b>Intensity ratio</b>	<b>FWHM (eV ± 0.1)</b>
<b>Cu L<sub>3</sub>M<sub>4,5</sub>M<sub>4,5</sub> A</b>	916.8	<sup>1</sup> G	1	2.1
<b>Cu L<sub>3</sub>M<sub>4,5</sub>M<sub>4,5</sub> B/C</b>	913.7	<sup>1</sup> S	0.6	5.4
<b>Cu L<sub>3</sub>M<sub>4,5</sub>M<sub>4,5</sub> D</b>	919.2	<sup>3</sup> P/ <sup>1</sup> D	0.4	2.4
<b>Cu L<sub>3</sub>M<sub>4,5</sub>M<sub>4,5</sub> E</b>	921.8	<sup>3</sup> F	0.1	2.5
<b>Zinc (II) Oxide, ZnO</b>				
<b>Peak</b>	<b>BE (eV ± 0.1)</b>	<b>FWHM (eV ± 0.1)</b>	<b>Line Shape</b>	
<b>Zn 2p<sub>3/2</sub></b>	1021.6	1.7	GL(70)	
<b>O 1s</b>	530.3	1.4	GL(40)	
<b>O 1s</b>	531.6	1.4	GL(40)	
<b>O 1s</b>	532.6	1.4	GL(40)	
	<b>KE (eV ± 0.1)</b>	<b>Attribution</b>	<b>Intensity ratio</b>	<b>FWHM (eV ± 0.1)</b>
<b>Zn L<sub>3</sub>M<sub>4,5</sub>M<sub>4,5</sub> A</b>	988.2	<sup>1</sup> G	1	2.9
<b>Zn L<sub>3</sub>M<sub>4,5</sub>M<sub>4,5</sub> B</b>	985.5		0.1	3.0
<b>Zn L<sub>3</sub>M<sub>4,5</sub>M<sub>4,5</sub> C</b>	982.6	<sup>1</sup> S	0.03	2.0
<b>Zn L<sub>3</sub>M<sub>4,5</sub>M<sub>4,5</sub> D</b>	989.7	<sup>3</sup> P/ <sup>1</sup> D	0.2	2.4
<b>Zn L<sub>3</sub>M<sub>4,5</sub>M<sub>4,5</sub> E</b>	991.6	<sup>3</sup> F	0.5	3.2

The Zn  $L_3M_{45}M_{45}$  Auger spectrum (Fig 5.9d) showed five components that appeared noisier, broader and shifted -0.7 eV in respect to ZnO. The shift to more positive BE values of the photoelectron signals of both copper and zinc is equal to the shift to more negative kinetic energies of the Auger signals, resulting in the same Auger parameter. The high-resolution spectra of Cu  $2p_{3/2}$ , Zn  $2p_{3/2}$ , Cu  $L_3M_{45}M_{45}$ , Zn  $L_3M_{45}M_{45}$  are shown in Figure 5.9; the energy values and the fit parameters are listed in Table 5.3

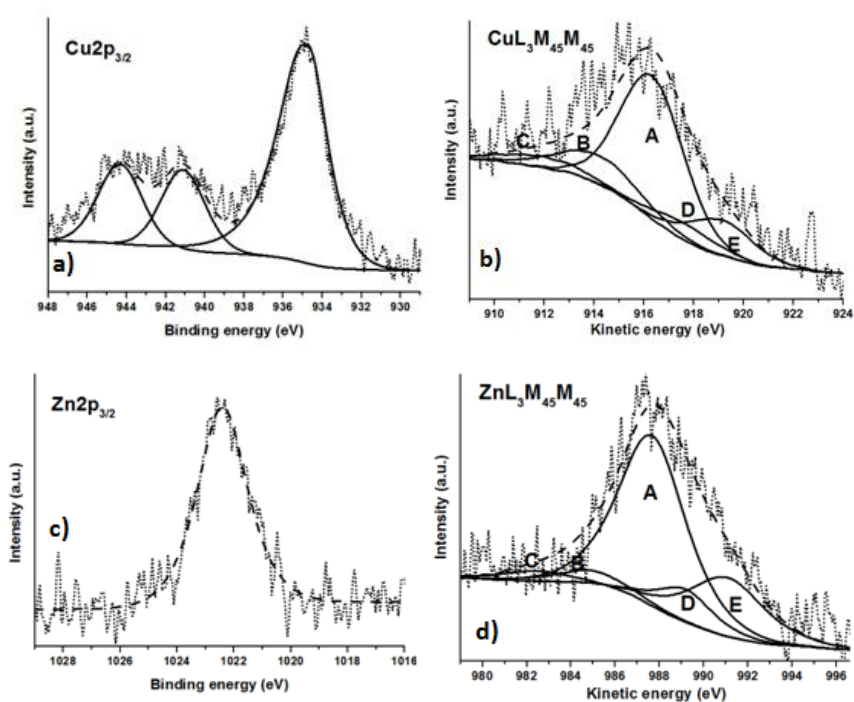


Figure 5. 9: The a) Cu  $2p_{3/2}$ , b) Cu  $L_3M_{45}M_{45}$ , c) Zn  $2p_{3/2}$ , d) Zn  $L_3M_{45}M_{45}$  high-resolution spectra of Cu37Zn in the as received state.

Table 5. 3: Peak parameters for fitting the O1s, Cu 2p<sub>3/2</sub>, Zn 2p<sub>3/2</sub>, Cu L<sub>3</sub>M<sub>4,5</sub>M<sub>4,5</sub> and Zn L<sub>3</sub>M<sub>4,5</sub>M<sub>4,5</sub> spectra of an as received Cu37Zn sample.

<b>Brass Cu37Zn model alloy “as received”</b>					
<b>Peak</b>	<b>BE (eV ± 0.1)</b>	<b>FWHM (eV ± 0.1)</b>	<b>Line shape</b>		
<b>Cu 2p<sub>3/2</sub></b>	934.8	2.4	GL(70)T(1.5)		
<b>Sat 1</b>	941.1	2.6	GL(30)		
<b>Sat 2</b>	944.3	2.6	GL(30)		
<b>Zn 2p<sub>3/2</sub></b>	1022.4	2.1	GL(70)		
<b>O 1s</b>	530.7	1.7	GL(40)		
<b>O 1s</b>	532.0	1.7	GL(40)		
<b>O 1s</b>	533.3	1.7	GL(40)		
<b>Signal</b>	<b>KE (eV ± 0.1)</b>	<b>Assignment</b>	<b>Intensity ratio</b>	<b>FWHM (eV ± 0.1)</b>	<b>Line shape</b>
<b>Cu L<sub>3</sub>M<sub>4,5</sub>M<sub>4,5</sub> A</b>	916.2	<sup>1</sup> G	1	3.0	GL(30)
<b>Cu L<sub>3</sub>M<sub>4,5</sub>M<sub>4,5</sub> B</b>	914.1		0.3	3.9	GL(30)
<b>Cu L<sub>3</sub>M<sub>4,5</sub>M<sub>4,5</sub> C</b>	911.7	<sup>1</sup> S	0.1	3.9	GL(30)
<b>Cu L<sub>3</sub>M<sub>4,5</sub>M<sub>4,5</sub> D</b>	917.5	<sup>3</sup> P/ <sup>1</sup> D	0.1	3.1	GL(30)
<b>Cu L<sub>3</sub>M<sub>4,5</sub>M<sub>4,5</sub> E</b>	919.0	<sup>3</sup> F	0.3	3.0	GL(30)
<b>Zn L<sub>3</sub>M<sub>4,5</sub>M<sub>4,5</sub> A</b>	987.5	<sup>1</sup> G	1	4.0	GL(30)
<b>Zn L<sub>3</sub>M<sub>4,5</sub>M<sub>4,5</sub> B</b>	984.8		0.1	3.0	GL(30)
<b>Zn L<sub>3</sub>M<sub>4,5</sub>M<sub>4,5</sub> C</b>	982.3	<sup>1</sup> S	0.03	2.0	GL(30)
<b>Zn L<sub>3</sub>M<sub>4,5</sub>M<sub>4,5</sub> D</b>	989.0	<sup>3</sup> P/ <sup>1</sup> D	0.2	3.3	GL(30)
<b>Zn L<sub>3</sub>M<sub>4,5</sub>M<sub>4,5</sub> E</b>	990.9	<sup>3</sup> F	0.3	4.4	GL(30)

### Sputter cleaned Cu37Zn brass model alloy.

Brass Cu37Zn model alloy was analysed after sputtering procedure using Ar<sup>+</sup> ions until complete disappearance of the contamination layer meaning the absence of C 1s and O 1s signals. The Cu 2p<sub>3/2</sub> (Fig. 5.10a) showed a single peak at 932.7 (0.1) eV, no satellite peaks were detected. The Cu L<sub>3</sub>M<sub>4,5</sub>M<sub>4,5</sub> (Fig. 5.10b) signal exhibited a complex fine structure as the spectra of the pure metallic copper. The Zn 2p<sub>3/2</sub> (Fig. 5.10c) photoelectron signals were found at 1021.3 (eV). The Zn L<sub>3</sub>M<sub>4,5</sub>M<sub>4,5</sub> (Fig. 5.10d) signal showed five components and presented a complex fine structure similar to that of the pure metallic zinc. The energy values and the fit parameters are listed in Table 5.4.

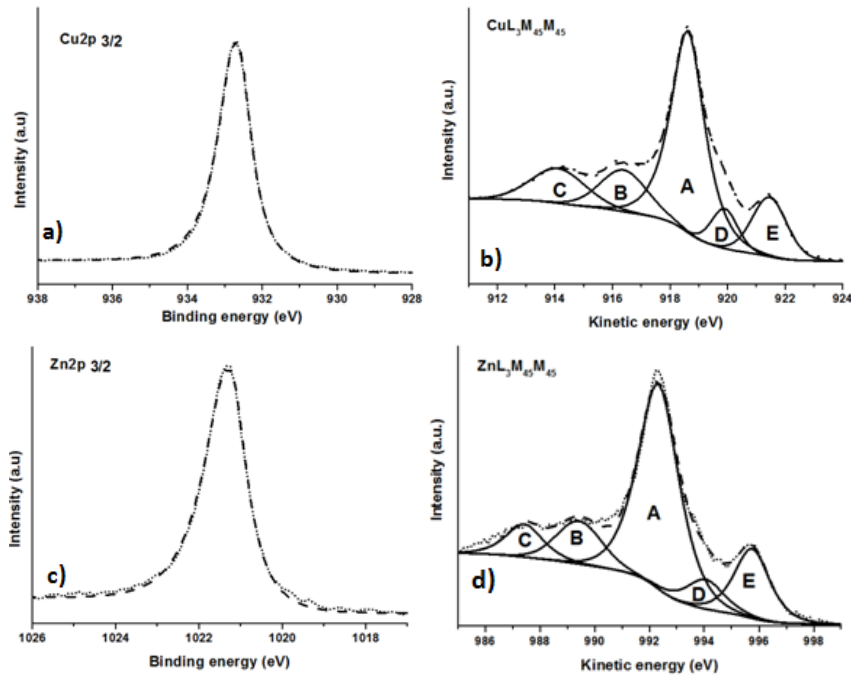


Figure 5. 10: Peak fitting for the O1s, Cu  $2p_{3/2}$ , Zn  $2p_{3/2}$ , Cu  $L_3M_{45}M_{45}$  and Zn  $L_3M_{45}M_{45}$  spectra of the sputter-cleaned alloy Cu37Zn

Table 5. 4: Peak parameters for fitting the O1s, Cu  $2p_{3/2}$ , Zn  $2p_{3/2}$ , Cu  $L_3M_{45}M_{45}$  and Zn  $L_3M_{45}M_{45}$  spectra of a sputtered Cu37Zn. Spectra were acquired using the Quantera<sup>SXM</sup>.

Brass Cu37Zn model alloy sputter cleaned					
Peak	BE (eV $\pm$ 0.1)	FWHM (eV $\pm$ 0.1)	Line shape		
Cu $2p_{3/2}$	932.7	0.9	GL(97)T(2)		
Zn $2p_{3/2}$	1021.3	0.9	GL(92)T(1.5)		
Signal	KE (eV $\pm$ 0.1)	Assignment	Intensity ratio	FWHM (eV $\pm$ 0.1)	Line shape
Cu $L_3M_{45}M_{45}$ A	918.6	$^1G$	1	1.4	GL(80)
Cu $L_3M_{45}M_{45}$ B	916.4	Sat.	0.3	1.9	GL(30)
Cu $L_3M_{45}M_{45}$ C	914.1	$^1S$	0.3	2.2	GL(30)
Cu $L_3M_{45}M_{45}$ D	920.0	$^3P/1D$	0.1	1.0	GL(30)
Cu $L_3M_{45}M_{45}$ E	921.4	$^3F$	0.3	1.4	GL(30)
Zn $L_3M_{45}M_{45}$ A	992.3	$^1G$	1	1.7	GL(70)
Zn $L_3M_{45}M_{45}$ B	989.5	Sat.	0.1	1.9	GL(70)
Zn $L_3M_{45}M_{45}$ C	987.4	$^1S$	0.1	1.6	GL(70)
Zn $L_3M_{45}M_{45}$ D	993.6	$^3P/1D$	0.2	1.6	GL(70)
Zn $L_3M_{45}M_{45}$ E	995.7	$^3F$	0.4	1.5	GL(70)

### Mechanically polished Cu37Zn brass model alloy.

Cu37Zn alloy was mechanically polished as reported in Section 5.2.1. The wide scan spectra showed the characteristic signals of oxygen and carbon meaning that a contamination layer and an oxide layer

are present on top of the sample. The characteristic signals of Cu, Zn were detected in the survey spectrum together with those of C and O. The line-shapes of Cu  $2p_{3/2}$ , Cu  $L_3M_{4,5}M_{4,5}$ , Zn  $2p_{3/2}$  and Zn  $L_3M_{4,5}M_{4,5}$  (Fig. 5.11 a,b,c,d) are different from those obtained on the pure reference materials. The differences were ascribed to the fact that on the mechanical polished brass, the contributions to the signal of both metal and oxide are simultaneously present. Furthermore, as it is apparent from the line-shapes and the curve fitting parameters are different for metals and oxides. The transition metals exhibit a tail at the higher binding energy side and the tail function takes into account electron-hole pair creation at the Fermi level for metallic systems [2]. The Cu  $2p_{3/2}$  showed a single peak at the same BE as in pure copper. As Cu  $2p_{3/2}$  also Zn  $2p_{3/2}$  showed the same BE of the pure zinc. The Cu  $L_3M_{4,5}M_{4,5}$  (Fig. 5.11b) and Zn  $L_3M_{4,5}M_{4,5}$  (Fig. 5.11d) XAES spectra showed different shapes from those of pure metals and pure oxide compounds. This was attributed to the presence of a thin oxide layer. As a consequence the Cu  $L_3M_{4,5}M_{4,5}$  and Zn  $L_3M_{4,5}M_{4,5}$  Auger peaks were fitted using the envelopes of the metallic states and the oxidized ones. This is to our knowledge the first time that Cu and Zn Auger signals of complex layered alloys have been resolved in their components. The energy values, FWHM and line shapes of both photoelectron and Auger peaks (GL ratio and tail function) are provided in Table 5.5.

Table 5. 5: Peak parameters for fitting the O1s, Cu  $2p_{3/2}$ , Zn  $2p_{3/2}$ , Cu  $L_3M_{4,5}M_{4,5}$  and Zn  $L_3M_{4,5}M_{4,5}$  spectra of a Cu37Zn sample following mechanical polishing. Spectra were acquired using the Thetaprobe.

<b>Brass Cu37Zn model alloy after mechanical polishing</b>			
<b>Peak</b>	<b>BE (eV ± 0.1)</b>	<b>FWHM (eV ± 0.1)</b>	<b>Line shape</b>
<b>Cu <math>2p_{3/2}</math></b>	932.5	1.3	GL(70)
<b>Zn <math>2p_{3/2}</math></b>	1021.7	1.7	GL (70)
<b>O 1s</b>	530.4	1.6	GL (45)
<b>O 1s</b>	531.8	1.6	GL (45)
<b>O 1s</b>	533.3	1.6	GL (45)
<b>Signal</b>	<b>KE (eV ± 0.1)</b>	<b>Attribution</b>	
<b>Cu <math>L_3M_{4,5}M_{4,5}</math> metal</b>	918.5	envelope	
<b>Cu <math>L_3M_{4,5}M_{4,5}</math> oxide</b>	916.8	envelope	
<b>Zn <math>L_3M_{4,5}M_{4,5}</math> metal</b>	992.3	envelope	
<b>Zn <math>L_3M_{4,5}M_{4,5}</math> oxide</b>	988.0	envelope	

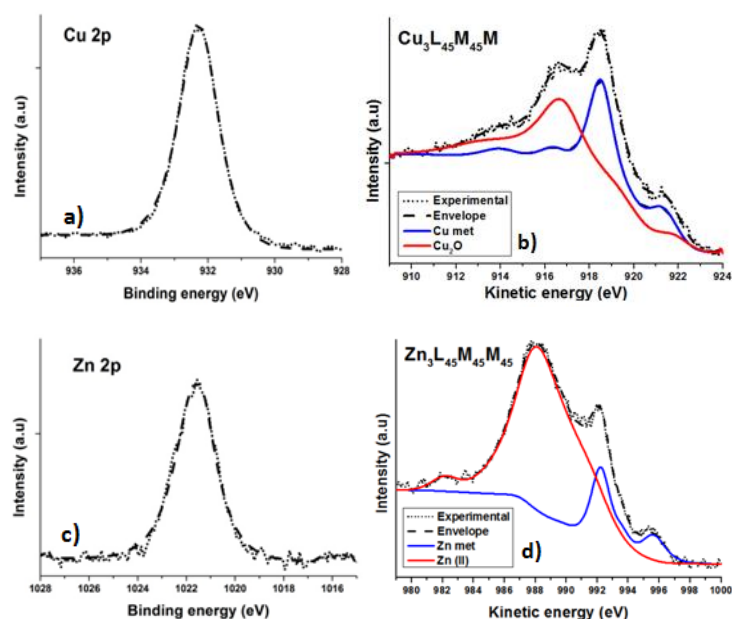


Figure 5. 11: The a) Cu  $2p_{3/2}$ , b) Cu  $L_3M_{4.5}M_{4.5}$ , c) Zn  $2p_{3/2}$ , d) Zn  $L_3M_{4.5}M_{4.5}$  high-resolution spectra of the mirror - like polished Cu37Zn sample.

### 5.3.5 As received brass alloys

The Cu18Zn, Cu28Zn, Cu35Zn1Pb and Cu38Zn2Pb were also characterized in the as received state. The wide scan spectra of the as received brass alloys showed together with peaks of Cu and Zn, an oxygen signal and an intense peak of carbon at 285.0 eV that was used to correct the binding energy scale. The presence of carbon and oxygen was due to a thick contamination layer whose presence was predictable since no special care was paid to the sample handling until it arrived at the laboratory.

*As received Cu18Zn.* The photoelectron and Auger signals and their relative BE and KE values are shown in Figure 5.12 and Table 5.6. The Cu  $2p_{3/2}$  spectrum showed two main signals located at 932.5 (0.1) eV and 935.1 (0.1) eV respectively. The first signal could be due to the presence of  $Cu_2O$ , instead the second component might be due to the presence of Cu(II) compounds confirmed by the presence of a satellite structure at higher binding energy characteristic of the presence of Cu(II) species (Fig 5.6a). As in the case of the Cu37Zn in the as received state, the Cu  $L_3M_{4.5}M_{4.5}$  Auger spectrum was quite noisy and the components were broader than those acquired on  $Cu_2O$ ; a curve fitting processing was attempted: five components were used to fit the signal showing a main component at KE of 916.3 (0.1) eV. This signal was related to the photoelectron peak at BE of 935.1 (0.1) eV assigned to the copper (II) hydroxide in agreement with other authors [8, 15, 28, 29]. The  $Cu_2O$  reference compound showed an Auger signal at 916.8 eV while in the case of this brass alloys the Auger signal was shifted – 0.5 eV. This could be due to the fact that the signal is very noisy and it was not possible distinguishing well the signal ascribable to the  $Cu_2O$ . The photoelectron signal was thus used to assign the chemical state since it could be possible to exclude the presence of a metallic component. The Zn  $2p_{3/2}$  was found at 1023.3 (0.1) eV shifted of 1.7 eV towards higher BE when comparing it with the

pure ZnO (Table 5.2). The relative Auger signal was found at 987.2 (0.1) shifted – 1.0 eV (KE) in respect to ZnO (988.2 eV). The spectrum resulted broader and extremely noisier compared to the pure ZnO and the as received Cu37Zn. The high-resolution spectra of Cu  $2p_{3/2}$ , Zn  $2p_{3/2}$ , Cu  $L_3M_{4,5}M_{4,5}$ , Zn  $L_3M_{4,5}M_{4,5}$  are shown in Figure 5.12.

*As received Cu28Zn.* The photoelectron and Auger signals and their relative BE and KE values are provided in Figure 5.13 and Table 5.6. The Cu  $2p_{3/2}$  spectrum of the as received Cu28Zn showed a signal at 932.5 (0.1) eV due to the presence of Cu<sub>2</sub>O, while the component at 934.6 (0.1) eV was assigned to the presence of Cu(II) species since the characteristic satellite structure appeared at the high binding energy side of the main photoelectron peak [24, 29, 32]. As in the case of Cu18Zn, the Auger signal was very noisy and broad showing five components. The main peak was located at 916.3 (0.1) that confirmed the hypothesis of the presence of copper (II) hydroxide in agreement with other authors [24, 29, 32]. The Zn  $2p_{3/2}$  was found at BE 1022.3 (0.1) eV and its related Auger signal at KE 988.1 (0.1) imputable to the presence of zinc hydroxide in agreement with the literature [31].

*As received Cu35Zn1Pb.* The photoelectron and Auger signals and the relative BE and KE values are shown in Figure 5.14 and Table 5.6. Also in this case, the Cu  $2p_{3/2}$  spectrum showed two main components at 932.6 (0.1) eV and 934.7 (0.1) eV respectively. Moreover a satellite structure related to the presence of Cu (II) compounds was clearly detectable. It was not possible to fit the Auger signal since it was very noisy also in comparison with the other as received brass alloys. It worth to note that in this case there was also the interference of the Zn  $L_3M_{2,3}M_{4,5}$ , as could be seen in Figure 5.13. However, it was possible to measure the centroid of the main peak that was found at KE 916.3 (0.1) eV. As for the previous analyzed brass alloys the component at 932.6 (0.1) eV could be due to the presence of Cu<sub>2</sub>O while the component at BE 934.7 (0.1) might be due to the presence of Cu(OH)<sub>2</sub> [24, 29, 32]. This assignment is substantiated by the presence of the satellite structure of the photoelectron peak and by the Auger signal at KE 916.3 (0.1) eV. The Zn  $2p_{3/2}$  was found at BE 1022.3 (0.1) eV and its related Auger signal at KE 987.3 (0.1) imputable to the presence of zinc hydroxide [31]. The Pb 4f was splitted in two components due to the spin-orbit coupling. The Pb  $4f_{7/2}$  was found at 138.9 (0.1) eV while the Pb  $4f_{5/2}$  was located at higher BE shifted of 4.8 eV. The Pb might be present as Lead oxide in agreement with the literature [3].

*As received Cu38Zn2Pb.* The photoelectron and Auger signals and their relative BE and KE values are shown in Figure 5.15 and Table 5.6. As the previous lead bearing alloy, the Cu  $2p_{3/2}$  signal showed two main components at 932.5 (0.1) eV and 934.8 (0.1) eV; at high BE a satellite structure related to the presence of Cu (II) compounds was found. Unlike the Cu35Zn1Pb case, for this as received alloy a curve fitting procedure was tempted revealing the presence of 5 components, with the main peak at KE 916.3 (0.1) eV. The Cu  $2p_{3/2}$  at 932.6 (0.1) eV could be due to the presence of Cu<sub>2</sub>O while the component at BE 934.8 (0.1) might be due to the presence of copper (II) hydroxide [24, 29, 32] confirmed by the presence of the satellite structure and by the Auger signal at KE 916.3 (0.1) eV. As it was described above for the Cu35Zn1Pb brass alloys, the zinc might be present as zinc hydroxide



according to literature [31] since the Zn  $2p_{3/2}$  was found at BE 1022.3 (0.1) eV and its related Auger signal at KE 987.3 (0.1) eV in agreement with the literature [32]. The Pb  $4f_{7/2}$  was found at 138.9 (0.1) eV while the Pb  $4f_{5/2}$  was located at higher BE shifted of 4.8 eV. The Pb might be present as Lead oxide in agreement with the literature [3].

Table 5. 6: Peak parameters for fitting the O 1s, Cu  $2p_{3/2}$ , Zn  $2p_{3/2}$ , Cu  $L_3M_{4,5}M_{4,5}$  and Zn  $L_3M_{4,5}M_{4,5}$  spectra of Cu18Zn, Cu28Zn, Cu35Zn1Pb and Cu38Zn2Pb samples in the as received state.

	<b>Cu18Zn</b>	<b>Cu28Zn</b>	<b>Cu35Zn1Pb</b>	<b>Cu38Zn2Pb</b>
	<b>BE (eV)</b>	<b>BE (eV)</b>	<b>BE (eV)</b>	<b>BE (eV)</b>
<b>Cu <math>2p_{3/2}</math></b>	932.5 (0.1)	932.5 (0.1)	932.6 (0.1)	932.5 (0.1)
<b>Cu <math>2p_{3/2}</math></b>	935.1 (0.1)	934.6 (0.1)	934.7 (0.1)	934.8 (0.1)
<b>sat 1</b>	941.7 (0.1)	941.2 (0.1)	941.6 (0.1)	941.7 (0.1)
<b>sat 2</b>	944.5 (0.1)	944.3 (0.1)	944.4 (0.1)	944.8 (0.1)
<b>O 1s</b>	531.1 (0.3)	530.5 (0.1)	530.9 (0.1)	530.5 (0.3)
<b>O 1s</b>	532.4 (0.2)	531.9 (0.1)	531.7 (0.1)	531.8 (0.2)
<b>O 1s</b>	533.7 (0.1)	533.3 (0.1)	532.7 (0.1)	533.0 (0.2)
<b>O 1s</b>	535.1 (0.1)	534.8 (0.3)	534.4 (0.3)	534.3 (0.3)
<b>Zn <math>2p_{3/2}</math></b>	1023.3 (0.1)	1022.3 (0.1)	1022.3 (0.1)	1022.3 (0.1)
<b>Pb <math>4f_{5/2}</math></b>			138.9 (0.1)	138.9 (0.1)
<b>Pb <math>4f_{7/2}</math></b>			143.8 (0.1)	143.8 (0.1)
<b>Name</b>	<b>KE (eV)</b>	<b>KE (eV)</b>	<b>KE (eV)</b>	<b>KE (eV)</b>
<b>Cu <math>L_3M_{4,5}M_{4,5}</math></b>	916.1 (0.1)	916.6 (0.1)	916.3 (0.1)	916.3 (0.1)
<b>Zn <math>L_3M_{4,5}M_{4,5}</math></b>	987.2 (0.1)	988.1 (0.1)	987.3 (0.1)	987.6 (0.1)

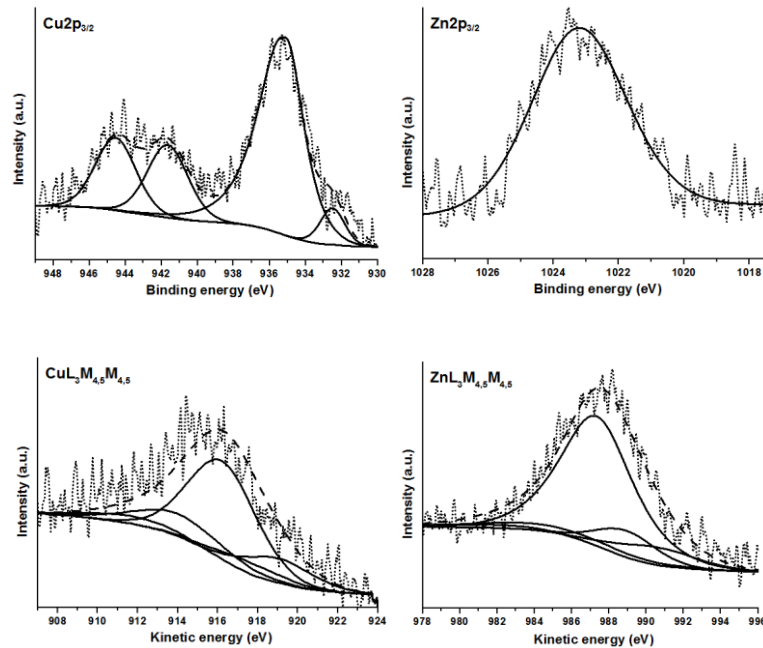


Figure 5. 12: The a) Cu  $2p_{3/2}$ , b) Cu  $L_3M_{4,5}M_{4,5}$ , c) Zn  $2p_{3/2}$ , d) Zn  $L_3M_{4,5}M_{4,5}$  high-resolution spectra of the as received Cu18Zn alloy.

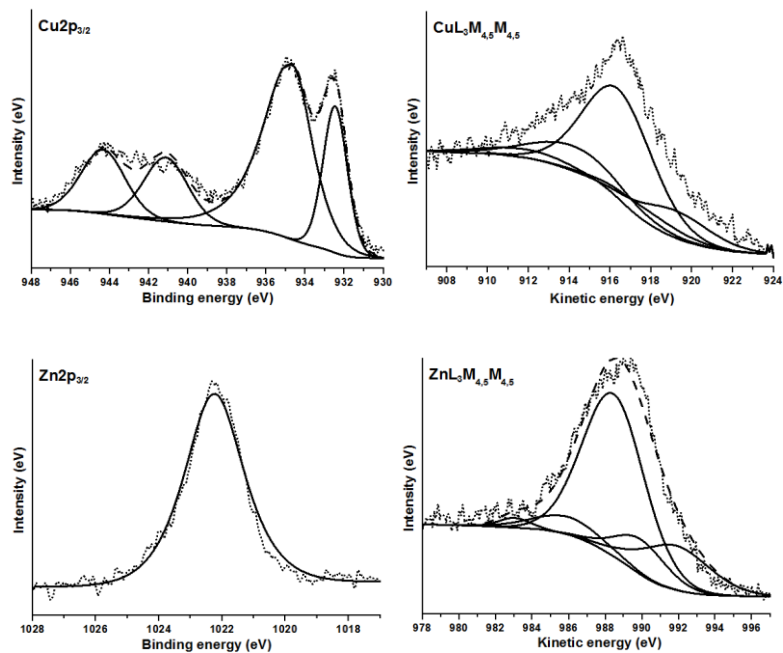


Figure 5. 13: High-resolution a) Cu 2p<sub>3/2</sub>, b) Cu L<sub>3</sub>M<sub>4,5</sub>M<sub>4,5</sub>, c) Zn 2p<sub>3/2</sub>, d) Zn L<sub>3</sub>M<sub>4,5</sub>M<sub>4,5</sub> spectra of the as received Cu<sub>28</sub>Zn alloy.

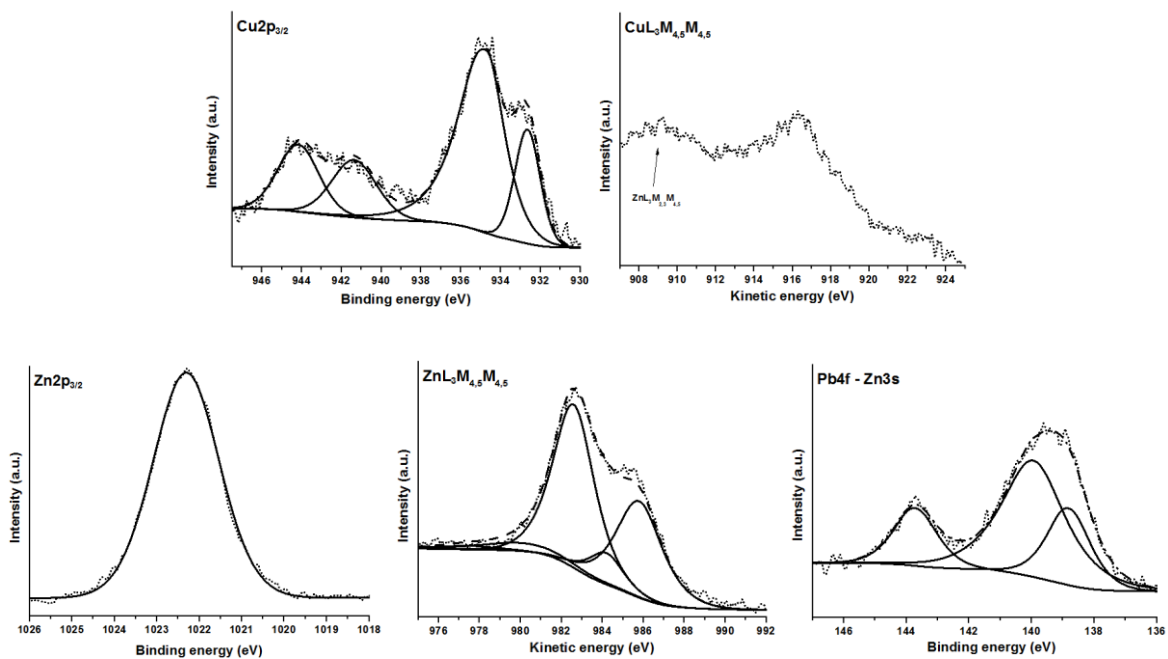


Figure 5. 14: High-resolution a) Cu 2p<sub>3/2</sub>, b) Cu L<sub>3</sub>M<sub>4,5</sub>M<sub>4,5</sub>, c) Zn 2p<sub>3/2</sub>, d) Zn L<sub>3</sub>M<sub>4,5</sub>M<sub>4,5</sub> spectra of the as received Cu<sub>35</sub>Zn<sub>1</sub>Pb alloy.

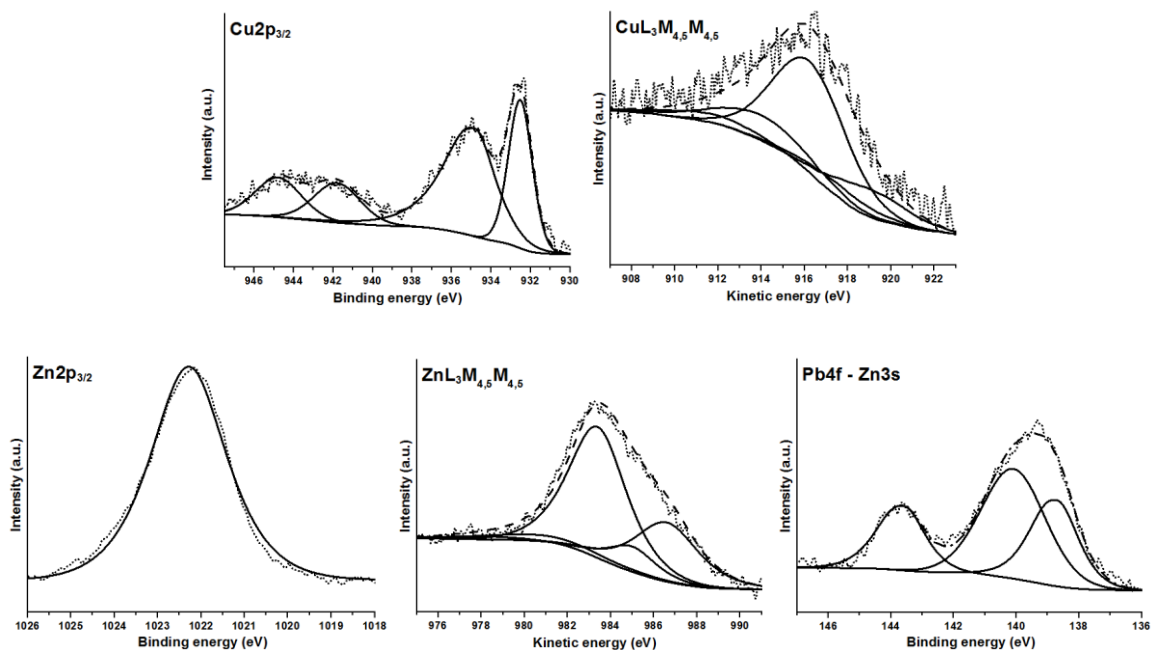


Figure 5. 15: High-resolution a) Cu  $2p_{3/2}$ , b) Cu  $L_3M_{4,5}M_{4,5}$ , c) Zn  $2p_{3/2}$ , d) Zn  $L_3M_{4,5}M_{4,5}$  spectra of the as received Cu35Zn2Pb

### 5.3.6 Mechanically polished brass alloys

Four brass alloys with zinc content of 18 and 37% respectively: Cu18Zn, Cu28Zn, Cu35Zn1Pb and Cu38Zn2Pb were also characterized after mechanical polishing procedure. The surface was observed by optical microscopy before and after the polishing procedure. In Table 5.7 are listed the BE and KE values of the O 1s, Cu  $2p_{3/2}$ , Zn  $2p_{3/2}$ , Cu  $L_3M_{4,5}M_{4,5}$  and Zn  $L_3M_{4,5}M_{4,5}$  spectra for the Cu18Zn, Cu28Zn, Cu35Zn1Pb and Cu38Zn2Pb samples following mechanical polishing procedure.

Curve-fitting parameters were determined from reference spectra acquired under the same experimental conditions. The XP-analysis of the reference compounds is reported in Section 5.3.4.1 of this Chapter. Area ratios and differences in kinetic energies of the XAES signals were constrained, so XAES envelops are characterized by the KE and the intensity of the main peak.

Survey spectra of all samples showed the characteristic signals of C and O, together with those of Cu, Zn and Pb. The presence of C and O is due also in these cases, to the presence of a thin contamination organic layer and an oxide layer at the surface of the alloys.

The Cu  $2p_{3/2}$ , Zn  $2p_{3/2}$ , Cu  $L_3M_{4,5}M_{4,5}$  and Zn  $L_3M_{4,5}M_{4,5}$  are reported in Figures 5.16 - 5.19. As found for the mechanically polished Cu37Zn alloy (Table 5.5) the Cu  $2p_{3/2}$  and Zn  $2p_{3/2}$  photoelectron signals of the Cu18Zn, Cu28Zn, Cu35Zn1Pb and Cu38Zn2Pb alloys showed single peaks found at about BE 932.5 eV and 1021.7 eV respectively. The line shape of the copper signals did not exhibit a satellite

structure so the presence of a Cu (II) component could be ruled out.

The Cu  $L_3M_{4,5}M_{4,5}$  spectra showed the simultaneous contributions to the signal of both metal and oxide. The signals of the components assigned to the metal substrate and to the oxidized layer were found at about KE 918.7 eV and 917.0 eV respectively, and the results are in agreement with those obtained for the mechanically polished Cu37Zn ones.

The Zn  $L_3M_{4,5}M_{4,5}$  XAES spectra showed the same complex fine structure of the mechanically polished Cu37Zn (Fig.5.11d). The component at about KE 992.3 eV was ascribed at the metallic component and the component at KE 988.2 eV at the oxidized component.

The characteristic signals of Pb appeared in all spectra of the lead-containing brasses: Cu35Zn1Pb and Cu38Zn2Pb. The most intense peak of lead is the Pb 4f, which showed a well-separated spin-orbit doublet; each signal exhibited a FWHM of 1.7 eV (Figures 5.18e and 5.19e). The Pb  $4f_{7/2}$  was found for both brasses at 138.6 eV (Table 5.7) and the Pb  $4f_{5/2}$  was found at about 4.9 eV on the high binding energy side of the Pb  $4f_{7/2}$ . The position of the signal suggests the presence of lead oxide [34].

The O 1s signal of Cu18Zn and Cu28Zn (Table 5.7) appeared as a three-component signal as in the case of the CuZ37Zn one. A fourth peak was observed in the case of lead-bearing brasses due to the presence of lead oxide.

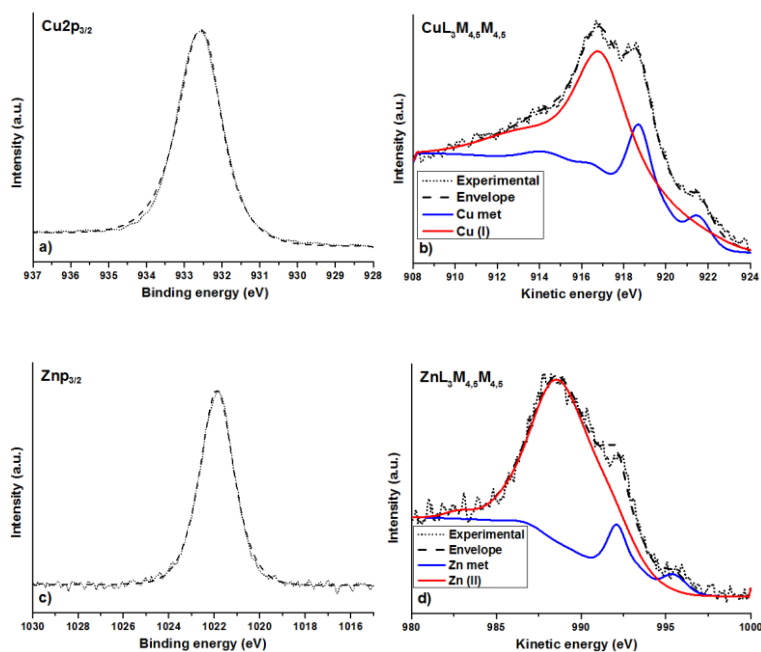


Figure 5. 16: High-resolution spectra of a) Cu  $2p_{3/2}$ , b) Cu  $L_3M_{4,5}M_{4,5}$ , c) Zn  $2p_{3/2}$ , d) Zn  $L_3M_{4,5}M_{4,5}$  of the mirror polished Cu18Zn.

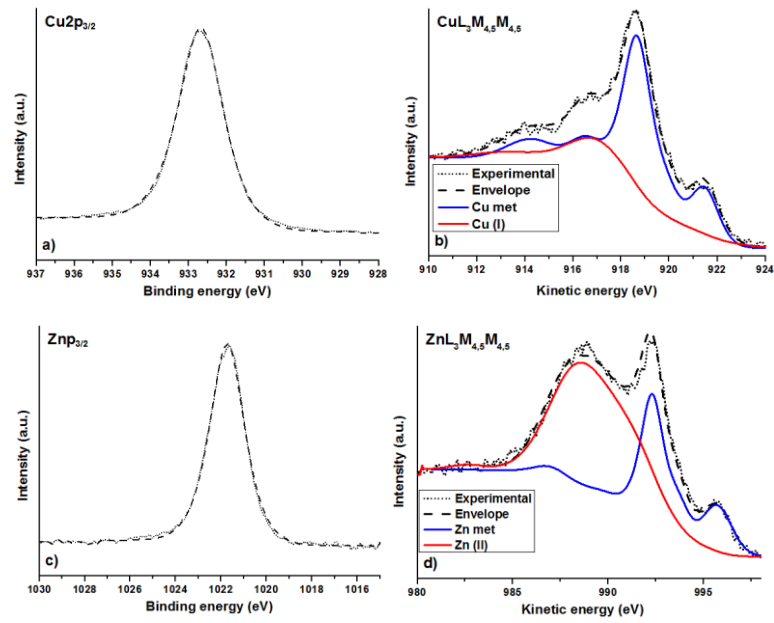


Figure 5.17: High-resolution spectra of a) Cu  $2p_{3/2}$ , b) Cu  $L_3M_{4.5}M_{4.5}$ , c) Zn  $2p_{3/2}$ , d) Zn  $L_3M_{4.5}M_{4.5}$  of the mirror polished Cu<sub>28</sub>Zn.

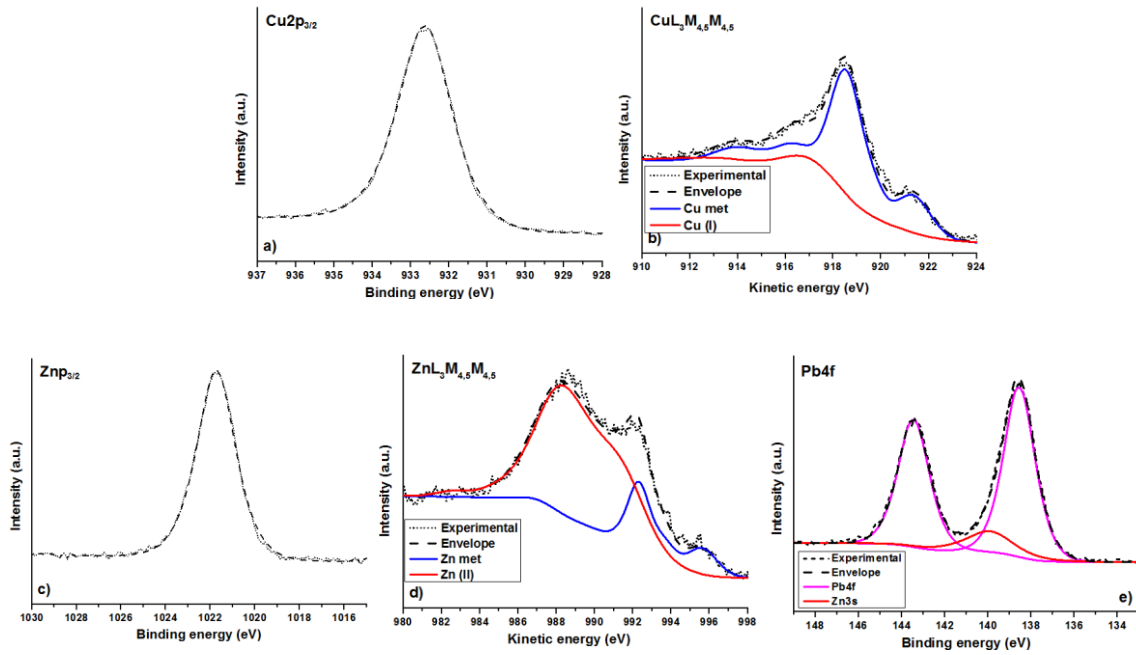


Figure 5.18: High-resolution spectra of a) Cu  $2p_{3/2}$ , b) Cu  $L_3M_{4.5}M_{4.5}$ , c) Zn  $2p_{3/2}$ , d) Zn  $L_3M_{4.5}M_{4.5}$  acquired on the mirror-like polished Cu<sub>35</sub>Zn<sub>1</sub>Pb alloy

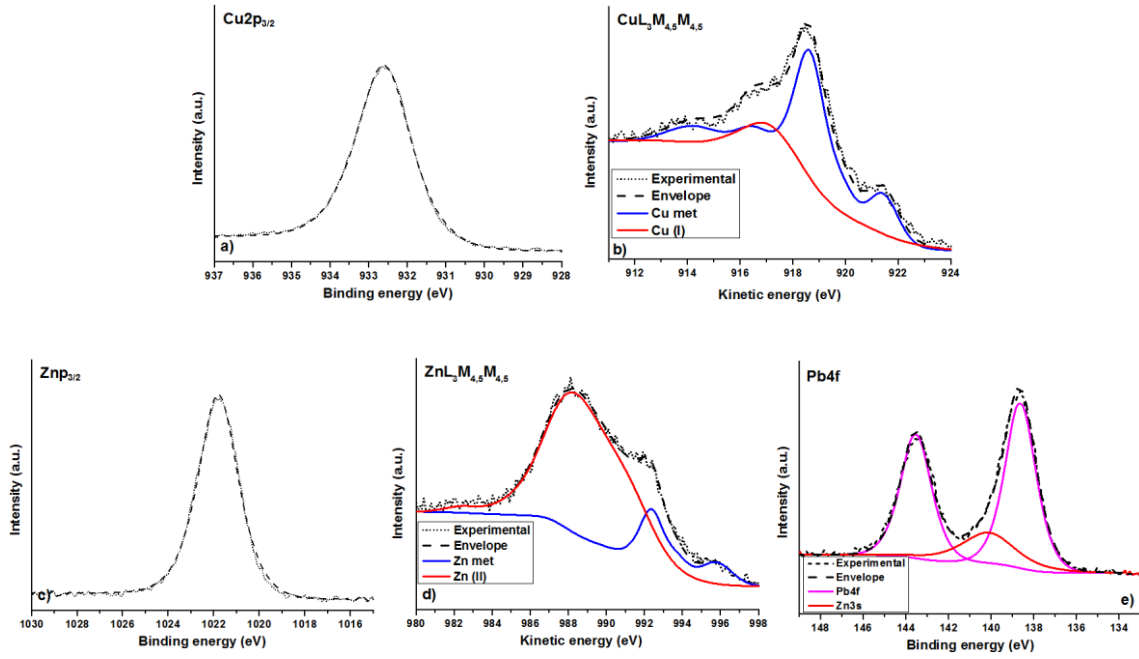


Figure 5. 19: High-resolution spectra of a) Cu  $2p_{3/2}$ , b) Cu  $L_{3}M_{4.5}M_{4.5}$ , c) Zn  $2p_{3/2}$ , d) Zn  $L_{3}M_{4.5}M_{4.5}$  acquired on the mirror-like polished Cu<sub>38</sub>Zn<sub>2</sub>Pb alloy.

Table 5. 7: Peak parameters for fitting the O 1s, Cu  $2p_{3/2}$ , Zn  $2p_{3/2}$ , Cu  $L_{3}M_{4.5}M_{4.5}$  and Zn  $L_{3}M_{4.5}M_{4.5}$  spectra of Cu<sub>18</sub>Zn, Cu<sub>28</sub>Zn, Cu<sub>35</sub>Zn<sub>1</sub>Pb and Cu<sub>38</sub>Zn<sub>2</sub>Pb samples following mechanical polishing.

	<b>Cu<sub>18</sub>Zn<sub>35</sub></b>	<b>Cu<sub>28</sub>Zn</b>	<b>Cu<sub>35</sub>Zn<sub>1</sub>Pb</b>	<b>Cu<sub>38</sub>Zn<sub>2</sub>Pb</b>
	<b>BE (eV)</b>	<b>BE (eV)</b>	<b>BE (eV)</b>	<b>BE (eV)</b>
<b>Cu <math>2p_{3/2}</math></b>	932.5 (0.1)	932.6 (0.1)	932.5 (0.2)	932.5 (0.1)
<b>O 1s</b>	530.4 (0.1)	530.3 (0.1)	530.0 (0.1)	530.2 (0.1)
	531.8 (0.1)	531.7 (0.1)	531.4 (0.1)	531.6 (0.1)
	533.2 (0.2)	533.1 (0.1)	532.5 (0.1)	532.7 (0.1)
			533.9 (0.1)	534.1 (0.2)
<b>Pb <math>4f_{7/2}</math></b>			138.6 (0.1)	138.5 (0.2)
<b>Pb <math>4f_{5/2}</math></b>			143.5 (0.1)	143.4 (0.2)
<b>Zn <math>2p_{3/2}</math></b>	1021.8 (0.1)	1021.7 (0.1)	1021.6 (0.2)	1021.7 (0.2)
	<b>KE (eV)</b>	<b>KE (eV)</b>	<b>KE (eV)</b>	<b>KE (eV)</b>
<b>Cu <math>L_{3}M_{4.5}M_{4.5}</math> Metal</b>	918.7 (0.1)	918.8 (0.1)	918.6 (0.1)	918.7 (0.1)
<b>Cu <math>L_{3}M_{4.5}M_{4.5}</math> Oxide</b>	917.0 (0.1)	917.0 (0.1)	917.0 (0.1)	916.9 (0.1)
<b>Zn <math>L_{3}M_{4.5}M_{4.5}</math> Metal</b>	992.3 (0.2)	992.4 (0.1)	992.3 (0.1)	992.5 (0.1)
<b>Zn <math>L_{3}M_{4.5}M_{4.5}</math> Oxide</b>	988.2 (0.1)	988.3 (0.1)	988.4 (0.1)	988.0 (0.1)

## 5.3.7 Angle resolved spectra

### 5.3.7.1 As received brass alloys

The angle resolved spectra of as received samples revealed only the presence of carbon and oxygen, no Cu, Zn and Pb signals were detected. This is due a thick contamination layer that was present on the brass sample. In Figures 5.20 and 5.21 the C 1s, O 1s, Cu 2p<sub>3/2</sub> and Zn 2p<sub>3/2</sub> signals acquired in angle resolved mode on the Cu18Zn and Cu37Zn are shown at different emission angles from 28.6°, the most surface angle, to the most inner angle 73.6°. As it could be seen C 1s and O 1s are observable at each angles, whereas no Cu 2p and Zn2p are detectable. The same trend was also found for the other as received brasses (not shown).

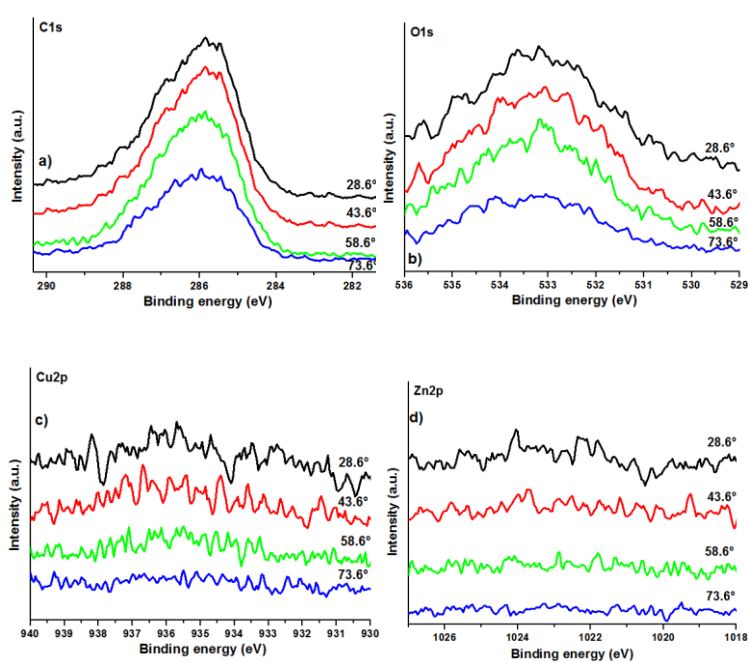


Figure 5. 20: Angle resolved high-resolution C 1s (a), O 1s (b), Cu 2p (c) and Zn 2p (d) spectra of the as received Cu18Zn acquired at different emission angles.

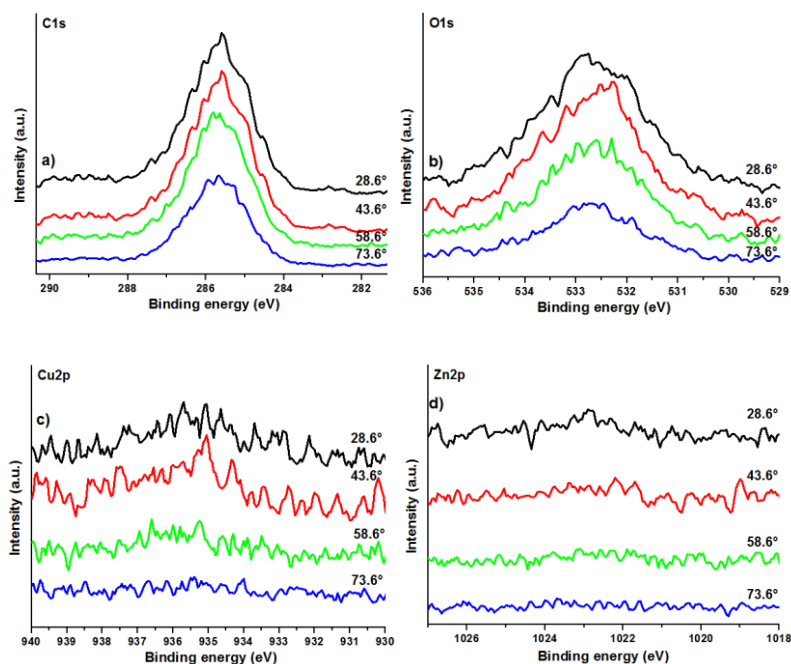


Figure 5. 21: Angle resolved high-resolution C 1s (a), O 1s (b), Cu 2p (c) and Zn 2p (d) spectra of the as received Cu37Zn acquired at different emission angles.

The apparent concentrations in atomic percentage versus the emission angle are shown in Figures 5.22, 5.23 and 5.24 of Cu18Zn, Cu28Zn and Cu37Zn respectively; the concentrations were calculated assuming the homogeneity within the whole analysed depth; the values at emission angle higher than  $60^\circ$  can be influenced by elastic scattering effects and should be corrected for it [2]. The Cu and Zn concentrations are calculated using the Cu  $2p_{3/2}$  and the Zn  $2p_{3/2}$  signals without distinguishing between the metallic and the oxidized contributions. In fact, the correction, which has to be applied to angle resolved XPS data when using the Theta Probe, the so-called angular signature, can be correctly applied only when the acquisition range is of about 20 eV. In the case of the Auger signals the required interval is almost the double and thus these data were not used for the identification of the copper and zinc chemical states. More measurements with a traditional approach are thus required by using another spectrometer. The plots of Figures 5.22a, 5.23a and 5.24a revealed the presence of an outermost layer mostly composed by carbon and oxygen on all the alloys investigated in this work.

In the case of the Cu18Zn (Fig. 5.22b) the copper and the zinc composition is constant for each emission angles and close to the composition calculated in the standard mode. The Zn content in the Cu28Zn (Fig. 5.23b) alloy is always higher than the nominal composition this might be due to a selective removal of zinc from the alloy leaving a copper-rich layer in the outermost layers. This might be the consequence of the mechanical polishing.

The angle resolved spectra of Cu37Zn (Fig. 5.24b) showed an increase of the Zn content at more surface angles where the composition is similar to the nominal one.



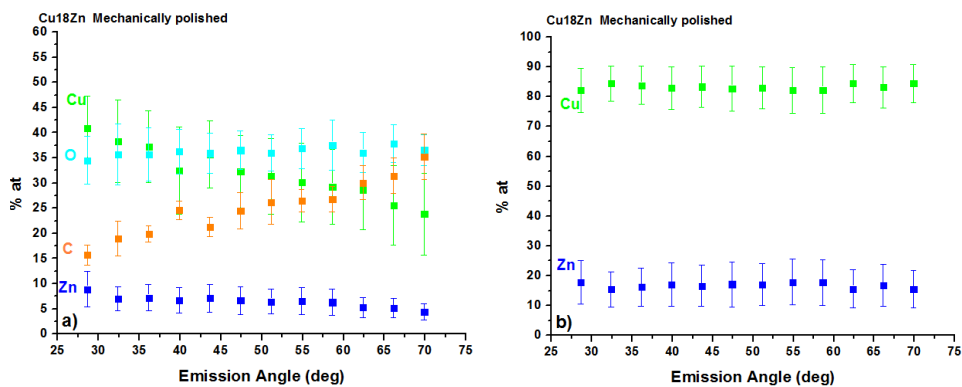


Figure 5. 22: Angle resolved results acquired on mechanically polished Cu18Zn. Mean and standard deviations were calculated over three independent measurements.

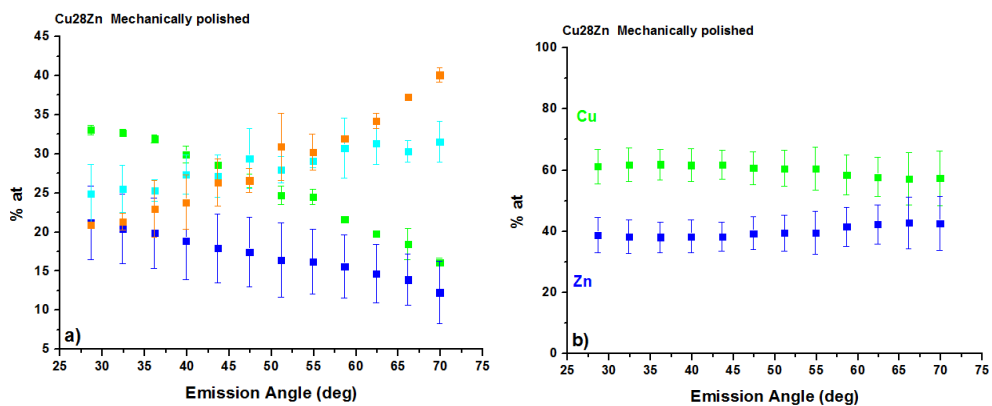


Figure 5. 23: Angle resolved results acquired on mechanically polished Cu28Zn. Mean and standard deviations were calculated over three independent measurements.

The apparent concentrations in atomic percentage versus the emission angle are shown in Figure 5.24b for the Cu37Zn alloy; an increase of the Zn content at more surface sensitive emission angles was found and it is similar to the nominal one.

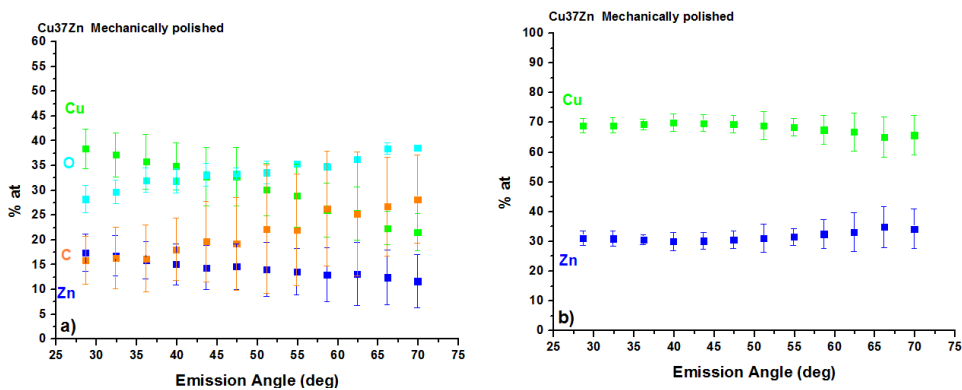


Figure 5. 24: Angle resolved results acquired on mechanically polished Cu37Zn alloy. Mean and standard deviation were calculated over three independent measurements.

The case of two lead-bearing brasses is quite different because of the presence of lead in the alloys. The Zn content in the alloy is found lower than the nominal composition and Pb-rich oxide films were found in both lead-containing brass alloys. The lower content of Zn in the film might be due to the dezincification process that induces the preferential removal of zinc from the alloy. The strong surface enrichment of lead in the oxide film might be due to mechanical effects as reported in the literature [35]. Lead was only found in the oxide layer since no metal components were detected in the spectrum after the curve fitting procedure. The Pb 4f<sub>7/2</sub> was found at BE of 138.6 eV and it was assigned to the presence of lead oxide in agreement with the literature [36]. The possible presence of carbonates and hydroxides cannot be assessed because these signals would have the same binding energy and the oxygen signal would exhibit the corresponding components at similar binding energy values of the zinc and copper compounds that are present at higher concentrations than lead in the alloy.

Figure 5.25 shows the composition versus emission angle: only the alloy elements are presented and also in this case the content of zinc and copper was calculated taking into account the areas under the Cu 2p<sub>3/2</sub> and Zn 2p<sub>3/2</sub> signals respectively. The trend of the curves is suggesting that the outermost layer is enriched of lead and the amount increases going towards more surface sensitive angles. No chemical shift for the Pb 4f<sub>7/2</sub> was observed. It has to be emphasised that the Zn 3s is partially interfering with the Pb 4f spectral region and the area of the Pb 4f was calculated after taking into account in the curve fitting the presence of the Zn3s contribution.

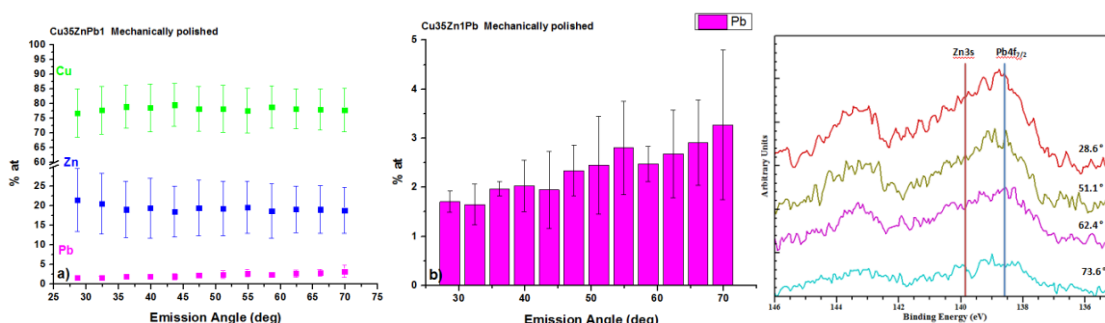


Figure 5. 25: Angle resolved results obtained on mechanically polished Cu35Zn1Pb. Only the alloy elements are shown. Copper and zinc are shown as total amount of metal and oxidized components.

The angle resolved results of Cu38Zn2Pb (Fig.5.26) showed an oxide layer enriched in lead in respect to the bulk composition. The Zn and Pb content increase as the emission angle was making XPS more surface sensitive. As far as the Cu35Zn1Pb no chemical shifts were observed for the Pb 4f<sub>7/2</sub> at different angles; its binding energy remained unchanged and equal to 138.7 eV

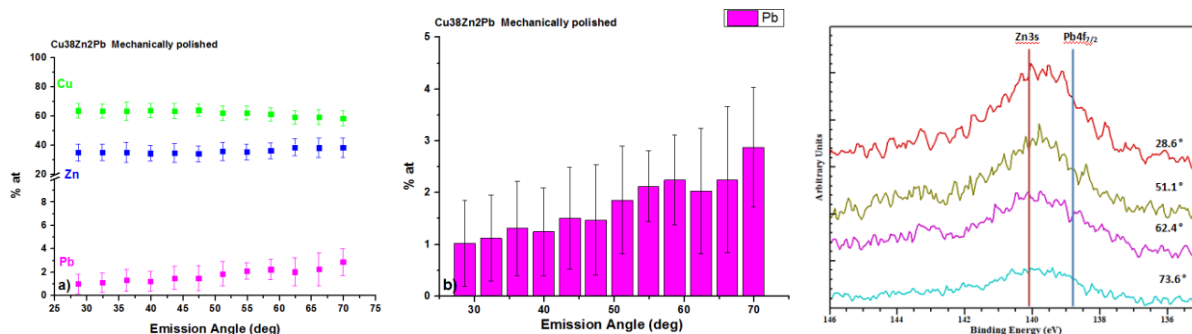


Figure 5. 26: Angle resolved results acquired on mechanically polished Cu38Zn2Pb. Only alloy elements are shown. Copper and zinc apparent concentrations were calculated using the Cu 2p<sub>3/2</sub> and Zn 2p<sub>3/2</sub> signals.

## 5.4 Discussion

On the basis exclusively on the photoelectron signal it is not possible distinguish between metallic and oxidized state of copper and zinc. The BE values of metallic and oxidized zinc are reported at 1021.6 eV, and for metallic copper and copper (I) oxide the BE at 932.5 eV. Hence in both cases it is not achievable the univocal identification of the two states. The x-ray induced Auger signals (XAES) show clear shifts in KE and changes in the shape of the spectra for the metals and oxide states. While many authors exploited the Auger spectra for the identification of the compounds when solely one chemical state was present in the sample under investigation [8, 10, 14 – 16, 37] the literature that reports the identification of the compounds when simultaneously present together with their quantitative evaluation results based on the XAE-spectra is scarce.

### 5.4.1 Curve fitting of X-ray induced Auger spectra

The XAES signals of pure copper and zinc metals and oxides are composed of several peaks, here the assignments were carried out following the results of the theoretical approach reported in literature predicting the differences in KE and intensity ratio [9, 14 - 16]. Each reference spectrum (envelope) could be reproduced based on the individual components and subsequently it was used for curve fitting more complex signals.

#### 5.4.1.1 Cu37Zn model brass alloy compared to reference compounds.

The Cu L<sub>3</sub>M<sub>45</sub>M<sub>45</sub> of Cu37Zn sputtered alloy (Fig. 5.10b) displayed an excellent agreement with the signal of the XAES signal of pure copper. The most intense peak assigned to <sup>1</sup>G splitting term related to the most probable transition was found at KE 918.6 eV for both the pure metallic copper and for the copper in the alloy. In addition, the energy difference between the individual signals and the intensity ratio are perfectly identical (Tab. 5.4).

The Zn  $L_3M_{45}M_{45}$  of Cu37Zn sputtered alloy (Fig. 5.10d) showed a similar line shape found for pure zinc but a small chemical shift of about + 0.2 eV of the most intense peak was detected. However, the energy difference and the intensity ratios between the individual signals are very close to those found for pure zinc (Table 5.1) and zinc in the sputtered alloy (Table 5.4).

A small but regular chemical shift of + 0.2 eV and - 0.1 eV that might also be considered within the experimental uncertainty was found for the Cu  $2p_{3/2}$  and Zn  $2p_{3/2}$  respectively when compared with the binding energy values obtained for the pure metals. The same results were found in studies of Cu-Zn alloys [8, 38]. These small differences can be attributed to changes in the electronic environment going from the pure metal to the alloy. The lattice parameter changes from 3.608 Å for pure copper to 3.6849 Å for a brass with 34.9% of Zn due to a higher size of zinc (Zn = 1.25 Å vs Cu = 1.179 Å) (see Chapter 2, Section 2.1.1). Hence, the electronic distribution on each atom might be expected different for pure copper and for the Cu37Zn alloy. Positive shifts for the BE and (nearly equal) negative shifts for the KE values, result in the same Auger parameter  $\alpha'$ , thus in similar final state effects.

The KE values and the line-shape of Cu  $L_3M_{45}M_{45}$  and Zn  $L_3M_{45}M_{45}$  allowed us to rule out the presence of Zn (0) and Cu (0) in the as received Cu37Zn (Fig. 5.9) alloy. On the contrary, the comparison of the XAES signals of ZnO with that of the “as received” Cu37Zn alloy showed good agreement. The difference between the KE values of the individual signals and their intensity ratios well matched those of the ZnO (Table 5.2). A shift of - 0.5 eV is found for the KE of the Zn LMM signal in the alloy (compared to the shift of + 0.8 eV in the Zn  $2p_{3/2}$  signal).

Based on both the Cu  $2p_{3/2}$  and the Cu  $L_3M_{45}M_{45}$  signals the presence of the copper oxide Cu<sub>2</sub>O (Fig. 5.7b) and of CuO (Fig. 5.6b) might be excluded. The comparison showed clear differences, thus at the surface of the “as received” alloy a different copper-compound is likely present. The presence of mainly copper hydroxide in the outer part of the surface film can be envisaged in agreement with what already reported in [15].

Regarding Cu  $2p_{3/2}$  and Zn  $2p_{3/2}$  of the mechanically polished Cu37Zn model alloy, the energy difference and the intensity ratios between the individual signals are almost identical, within the experimental error, to those of pure copper and zinc (Table 5.1) and copper and zinc in the Cu37Zn sputtered alloy (Table 5.4). Similar results were found for the Cu  $L_3M_{45}M_{45}$  and Zn  $L_3M_{45}M_{45}$ .

#### **5.4.1.2 Cu18Zn, Cu28Zn, Cu35Zn1Pb, Cu38Zn2Pb model brass alloy compared to reference compounds.**

These alloys were characterized in the as received state and after mechanically polished procedure.

*As received alloys.*

The Cu18Zn, Cu28Zn, Cu35Zn1Pb and Cu38Zn2Pb brass alloys in the as received state showed the presence of a thick contamination layer, at least greater than the XPS sampling depth. As a consequence no Cu and Zn signals were detected in the ARXPS spectra meaning that a contamination

layer and a thick oxide film are covering the characteristic elements of the alloy. The presence of the contamination layer, as it was pointed out above, was quite predictable since the samples were exposed to the atmosphere for long time before the XPS analysis. The history of the samples might be different and thus also the compounds that might be present at the surface of each sample might differ.

As far as concerns the Cu  $L_3M_{45}M_{45}$  and Zn  $L_3M_{45}M_{45}$  of as received samples, they appeared broader and noisier than the mechanically polished ones and their KE values and line-shapes ruled out the presence of Zn (0) and Cu (0). In this case the KE values were not in good agreement with the KE value of ZnO but it was difficult to identify all contributions because the signal-to-noise ratio was too small rendering the curve fitting quite challenging.

Based on both the Cu  $2p_{3/2}$  and the Cu  $L_3M_{45}M_{45}$  signals the presence of copper oxide  $Cu_2O$  (Fig. 5.7b),  $CuO$  (Fig.5.6b) might be excluded. The comparison showed clear differences, thus at the surface of the “as received” alloy a different copper-compound is likely to be present. The presence of mainly copper hydroxide in the outer part of the surface film can be envisaged in agreement with what is reported in [15].

#### *Mechanically polished alloys.*

The BE values of Cu  $2p_{3/2}$  and Zn  $2p_{3/2}$  signals concerning the mechanically polished Cu18Zn, Cu28Zn, Cu35Zn1Pb, Cu38Zn2Pb model alloys were in agreement with the values of Cu and Zn in the pure metals, in the Cu37Zn sputtered alloy and in the mechanically polished Cu37Zn as it can be seen from Tables 5.4 and 5.5.

Similarly, the KEs of the Cu  $L_3M_{45}M_{45}$  and Zn  $L_3M_{45}M_{45}$  signals were found in agreement with the values of Cu and Zn in pure metal compounds and the Cu37Zn sputtered alloy. The only appreciable difference was found in the Zn  $L_3M_{45}M_{45}$  signal of the lead-containing brass with the higher Pb and Zn contents. The difference between the Zn  $L_3M_{45}M_{45}$  of the pure zinc and Cu38Zn2Pb was found to be 0.4 (0.1) eV. This finding could be interpreted as the difference in the final state effects due to the presence of lead in alloy.

### **5.4.2 Chemical state plot**

The chemical state identification by XPS surface analysis has become routine for most of the elements in the periodic table [37]. However, for copper and zinc the chemical state identification based on the BE only is challenging since it is not possible distinguishing between Zn (II) and Zn (0) in the Zn 2p and between Cu (I) and Cu (0) in the Cu 2p spectra [37]

Moretti [9] showed that the chemical state plot and the modified Auger parameter concept are particularly important for copper and zinc compounds because the two dimensional representation of photoelectron BE versus XAES KE in the chemical state plot also known as Wagner chemical state plot, allows a more accurate assignment.

*Copper compounds:* Wagner chemical state plot of copper is shown in Figure 5.27; KE, BE and Auger parameters of the different compounds are summarized in Table 5.8.

The reference compounds (metallic copper, CuO, Cu<sub>2</sub>O and in addition Cu(OH)<sub>2</sub> [28, 29] are shown together with copper in the Cu37Zn model brass alloy after Ar<sup>+</sup> ion sputtering, after mechanical polishing and in the “as received” state. In addition Cu18Zn, Cu28Zn, Cu35Zn1Pb and CuZn2Pb in the as received state and after mechanical polishing procedure are also shown in the Wagner plot.

Metallic copper and Cu<sub>2</sub>O have the same BE at 932.5 (0.1) eV whereas CuO and Cu(OH)<sub>2</sub> clearly show higher binding energies. Interesting to note that the Auger parameter (Table 5.8 and diagonal line in the plot in Figure 5.27)  $\alpha' = 1851.1$  (0.1) eV is the same for metallic copper and Cu(OH)<sub>2</sub>, indicating a similarity of the copper chemical state. Cu<sub>2</sub>O instead, a copper Cu(I) compound, has an Auger parameter of  $\alpha' = 1849.2$  (0.1) eV (Table 5.8).

The copper signal of the sputtered alloy Cu37Zn coincides with that of the metallic copper. Copper in the “as received” alloy is found close to the Cu(OH)<sub>2</sub> reference material, confirming that the outmost surface is mainly constituted of copper hydroxide.

The copper signal of the Cu18Zn, Cu28Zn, Cu35Zn1Pb and CuZn2Pb in the as received state showed two main components: one at about 932.5 and the second at 935.0 eV. The first main component is related to the presence of Cu<sub>2</sub>O, unfortunately it was not possible a curve fitting procedure of the related Auger signal since this signal was very noise due to the attenuation of the Auger electrons by the presence of the thick contamination layer. These Auger signals were fitted using only 5 components; the most intense peak was found at about KE 916.1 eV. The Auger parameters,  $\alpha'$ , calculated using the Cu 2p<sub>3/2</sub> at 932.5 eV and the Cu L<sub>3</sub>M<sub>45</sub>M<sub>45</sub> at about 916.1 - 916.3 eV were found to be equal to 1851.2 (0.1) eV for Cu18Zn, 1850.9 (0.1) eV for the Cu18Zn, 1851.0 (0.1) eV for Cu35Zn1Pb, and 1851.1 (0.1) eV for the Cu38Zn2Pb alloy. These values were all close to the one of Cu(OH)<sub>2</sub> 1851.1 eV, thus confirming that the outmost surface of the Cu18Zn, Cu28Zn, Cu35Zn1Pb and CuZn2Pb brass alloys in the as received state is mainly composed of copper hydroxide.

The Cu18Zn, Cu28Zn, Cu37Zn, Cu35Zn1Pb and CuZn2Pb mechanically polished alloys showed single photoelectron peaks found at about BE 932.5 eV while the Auger signals showed two peaks: one at about KE 918.5 eV and the other at 916.9 eV. The Auger parameters were calculated and revealed the presence of two different chemical states: the first one is close to the metallic copper found at 1851.1 (0.1); 1)  $\alpha'_{\text{Cu18Zn}} = 1851.2$  (0.1) eV, 2)  $\alpha'_{\text{Cu28Zn}} = 1851.4$  (0.1) eV, 3)  $\alpha'_{\text{Cu37Zn}} = 1851.0$  (0.1) eV 4)  $\alpha'_{\text{Cu35Zn1Pb}} = 1851.1$  (0.2) eV and 5)  $\alpha'_{\text{Cu38Zn2Pb}} = 1851.2$  (0.1) eV.

The second calculated  $\alpha'$  was found close to the value obtained in the case of Cu<sub>2</sub>O (1849.2 (0.1)): 1)  $\alpha'_{\text{Cu18Zn}} = 1849.5$  (0.1), 2)  $\alpha'_{\text{Cu28Zn}} = 1849.6$  (0.1), 3)  $\alpha'_{\text{Cu37Zn}} = 1849.3$  (0.1), 4)  $\alpha'_{\text{Cu35Zn1Pb}} = 1849.5$  (0.2) and 5)  $\alpha'_{\text{Cu38Zn2Pb}} = 1849.4$  (0.1).

This indicates that on top of the alloys a thin oxide film was present. If, as very often is done, only the most intense Auger line of copper (918.5 (0.1) eV, Figure 5.11b) would have been used for speciation, the presence of Cu<sub>2</sub>O would not have been revealed.

Table 5. 8: Column 2 and 3 reports the BEs of the Cu 2p<sub>3/2</sub> and KEs of the Cu L<sub>3</sub>M<sub>45</sub>M<sub>45</sub> signals of the analysed materials (column 1). In column 4 the Auger parameters calculated using the different components for the XAES signals. Mean values and standard deviations were calculated over at least three independent measurements.

<b>Copper-containing materials</b>	<b>BE<sub>phot</sub> (eV)</b>	<b>KE<sub>Auger</sub> (eV)</b>	<b>α'</b>
<b>Cu (0)</b>	932.5 (0.1)	918.6 (0.1)	1851.1 (0.1)
<b>Cu<sub>2</sub>O</b>	932.4 (0.1)	916.8 (0.1)	1849.2 (0.1)
<b>CuO</b>	933.9 (0.1)	917.8 (0.1)	1851.7 (0.1)
<b>Cu37Zn Mech pol Met</b>	932.5 (0.1)	918.5 (0.1)	1851.0 (0.1)
<b>Cu37Zn Mech pol Ox</b>	932.5 (0.1)	916.8 (0.1)	1849.3 (0.1)
<b>Cu37Zn sputtered</b>	932.7 (0.1)	918.6 (0.1)	1851.3 (0.1)
<b>Cu37Zn as received</b>	935.0 (0.1)	916.2 (0.1)	1851.2 (0.1)
<b>Cu18Zn As rec Ox</b>	935.1 (0.1)	916.1 (0.1)	1851.2 (0.1)
<b>Cu18Zn As rec Ox</b>	932.5 (0.1)	916.1 (0.1)	1848.6 (0.1)
<b>Cu28Zn As rec Ox</b>	932.5 (0.1)	916.3 (0.1)	1848.8 (0.1)
<b>Cu28Zn As rec Ox</b>	934.6 (0.1)	916.3 (0.1)	1850.9 (0.1)
<b>Cu35Zn1Pb As rec Ox</b>	932.6 (0.1)	916.3 (0.1)	1848.9 (0.1)
<b>Cu35Zn1Pb As rec Ox</b>	934.7 (0.1)	916.3 (0.1)	1851.0 (0.1)
<b>Cu38Zn2Pb As rec Ox</b>	932.5 (0.1)	916.3 (0.1)	1848.8 (0.1)
<b>Cu38Zn2Pb As rec Ox</b>	934.8 (0.1)	916.3 (0.1)	1851.1 (0.1)
<b>Cu18Zn Mech pol Met</b>	932.5 (0.1)	918.7 (0.1)	1851.2 (0.1)
<b>Cu18Zn Mech pol Ox</b>	932.5 (0.1)	917.0 (0.1)	1849.5 (0.1)
<b>Cu28Zn Mech pol Met</b>	932.6 (0.1)	918.8 (0.1)	1851.4 (0.1)
<b>Cu28Zn Mech pol Ox</b>	932.6 (0.1)	917.0 (0.1)	1849.6 (0.1)
<b>Cu35Zn1Pb Mech pol Met</b>	932.5 (0.2)	918.6 (0.1)	1851.1 (0.2)
<b>Cu35Zn1Pb Mech pol Ox</b>	932.5 (0.2)	917.0 (0.1)	1849.5 (0.2)
<b>Cu38Zn2Pb Mech pol Met</b>	932.5 (0.1)	918.7 (0.1)	1851.2 (0.1)
<b>Cu38Zn2Pb Mech pol Ox</b>	932.5 (0.1)	916.9 (0.1)	1849.4 (0.1)

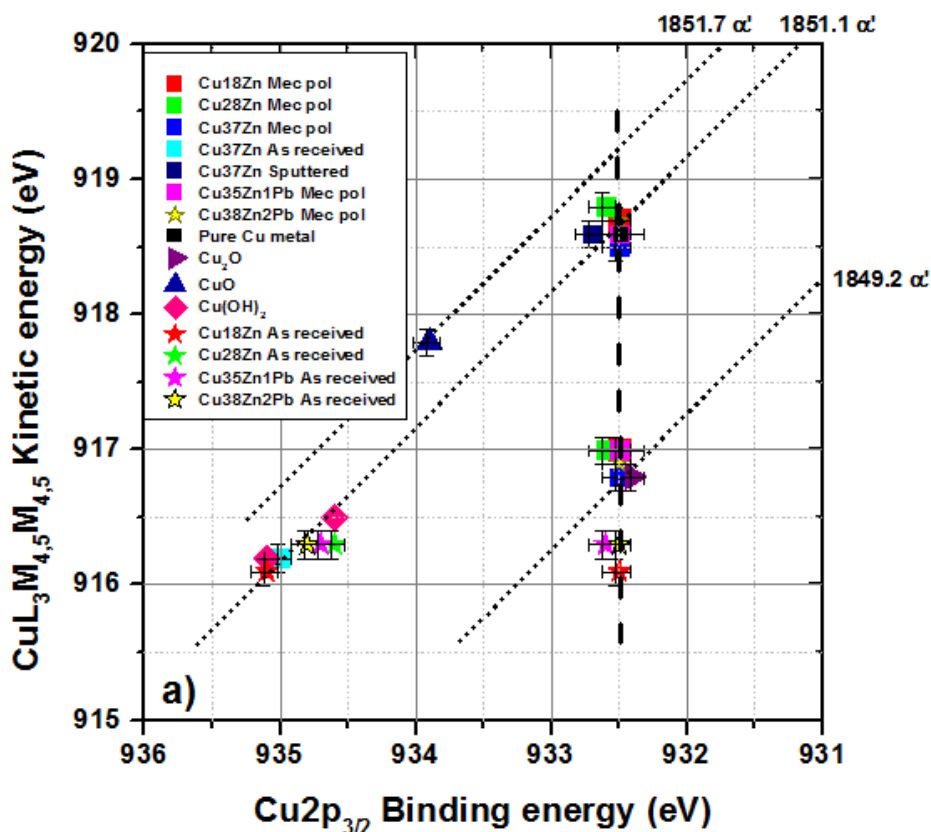


Figure 5. 27: Copper chemical state plot using data listed in Table 5.8.

*Zinc compounds:* Wagner chemical state plot of zinc is shown in Figure 5.28; KE, BE and Auger parameters of the different compounds are summarized in Table 5.9.

Zn (II) and Zn (0) compounds cannot be distinguished on the basis of the BE. Considering also the x-ray excited Auger signals and the chemical state plot, different chemical states became distinguishable. The Auger parameter for metallic zinc is  $\alpha' = 2013.7 (0.2)$  eV, for ZnO the Auger parameter is  $\alpha' = 2009.8 \pm 0.2$  eV. This is mainly due to a difference in the XAES Zn LMM kinetic energy (Table 5.9).

The  $\alpha'$  calculated for the Cu37Zn sputtered alloy was found to be 2014.0 (0.2) eV indicating that is close to that of metallic zinc chemical state ( $\alpha' = 2013.7 (0.2)$ ).

The  $\alpha'$  values of the Cu18Zn, Cu28Zn, Cu37Zn, Cu35Zn1Pb and CuZn2Pb as received alloys calculated were found to be: 1)  $\alpha'_{\text{Cu18Zn}} = 2010.5 (0.2)$  eV, 2)  $\alpha'_{\text{Cu28Zn}} = 2014.1 (0.2)$  eV, 3)  $\alpha'_{\text{Cu37Zn}} = 2010.1 (0.2)$  eV, 4)  $\alpha'_{\text{Cu35Zn1Pb}} = 2009.6 (0.2)$  eV and 5)  $\alpha'_{\text{Cu38Zn2Pb}} = 2009.6 (0.2)$  eV related to the presence of Zn(OH)<sub>2</sub> and ZnO according to literature [10, 31, 32].

The Cu18Zn, Cu28Zn, Cu37Zn, Cu35Zn1Pb and CuZn2Pb mechanically polished alloys showed single photoelectron peaks at about BE 1021.7 eV while the Auger showed two main peaks at about



KE 988.1 eV and 992.1 eV. The Auger parameter calculated revealed the presence of two different chemical states.

The first  $\alpha'$  is close to the metallic zinc 2013.7 (0.2) eV: 1)  $\alpha'_{\text{Cu18Zn}} = 2014.1$  (0.3) eV, 2)  $\alpha'_{\text{Cu28Zn}} = 2014.1$  (0.2) eV, 3)  $\alpha'_{\text{Cu37Zn}} = 2014.0$  (0.2) eV, 4)  $\alpha'_{\text{Cu35Zn1Pb}} = 2013.9$  (0.3) eV and 5)  $\alpha'_{\text{Cu38Zn2Pb}} = 2014.2$  (0.3) eV.

The second calculated  $\alpha'$  is close to the ZnO (2009.8 (0.2) eV): 1)  $\alpha'_{\text{Cu18Zn}} = 2010.0$  (0.2) eV, 2)  $\alpha'_{\text{Cu28Zn}} = 2010.0$  (0.2) eV, 3)  $\alpha'_{\text{Cu37Zn}} = 2009.7$  (0.2) eV, 4)  $\alpha'_{\text{Cu35Zn1Pb}} = 2010.0$  (0.3) eV and 5)  $\alpha'_{\text{Cu38Zn2Pb}} = 2009.7$  (0.3) eV.

Hence, the Wagner plot shows that at the surface of the mechanically polished samples both metallic Zinc and ZnO could be detected, thus supporting that a thin oxide layer is present on top of the alloy.

As mentioned above for copper, if only the most intense Auger line of zinc would have been considered, only the presence of ZnO (or Zn(0) respectively) would have been revealed.

Table 5. 9: in column 2 and 3 are listed the BEs of the Zn 2p<sub>3/2</sub> and KEs of the Zn L<sub>3</sub>M<sub>45</sub>M<sub>45</sub> signals of the analysed compounds (column 1). In column 4 the Auger parameters calculated using the different components for the XAES signals. (Standard deviations are reported in brackets)

<b>Zinc- containg materials</b>	<b>BE<sub>phot</sub> (eV)</b>	<b>KE<sub>Auger</sub> (eV)</b>	<b><math>\alpha'</math> (eV)</b>
<b>Zn(0)</b>	1021.6 (0.1)	992.1 (0.1)	2013.7 (0.2)
<b>ZnO</b>	1021.6 (0.1)	988.2 (0.1)	2009.8 (0.2)
<b>Cu37Zn Mech pol Met</b>	1021.7 (0.1)	992.3 (0.1)	2014.0 (0.2)
<b>Cu37Zn Mech pol Ox</b>	1021.7 (0.1)	988 (0.1)	2009.7 (0.2)
<b>Cu37Zn sputtered</b>	1021.7 (0.1)	992.3 (0.1)	2014.0 (0.2)
<b>Cu37Zn as received</b>	1022.4 (0.1)	987.7 (0.1)	2010.1 (0.2)
<b>Cu18Zn As rec Ox</b>	1023.3 (0.1)	987.2 (0.1)	2010.5 (0.2)
<b>Cu28Zn As rec Ox</b>	1022.3 (0.1)	988.1 (0.1)	2010.4 (0.2)
<b>Cu35Zn1Pb As rec Ox</b>	1022.3 (0.1)	987.3 (0.1)	2009.6 (0.2)
<b>Cu38Zn2Pb As rec Ox</b>	1022.3 (0.1)	987.3 (0.1)	2009.6 (0.2)
<b>Cu18Zn Mech pol Met</b>	1021.8 (0.1)	992.3 (0.2)	2014.1 (0.3)
<b>Cu18Zn Mech pol Ox</b>	1021.8 (0.1)	988.2 (0.1)	2010.0 (0.2)
<b>Cu28Zn Mech pol Met</b>	1021.7 (0.1)	992.4 (0.1)	2014.1 (0.2)
<b>Cu28Zn Mech pol Ox</b>	1021.7 (0.1)	988.3 (0.1)	2010.0 (0.2)
<b>Cu35Zn1Pb Mech pol Met</b>	1021.6 (0.2)	992.3 (0.1)	2013.9 (0.3)
<b>Cu35Zn1Pb Mech pol Ox</b>	1021.6 (0.2)	988.4 (0.1)	2010.0 (0.3)
<b>Cu38Zn2Pb Mech pol Met</b>	1021.7 (0.2)	992.5 (0.1)	2014.2 (0.3)
<b>Cu38Zn2Pb Mech pol Ox</b>	1021.7 (0.2)	988.0 (0.1)	2009.7 (0.3)

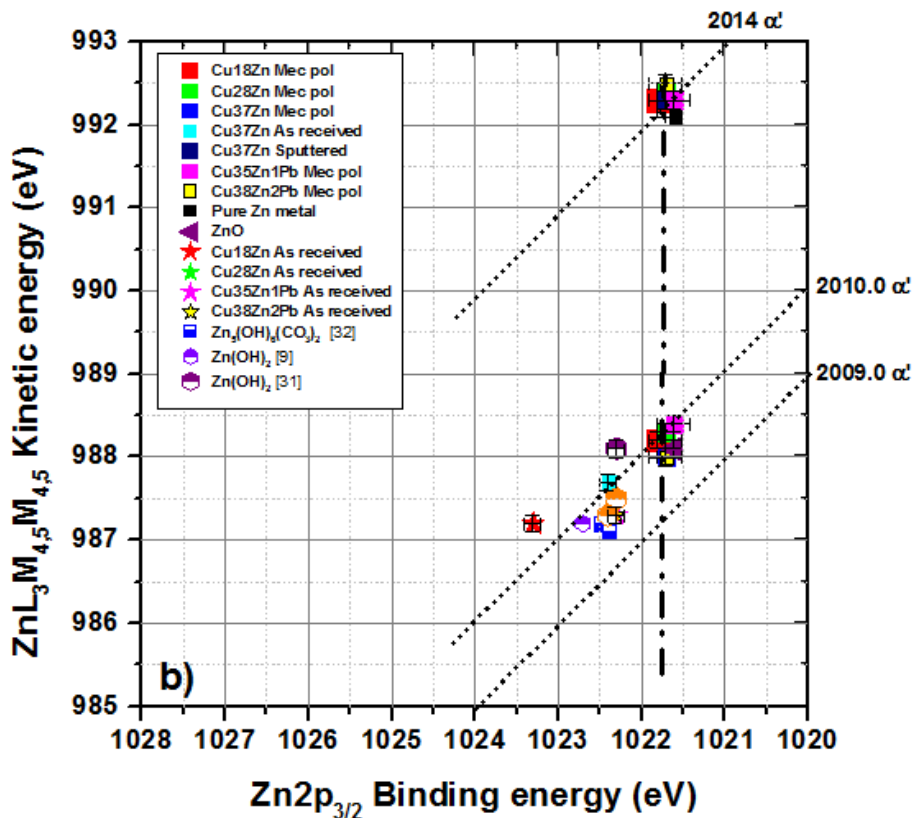


Figure 5. 28: Zinc chemical state plot using data listed in Table 5.9.

Thanks to the chemical state plot the identification of the different compounds present at the surface of the brass samples was possible using the combination of photoelectron and Auger lines. The starting point was the curve fitting of Cu  $L_3M_{4,5}M_{4,5}$  and Zn  $L_3M_{4,5}M_{4,5}$  Auger signals based on theoretical descriptions. Thanks to the curve fitting procedure of the Auger signals it was possible the use of the KE values of the different components to construct the Wagner plot.

Once we got information about the compounds present at the surface of the samples, the second step is the achievement of the quantitative information about these compounds.

The quantitative analysis regarding copper-zinc alloys (brasses) with an oxidized surface layer in the nano-meter range is reported in only few examples [9, 14 - 16].

Here, the discussion on a novel approach for univocal assignment to the various copper and zinc chemical states when they are simultaneously present is described. In the second part the description of a quantitative analysis method to be followed when a thin-layer of copper and zinc oxy-hydroxides is present on the surface of the alloy is presented.

### 5.4.3 Development of analytical strategy for simultaneous quantification of copper and zinc in complex nanostructured systems

As it has been previously described, the quantitative analysis of a system such as a brass alloy with a thin oxidized surface film on top is not possible straightforward because the copper and zinc photoelectron signals do not allowed the differentiation between metallic and oxidized states. However, the distinction is possible exploiting the x-ray excited Auger signals that allow a clear and quantitative distinction between metallic and oxidized states.

A procedure and a formula that allows transfer the experimental intensity ratio from the Auger signal to the intensity ratio of the 2p signals is presented.

Copper and zinc of the analysed reference compounds as well as the Cu<sub>37</sub>Zn brass alloy after sputtering and in the as received state showed only one chemical state, either metallic or oxidized. Thus on these samples the experimental intensity ratio, *R*, defined as:

$$R = \frac{I_{2p}}{I_{LMM}} \quad \text{eq. 5. 1}$$

could be calculated both for metallic and oxidized components.

The intensity of *I*<sub>2p</sub> and *I*<sub>LMM</sub> obtained following the curve fitting of the spectra were corrected for the analyser transmission function *Q*(*E*) [20] and the attenuation lengths *Λ* [34].

The experimentally determined intensity ratios *R* (Table 5.10) are different for copper and zinc, but it also results different for the metallic (*R*<sub>met</sub>) and the oxidized (*R*<sub>ox</sub>) state.

The common assumption of an elemental sensitivity factor *S*, reported also as cross section *σ*, for a given transition, is that it is independent on its chemical environment, but here this assumption cannot be applied (Table 5.10).

It was also been found that *R* values depend on the geometry of the instrument. Thus, a correction factor *k*, defined as:

$$k = \frac{R_{ox}}{R_{Met}} \quad \text{eq. 5. 2}$$

could be proposed for the calculation of the surface composition; *k* was found to be 1.5 for copper and equal to 0.8 for zinc (Table 5.10).

The experimentally determined ratios, *R*, between the photoelectron intensity *I*<sub>2p</sub> and the Auger signal intensity *I*<sub>LMM</sub> for the “as received” Cu<sub>37</sub>Zn alloy were found to be very different from those of CuO (Table 5.2). This finding might be explained taking into account the attenuation of the photoelectrons (KE 552 eV) and of the x-ray excited Auger electrons (KE 917 eV) by the thick contamination layer

present on the as-received alloy. Assuming the presence of 5 nm thick contamination layer (Table 11), the attenuation of the 2p photoelectrons is twice as strong as for the x-ray excited Auger ones. The R ratio corrected for the attenuation due to the presence of the contamination layer (Table 5.10) is also given and results to be close to the value calculated for the pure oxide. As a consequence, also the k value is identical to the one of the pure copper oxide after the correction (Table 5.10). The same reasoning holds for the zinc signals.

Table 5. 10: Ratio of the intensity of Cu 2p<sub>3/2</sub> and Cu L<sub>3</sub>M<sub>4,5</sub>M<sub>4,5</sub> and of Zn 2p<sub>3/2</sub> and Zn L<sub>3</sub>M<sub>4,5</sub>M<sub>4,5</sub>; the correction factor k = R<sub>ox</sub>/R<sub>met</sub> for copper and zinc compounds is also reported: spectra were acquired with two spectrometers and areas were corrected for the geometry of the instruments.

Signal	Sample	$R = \frac{I_{2p}}{I_{LMM}}$		$k = \frac{R_{OX}}{R_{Met}}$	
		Theta	Quantera	Theta	Quantera
Cu metal	Pure metal	3.4	2.0	1.56	1.5
Cu metal	Sputtered alloy	-	1.9	-	1.55
CuO	Pure oxide	5.3	3.0	1.56	1.5
Cu-oxide	As received alloy	2.5	1.5	0.74	0.75
Cu-oxide corr.	As rec. corrected for the contamination layer	5.1	3.0	1.5	1.5
Zn metal	Pure metal	3.8	2.3	0.79	0.74
Zn metal	Sputtered alloy	-	2.0	-	0.87
ZnO	Pure oxide	3.0	1.7	0.79	0.74
Zn - oxide	As received alloy	1.4	1.2	0.36	0.52
Zn - oxide corr.	As rec. corrected for the contamination layer	3.2		0.83	

The Cu L<sub>3</sub>M<sub>4,5</sub>M<sub>4,5</sub> (Fig. 5.11b) and Zn L<sub>3</sub>M<sub>4,5</sub>M<sub>4,5</sub> (Fig. 5.11d) spectra of brass alloys with a thin surface film allow determining the intensity of the metallic and the oxide contribution. This is the case of the mechanically polished sample. From these intensities the intensity ratio, r:

$$r = \frac{LMM_{ox}}{LMMM_{Met}} \quad \text{eq. 5. 3}$$

is calculated.

The r values calculated for copper and zinc were found equal to 1 in the case of copper and equal to 4 in the case of Zn (Table 5.11). The r and the k values allow the calculation of the corresponding intensity ratio for the 2p signals. The equation derived for the calculation is:

$$\% 2p_{ox} = \frac{100 \cdot r \cdot k}{(1+k \cdot r)} \quad \text{eq. 5. 4}$$

Where:

k: is the (element specific) correction factor (Table 5.10)

r: is the experimentally determined ratio of the x-ray induced Auger signals of the same element but in different oxidation state:  $LMM_{ox}/LMM_{met}$  (Table 5.10)

The figure 5.16 shows the calculated percentage of oxidized and metallic compound in the 2p signal for both copper and zinc as a function of the input data  $r = LMM_{ox}/LMM_{met}$ .

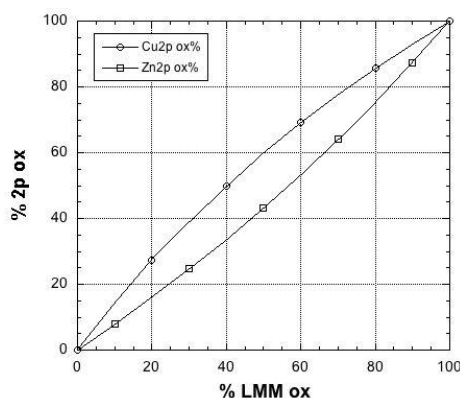


Figure 5. 29: Percentage of oxidized component in the 2p signal vs percentage of the oxidized component in the LMM signal for copper and zinc

The intensity of the oxide in the case of copper increases by about 20% whereas for zinc the intensity of the metal increases by 20%.

Table 5. 11: Input parameters and results of calculations to determine the metallic and oxide intensity in the (unresolved) 2p photoelectron peak of copper and zinc in the case of the Cu37Zn mechanically polished sample.

Metal	% ox LMM	% met LMM	ratio r ox/met	correction factor k	% ox in 2p	$I_{ox\ 2p}$	$I_{met\ 2p}$
Copper	50	50	1	1.55	61	55066	35206
Zinc	80	20	4	0.8	76	41269	13068

In the following, the discussion about the theoretical background of this empirical approach, especially of the intensity ratio  $R = I_{2p} / I_{LMM}$  (Table 5.10) is provided.

While the intensity ratios of different x-ray excited Auger signals, e.g.  $L_{23}M_{45}M_{45} / L_{23}M_{45}M_{45}$  for Ni, Cu and Zn could be related to the effective charge  $\Delta q$  on the metal atom in the different compounds [38, 40], such a theoretical basis for the intensity ratio between 2p photoelectron and LMM x-ray excited Auger electrons signals is lacking.

An attempt to use intensity ratio between 2p photoelectrons and LMM Auger electrons was made to quantify  $Cu_2O$  on Cu [14].

In later studies [15, 16] the ratio of experimental intensities  $I_{2p}/I_{LMM}$  was used to determine the sensitivity factor for the Auger signals  $\sigma_{LMM}$  of copper and zinc, assuming this factor to be the same for metallic and oxidized compounds. As in this work  $R_{ox}$  and  $R_{met}$  were different both for copper and zinc (see Table 5.10) meaning that also the calculated cross sections  $\sigma_{LMM,ox}$  and  $\sigma_{LMM,met}$  were different. The assumption of equal cross sections [14 – 16] does not hold for complex layered systems.

Only the experimentally determined factor  $k = R_{ox}/R_{met}$  as proposed in this work, is characteristic for an element (copper, zinc), reasonably constant and independent on the instrument used for the analysis.

Thus the factor  $k$  can be used to convert  $LMM_{ox}/LMM_{met}$  ratios resulted from the curve fitting of x-ray excited Auger signals (Fig. 11b,d) into intensity ratios of the photoelectron signal  $2p_{ox}/2p_{met}$  needed for obtaining the intensities of each metallic and oxidized component. These data are required for the quantitative analysis of nano-structured layered systems.

#### 5.4.4 Testing the analytical strategy on a model system: Cu37Zn model brass alloy

Quantitative analysis was performed on the Cu37Zn sputtered alloy where no contamination and no oxides were detected on the surface, thus Cu 2p and Zn2p and their corresponding XAES signals refer to the metallic state only. The quantitative analysis was performed using the first-principles model and the results are summarized in Table 5.12.

Table 5. 12: Quantitative analysis results of Cu37Zn sputtered model brass alloy (wt.%).

Point	Cu met	Zn met
1	74%	26%
2	80%	20%

The inelastic mean free path (IMFP) used in this work to correct the intensity signals are calculated according to Tanuma et al. [39] and are called IMFP TPP-2M. These values take into account the different material densities from which the electrons are photo-emitted, the energy gap and the number

of valence electrons. The difference with the nominal composition can be ascribed to a preferential sputtering effect that was already reported in [40]

The as received Cu37Zn model alloy showed the C1s signal which can be associated to the thick contamination layer: in fact, despite a slight sputtering the layer was not removed and no metallic signals from the underlying alloy were detected. Quantitative analysis was performed following the first principles approach. The results are presented in Table 5.13.

Table 5. 13: Quantitative analysis results of the oxide film on the “as received” Cu37Zn model brass alloy

<b>Point</b>	<b>Oxide film Thickness (nm)</b>	<b>Contamination layer thickness (nm)</b>	<b>Cu ox at %</b>	<b>Zn ox at %</b>
<b>1</b>	> 10	4.5	83	17
<b>2</b>	> 10	3.8	84	16
<b>3</b>	> 10	4.5	85	15
<b>4</b>	> 10	4.0	83	17

#### **5.4.5 Application of the analytical strategy: brass alloys with thin oxide film**

##### **5.4.5.1 Cu37Zn mechanically polished**

The Cu  $L_{3M_{4.5}M_{4.5}}$  and Zn  $L_{3M_{4.5}M_{4.5}}$  Auger signals (Fig.5.11b,d) revealed the presence of two different chemical states, one associated with the metallic state and the other to the oxide state for both copper and zinc. In such layered system the intensities of the metallic and oxidized components in the 2p photoelectron signal were calculated following the approach outlined above, results of one example are provided in Table 5.14, working on the intensity of the XAES components. Once the photoelectron intensities  $ICu_{met}$ ,  $ICu_{Ox}$ ,  $IZn_{met}$  and  $IZn_{Ox}$  and of the contamination  $Ic$  are known, the quantitative analysis of such a thin-layered system was performed following the three-layer model [19, 41, 42] assuming the presence of a contamination layer and of a homogeneous oxide film on top of the alloy. The density for Cu37Zn alloy was taken as  $8.5 \text{ g/cm}^3$ , the density of the oxide film was assumed to be  $6 \text{ g/cm}^3$  ( $6.14 \text{ g/cm}^3$  for  $Cu_2O$  and  $5.61 \text{ g/cm}^3$  for  $ZnO$ ). The results of the quantitative analysis of the mechanically polished Cu37Zn alloy obtained for three different analysis points are provided in Table 5.14.

A thin oxide film is present on the surface of the alloy. The oxide film is rich in copper oxide ( $Cu_2O$ ) and contains about 33% of zinc oxide ( $ZnO$ ). The alloy composition beneath the oxide film is in average very close to the nominal composition, 64.5 (1.5) % copper and 35.5 (1.5)% zinc. One of three samples even shows 37% zinc.

Table 5. 14: Quantitative analysis results of the oxide film and the alloy beneath the oxide film formed on Cu37Zn brass model alloy after mechanical polishing are reported. The thickness of the oxide layer and the contamination film are also listed in the table.

Area of analysis	Oxide film thickness (nm)	Contamination layer thickness (nm)	Cu ox wt. %	Zn ox wt. %	Cu met wt. %	Zn met wt. %
1	1.9	0.7	61	39	63.4	36.6
2	1.5	1.7	70	30	62.6	37.4
3	0.5	2.4	69	31	65.8	34.2

#### 5.4.5.2 Mechanically polished Cu18Zn, Cu28Zn, Cu35Zn1Pb and Cu38Zn2Pb brass alloys

The quantitative analysis was also performed on the Cu18Zn, Cu28Zn, Cu35Zn1Pb and Cu38Zn2Pb brass alloys after mechanically polishing procedure.

A contamination layer was found on the samples due to presence of the C1s signal. The XAES spectra of both copper and zinc showed the same shape of those acquired on the Cu37Zn mirror-like polished sample. In fact the presence of metallic and oxidized components, indicating a thin oxide layer on the brass surface, were observed. The Cu  $L_3M_{4,5}M_{4,5}$  (Fig. 16-19b) and Zn  $L_3M_{4,5}M_{4,5}$  (Fig. 16-19d) areas were used to calculate the ratio  $r$  of metallic and oxidized copper and zinc respectively. The intensities of the metallic and oxidized components in the 2p photoelectron signals were calculated following the approach outlined above as in the case of the Cu37Zn brass model alloy.

The results of the quantitative analyses performed using the three-layer model [19] for the different brass compositions are listed in Table 5.15.

Table 5. 15: Quantitative results obtained for mechanically polished Cu18Zn, Cu28Zn, Cu35Zn1Pb and Cu38Zn2Pb brass model alloys.

	$t$ (nm)	$l_c$ (nm)	CuOx at. %	ZnOx at. %	Cu met at. %	Zn met at. %
<b>Cu18Zn Mech pol</b>	1.8 (0.3)	0.7 (0.2)	75 (2)	25 (2)	74 (4)	26 (4)
<b>Cu28Zn Mech pol</b>	1.0 (0.3)	2 (1)	53 (2)	47 (2)	63 (1)	37 (1)
<b>Cu35Zn1Pb Mech pol</b>	1.0 (0.2)	1.0 (0.1)	43 (1)	57 (1)	68 (1)	32 (1)
<b>Cu38Zn2Pb Mech pol</b>	1.2 (0.3)	1.8 (0.2)	26 (1)	74 (1)	67 (1)	33 (1)

In the above Table (tab. 5.15) the atomic percentage of lead is not showed since no metallic component has been found in both lead-bearing brasses, thus the percentage of lead obtained by the three- layer model resulted to be 100 at. % in its oxidized form. The Pb  $4f_{7/2}$  was found at BE 138.6 eV ascribable to the presence of  $Pb_3O_4$  in agreement with the literature [41].



It is evident that the alloys after mechanical polishing procedure showed a Zn enriched layer. The amount of Zn increases with increasing the Zn content in the alloy. As it is known from the literature [45 – 52] brass alloys suffering of a specific form of corrosion called dezincification, a form of dealloying which involves selective leaching of the less noble metal. The presence of Zn in the oxide layer could be also due to a mechanical effect inducing also a lead enrichment [40].

The quantitative analysis was also performed on the same alloys in the as received state. The results are shown in Table 5.16. The results differ from each other and no evident correlation could be found since the exact history of the samples is unknown. However it is evident that the copper is mainly present as copper (II) hydroxide at the surface of each samples at the same time the Cu<sub>2</sub>O is present in lower amount.

Table 5. 16: Quantitative results of as received Cu18Zn, Cu28Zn, Cu35Zn1Pb and Cu38Zn2Pb brass model alloys.

	<b>Oxide film (nm)</b>	<b>Cu(OH)<sub>2</sub> (at.%)</b>	<b>Cu<sub>2</sub>O (at.%)</b>	<b>Zn(OH)<sub>2</sub> (at.%)</b>	<b>Lead oxide (at.%)</b>
<b>Cu18Zn</b>	> 10 nm	75 (5)	7 (4)	18 (1)	
<b>Cu28Zn</b>	> 10 nm	71 (5)	17 (1)	12 (1)	
<b>Cu35Zn1Pb</b>	> 10 nm	38 (2)	9 (1)	42 (4)	11 (1)
<b>Cu38Zn2Pb</b>	> 10 nm	37 (1)	13 (1)	23 (2)	28 (1)

#### 5.4.5.3 Thickness and composition of the oxide layer

On the basis of the results reported in the Wagner plot (Section 5.4.2) it can be affirmed that following the mechanical polishing procedure, the surface of the alloys were covered by an oxide layer mainly constituted of ZnO and Cu<sub>2</sub>O in addition lead oxide was found in the case of lead - bearing brasses.

The thickness of the layer is supposed to be in the nanometre range since the metallic component of copper and zinc were revealed. A depth profile analysis was carried out by angle resolved XPS analysis. The angle resolved XPS results showed that the metallic components of copper and zinc were detectable even at small emission angles, substantiating the hypothesis of the presence of a nanometre oxide film covering the alloys. In Figure 5.30 are shown the Cu L<sub>3</sub>M<sub>4,5</sub>M<sub>4,5</sub> Auger signals acquired at two different emission angles (one deeper than the other one) of the analysed samples.

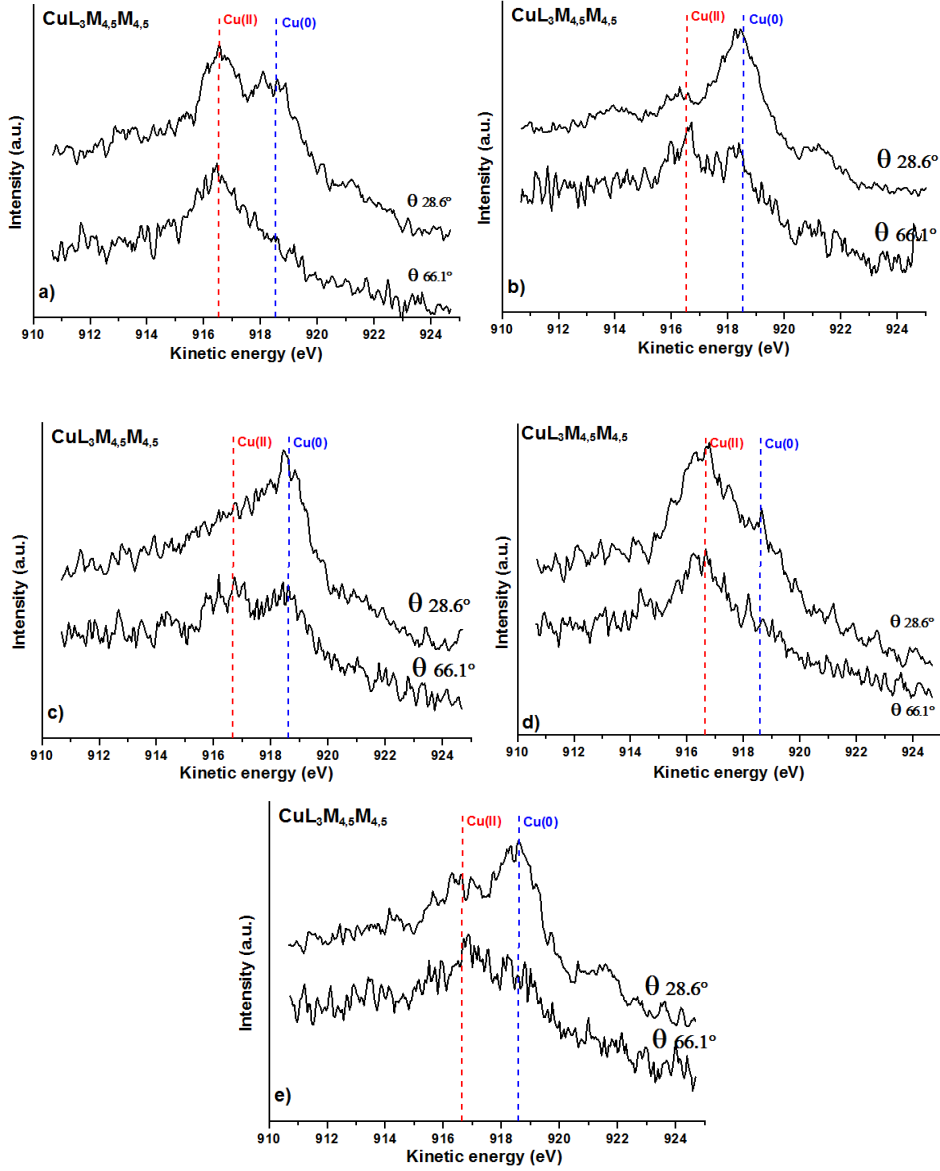


Figure 5. 30: CuLMM high-resolution spectra of a) Cu18Zn, b) Cu28Zn, c) Cu35Zn1Pb and d) Cu38Zn2Pb acquired at two different emission angles,  $\theta$ : 28.6° and 66.1° respectively.

Taking into account the Cu  $L_{45}M_{45}M_{45}$  intensities of two different emission angles, it was possible the estimation of the thickness of the surface layer, exploiting the equation (eq.5.5) [2]:

$$\frac{Im(\theta_1)}{Im(\theta_2)} = \exp\left[-\frac{t^*}{\lambda_{ox}} \left( \frac{1}{\cos\theta_2} - \frac{1}{\cos\theta_1} \right)\right] \quad \text{eq. 5. 5}$$

where:

$\theta_{1,2}$  are two emission angles

$Im(\theta_1)$  and  $Im(\theta_2)$  are the intensities of the metallic components at  $\theta_1$  and  $\theta_2$

$\lambda_{ox}$  is the inelastic mean free path of the oxide

$t^*$  is the thickness of the contamination and the oxide layer

In Table 5.17 are listed the obtained results. It can be seen that the thickness is in the nanometer range and is in good agreement with the results obtained by the three layer model (Table 5.15 for Cu37Zn mechanically polished and Table 5.14 for the other brass alloys).

Table 5. 17: In table are reported the thickness values obtained by eq (5). Standard deviations are reported in brackets.

	<b>t* (nm)</b>
<b>Cu18Zn</b>	1.1 (0.1)
<b>Cu28Zn</b>	1.0 (0.1)
<b>Cu37Zn</b>	1.3 (0.1)
<b>Cu35Zn1Pb</b>	0.8 (0.1)
<b>Cu38Zn2Pb</b>	0.9 (0.1)

## 5.5 Conclusions

Curve fitting of the X-ray excited Auger spectra of copper Cu L<sub>3</sub>M<sub>4,5</sub>M<sub>4,5</sub> and zinc Zn L<sub>3</sub>M<sub>4,5</sub>M<sub>4,5</sub> allows the discrimination of the different chemical states in complex systems. A novel analytical strategy for simultaneous chemical state identification and quantification of copper and zinc in complex, thin-layered systems has been established. Standards of pure metals and oxides are essential to accurately determine the envelopes of the complex Auger signals for curve fitting and for calculating the experimental intensity ratios  $R = I_{2p} / I_{LMM}$  between photoelectron and Auger intensity required for quantification. The experimentally determined quantification factor  $k = R_{ox}/R_{met}$  as proposed in this work is characteristic for an element (copper, zinc), reasonably constant and independent on the instrument used for the analysis.

Thanks to the chemical state plot was possible an unambiguous assignment of the chemical state of both elements.

The composition of the alloy beneath the thin oxide film mechanically polished samples of Cu37Zn was calculated with the new analytical strategy and presented in this work and it is found to be very close to the nominal composition. The new analytical approach for quantification has been tested on Cu37Zn model brass alloys after different surface pre-treatments and has proven to be successful.

The novel approach allowed the identification and the quantification of the species present at the surface of the brass alloys. The free – lead brasses are covered by a Cu<sub>2</sub>O and ZnO oxide film, while the XPS results of the lead - bearing brasses show that the oxide layer is enriched in lead. Thus, the outermost layer is mainly composed by ZnO and lead oxide.

## References

1. J. F. Watts, J. Wolstenholme, An introduction to surface analysis by XPS and AES, John Wiley and Sons Ltd, West Sussex, 2003
2. D. Briggs and J.T. Grant, Surface Analysis by Auger and X-ray Photoelectron Spectroscopy, IM Publications and Surface Publication Data, West Sussex, 2003
3. NIST Standard Reference Database 20 Version 4.1, accessed October 2016,
4. D.C. Frost, A. Ishitani and C.A. McDowell, Molecular Physics, 24 (1982) 861-888.
5. P.E Larson, Journal of Electron Spectroscopy and Related Phenomena, 4 (1984) 213-218.
6. I. Platzman, R. Brener, H. Haick and R. Tannenbaum, Journal of Physical Chemistry C, 112 (2008) 1101-1108
7. M. Fantauzzi, D. Atzei, B. Elsener, P. Lattanzi and A. Rossi, Surface and Interface Analysis, 38 (2006) 922-930
8. G. Moretti, Journal of Electron Spectroscopy and Related Phenomena 95 (1998) 95-
9. G. Moretti, S. De Rossi, G. Ferraris, Applied Surface Science, 45 (1990) 341-349
10. G. Deroubaix and P. Marcus, Surface and Interface Analysis, 18 (1992) 39-46
11. E. Antonides and G.A. Sawatzky, Journal of Physics C-Solid State Physics, 9 (1986) 548-552
12. G. Moretti, Journal of Electron Spectroscopy and Related Phenomena 86 (1995) 365 – 380
13. C.D.Wagner, A. Joshi, Journal of Electron Spectroscopy and Related Phenomena 48 (1988) 283
14. Speckmann, S. Haupt and H.H. Strehblow, Surface and Interface Analysis, 11 (1988) 148-155
15. P. Druska and H.H. Strehblow, Surface and Interface Analysis, 23 (1995) 440-450
16. I. Milosev and H.H. Strehblow, Journal of the Electron Society, 150 (2003) 518-524
17. N. Fairley, CASAXPS, Version 2.3.15, Casa Software Ltd, Wilmslow, UK, 2010
18. D. A. Shirley, Physical Review B: Solid State, 5 (1982) 4809–4814
19. A. Rossi and B. Elsener, Surface and Interface Analysis, 18 (1992) 499–504
20. M. Fantauzzi, A. Pacella, J. Fournier, A. Gianfagna, G. B. Andreozzi and A. Rossi, Analytical and Bioanalytical Chemistry, 404 (2012) 821– 833.
21. S. R. Barman and D. D. Sarma, Journal of Physics: Condensed Matter, 4 (1992) 8608–8616
22. S. P. Kowalczyk, R. A. Pollak, F. R. McFeely, L. Ley and D. A. Shirley, Physical Review B: Solid State, 8 (1983) 2388–2391
23. J. Ghijsen, L. H. Tjeng, J. van Elp, H. Eskes, J. Westerink, G. A. Sawatzky and M. T. Czyzyk, Physical Review B, 38 (1988) 11322–11330.
24. E. Antonides, E. C. Janse and G. A. Sawatzky, Physical Review B: Solid State, 15 (1988) 1669–1689.
25. E. D. Roberts, P. Weightman and C. E. Johnson, Journal of Physics C: Solid State Physics, 8 (1985) L301–L304.
26. G. G. Kleiman, Journal of Electron Spectroscopy and Related Phenomena, 100 (1999) 18–34.

27. G. G. Kleiman, R. Landers, P. A. P. Nascente and S. G. C. de Castro, *Physical Review B: Condensed Matter Physics*, 46 (1992) 4405–4413.
28. S. K. Chawla, N. Sankarraman and J. H. Payer, *Journal of Electron Spectroscopy and Related Phenomena*, 61 (1992) 1–18
29. N. S. McIntyre and M. G. Cook, *Analytical Chemistry*, 48 (1985) 2208–2213.
30. J. F. Moulder, W. F. Stickle, P. E. Sobol and K. D. Bomben, *Handbook of X-ray Photoelectron Spectroscopy*, Perkin-Elmer Corp., Physical electronics, Minnesota, 1992.
31. T.L. Barr, J.J. Hackenberg, *Journal of the American Chemical Society* 104 (1982) 5390-5394].
32. L. S. Dake, D. R. her and J. M. Zachara, *Surface And Interface Analysis*, 14 (1989) 71-75].
33. J.H. Scofield, *J. Electron Related Phenomena*, 8 (1976) 129 – 137
34. J.X.Wu, M.R.Ji, M.Galeotti, A.M.Giusti, G.Rovida, *Surface And Interface Analysis*, 22 (1994) 323-326
35. J. X. WU, M. R. Ji, M. Galeotti, A. M. Giusti, G. Rovid, *Surface And Interface Analysis*, 22, 323-326 (1994)
36. D. Atzei, B. Elsener, M. Fantauzzi, F. Brundu, A. Rossi, *Spectrochimica Acta Part B* 121 (2016) 38–46
37. M. C. Biesinger, L. W. M. Lau, A. R. Gerson and R. S. C. Smart, *Applied Surface Science*, 257 (2010) 887–898
38. J.A. Rodriguez and J. Hrbek, *Journal of Vacuum Science and Technology*, 11 (1993) 1998-2002
39. S. Tanuma, C.J. Powell and D.R. Penn, *Surface and Interface Analysis*, 35 (2003) 268-275
40. G.E. Hammer and R.M. Shemanski, *Surface and Interface Analysis*, 10 (1987) 355-359
41. D. De Filippo, A. Rossi, B. Elsener and S. Virtanen, *Surface and Interface Analysis*, 15 (1990) 668-674,
42. A. Rossi and B. Elsener, *Materials Science Forum*, 185 (1995) 337-346
43. S. Yashonath and M.S. Hedge, *Journal of Chemical Sciences, Proceedings Indian Academy of Sciences*, 89 (1980) 489-494
44. Rabab M. El-Sherif, Khaled M. Ismail, Waheed A. Badawy, *Electrochimica Acta*, 49 (2004) 5139 – 5150
45. E.P. Polubkin, M. Shuldner, *TAIME*, 161 (1945) 214
46. E.E. Langenegger, F.P.A. Robinson, *Corrosion Science*, 25 (1968) 59
47. C. H. Stiwell, E. C. Turniseed, *Industrial and Engineering Chemistry*, 26 (1934) 740
48. U.R. Evans, *The corrosion of Oxidation of Metals*, ed. Edward Arnold, London (1960)
49. G.D. Bengough, R. May, *Journal of the Institute of Metals*, 32 (1924), p. 81
50. S. Selvaraj, S. Ponmariappan, M. Natesan, N. Palaniswamy, *Corrosion Reviews*, 21 (2003) 41 – 74
51. H. Sugawara, H. Ebiko, *Corrosion Science*, 1967 (1967) 513 – 523

52. R. W. FINK, Transactions of the American Electrochemical Society, 75 (1939) 441
53. R. Karpagavalli, R. Balasubramaniam, Corrosion Science 49 (2007) 963–979
54. G.V. Korshin, J.F. Ferguson, A.N. Lancaster, Corrosion Science 42 (2000) 53-66

# Chapter 6

## *Development of an in-situ and non-destructive electrochemical sensor for the determination of the corrosion rate inside historical brass wind instruments*

*In this Chapter a work concerning the development of an in-situ and non-destructive electrochemical sensor for the determination of the corrosion rate inside historical brass wind instruments is presented. The electrochemical sensor, containing a reference and counter electrode, has been tested on reference samples in a diluted phosphate buffer solution, pH 7, with  $10^{-3}$  M chlorides. This solution does not alter the surface composition as shown by X-ray photoelectron spectroscopy. To calibrate the sensor the same materials and solutions were used in a traditional three-electrode cell and with the sensor; the results were in good agreement. The sensor is fit for purpose and has already been applied for corrosion monitoring in brass wind instruments.*

*This work has been published in Materials and Corrosion Journal (WILEY-VCH Verlag GmbH & Co. KGaA, Weinheim): B. Elsener, F. Cocco, M. Fantauzzi, S. Palomba and A. Rossi, Determination of the corrosion rate inside historical brass wind instruments – Proof of concept, Materials and Corrosion 67 (2016) 1336 – 1343.*

*The electrochemical measurements were carried out at the laboratory of the Institute of Building Materials, ETH Zurich, (Switzerland), the X-ray photoelectron spectroscopy were carried out the Department of Material Science - Laboratory of Surface Science Materials - ETH Zurich, (Switzerland) during my internship at the ETH Zurich.*

*Prof. A. Rossi, Prof. B. Elsener and Dr M. Fantauzzi supported the work with discussions and thorough revisions of the results.*

## 6.1 Introduction

The corrosion resistance of materials exposed to specific environments, the corrosion mechanisms and corrosion protection methods are widely studied by scientists working in corrosion science using electrochemical techniques [1]. These techniques are also being used in the field of conservation to analyze metal artefacts [2]. Electrochemical techniques have been used since the 19<sup>th</sup> century [2] to stabilize and clean archeological artifacts, but it is only since the 1990s that these treatments were correctly monitored [3]. The first scientist employing these techniques was Rathgen from Germany who applied cathodic polarization on bronze artifacts [3]. Since then electrochemical techniques have been used for a variety of applications such as monitoring of marine metal artefacts [4], to study the electrochemical behavior of natural patinas on metal artefacts [5] or to monitor the storage of the artefacts in solution [6]. Hence, the corrosion mechanisms affecting archaeological and historic metal artefacts before or during their treatment can be more easily understood using electrochemical techniques [2].

Following this line, this work intends to develop an electrochemical sensor to understand the mechanism of corrosion and to monitor its evolution over time on brass musical instruments of the 19<sup>th</sup> and 20<sup>th</sup> century. These artefacts are conserved in a private collection, the Burri Museum in Bern (Switzerland) with more than 1200 brass wind instruments [7]. The ‘historically informed performance practice’ (HIP) [8] is a dominant trend in contemporary musical practice that intends to play original ‘period instruments’ which are restored, in concerts. So the criteria for the use of period instruments negotiate between the two extremes: being displayed only in museum cases, or being subjected to ‘normal’ concert use.

Private and public instrument collections have to confront more and more with such issues. The main concern of museums and conservators is corrosion of the brass instruments due to the high humidity inside the instruments during and after playing. In general copper and brass alloys are highly resistant to atmospheric corrosion due to the formation of protective layers of corrosion products, which reduce the rate of attack [9 - 11]. Regularly played instruments have constantly a high level of internal relative humidity (RH) that, as a result, increases the risk of metal corrosion. Indeed, in a recent study [12] the humidity conditions were assessed inside different historical brass wind instruments before, during and after being played. It was shown that during playing the RH reached 90% in few minutes, and it takes several days to reach ambient RH again. Hence, a thin film of water can be present for quite a long time inside the instruments and corrosion damage of the brass instruments might occur on long-term.

The scientific approach to this conservation problem according to the Conservation Committee of the International Council of Museums (ICOM-CC) is preventive conservation, defined as “all measures and actions aimed at avoiding or minimizing future deterioration and loss.” [ICOM-CC 2008:2]. In order to propose preventive measures able to control the conditions that might cause damage of artefacts, it is necessary to be able to monitor the evolution of corrosion over time and to understand



the mechanism of corrosion.

Non-destructive techniques to assess the conservation state of the artefacts by means of in-situ measurements are thus very important tools for conservators to obtain the relevant information on the corrosion state and rate inside the instruments and to control the efficiency of preventive conservation measures.

Electrochemical techniques were used in this work since the corrosion of metals is an electrochemical process. The measurement of the corrosion potential and of the polarization resistance ( $R_p$ ), from which it can be possible to calculate the instantaneous corrosion rate, were chosen as a tool to assess information about the conservation state of the artefacts.

This goal could be achieved using a miniaturized electrochemical cell that could be used outside but especially inside the historical instruments (tuning slides). In order to be suitable for the use in ancient musical instruments the miniaturized cell has to fulfil three requirements: the measurements have to be fast to minimize the contact time between the sensor and the artefact; non-aggressive test solutions have to be used to avoid damaging of the instruments, since the measurements have to be non-destructive; the conservators should be able to carry out the measurement in situ and achieve rapid information.

Firstly, the work has involved the development of the electrochemical sensor and subsequently its calibration, afterward the sensor has been applied on reference materials. The ultimate goal is to apply the sensor on the historical brass musical instruments.

## 6.2 Experimental

### 6.2.1 Development of the electrochemical sensor

An electrochemical sensor that consists of a combined Ag/AgCl solid-state reference electrode and a small platinum grid as counter electrode, both embedded in a thin sponge, was developed. The first sensor prototype had a surface of about  $2 \text{ cm}^2$  ( $1.5 \times 1.5 \text{ cm}$ ) and it was about 2 mm thick. This sensor was used for the proof of concept on flat samples only. The schematic representation of the sensor for electrochemical measurements on flat samples and a photograph are shown in Figure 6.1

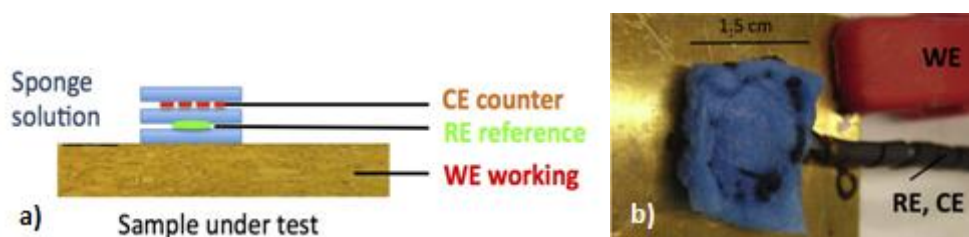


Figure 6. 1: a) Schematic drawing of the newly developed sensor for in-situ electrochemical measurements. The sponge is ca.  $1.5 \times 1.5 \text{ cm}$  (area  $2 \text{ cm}^2$ ), b) the photograph of the first developed sensor.

The reference electrode (RE) used for the sensor was a very small Ag/AgCl electrode from a commercial producer. This tiny electrode is used since long time as chloride sensitive sensor in cement

based materials to measure the free chloride content in the pore solution [13, 14]. In order to operate as reference electrode and to measure a stable and reproducible potential, the electrolyte in the sensor sponge must contain a small, constant chloride concentration. Instead, an Ag/AgCl in saturated KCl was used for the traditional three electrodes cell to carry out the calibration test. Both the traditional Ag/AgCl (sat) and the calomel  $\text{Hg}_2\text{Cl}_2$  reference electrodes could not be used for the sensor since the reference electrode for the in-situ measurements had to be as small as possible and flexible.

A small platinum grid connected to a platinum wire was used as counter electrode. The distance between counter electrode and reference electrode should not be too small; in the sensor the distance is about 1 mm (Figure 6.1a). The distance between the counter electrode and the sample (working electrode) is about 2 mm. The use of a very thin platinum grid allowed easy deformation of the sensor that can also be easily adapted to tubular samples.

A further development consisted in a tubular sensor mounted on a thin plastic tube in order to insert the sensor in the brass instruments. This sensor can be pressed against the inside of the brass tuning slides by a small balloon that can be inflated by air pressure and released after the measurements.

### 6.2.2 Materials and solutions

The brass alloys used in this work were Cu18Zn, Cu28Zn, Cu37Zn, Cu35Zn1Pb and Cu38Zn2Pb that are described in more detailed in Chapter 4 (§4.1.2) and Chapter 5. These samples were produced as thin sheets and their metallurgical structure was similar to the structure of the artefacts from the 19<sup>th</sup> century [15]. These alloys were tested both in “as received” conditions and after mechanical polishing with diamond paste in ethanol.

The electrochemical measurements were performed both in a traditional electrochemical cell and with the sensor, in a non-aggressive diluted phosphate buffer solution of pH 7 (Fluka). In order to get a stable potential of the Ag/AgCl solid-state electrode potential, chloride ions have to be present in the solution. Three solutions  $10^{-2}$ ,  $10^{-3}$  and  $10^{-4}$  M NaCl were tested in order to find a solution that provides the required stability of the reference electrode potential and a negligible alteration of the brass surface.

### 6.2.3 Electrochemical measurements

An Autolab potentiostat/galvanostat (ECO Chemie NL) under computer control was used for the measurements. Open circuit potentials (OCP) were measured over seven minutes. Polarization resistance ( $R_p$ ) was measured after five minutes. The  $R_p$  measurements were programmed for  $\pm 15$  mV vs OCP, starting the sweep from the OCP in anodic direction. The sweep rate was 0.5 mV/sec.

The traditional electrochemical cell was a Plexiglas vessel with an opening of 1 cm diameter, exposing a defined part ( $0.78 \text{ cm}^2$ ) of the sample surface to the solution. As reference electrode a saturated Ag/AgCl electrode with a Luggin capillary filled with the test solution was used, its potential is 0.197 V vs normal hydrogen electrode (NHE).

The potential difference between the standard reference electrode (Ag/AgCl sat.) and the AgCl electrode in the sensor was measured before each series of measurements with the sensor. It was found to be important to soak the sensor sponge for about 15 min in the solution in order to have a reproducible solution composition, especially the chloride concentration, in the sponge before starting a series of measurements.

### 6.2.4 Surface characterization

The sample surface before and after the electrochemical measurements with the sensor was characterized by optical microscopy by using an AX10 Imager M1m (Carl Zeiss, Oberkochen, Germany) equipped with a CCD camera.

Surface composition of Cu37Zn was monitored by X-ray photoelectron spectroscopy (XPS) using the Thetaprobe (ThermoFisher, East Grinstead UK). Details about the technique, the instruments and the data processing are reported in Chapter 3 (§3.4) and Chapter 4 (§4.7). The quantitative analysis was carried out on the basis of the first principle approach detailed in Chapter 4 (§4.7.3).

## 6.3 Results

### 6.3.1 Measurements in the electrochemical cell

The as received brass alloys with 18 and 37 wt.% of zinc and the mechanically polished alloys were exposed to the buffer solution at pH 7 with different NaCl concentrations. The results of open circuit potential (OCP) measurements versus time showed good reproducibility and were stable after about 5 min. In Figure 6.2 the OCP measurements of the alloys Cu18Zn and Cu37Zn after mechanical polishing procedure are shown. Table 6.1 provides the mean values of the OCP for the two alloys, in the two different surface states and for three different chloride concentrations. It can be observed that the Cu37Zn alloy exhibits more negative OCP values than the Cu18Zn samples.

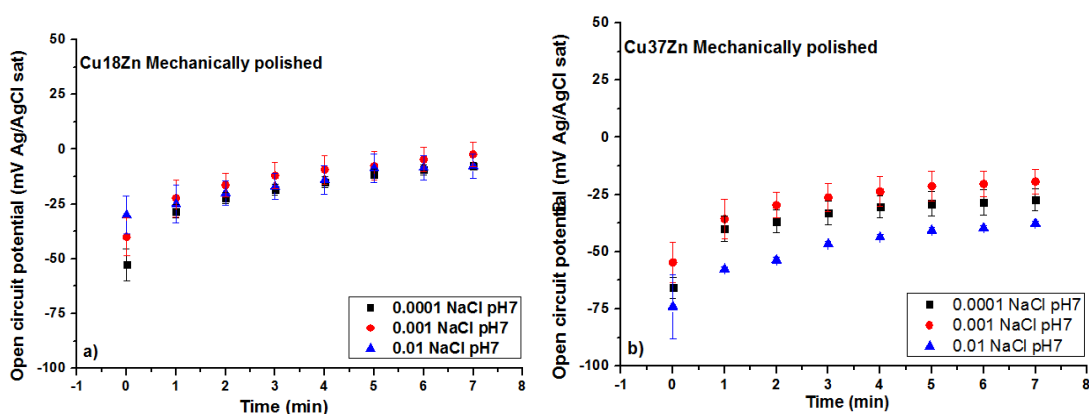


Figure 6.2: Open circuit potentials (OCP) versus contact time with the pH = 7 phosphate buffer solution containing NaCl ( $10^{-4}$ ,  $10^{-3}$  and  $10^{-2}$ M) measured using the electrochemical cell for the (a) Cu18Zn and (b) Cu37Zn after mechanically polishing procedure.

The polarization resistance measurements (Figure 6.4) show a linear  $I/\epsilon$  curve at  $\pm 15$  mV vs the OCP. The experimental  $R_p$  values were multiplied for the test area ( $0.78 \text{ cm}^2$ ); the resulting specific values ( $\text{k}\Omega\text{cm}^2$ ) for the different alloys are listed in Table 6.2.

### 6.3.2 Measurements with the electrochemical sensor

Open circuit potential (OCP) and polarization resistance ( $R_p$ ) were measured with the electrochemical sensor on the same brass alloys as in the electrochemical cell. The sponge of the sensor was soaked with the test solution, put on a filter paper to remove the excess of the solution, and then the sensor with Ag/AgCl reference and platinum counter electrode (Fig. 6.1) was pressed with a small plastic bar onto the sample surface in order to get reproducible contact conditions. The OCP measurements carried out using the sensor (Fig. 6.3) are stable after about 5 min. The mean values of the OCP for the different alloys, surface states and chloride concentrations in the test solution obtained with the sensor are given in Table 6.1. It can be noted that the scatter between individual measurements performed with the sensor is slightly higher compared to the electrochemical cell.

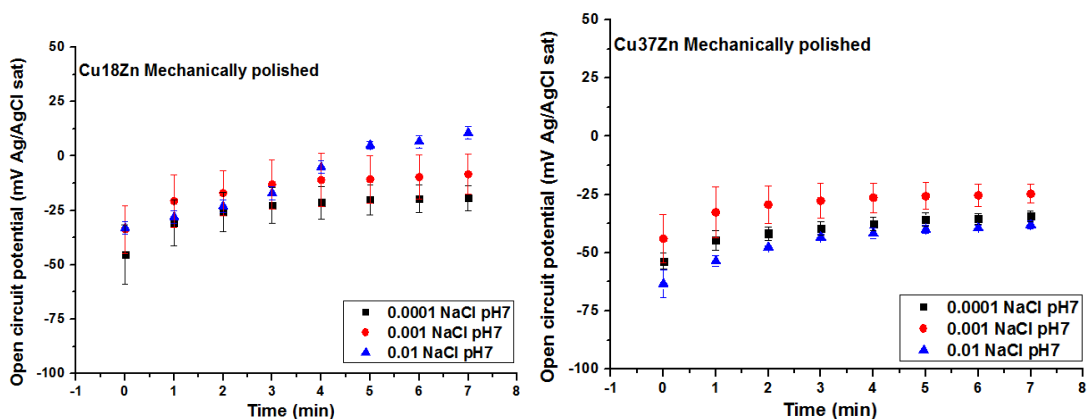


Figure 6.3: Open circuit potentials (OCP) versus contact time with the pH = 7 phosphate buffer solution containing NaCl ( $10^{-4}$ ,  $10^{-3}$  and  $10^{-2}$ M) measured using the electrochemical sensor for the (a) Cu18Zn and (b) Cu37Zn after mechanically polishing procedure.

Table 6. 1: Open circuit potential (OCP) and Polarization resistance measurements ( $R_p$ ) obtained on brass alloys using the traditional electrochemical cell and the sensor. Electrolyte: pH = 7 phosphate buffer solution containing  $10^{-2}$ ,  $10^{-3}$  and  $10^{-4}$  M NaCl. OCP are given vs Ag/AgCl saturated electrode.

Alloy / chloride conc.	Electrochemical cell		Electrochemical sensor	
	OCP (mV)	$R_p$ ( $k\Omega cm^2$ )	OCP (mV)	$R_p$ ( $k\Omega cm^2$ )
<b>As received 0.01 M</b>				
<b>Cu18Zn</b>	$-4 \pm 8$	$79 \pm 8$	$-15 \pm 20$	$80 \pm 10$
<b>Cu37Zn</b>	$-40 \pm 5$	$39 \pm 5$	$-35 \pm 8$	$36 \pm 8$
<b>Mech. Polished 0.01 M</b>				
<b>Cu18Zn</b>	$-7 \pm 5$	$14 \pm 4$	$-9 \pm 4$	$20 \pm 3$
<b>Cu37Zn</b>	$-39 \pm 3$	$11 \pm 2$	$-38 \pm 5$	$15 \pm 5$
<b>Mech. Polished 0.001 M</b>				
<b>Cu18Zn</b>	$-2 \pm 5$	$24 \pm 4$	$-7 \pm 5$	$25 \pm 5$
<b>Cu37Zn</b>	$-19 \pm 4$	$21 \pm 2$	$-26 \pm 6$	$20 \pm 4$
<b>Mech. Polished 0.0001 M</b>				
<b>Cu18Zn</b>	$-9 \pm 3$	$21 \pm 3$	$-15(6)$	$34 \pm 8$
<b>Cu37Zn</b>	$-27 \pm 5$	$26 \pm 2$	$-30 \pm 8$	$18 \pm 4$

The  $R_p$  measurements obtained using the sensor are shown in Fig. 6.4. A slight hysteresis is observed that might be due to the tarnish film on the “as received” brass alloys or due to the relatively high sweep rate of 0.5 mV/s. The  $R_p$  values were multiplied with the test area ( $2 \text{ cm}^2$ ), the resulting specific  $R_p$  values ( $k\Omega cm^2$ ) for the different alloys are summarized in Table 6.1.

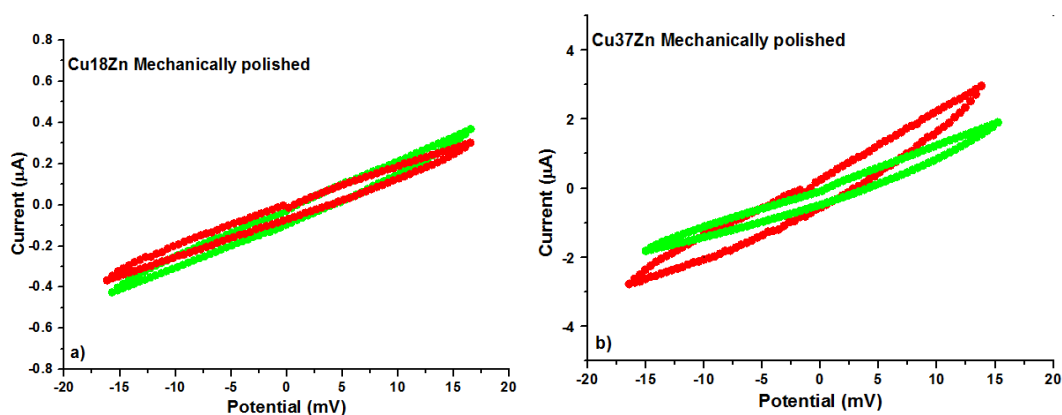


Figure 6.4: Examples of polarization resistance measurements: brass alloys in pH = 7 phosphate buffer solution containing  $10^{-2}$ ,  $10^{-3}$  and  $10^{-4}$  M NaCl performed with the sensor (red line; Area =  $2 \text{ cm}^2$ ) and in the electrochemical cell (green line; area =  $0.78 \text{ cm}^2$ ). (a) Cu18Zn as received, (b) Cu37Zn mechanically polished

### 6.3.3 XPS surface characterization

XPS survey scans and high-resolution spectra were acquired in order to identify and quantify all the elements present at the surface of the model brass alloys after exposure to the phosphate buffer solutions with different chloride concentrations.

Figure 6.5 shows the XPS spectra of the mechanically polished brass alloy with 37 wt.% of zinc before and after exposure to a buffer phosphate solution (pH 7) with different NaCl concentrations. The measurements were repeated three times for each solution. The spectrum of the brass alloy in contact with the buffer solution without NaCl is also provided for comparison. The characteristic signals of Cu, Zn and O are detected together with carbon signals due to the adventitious carbon. P and Ca signals were found in all samples, except in the case of the mechanically polished one, due do the contact with the phosphate buffer solution. Chlorine was below the detection limit of the technique for all NaCl concentrations.

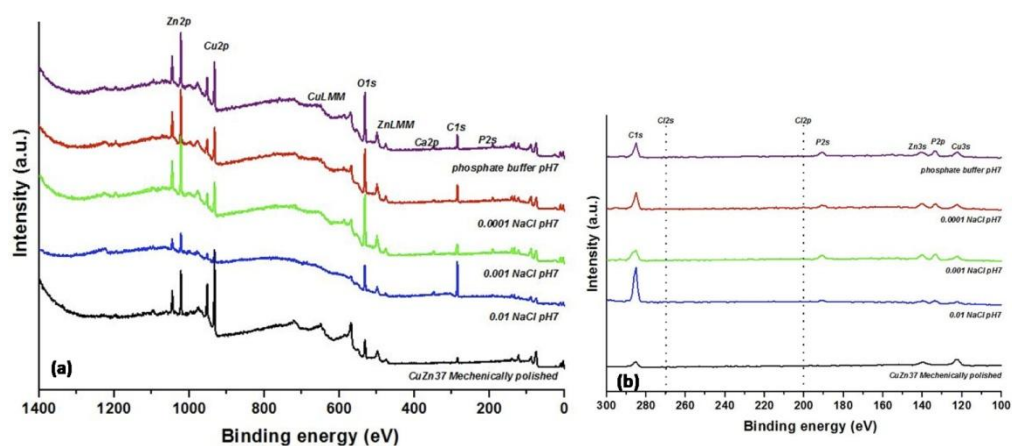


Figure 6.5: XPS spectra of the sample Cu<sub>37</sub>Zn mechanically polished before and after the electrochemical tests performed with the sensor using phosphate buffer solution at pH 7 with different chloride concentrations. (a) Survey spectrum, (b) magnification of the region from 300 to 100 eV

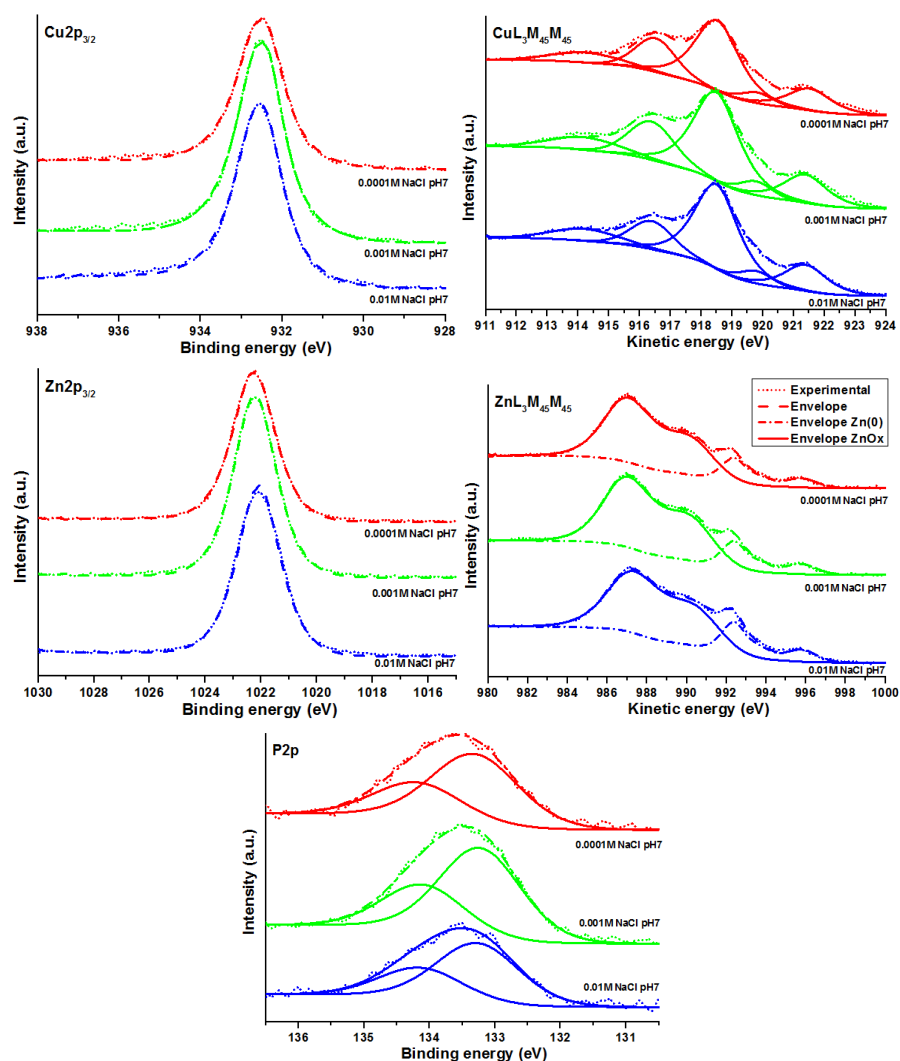


Figure 6.6: XPS high resolution spectra of Cu  $2p_{3/2}$ , Zn  $2p_{3/2}$ , Cu  $L_3M_{4.5}M_{4.5}$ , Zn  $L_3M_{4.5}M_{4.5}$  and P  $2p$  of the sample mechanically polished Cu37Zn before the electrochemical tests performed with the sensor using phosphate buffer solution at pH 7 with different chloride concentrations.

The photoelectron signal Cu  $2p_{3/2}$  showed a single peak at 932.5 (0.1) eV, while its related Cu  $L_3M_{4.5}M_{4.5}$  Auger peak showed five components, the main component was found at 918.5 (0.1) eV, for all the analyzed solutions. These are the characteristic BE and KE values for metallic copper [16 – 18]. No oxide component of copper was found at the surface of the samples in phosphate buffer solution.

The Zn  $2p_{3/2}$  photoelectron signal showed a single peak at 1022.3-1 (0.1) eV. The Auger signal showed both the oxide and the metallic components. The main component of the oxide part of the signal was found at 987.0 (0.1) eV while the main component related to the metallic zinc was found at 992.3 (0.1) eV. The oxide component might be assigned to zinc orthophosphate according to literature [19].

The phosphorus 2p signal consisted of the  $2p_{3/2}$  and  $2p_{1/2}$  doublet, due to spin-orbit coupling. Curve fitting procedure was performed constraining the integrated intensity ratio between these two signals

to 2 and their energy separation to 0.85 eV. The BE of the 2p<sub>3/2</sub> component of phosphorus was found to be 133.3 (0.1) eV and could be due to the presence of zinc orthophosphate according to [19].

Table 6.2 BE and KE values of Cu 2p<sub>3/2</sub>, Zn 2p<sub>3/2</sub>, Cu L<sub>3</sub>M<sub>4,5</sub> M<sub>4,5</sub>, Zn L<sub>3</sub>M<sub>4,5</sub> M<sub>4,5</sub> and P 2p signals of the mechanically polished Cu37Zn after the measurement with the sensor. Electrolyte: buffer phosphate at pH 7 + 10<sup>-2</sup>, 10<sup>-3</sup> and 10<sup>-4</sup> M NaCl.

<b>Cu37Zn MP</b>	<b>10<sup>-4</sup> M NaCl pH7</b>	<b>10<sup>-3</sup> M NaCl pH7</b>	<b>10<sup>-2</sup> M NaCl pH7</b>
	<b>BE (eV)</b>	<b>BE (eV)</b>	<b>BE (eV)</b>
<b>Cu 2p<sub>3/2</sub></b>	932.5 (0.1)	932.5 (0.1)	932.5 (0.1)
<b>O 1s</b>	530.9 (0.1)	530.9 (0.1)	530.9 (0.1)
	531.7 (0.1)	531.7 (0.1)	531.7 (0.1)
	533.0 (0.1)	533.0 (0.1)	533.0 (0.1)
<b>P 2p</b>	133.3 (0.1)	133.3 (0.1)	133.3 (0.1)
	134.2 (0.1)	134.2 (0.1)	134.2 (0.1)
<b>Zn 2p<sub>3/2</sub></b>	1022.3 (0.1)	1022.3 (0.1)	1022.1 (0.1)
	<b>KE (eV)</b>	<b>KE (eV)</b>	<b>KE (eV)</b>
<b>Cu L<sub>3</sub>M<sub>4,5</sub>M<sub>4,5</sub> Met</b>	918.5 (0.1)	918.5 (0.1)	918.5 (0.1)
<b>Zn L<sub>3</sub>M<sub>4,5</sub>M<sub>4,5</sub> Met</b>	992.4 (0.1)	992.3 (0.1)	992.3 (0.1)
<b>Zn L<sub>3</sub>M<sub>4,5</sub>M<sub>4,5</sub> Ox</b>	987.0 (0.1)	986.9 (0.1)	987.1 (0.1)

Table 6.3: Surface composition (wt.%) determined by XPS analysis; in brackets the standard deviation.

	<b>Cu wt.%</b>	<b>Zn wt.%</b>
<b><i>Mech. Polished</i></b>		
<b>Cu37Zn</b>	64 (2)	36 (2)
<b><i>Mech. Polished 0.0001 M</i></b>		
<b>Cu37Zn</b>	66 (7)	34 (7)
<b><i>Mech. Polished 0.001 M</i></b>		
<b>Cu37Zn</b>	69 (5)	32 (5)
<b><i>Mech. Polished 0.01 M</i></b>		
<b>Cu37Zn</b>	67 (6)	34 (6)

The quantitative analysis was also performed on the Cu37Zn brass alloys after the 7 minutes measurement with the sensor. Table 6.3 provides the composition of the brass alloy before and after the exposure to the electrolytes. The results are averaged over three or more measurements and are in good agreement with the expected composition of the alloy within the experimental uncertainty.



## 6.4 Discussion

The overall goal of the work reported in this chapter was to obtain an electrochemical sensor that was able to monitor the corrosion behavior of historical artifacts before and after the musical performance. The measurement must be non – destructive according to the ethics of conservators and it has to avoid damaging of the instruments, in order to not affect the visual appearance, the roughness and not alter the surface composition. The measurement should be applied in situ on the brass instruments. The electrochemical sensor developed for in-situ measurements in historical brass wind instruments was first tested on flat brass samples in order to check the working conditions (stability, noise etc.). The influence of the solution composition, mainly the chloride concentration, on the surface morphology and composition of the brass alloys following the contact with the sensor was evaluated. In a second step the sensor was calibrated by comparing the measurements obtained by a traditional electrochemical cell with those obtained using the sensor on reference materials.

### 6.4.1 Working characteristics and calibration of the sensor

The reference electrode used for the sensor was an Ag/AgCl solid-state electrode which is an ion selective electrode consisting of silver covered by a layer of silver chloride used to measure the free chloride content in the pore solution of concrete samples [13, 14]. The stability and reproducibility of the solid-state electrode was tested with a standard reference electrode. The control measurements were carried out controlling the potential difference versus an Ag/AgCl in saturated KCl with the Luggin capillary filled with the test solution (§6.2.2). A constant potential difference of  $140 \pm 3$  mV was measured for 0.01 M NaCl solution,  $196 \pm 5$  mV were found for 0.001 M NaCl solution and  $258 \pm 15$  mV were found for  $10^{-4}$  M NaCl. The potential of the saturated Ag/AgCl electrode is 0.197 V. The potential of the Ag/AgCl electrode in 0.01 M NaCl can be calculated from the Nernst equation:

$$E_{\text{Ag/AgCl}} = 0.222 - 0.059 * \log (0.01) = 0.340 \text{ V} \quad \text{eq. 6.1}$$

The theoretical potential difference results in 143 mV, compared to the experimentally found value of  $140 \pm 3$  mV an excellent agreement. A good agreement was found also for the lower chloride concentrations, showing Nernstian behaviour. The reproducibility however became worse at lower chloride concentrations in the sponge. Before starting the measurements, the sponge sensor had to be well soaked for about 15 minutes into the test solution in order to reach the correct potential. The noise level was measured by the Autolab potentiostat and, although no Faraday cage was used, it was at the minimum value. The electrochemical sensor worked, together with the sample as working electrode, as a traditional three-electrode electrochemical cell. This finding was confirmed by comparing the polarization resistance measurements (Figure 6.3 and Table 6.1).

The calibration of the sensor was done performing the same measurements with a traditional three-electrode cell. Both open circuit potential and polarization resistance measurements were performed on the same reference alloys (Cu18Zn and Cu37Zn) in the as received state and after mechanically polishing procedure. Table 6.1 shows that the open circuit potential and the polarization resistance

values obtained by the sensor and the traditional cell were comparable but not identical. The reason of this discrepancy might be due to the much higher volume of the solution and to an unrestricted diffusion of the ions going into solution in the electrochemical cell. The electrolyte volume contained in the sensor sponge is very small (about 3 mL), thus dissolved ions might be accumulated at the sample surface. Moreover, the oxygen access in the sensor might be facilitated resulting in a higher  $O_2$  content at the sample surface.

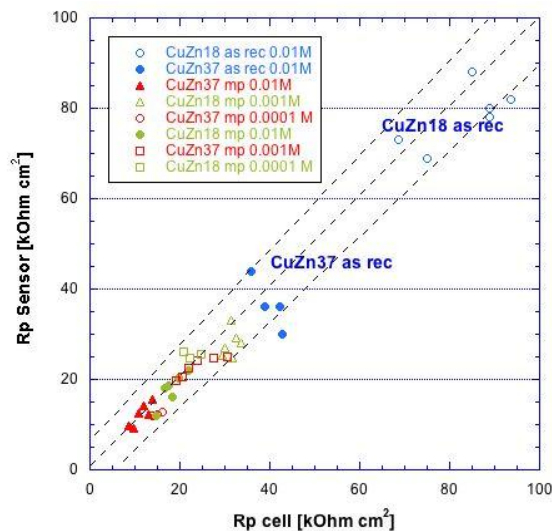


Figure 6. 7: The specific polarization resistance,  $R_p$ , measured by the sensor versus the specific  $R_p$  measured using the electrochemical cell for the Cu18Zn and Zu37Zn in as received and mechanically polished states in the different test solutions. The dotted lines differ for  $\pm 10\%$ .

Figure 6.7 shows the graph of the specific polarization resistance,  $R_p$ , related to the as received and mechanically polished Cu18Zn and Cu37Zn after immersion in the different test solutions ( $10^{-2}$ ,  $10^{-3}$  and  $10^{-4}$  M NaCl in pH 7 phosphate buffer). The  $R_p$  values obtained by the sensor versus the  $R_p$  values obtained by the electrochemical cell are plotted. The polarization resistance values of the as received alloys were higher than the polarization resistance of the mechanically polished ones; the highest  $R_p$  value was observed for the Cu18Zn ( $80 \text{ k}\Omega\text{cm}^2$ ) and lowest  $R_p$  values (about  $10\text{--}20 \text{ k}\Omega\text{cm}^2$ ) were observed for the mechanically polished Cu37Zn samples. The lower  $R_p$  values might be ascribed to the fact that the polishing procedure removed the oxide layer thus exposing a fresh surface with a composition that differ from the as received one.

Overall, despite some scatter in the single results, a line with the slope of about 0.95 can be found, indicating that the sensor is working properly and reproduces the exposure situation of a traditional electrochemical cell. In the light of the not perfectly known contact surface of the sensor sponge, the accuracy is good and can be estimated to be about 20% over two orders of magnitude.

#### 6.4.2 Alteration of the surface state

As it was pointed out previously, the ultimate application of the sensor is on historical brass musical instruments whose preservation is extremely important. The measurements performed on historical artifacts should be non-destructive and they have not to affect the surface state and to alter the surface

composition. As the sensor is soaked with a chloride containing solution, even a short contact time with the brass alloy could, in principle, lead to surface alteration or corrosion, especially dezincification. Visual inspection under the optical microscope was carried out on the Cu37Zn before and after the measurement with the sensor. The micrographs are shown in Figure 6.8. Even at higher magnification the inspection did not reveal any alteration of the surface.

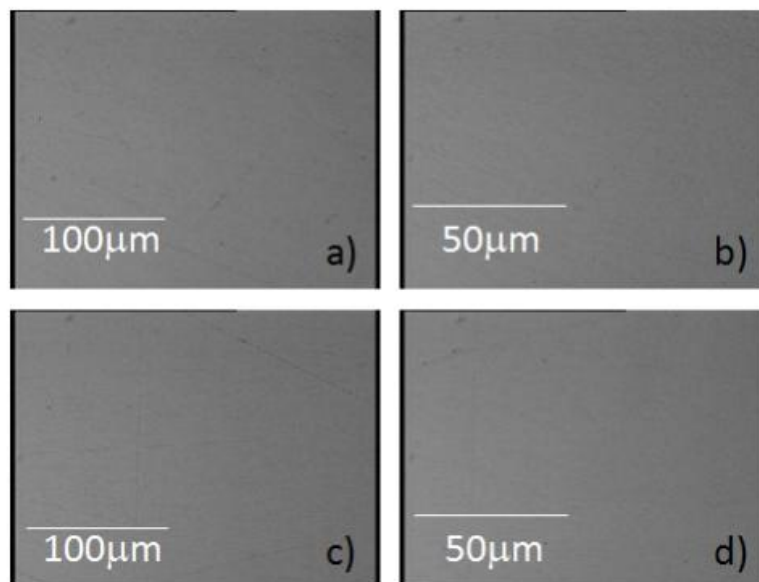


Figure 6.8: Optical micrographs of the mirror polished Cu37Zn before (a, b) and after (c, d) the 7 minutes measurement with the sensor at two magnification: x100 (a, c) and x200 (b, d).

XPS high-resolution spectra did not show a chemical shift or a variation of the spectra shape when changing the test solution. The chemical state identification revealed the presence of signals of both metallic copper and zinc, together with an oxide signal of Zn that might be associated to the presence of zinc orthophosphate according to literature [19].

The highly surface sensitive XPS did not reveal chloride on the surface (Fig. 6.5b) even for the highest concentration of NaCl ( $10^{-2}$  M). The surface composition of the mechanically polished samples was found to be identical within the experimental uncertainty, which is estimated to be 10%, before and after the contact with the sensor (Table 6.3) irrespective of the chloride ion concentration. As the zinc content was the lowest for a chloride concentration of  $10^{-2}$  M NaCl (indicating possible dezincification), this chloride concentration was considered too high for in situ application inside the brass wind instruments. The electrochemical results (Table 6.1) showed that the  $R_p$  values increased with decreasing chloride concentration in the phosphate buffer solution for both alloys tested. Also from these results, it is concluded that a concentration of  $10^{-2}$  M NaCl is too high. XPS surface analysis has shown that the sensor does not induce alteration of the surface composition of the brass model alloys thanks to the short time required to carry out the measurements and the very low corrosion rate in the pH 7 phosphate buffer solution.

### 6.4.3 Efficiency of preventative conservation measures

In the framework of the project (Chapter 1), the sensor was used to determine the corrosion state and rate inside the historical brass wind instruments before and after playing and to control the efficiency of the proposed preventative conservation action. XPS surface analysis has shown that the sensor does not induce alteration of the surface composition of the brass model alloys thanks to the short time required to carry out the measurements and the very low corrosion rate in the phosphate buffer solution of pH 7.

Measurements with the sensor soaked with the solution pH = 7 buffer solution containing  $10^{-3}$ M NaCl were performed also on Cu28Zn, Cu35ZnPb1 and Cu38ZnPb2 in both as received state and mechanically polished state. Table 6.4 reports the summary of the results.

Table 6. 4: Results of the OCP, Rp,  $i_{\text{corr}}$  and of estimated instantaneous corrosion rates for brass alloys in the as received and mechanically polished states.

As received brass alloys				
	OCP (mV)	Rp ( $k\Omega\text{cm}^2$ )	$i_{\text{corr}}$ ( $\mu\text{A}/\text{cm}^2$ )	$v_{\text{corr}}$ ( $\mu\text{m}/\text{a}$ )
<b>Cu18Zn</b>	-10 (20)	80 (1)	0.3 (0.1)	4 (1)
<b>Cu28Zn</b>	-25 (7)	45 (5)	0.6(0.1)	7 (1)
<b>Cu37Zn</b>	-35 (8)	40 (1)	0.7 (0.1)	8 (2)
<b>Cu35Zn1Pb</b>	-54 (6)	45 (6)	0.6 (0.1)	7 (1)
<b>Cu38Zn2Pb</b>	-65 (5)	87 (10)	0.3 (0.1)	3 (1)
Mechanically polished brass alloys				
MP	OCP (mV)	Rp ( $k\Omega\text{cm}^2$ )	$i_{\text{corr}}$ ( $\mu\text{A}/\text{cm}^2$ )	$v_{\text{corr}}$ ( $\mu\text{m}/\text{a}$ )
<b>Cu18Zn</b>	-7 (5)	15 (1)	1.7 (0.3)	20 (3)
<b>Cu28Zn</b>	-18 (1)	20 (2)	1.3 (0.3)	15 (2)
<b>Cu37Zn</b>	-38 (5)	10 (2)	2.6 (0.5)	31 (5)
<b>Cu35Zn1Pb</b>	-55 (2)	12 (1)	2.2 (0.4)	25 (4)
<b>Cu38Zn2Pb</b>	-49 (7)	15 (2)	1.7 (0.3)	20 (3)

For homogeneous corrosion situations, the instantaneous corrosion rate  $i_{\text{corr}}$  can be calculated from the measured specific polarisation resistance, Rp, with the Stern-Geary equation (eq 6.2) [20]:

$$i_{\text{corr}} = B / R_p \quad \text{eq 6.2}$$

Where the constant B is:

$$B = \frac{\beta_a \beta_c}{2.303 (\beta_a + \beta_c)} \quad \text{eq 6.3}$$

The  $\beta_a$  and  $\beta_b$  are the Tafel constants of the anodic and cathodic reactions. Calculation of the B value according to eq. 6.3, has shown that the function “product / sum” is not very sensitive to variations in anodic and cathodic Tafel slopes. As the Tafel slopes are often not known, a value of 26 mV for B with a maximum variation of a factor 1.5 is usually observed for active corrosion. Based on the above

and theoretical considerations [20], a maximum variation of a factor 2 in the conversion of  $R_p$  to corrosion rate  $i_{\text{corr}}$  results.

The corrosion rate  $v_{\text{corr}}$  (in  $\mu\text{m}/\text{year}$ ) can then be calculated by applying Faraday's law. The resulting conversion factor for pure copper is 12, thus  $1 \mu\text{A}/\text{cm}^2$  corresponds to  $12 \mu\text{m}/\text{year}$ . Table 6.4 shows the instantaneous corrosion rates ( $\mu\text{m}/\text{a}$ ) for some typical situations.

Samples can be differentiated on the basis of their  $R_p$  values. In fact, the freshly cleaned mechanically polished brass alloys were found at lower  $R_p$  ( $<15\text{k}\Omega\text{cm}^2$ ) values and higher  $v_{\text{corr}}$  values ( $>15 \mu\text{m}/\text{a}$ ) compared to the as received alloys. The sensor allows determining the instantaneous corrosion rate of the brass alloys in a wide range of surface states and composition and can be used to control alterations of the surface over time.

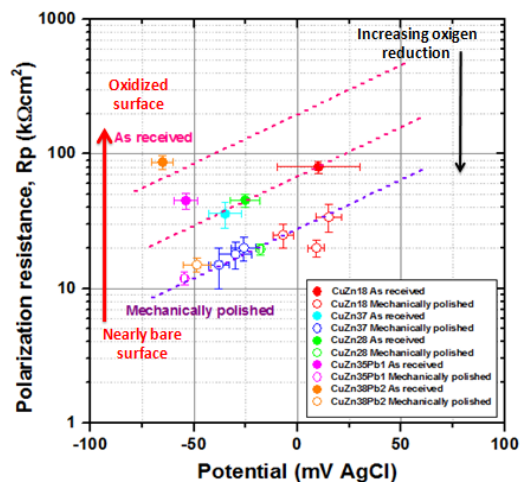


Figure 6.9: Diagram log  $R_p$  versus OCP of Cu18Zn, Cu28Zn, Cu37Zn, Cu35Zn1Pb and Cu38Zn2Pb brass alloys in the as received state and after mechanical polishing. The measurements were carried out with the sensor after 5 minutes of contact with the pH = 7 buffer solution containing different NaCl concentration.

The diagonal trend lines correspond to the increasing degree of oxidation of the surface and correspondingly to the increasing intensity of oxygen reduction current (in the opposite direction).

Plotting the specific polarization resistance  $R_p$  versus the open circuit potential in a log  $R_p$  versus OCP graph (Fig. 6.9), three groups (diagonal trend lines) with different  $R_p$  ranges are clearly revealed: the line with the highest  $R_p$  belongs to the as received Pb bearing brasses, the line in the middle comprises the as received brass alloys without lead and the line with the lowest  $R_p$  values includes all mechanically polished samples. The alloy with more copper (Cu18Zn) shows more positive potentials and slightly higher  $R_p$  values compared to the other alloys of each group. The log  $R_p$  versus OCP plot (Fig. 6.9) allows a tentative mechanistic interpretation. At the open circuit potential, the corrosion rate,  $i_{\text{corr}}$ , is equal to the cathodic oxygen reduction current, thus, a high  $R_p$  value indicates a small cathodic oxygen reduction current. A nearly bare surface (mechanically polished) has the highest oxygen reduction currents, the as received alloys with a thicker oxide film the lowest ones. This is in

agreement with literature where it is reported that copper becomes less active for oxygen reduction as its surface is more oxidized [21]. The inhibitory effect on the kinetics of oxygen reduction and on the cathodic current density was found to be particularly strong on brass [22]. XPS surface analysis on as received brass alloys revealed a thick oxide film (>10 nm) as reported in Chapter 5. The as received alloys showed a surface mainly composed by copper and zinc hydroxide and copper (I) oxide, in addition lead oxide was found in the case of leaded brasses. The presence of the oxide layer is correlated to higher corrosion resistance compared to the mechanically polished once in which it is in general present a nanometric oxide layer (< 2 nm) mainly composed of ZnO, PbO and Cu<sub>2</sub>O. The influence of the oxide layer on the cathodic oxygen reduction currents and thus on R<sub>p</sub> it is confirmed.

## 6.5 Conclusions

The investigation of the conservation state of brass artifacts by means of corrosion state and rate is an important tool for conservation scientists to control the efficiency of preventive conservation actions without altering the surface appearance. The electrochemical sensor developed during this work could be used directly on the brass artifacts. The sensor is properly working and differences in the corrosion rate of different brass alloys can be revealed. The electrochemical response of the sensor was in agreement with the results obtained with a traditional three-electrode electrochemical cell. The potentials of the tiny Ag/AgCl electrode are stable, reproducible and no significant noise is observed. The sensor is calibrated and the application on historical brass wind instruments is realizable.

XPS surface analysis has shown that the sensor does not induce alteration of the surface composition of the brass model alloys thanks to the short time required to carry out the measurements and the very low corrosion rate in the pH 7 phosphate buffer solution containing 10<sup>-3</sup> M NaCl. The electrochemical response of the brass surface under test is dominated by its degree of oxidation. Mechanically polished samples with an oxide layer in the nanometer range exhibit the lowest R<sub>p</sub> values, because their surfaces are very reactive; those samples with a thick oxide layer due to a prolonged exposure to the atmosphere showed more positive potentials and very high R<sub>p</sub> values. The electrochemical measurements performed on the model alloys with bulk composition of 18 and 37 wt.% of zinc, respectively, revealed that the bulk composition seems to have only a minor influence on the corrosion rate. Based on this work, the sensor has been applied for testing and controlling the corrosion rate inside historical brass wind instruments at critical points (tuning slides, mouthpiece) where corrosion due to condensed water and saliva is expected to be deposited and thus in contact with the inner walls of the instrument.

## References

1. B. Trémillon, *Actualité Chimique* 10 (2009) 327–328
2. C. Degriigny, *J Solid State Electrochem* 14 (2010) 353–361
3. C. Degriigny, electrochemical techniques for the conservation of metal artefacts: A review, chapter 3 of A. Coelho Ferreira da Silva, P. Menino Homen, *Ligas metálicas investigação e conservação*, ed. U. Porto (2008)
4. MacLeod ID (2002) In-situ corrosion measurements and managing shipwreck sites. In: Ruppe CV, Barstad JF (eds) *International handbook of underwater archaeology*. Plenum, New York, pp 697–714
5. D. E. Arceo-Gómez<sup>1</sup>, J. Reyes-Trujeque<sup>1</sup>, G. E. Zambrano-Rengel<sup>1,2</sup>, T. Pérez-López<sup>1</sup>, R. Orozco-Cruz, *International Journal of Electrochemical Science*, 11 (2016) 9379 – 9393
6. C. Degriigny, L. Spiteri, Electrochemical monitoring of marine iron artefacts during their storage/stabilisation in alkaline solutions. In: J. Ashton and D. Hallam (ed) *METAL04. Proceedings of the ICOM-CC Metal WG interim meeting*, National Museum of Australia, Canberra (2004), pp 315–331
7. A. von Steiger, *Die Instrumentensammlung Burri, Hintergründe und Herausforderungen*, Bern. Eigenverlag, 2013
8. J. Butt, *Playing with History - The Historical Approach to Musical Performance*, Cambridge University Press (2002), ISBN 0 521 81 352 2
9. E. Mattson, R. Holm, Atmospheric corrosion of copper and its alloys, in “*Atmospheric Corrosion*”, ed. W.H. Ailor, WILEY (1982) p. 365 – 392
10. Copper and Copper alloys, in “*Corrosion Metal/Environmental Reactions Vol. 1 (third edition 1994)* ed. L.L. Shreir, R. Jarman, G.T. Burstein, p. 4:38 – 4:75
11. C. D. S Tuck, C. A. Powell, J. Nuttall, Corrosion of Copper and its alloys, in “*SHREIR'S CORROSION, Vol 3: Corrosion and Degradation of Engineering Metals*”. Ed. T. Richardson (2010) pp. 1937 – 1973
12. M. Ledergerber, E. Cornet, E. Hildbrand, Humidity in brass instruments and the prevention of corrosion, accepted to the International Conference Vienna Talk 2015, on Music Acoustics “*Bridging the Gaps*” [http://viennatalk2015.mdw.ac.at/?page\\_id=1000](http://viennatalk2015.mdw.ac.at/?page_id=1000)
13. B. Elsener, L. Zimmermann, H. Böhni, *Materials and Corrosion* 54 (2003) 440 – 446
14. Y. Segui Femenias, U. Angst, F. Caruso, B. Elsener, *Materials and Structures* 49 (2016) 2637–2651
15. M. Senn, H. J. Leber, M. Tuchschnid, N. Rizvic, in: *Romantic Brass II: Französische Hornpraxis und historisch informierter Blechblasinstrumentenbau*, Bern, 2016, Edition Argus, Musikforschung der Hochschule der Künste Bern, Band 6, ed. D. Allenbach, A. von Steiger und M. Skamletz, p. 398–419

16. S. Speckmann, H. Haupt and H.H. Strehblow, *Surface and Interface Analysis*, 11 (1988) 148-155
17. P. Druska and H.H. Strehblow, *Surface and Interface Analysis*, 23 (1995) 440-450
18. I. Milosev and H.H. Strehblow, *Journal of the Electrochemical Society*, 150 (2003) 518-524
19. E.C. Onyiriuka, *Journal of Non-Crystalline Solids*, 163 (1993) 268-273
20. M. Stern, A. L. Geary, *Journal of Electrochemical Society*, 104 (1957) 56
21. M. V. Vasquez, S. R. de Sanchez, E. J. Calvo, D. J. Schiffrin, *Journal of the Electroanalytical Chemistry*, 374 (1994) 189
22. R. Procaccini, M. Vasquez, S. Cer\_e, *Electrochimica Acta* 54 (2009) 7324



# Chapter 7

## *XPS and EIS studies on the protective films formed on Cu-Zn alloys after aging in neutral solutions*

*In this Chapter extensive work on the dissolution of brass alloys in neutral solutions is reported. The mechanically polished brasses were exposed in artificial saliva (pH 7.4) and in diluted phosphate buffer solution (pH 7) at room temperature. Open circuit potential (OCP), linear polarization ( $R_p$ ) and electrochemical impedance spectroscopy (EIS) were measured to follow the ageing process. The surface film composition before and after the exposure was characterized by X-ray photoelectron spectroscopy (XPS) and X-ray induced Auger electron spectroscopy (XAES). Moreover, the occurrence of the corrosion phenomena due to the exposure to the different electrolytes was examined by using optic and Scanning Electron microcopies.*

*Part of this work was published in RSC Advances [F. Cocco, M. Fantauzzi, B. Elsener, A. Rossi, RSC Advances 6 (2016) 90654 - 90665], according to the journal policy it was not necessary to ask for the permission to report in this thesis.*

*The major part of the work outlined in this Chapter was carried out by myself. Cristiana Passiu (PhD student at the ETH Zurich – Department of Material Science - Laboratory of Surface Science Materials) kindly performed the SEM and the AFM analyses. Part of the electrochemical measurements was carried out at the laboratory of the Institute of Building Materials, ETH Zurich, (Switzerland). Part of the X-ray photoelectron spectroscopy were carried out at the Department of Material Science - Laboratory of Surface Science Materials - ETH Zurich , (Switzerland) during my internship at the ETH Zurich.*

*Prof. A. Rossi, Prof. B. Elsener and Dr M. Fantauzzi supported the work with discussions and thorough revisions of the results.*

## 7.1 Introduction

Many investigations were carried out for understanding the electrochemical behaviour of brass alloys in slightly alkaline [1– 4], neutral [3, 4, 7 – 10] and acidic [3, 4] solutions covering a pH range from 2 to 12. The influence of the pH [3, 4], chloride concentration [5, 9] and alloy composition [2, 4, 5, 8] on the film formation was studied. The results have largely been explained on the basis of selective dissolution and dezincification mechanism caused by the difference in the electrochemical potential between copper and zinc. Chloride ions were found to facilitate the dissolution of possibly protective corrosion product layers, causing an increase of the corrosion rate of brass [9].

Regarding corrosion inside the brass wind instruments, the aqueous solutions present in the instruments during and after playing are unknown in composition and physical properties. It might be assumed that condensed water (pH near neutral or slightly acidic) can be present in some regions inside the instrument. In other regions solution containing different ions with various concentrations might also be present. Furthermore the concentration of the aqueous solution might depend on playing time and intensity [11]. In this Chapter the electrochemical and corrosion behaviour of brass alloys with zinc content ranging from 18 to 38 wt.% were investigated over time at the open circuit potential (OCP) in contact with two neutral solutions: artificial saliva solution, as an aggressive medium, and diluted pH = 7 phosphate buffer solution as a mild exposure condition.

Saliva is a complex fluid that is produced from major glands such as the paired parotid glands (20%), the submandibular (65%) and sublingual glands (7 – 8%) and from minor glands (10%) which are found in the tongue, palate, lower lip and pharynx [12]. Between 1 and 1.5 L of saliva daily flow in a healthy human [12]. Saliva is composed of water (more than 99%) and of a variety of electrolytes including sodium, potassium, calcium, magnesium, bicarbonate, and phosphates. It is also composed by organic constituents: immunoglobulins, proteins, enzymes, mucins, and nitrogenous products, such as urea and ammonia. Bicarbonates, phosphates, and urea act to modulate the pH and the buffering capacity of saliva, while macromolecule proteins and mucins provide to cleanse, aggregate and contribute to dental plaque metabolism. The demineralization and re-mineralization modulation are operated by calcium, phosphate, and proteins and moreover they work together as an anti-solubility factor. The antibacterial action is provided by immunoglobulins, proteins, and enzymes [12].

The normal pH of saliva ranges between 6.2 and 7.6 and it can vary during the day [13]. The saliva has a wide composition variation that may differ considerably from each other and can be affected by the type and intensity of stimulation, diet, age, time of day, diseases and pharmacological agents. Hence, an exact replica of human saliva is quite impossible. Different formulations have been developed for different purposes. Here the Tani-Zucchi artificial saliva has been chosen because its composition is very close to the actual conditions existent in a cavity media [14].

In this Chapter the results of the open circuit potential (OCP) and polarization resistance ( $R_p$ ) measurements are presented together with a comparison of corrosion rate and the reaction mechanism in the two solutions. The electrochemical behaviour of brasses were also investigated by Electrochemical Impedance Spectroscopy (EIS). A further insight on the composition of surface films was gained by XPS/XAES surface analysis. The composition of surface films as determined by XPS, contributed to explain the dissolution mechanism and the corrosion behaviour. The occurrence of corrosion phenomena due to the exposure to the different electrolytes was also examined by optical and Scanning Electron microcopies (SEM).

## **7.2 Experimental**

### **7.2.1 Materials and surface preparation**

The brass alloys used in this work were Cu18Zn, Cu28Zn, Cu35Zn1Pb and Cu38Zn2Pb produced as thin sheets with metallurgical structures similar to those found in the artefacts from the 19<sup>th</sup> century. The ageing test were performed on the brass alloys after mechanical polishing; samples were abraded with abrasive silicon carbide paper up to 4000 mesh (Struers) using ethanol as cooling lubricant during the grinding, followed by ultrasonically cleaning in ethanol for 5 minutes. After the grinding procedure, the surface was polished with a DP Dur cloth with 1 and  $\frac{1}{4}$   $\mu\text{m}$  polycrystalline diamond paste spray supplied by Struers, cleaned with ethanol and dried using an argon stream. More details about the materials are reported in Chapter 4.

### **7.2.2 Solutions**

The ageing test were performed exposing the samples to a phosphate buffer solution pH7 (Fluka) and to an artificial saliva solution prepared according the “modified- Tani Zucchi” composition [14]:  $\text{NaHCO}_3$  1.2636 g  $\text{cm}^{-3}$ ,  $\text{KSCN}$  0.515 g  $\text{cm}^{-3}$ ,  $\text{KCl}$  1.4901 g  $\text{cm}^{-3}$ ,  $\text{NaH}_2\text{PO}_4$  0.1236 g  $\text{cm}^{-3}$ , Urea ( $\text{CH}_4\text{N}_2\text{O}$ ) 0.1003 g  $\text{cm}^{-3}$ ,  $\alpha$ -Amilase 0.9687 g  $\text{cm}^{-3}$ ; all the reagents were supplied by Sigma Aldrich (Sigma-Aldrich S.r.l. Milan, Italy). The solutions were prepared in distilled water with conductivity 1.1  $\mu\text{S cm}^{-1}$ . All the measurements were performed at room temperature open to air.

### **7.2.3 Electrochemical tests**

A VersaSTAT 4 Model 400 potentiostat/galvanostat (Ametek Inc. PAR, USA) was used to perform the electrochemical measurements under computer control (USB port, software Versa Studio v2). The electrochemical cell was a conventional three-electrode cell described in Chapter 4 (§4.6.1) with a platinum counter electrode and a saturated calomel reference electrode ( $E = +0.241$  V vs. NHE). All potentials are referred to the saturated calomel electrode (SCE). All measurements were performed at room temperature ( $25 \pm 2$  °C) in naturally aerated solutions. Each experiment was carried out in a freshly prepared solution and with a newly polished electrode surface. Each experiment was performed three times.

Open circuit potential and Polarization Resistance measurements: Samples were immersed for 1h, 3h and 16h in the electrolyte. At the end of the exposure period the polarization resistance was measured. A small polarization of  $\pm 20$  mV vs open circuit potential (OCP) was imposed on the sample and the resulting current measured. The scan rate was 0.167 mV/s.

Cathodic and anodic polarization curves were acquired at a scan rate of 0.167 mV/s following one-hour immersion at the open circuit potential. The scan was started in the cathodic region (at -0.25 V vs. OCP) and run in the anodic direction to +0.25 V vs. OCP.

Electrochemical impedance spectroscopy (EIS) measurements were carried out over a frequency domain from 10 kHz to 0.01 Hz by 7 points per decade using an AC voltage of 5 mV. The EIS spectra were acquired after 20 min and 3 hours exposure to the test solutions.

## **7.2.4 Characterization methods**

### ***X-ray photoelectron spectroscopy***

Surface composition was monitored by X-ray photoelectron spectroscopy (XPS) using the Thetaprobe (ThermoFisher, East Grinstead UK). Details about the technique, the instruments and the data processing are reported in Chapter 3 (§3.4) and Chapter 4 (§4.7). The quantitative analysis was carried out on the basis of the first principle approach detailed in Chapter 4 (§4.7.3).

about the technique, the instruments and the data processing are reported in Chapters 3 and 4.

### ***Scanning electron microscopy***

Scanning Electron Microscopy (SEM, SEM) was used to observe the surface of the brass alloys before and after the electrochemical measurements. The Scanning Electron Microscope used in this work was a Zeiss Ultra-55 (Carl Zeiss, Feldbach, Switzerland) equipped with InLens, SE2 (Everhart-Thornley Secondary Electron) e EsB (Energy selective Backscattered) detectors but only the InLens and SE2 were used in this work. The details about the technique, the instruments and the data processing are reported in Chapters 3 and 4.

## **7.3 Results**

### **7.3.1 Electrochemical Results**

#### **7.3.1.1 Open circuit potential measurements**

The open circuit potential (OCP) measurements of all the alloys were performed for 1h, 3h and 16 h of immersion in solutions open to air. The OCP recorded over 16 hours are reported in Fig. 7.1 for copper-zinc alloys Cu<sub>18</sub>Zn (a), Cu<sub>37</sub>Zn (b), Cu<sub>28</sub>Zn (c) Cu<sub>35</sub>Zn<sub>1</sub>Pb (d) and Cu<sub>38</sub>Zn<sub>2</sub>Pb (e); the OCP vs time curves are reported also for the pure copper (f). The OCP versus time curves in artificial saliva for copper-zinc alloys exhibited all the same trend as for pure copper: immediately after immersion, the potential (initial potential  $E_{(0)}$ ) was relatively positive, diminished then rapidly to more negative values and started to increase after ca. one hour reaching asymptotically a stable value (potential  $E_{(16h)}$ ).

The average potential values and their standard deviations are summarized in Table 7.1. With increasing zinc content in the alloys the potentials became more negative.

Table 7. 1: Average of the initial ( $E_{t0}$ ) and final ( $E_{1,3,16h}$ ) open circuit potential values (mV vs SCE) of copper and brass samples exposed to artificial saliva for 1, 3 and 16 h. Standard deviations are given in parentheses.

Sample	1h		3h		16h	
	$E_{t0}$	$E_{1h}$	$E_{t0l}$	$E_{3h}$	$E_{t0}$	$E_{16h}$
<b>Cu</b>	-223 (13)	-348 (4)	-214 (10)	-311 (20)	-224 (9)	-195 (19)
<b>Cu18Zn</b>	-300 (8)	-344 (5)	-309 (11)	-260 (35)	-297 (11)	-222 (6)
<b>Cu28Zn</b>	-305 (7)	-320 (11)	-298 (16)	-292 (2)	-308 (14)	-265 (7)
<b>Cu37Zn</b>	-307 (27)	-319 (3)	-309 (11)	-281 (21)	-306 (33)	-266 (9)
<b>Cu35Zn1Pb</b>	-306 (16)	-322 (14)	-283 (33)	-310 (16)	-292 (35)	-269 (11)
<b>Cu38Zn2Pb</b>	-310 (21)	-321 (16)	-310 (7)	-295 (23)	-299 (27)	-281 (4)

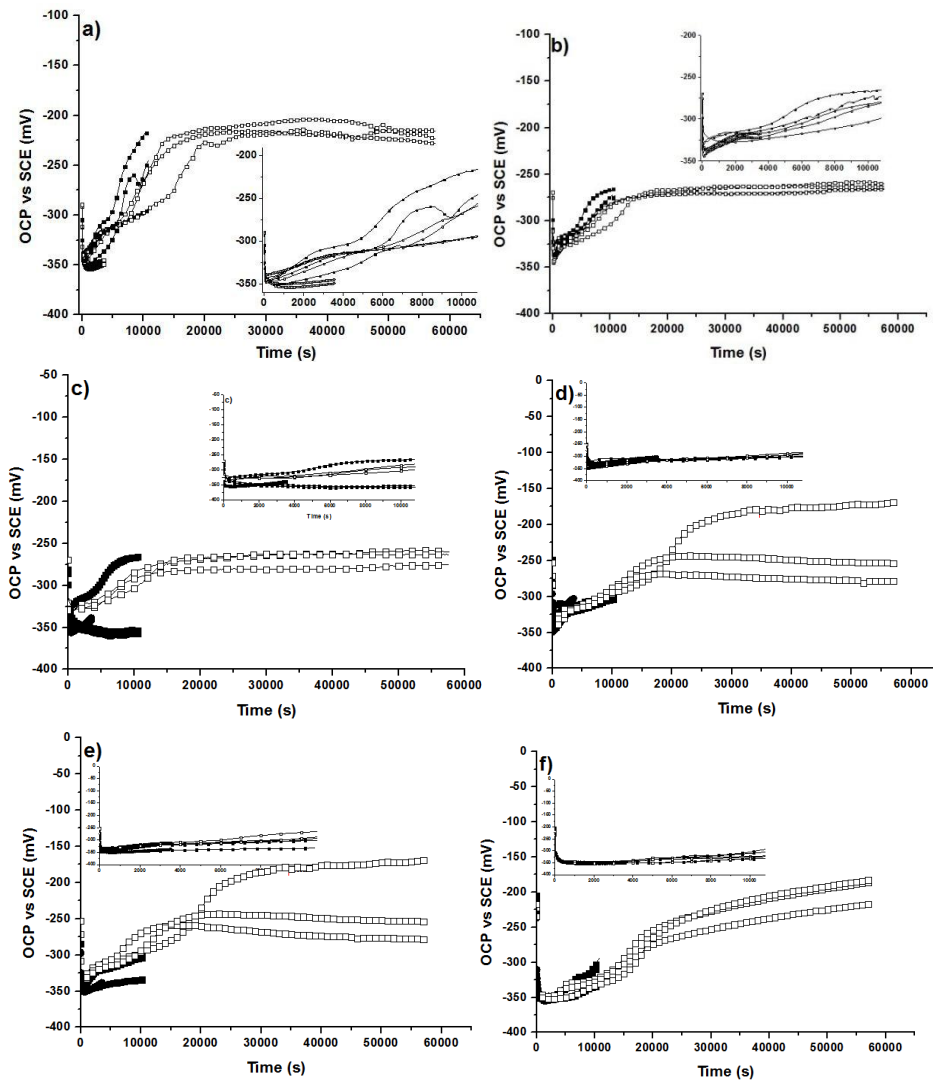


Figure 7. 1: Open circuit potential versus time curves for a) Cu18Zn, b) Cu37Zn, c) Cu28Zn, d) Cu35Zn1Pb, e) Cu38Zn2Pb and f) pure copper following mechanical polishing and exposure to artificial saliva. Inserts show OCP vs time for the first three hours.

In figure 7.2 the OCP recorded from 0 to 16 hours of contact with the phosphate buffer solution for copper-zinc alloys Cu18Zn (a), Cu37Zn (b), Cu28Zn (c) Cu35Zn1Pb (d) and Cu38Zn2Pb (e) and for the pure copper (f) are shown. The OCP versus time curves in the pH = 7 buffer solution for pure copper and the copper-zinc alloys are similar to those obtained for Cu18Zn (Fig. 2a) and Cu37Zn (Fig. 2b): immediately after immersion the potential (initial potential  $E_{t0}$ ) was negative and increased slightly to more positive values reaching a stable potential (potential  $E_{3h}$ ,  $E_{16h}$ ). In contrast to the artificial saliva, the OCP values remained stable already after ca. 1 h. The average potential values  $E_{t0}$ ,  $E_{3h}$ ,  $E_{16h}$  and their standard deviations are summarized in Table 7.2. The potentials became more negative with increasing zinc content in the alloys.

Table 7. 2: Average and standard deviation of the initial ( $E_{t0}$ ) and final ( $E_{1,3,16h}$ ) open circuit potentials (mV vs SCE) of copper and brass samples exposed to phosphate buffer pH 7 for 1, 3 and 16 h.

Sample	1h		3h		16h	
	$E_{t0}$	$E_{1h}$	$E_{t0}$	$E_{3h}$	$E_{t0}$	$E_{16h}$
<b>Cu</b>	-80 (5)	-50 (4)	-86 (5)	-55 (3)	-84 (2)	-48 (8)
<b>Cu18Zn</b>	-145 (4)	-60 (2)	-139 (4)	-65 (1)	-144 (18)	-62 (3)
<b>Cu28Zn</b>	-143 (3)	-68 (3)	-110 (23)	-84 (21)	-135 (8)	-59 (5)
<b>Cu37Zn</b>	-166 (5)	-83 (2)	-163 (4)	-76 (3)	-150 (17)	-73 (5)
<b>Cu35Zn1Pb</b>	-159 (23)	-85 (14)	-149 (14)	-65 (8)	-162 (13)	-65 (8)
<b>Cu38Zn2Pb</b>	-164 (7)	-89 (1)	-156 (9)	-79 (4)	-157 (2)8	-80 (5)

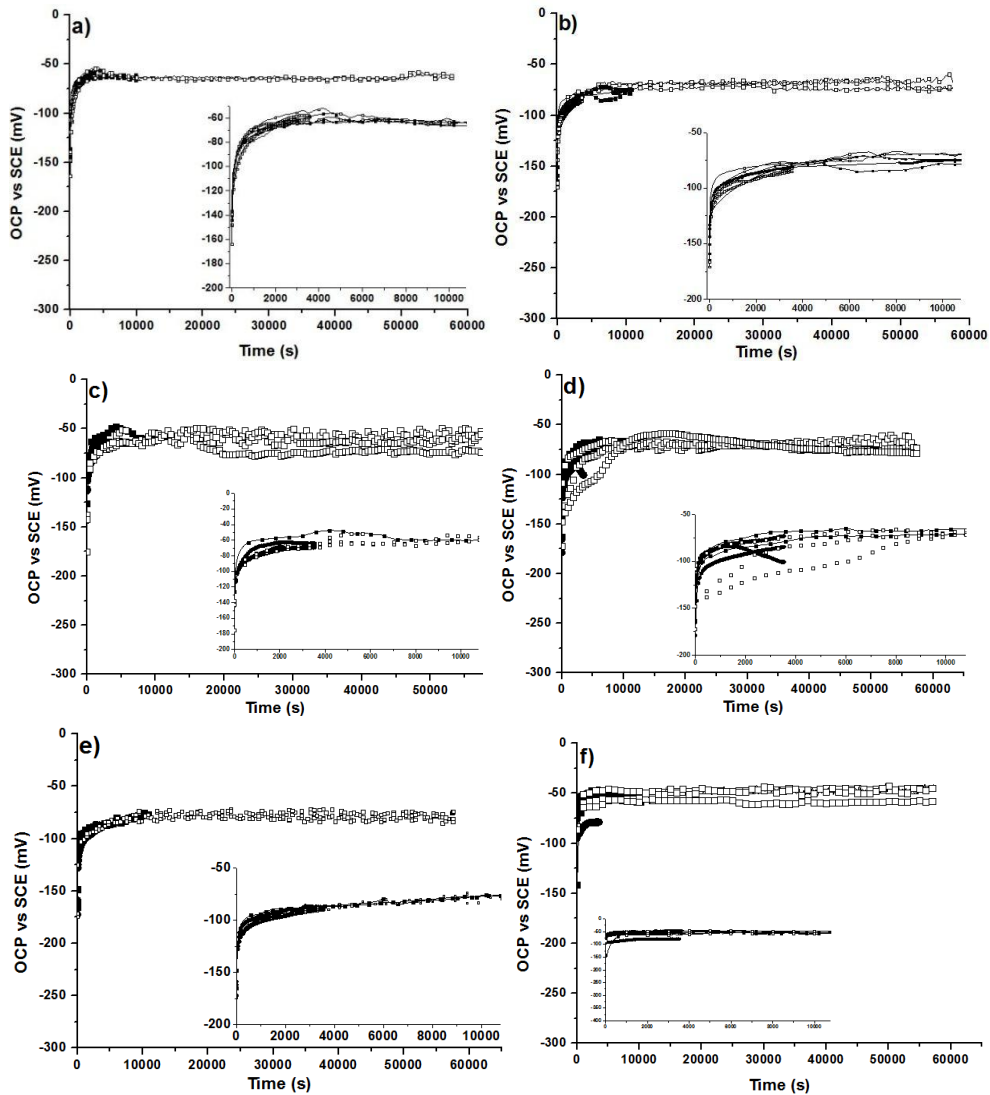


Figure 7. 2: Open circuit potential versus time curves for mechanically polished a) Cu18Zn, b) Cu37Zn, c) Cu28Zn, d) Cu35Zn1Pb, e) Cu38Zn2Pb and f) pure copper in pH = 7 phosphate buffer. Inserts show OCP vs time for the first three hours.

### 7.3.1.2 Polarization resistance measurements – corrosion rate

Linear polarization resistance measurements (LPR) were performed at the end of each exposure period of 1h, 3h and 16 h. The LPR plots measured in artificial saliva and in buffer solutions showed very good linearity at  $\pm 10$  mV around OCP. The average  $R_p$  values and standard deviation determined after the different exposure times are summarized in Table 7.3 where the results regarding the artificial saliva solution are reported, while the results regarding the phosphate buffer solution are summarized in Table 7.2; the uncertainty of the  $R_p$  value calculated by a linear fit was below 2%.

The  $R_p$  measurements allow us to estimate the corrosion rate of brass alloys in the two different solutions applying the Stern-Geary equation [15] with the constant  $B$  set to 26 mV [16]. For brass alloys with 18 to 37% of zinc in phosphate buffer solution the corrosion current density  $i_{\text{corr}}$  ranged between 0.2 – 0.4  $\mu\text{A}/\text{cm}^2$ , corresponding to a corrosion rate  $v_{\text{corr}}$  of 3 – 5  $\mu\text{m}/\text{year}$ . In the artificial saliva solution, the corrosion rate after 1 h was very high (60  $\mu\text{m}/\text{year}$ ) but decreased markedly; after

16 h of ageing  $v_{\text{corr}}$  is lower than  $0.5\mu\text{m}/\text{year}$ . This is an important result for conservators when historical instruments are played in concerts and when using electrochemical sensors to probe the corrosion state (Chapters 6 and 8).

Table 7. 3: Average polarization resistance  $R_p$  ( $\text{k}\Omega \text{ cm}^2$ ) of copper and brass samples exposed to artificial saliva for 1, 3 and 16 h. The standard deviations are given in parentheses.

Sample	1h	3h	16h
<b>Cu</b>	4.1 (0.4)	53 (10)	473 (35)
<b>Cu18Zn</b>	2.7 (0.3)	87 (11)	173 (59)
<b>Cu28Zn</b>	3.3 (0.3)	148 (32)	235 (11)
<b>Cu37Zn</b>	5.7 (0.6)	74 (15)	180 (55)
<b>Cu35Zn1Pb</b>	5 (2)	48 (10)	583 (130)
<b>Cu38Zn2Pb</b>	5 (1)	76 (24)	120 (10)

Table 7. 4: Average polarization resistance  $R_p$  ( $\text{k}\Omega \text{ cm}^2$ ) of copper and brass samples exposed to pH = 7 phosphate buffer for 1, 3 and 16 h. The standard deviations are given in parentheses.

Sample	1h	3h	16h
<b>Cu</b>	60 (1)	90 (5)	200 (5)
<b>Cu18Zn</b>	60 (5)	70 (12)	100 (7)
<b>Cu28Zn</b>	30 (5)	100 (11)	100 (5)
<b>Cu37Zn</b>	40 (4)	50 (8)	60 (6)
<b>Cu35Zn1Pb</b>	30 (3)	70 (8)	70 (8)
<b>Cu38Zn2Pb</b>	30 (3)	50 (6)	80 (7)

### 7.3.1.3 Polarization curves

Potentiodynamic polarization curves were recorded after 1 h exposure to the test solutions. It can be noted that the potential at  $i = 0$  agrees well with the open circuit potential measured after 1 h of immersion. In artificial saliva (Fig. 7.3a) the curves of all the brass alloys were similar: the cathodic part showed a Tafel behavior with a high cathodic Tafel slope  $b_c$  of about  $250 \text{ mV}/\text{dec}$ . The cathodic current density was slightly lower for alloys with low zinc content. The anodic part showed a peak at ca.  $-300 \text{ mV SCE}$  that was more pronounced with increasing zinc content in the alloy. This peak could be tentatively assigned to the oxidation of  $\text{Cu}_2\text{O}$  in the film (see XPS data below) to  $\text{CuO}$ . At more anodic potentials the current density reaches a value of ca.  $3 \mu\text{A}/\text{cm}^2$ .

In the phosphate buffer solution of pH 7 the polarization curves (Fig. 7.3b) exhibited a constant current (plateau) with current density of about  $1 - 2 \mu\text{A}/\text{cm}^2$  in the anodic range and a marked current



increase at about +150 mV SCE. The cathodic part of the polarization curves showed no Tafel behavior but a quite constant current density that seems to be a limiting current.

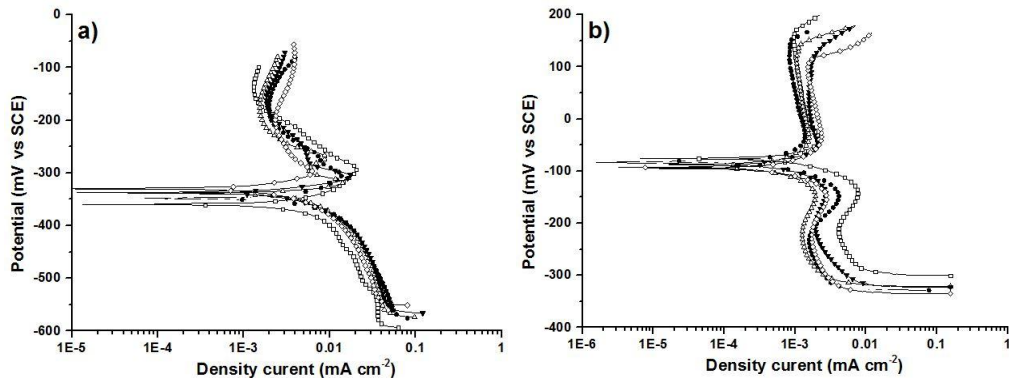


Figure 7. 3: Potentiodynamic polarization curves of brass alloys after 1h of exposure to (a) the artificial saliva solution and (b) the phosphate buffer solution.

### 7.3.1.4 Impedance spectroscopy

The EIS data were acquired after 1 and 3 hours of immersion in naturally aerated phosphate buffer solution (pH = 7) and in artificial saliva (pH 7.4). In buffer solution the electrode potential is already stable over time after 1 h (Fig. 7.2), while in saliva (Fig. 7.1) the steady state was reached only after 3 hours. The impedance spectra presented as Nyquist and as Bode plot are shown in Fig. 7.4 and 7.5 for buffer solution and Fig. 7.6 for artificial saliva.

In the Nyquist plots (Fig. 7.4a – Fig. 7.6a) only one, slightly depressed semicircle can be seen. The extrapolation to the x-axis roughly indicates the polarization resistance  $R_p$ . The Bode plots (Fig 7.4 – 7.6b) show two maxima in the phase angle, indicating two time constants. The two time constants are represented by a film resistance  $R_{film}$ /film capacitance  $C_{film}$  and by the charge transfer resistance  $R_{ct}$ /double layer capacitance  $C_{dl}$ .

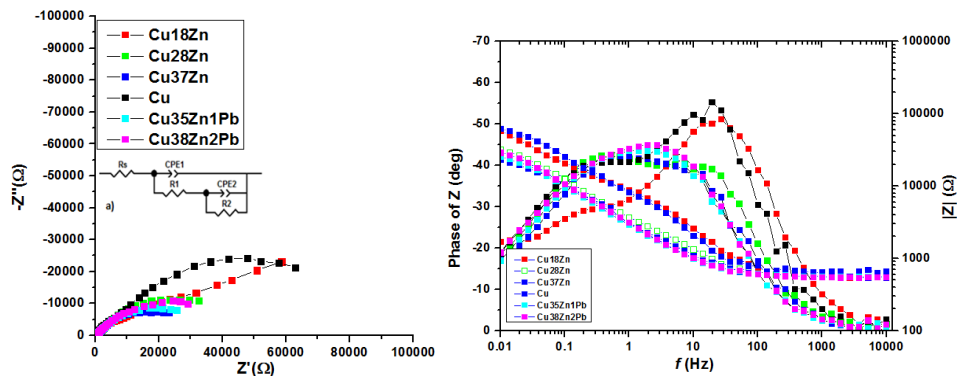


Figure 7. 4: Nyquist (a) and Bode (b) plots of the five different brass alloys after 1 h immersion in a naturally aerated pH = 7 buffer solution (copper is also shown).

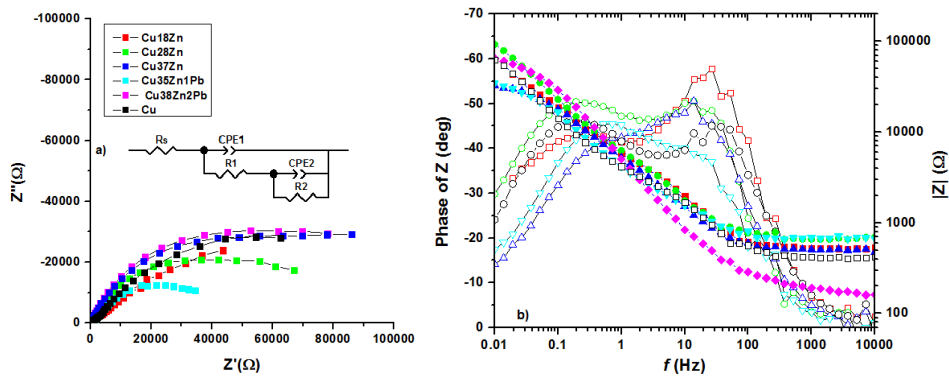


Figure 7. 5: Nyquist (a) and Bode (b) plots of the five different brass alloys after 3 h immersion in a naturally aerated  $\text{pH} = 7$  buffer solution (copper is also shown).

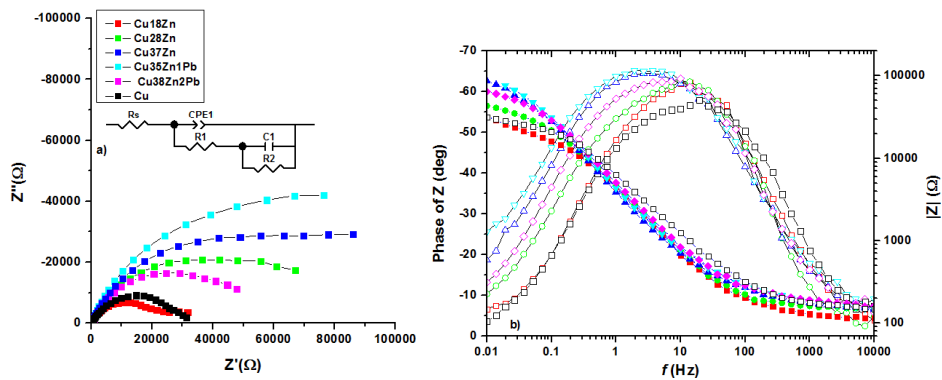


Figure 7. 6: Nyquist (a) and Bode (b) plots of the five different brass alloys after 3 h immersion in a naturally aerated saliva solution (copper is also shown).

### Analysis of EIS spectra

The results of the impedance measurements have been analysed using the equivalent circuit shown in Fig. 7.7. The equivalent circuit consisted of a resistance  $R_s$  that represents the solution resistance (or ohmic resistance).  $R_s$  was in series with two time constants,  $R1/CPE1$  and  $R2/CPE2$ . The first,  $R1/CPE1$ , was related to the resistive and capacitive effects of the oxide film:  $R1$  can be interpreted as the film resistance,  $R_{\text{film}}$  (blocking ionic or electronic transport) and the  $CPE1$  as the oxide film capacitance,  $CPE_{\text{film}}$ . In the second time constant,  $R2$  could be associated to the charge transfer resistance ( $R_{ct}$ ) and the related  $CPE2$  describe the capacitance of the double layer,  $CPE_{dl}$ . The results are listed in tables 7.5 and 7.6.

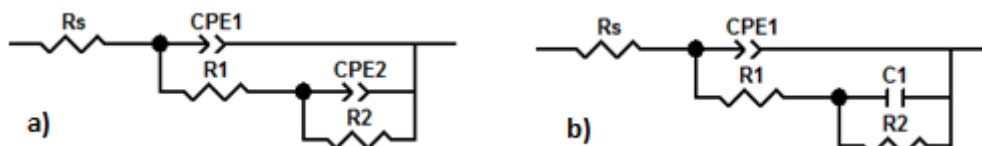


Figure 7. 7: Equivalent circuits used to analyse the impedance spectra. a) in phosphate buffer solution, b) in saliva solution.

*Buffer solution*

As shown in Tables 7.5 and 7.6, the  $R_{\text{film}}$  and the  $CPE_{\text{film}}$  of copper and brass alloys exposed to the buffer solution did not change significantly with time, suggesting a small variation on the film thickness over time. The charge transfer resistance,  $R_{\text{ct}}$ , in the case of the buffer solution is higher than the values associated to the film resistance,  $R_{\text{film}}$ , meaning that the system is charge transfer controlled.

Table 7. 5: Calculated fitting parameters for brass alloys after 1 hour of immersion in phosphate buffer solution (standard deviation percentage is reported in brackets).

	$R(\Omega)$	$CPE_{\text{film}}(\mu\text{Fcm}^{-2})$	n1	$R_{\text{film}}(\text{k}\Omega\text{cm}^2)$	$CPE_{2\text{dl}}(\mu\text{Fcm}^{-2})$	n2	$R_{\text{ct}}(\text{k}\Omega\text{cm}^2)$
<b>Cu</b>	583 (13)	15 (40)	0.9 (8)	3 (32)	98 (16)	0.7 (8)	35 (24)
<b>Cu18Zn</b>	614 (8)	18 (30)	0.9 (7)	2 (16)	88 (5)	0.7 (3)	37 (9)
<b>Cu28Zn</b>	603 (6)	22 (16)	0.8 (2)	4 (21)	71 (19)	0.7 (2)	31 (20)
<b>Cu37Zn</b>	652 (6)	21 (33)	0.9 (5)	2 (27)	90 (14)	0.6 (3)	32 (12)
<b>Cu35Zn1Pb</b>	618 (1)	31 (25)	0.8 (7)	3 (30)	91 (17)	0.6 (12)	26 (25)
<b>Cu38Zn2Pb</b>	623 (10)	53 (6)	0.8 (3)	6 (16)	90 (6)	0.6 (12)	23 (20)

Table 7. 6: Calculated fitting parameters for brass alloys after 3 hours of immersion in phosphate buffer solution (standard deviation percentage is reported in brackets).

	$R(\Omega)$	$CPE_{\text{film}}(\mu\text{Fcm}^{-2})$	n1	$R_{\text{film}}(\text{k}\Omega\text{cm}^2)$	$CPE_{2\text{dl}}(\mu\text{Fcm}^{-2})$	n2	$R_{\text{ct}}(\text{k}\Omega\text{cm}^2)$
<b>Cu18Zn</b>	594 (10)	11 (3)	0.9 (2)	7 (20)	51 (14)	0.7 (6)	79 (36)
<b>Cu28Zn</b>	653 (8)	10 (20)	0.9 (7)	5 (23)	59 (6)	0.7 (12)	87 (20)
<b>Cu37Zn</b>	683 (3)	10 (17)	0.9 (3)	5 (20)	47 (12)	0.7 (1)	12 (14)
<b>Cu35Zn1Pb</b>	565 (10)	18 (18)	1 (7)	3 (30)	69 (16)	0.6 (5)	40 (27)
<b>Cu38Zn2Pb</b>	661 (4)	18 (30)	1 (11)	3 (22)	53 (3)	0.7 (5)	56 (30)
<b>Cu18Zn</b>	656 (6)	17 (25)	0.9 (8)	4 (23)	58 (13)	0.6 (5)	49 (32)

Table 7. 7: Calculated fitting parameters for brass alloys after 3 hours of immersion in artificial saliva solution (standard deviation percentage is reported in brackets).

	$R(\Omega)$	$CPE_{\text{film}}(\mu\text{Fcm}^{-2})$	n1	$R_{\text{film}}(\text{k}\Omega\text{cm}^2)$	$C_{\text{dl}}(\mu\text{Fcm}^{-2})$	$R_{\text{ct}}(\Omega\text{cm}^2)$
<b>Cu18Zn</b>	165(12)	30(15)	0.8(1)	26(43)	85 (40)	14(10)
<b>Cu28Zn</b>	165(12)	30(15)	0.8(1)	35(43)	80 (30)	12(14)
<b>Cu37Zn</b>	176(7)	32(22)	0.8(1)	46(29)	382(20)	10(56)
<b>Cu35Zn1Pb</b>	170(4)	38(15)	0.8(1)	65(37)	828(33)	18(46)
<b>Cu38Zn2Pb</b>	164(2)	41(22)	0.7(8)	38(19)	328(47)	7 (10)

### 7.3.2 Results of XPS – XAES surface analysis – buffer solutions

Brass samples were analysed after mechanical polishing and after exposure to the test solutions. The XPS results after mechanical polishing were reported and discussed in Chapter 5. Here, the XPS-XAES results of the copper-zinc alloys exposed to phosphate buffer solution up to 16 hours will be shown. Results of a low Zn alloy (Cu18Zn), a high Zn alloy (Cu37Zn) and a lead bearing alloy (Cu38Zn2Pb) are presented in detail. Results of the other alloys are shown in appendix 1.

#### Cu18Zn alloy exposed to buffer solutions

##### High-resolution photoelectron and Auger signals

The high-resolution spectra of Cu18Zn acquired after 1, 3 and 16 hours of contact with the phosphate buffer solution are shown in Fig. 7.8, Fig. 7.9 and Fig. 7.10. The values of the binding energy, kinetic energy and the full-width at half maximum (FWHM) are shown in Table 7.8. Curve fitting of the spectra was performed using parameters obtained in reference materials (see Chapter 5). In particular the differences in kinetic energies and area ratios of the different components ascribed to the different chemical states in XAES signals were kept constant and equal to those determined on the reference materials.

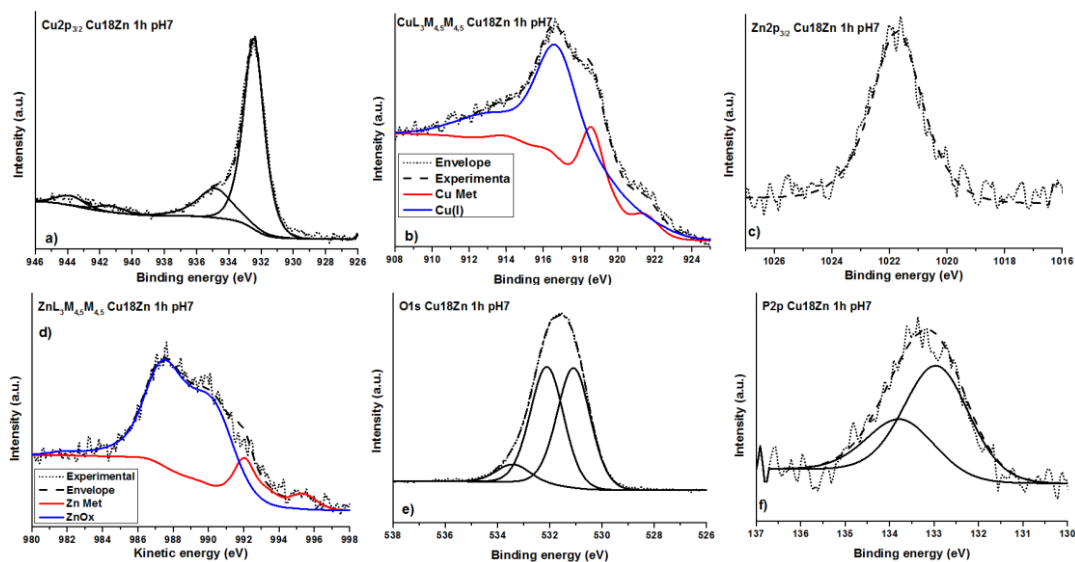


Figure 7. 8: Cu  $2p_{3/2}$  (a), Cu  $L_3M_{45}M_{45}$  (b), Zn  $2p_{3/2}$  (c), Zn  $L_3M_{45}M_{45}$  (d), O  $1s$  (e), P  $2p$  (f) signals for the Cu18Zn alloy after 1 hours of contact with the phosphate buffer solution.

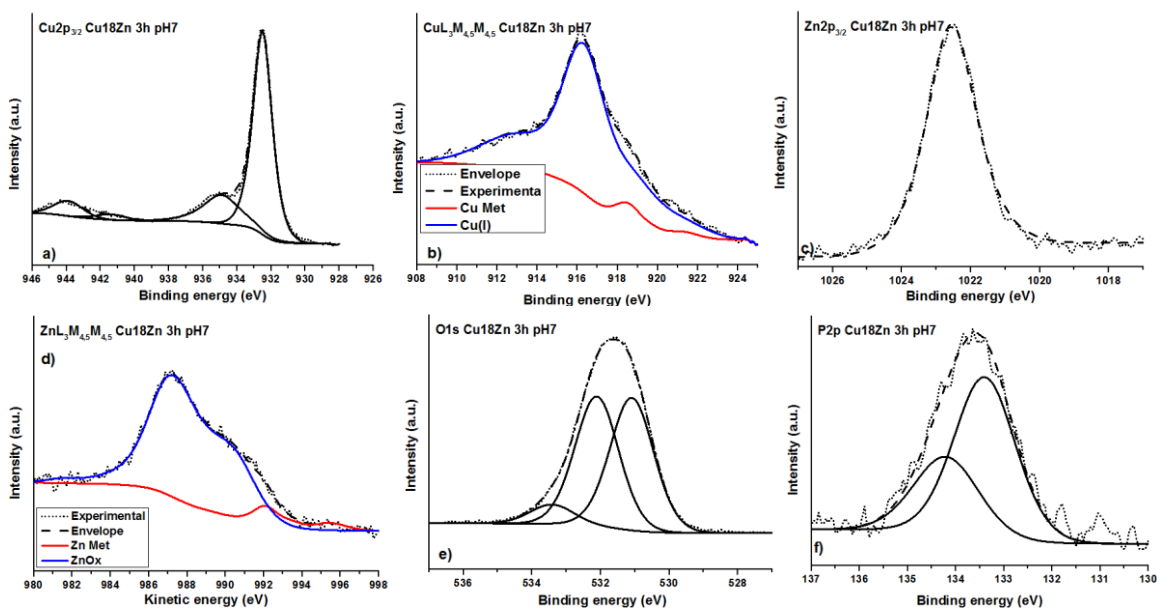


Figure 7. 9: Cu  $2p_{3/2}$  (a), Cu  $L_3M_{45}M_{45}$  (b), Zn  $2p_{3/2}$  (c), Zn  $L_3M_{45}M_{45}$  (d), O 1s (e), P 2p (f) signals for the Cu18Zn alloy after 3 hours of contact with the phosphate buffer solution.

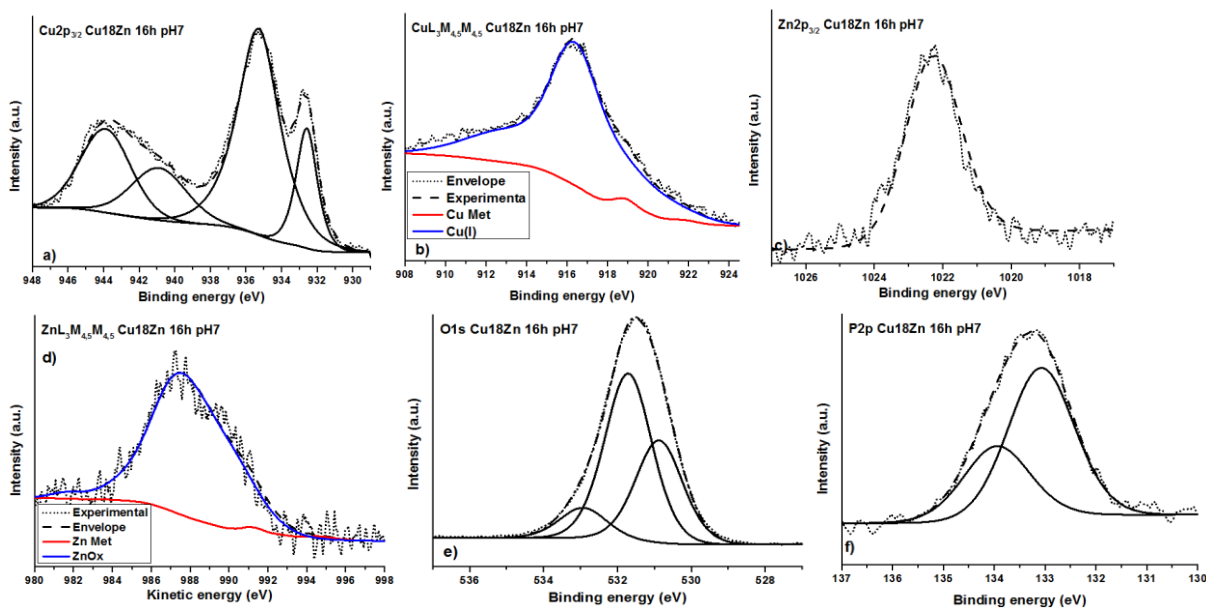


Figure 7. 10: Cu  $2p_{3/2}$  (a), Cu  $L_3M_{45}M_{45}$  (b), Zn  $2p_{3/2}$  (c), Zn  $L_3M_{45}M_{45}$  (d), O 1s (e), P 2p (f) signals for the Cu18Zn alloy after 16 hours of contact with the phosphate buffer solution.

The Cu  $2p_{3/2}$  spectrum showed for all the contact times two main signals located at about BE 932.6 eV and 935.1 eV. The first component could be assigned to the presence of metallic copper or  $Cu_2O$ , the second one might be due to the presence of Cu (II) compounds confirmed by the presence of a satellite structure characteristic of the presence of Cu (II) species at the high binding energy side (944.0 eV Sat 1, 941.5 eV Sat 2), as in the case of the reference compound CuO (Fig 5.6a).

The X-ray induced Cu L<sub>3</sub>M<sub>45</sub>M<sub>45</sub> Auger spectra showed both contributions from the metal and the oxide film. The most intense components (<sup>1</sup>G) of the multiplet associated to the metal and to the oxidized copper were found at about KE 918.8 eV and 917.0 eV respectively. The results were in agreement with those obtained on pure copper and copper (I) oxide reported in Chapter 5: for the pure copper the main peak (<sup>1</sup>G) of the Auger signal was found at 918.6 (0.1) eV, while the main peak (<sup>1</sup>G) of the Cu<sub>2</sub>O was found at 916.8 (0.1) eV (Tables 5.1 and 5.2).

The Zn 2p<sub>3/2</sub> photoelectron signal showed a single peak at BE 1021.9 - 1022.2 eV. The Auger signal showed both the oxide and the metallic components. The main component of the oxidized zinc was found at KE 987.5 – 988 eV while the main component related to the metallic zinc was found at 992.4 (0.1) eV. The former might be assigned to zinc orthophosphate according to literature [17].

The phosphorus P 2p signal consisted of the 2p<sub>3/2</sub> and 2p<sub>1/2</sub> doublet due to spin-orbit coupling. Curve fitting procedure was performed constraining the integrated intensity ratio of these two signals to 2 and their energy separation to 0.85 eV. The binding energy of the 2p<sub>3/2</sub> component of phosphorus was found to be 133.3 (0.1) eV and it could be associated with the presence of zinc orthophosphate according to [17].

The metallic components of both copper and zinc were still revealed after 16 hours of contact with the phosphate buffer solution and the presence of a thin oxide film in the nanometre range (<10nm) can be hypothesized.

Table 7.8a: Binding energy (BE) and FWHM of the most intense peaks of the elements detected on the Cu18Zn samples after contact with the phosphate buffer solution for 1, 3 and 16 hours. Standard deviations are given in parentheses.

Cu18Zn	1h pH7		3h pH7		16h pH7	
	BE (eV)	FWHM (eV)	BE (eV)	FWHM (eV)	BE (eV)	FWHM (eV)
<b>Cu 2p<sub>3/2</sub> Cu(0)</b>	932.6 (0.1)	1.4 (0.1)	932.6 (0.1)	1.4 (0.1)	932.6 (0.1)	1.4 (0.1)
<b>Cu 2p<sub>3/2</sub> Cu(I)</b>	932.6 (0.1)	1.4 (0.1)	932.6 (0.1)	1.4 (0.1)	932.6 (0.1)	1.4 (0.1)
<b>Cu 2p<sub>3/2</sub> Cu(II)</b>	935.0 (0.1)	2.6 (0.1)	935.0 (0.1)	2.6 (0.1)	935.3 (0.1)	2.7 (0.1)
<b>Sat 1</b>	944.0 (0.1)	2.2 (0.1)	944.0 (0.1)	2.2 (0.2)	944.0 (0.1)	2.3 (0.2)
<b>Sat 2</b>	941.5 (0.1)	2.1 (0.1)	941.6 (0.1)	2.2 (0.2)	941.1 (0.1)	2.3 (0.2)
<b>O 1s</b>	530.6 (0.1)	1.5 (0.1)	530.7 (0.1)	1.5 (0.1)	530.8 (0.1)	1.5 (0.1)
	531.7 (0.1)	1.5 (0.1)	531.7 (0.1)	1.5 (0.1)	531.7 (0.1)	1.5 (0.1)
	532.9 (0.2)	1.5 (0.1)	532.9 (0.2)	1.5 (0.1)	532.8 (0.1)	1.5 (0.1)
<b>P 2p</b>	132.9 (0.1)	1.5 (0.1)	133.0 (0.1)	1.5 (0.1)	133.1 (0.1)	1.5 (0.1)
	133.7 (0.1)	1.5 (0.1)	133.8 (0.1)	1.7 (0.1)	134.0 (0.1)	1.5 (0.1)
<b>Zn 2p<sub>3/2</sub> Zn(0)</b>	1021.9 (0.1)	1.7 (0.1)	1022.2 (0.1)	1.7 (0.1)	1022.4 (0.1)	1.8 (0.1)
<b>Zn 2p<sub>3/2</sub> Zn(II)</b>	1021.9 (0.1)	1.7 (0.1)	1022.2 (0.1)	1.7 (0.1)	1022.4 (0.1)	1.8 (0.1)

Table 7.8b: Average kinetic energy (KE) and FWHM of the most intense peaks of the elements detected on the Cu18Zn samples after contact with the phosphate buffer solution for 1, 3 and 16 hours. Standard deviations are given in parentheses.

Cu18Zn	1h pH7		3h pH7		16h pH7	
	KE (eV)	FWHM (eV)	KE (eV)	FWHM (eV)	KE (eV)	FWHM (eV)
<b>Cu LMM met</b>	918.8 (0.1)	1.5 (0.1)	918.9 (0.2)	1.5 (0.1)	918.9 (0.2)	1.5 (0.1)
<b>Cu LMM Ox</b>	917.0 (0.1)	2.7 (0.1)	916.6 (0.1)	2.7 (0.2)	916.8 (0.1)	2.7 (0.2)
	KE (eV)	FWHM (eV)	KE (eV)	FWHM (eV)	KE (eV)	FWHM (eV)
<b>Zn LMM met</b>	992.4 (0.2)	FWHM	992.5 (0.2)	1.5 (0.1)	992.3 (0.2)	1.5 (0.1)
<b>Zn LMM Ox</b>	987.5 (0.2)	1.5 (0.1)	987.5 (0.1)	2.8 (0.2)	987.3 (0.1)	2.8 (0.2)

*Composition obtained from angle resolved XPS measurements*

The apparent concentration of the elements on the surface of the Cu18Zn alloy in atomic percentage versus the emission angle, calculated from angle resolved experiments assuming the homogeneity within the whole analysed depth, is shown in figure 7.11. The Cu and Zn concentrations are calculated using the Cu 2p<sub>3/2</sub> and the Zn 2p<sub>3/2</sub> signals without distinguishing between the metallic and the oxidized contributions. In fact, the correction, which has to be applied to angle resolved XPS data when using the Theta Probe, the so-called angular signature, can be correctly applied only when the acquisition range is of about 20 eV. In the case of the Auger signals the required interval is almost the double and thus these data were not used for the identification of the copper and zinc chemical states. The plots in Figures 7. 11 (left column) revealed the presence of an outermost layer mostly composed by carbon and oxygen. If C, O and P are excluded (Fig. 7.11 right column) and only copper and zinc are taken into account, it is possible to observe that after 16 hours of immersion the copper is mainly present as Cu(II) while for shorter time the predominant component is the Cu(0)/Cu(I). The zinc content is in average within the nominal composition but after 16 hours of exposure an increase of Zn content above 30 at.% is observed. The apparent concentration seems to not depend on the emission angle, indicating that the composition of the oxide layer is not changing with depth for exposure times up to three hours; after 16 hours Zn enrichment and Cu(0)/Cu (I) depletion of the outermost layer (higher emission angles) is observed.

Starting from the areas of the main peaks acquired in standard mode XPS corrected according to the first principle method, it is possible to calculate the composition of the film and also the percentage of the different oxides, thanks to the approach presented in Chapter 5. Each sample showed a C content of about 40 at.% due to the presence of a contamination layer. If total copper and zinc are taken into account, the composition after 1 and 3 hours was close to the nominal one; prolonged exposure induced a decrease of the Zn content probably due to a preferential dissolution of the element known as dezincification process. Zn (0) content decreases with increasing the exposure time. As well as the Zn metal, also the copper metal component decrease with exposure time going from 40 %at to 1 %at. The oxide layer after 16 hours was mainly composed of Cu (II) and Zn (II) compounds.

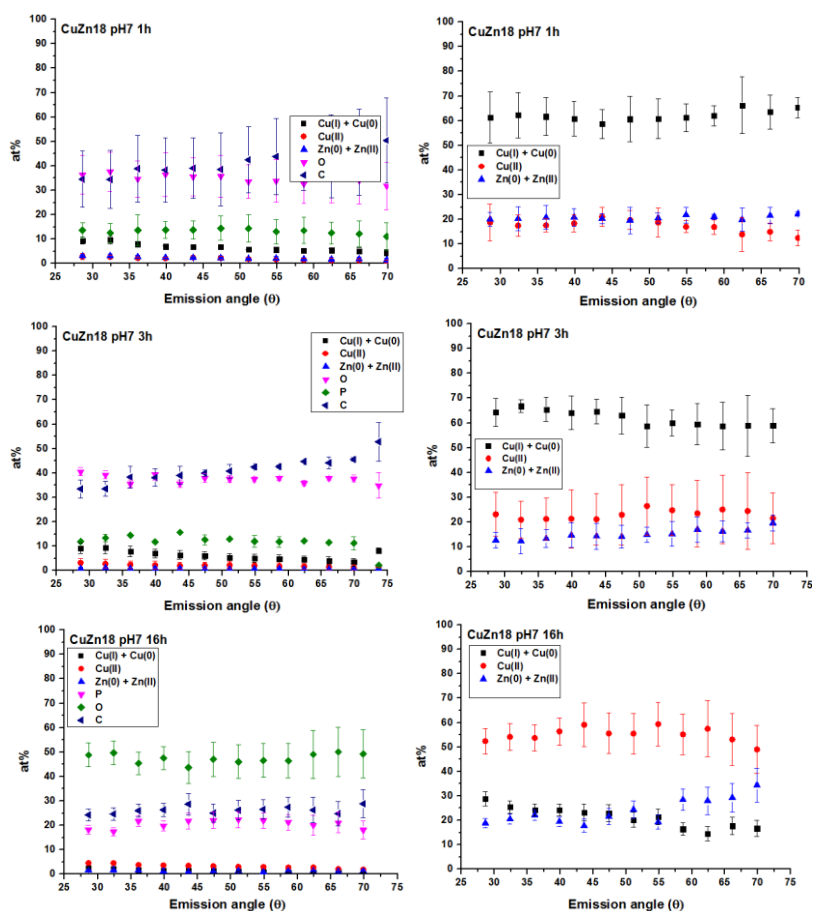


Figure 7. 11: Apparent composition (at.%) vs emission angle from ARXPS data for Cu18Zn after 1, 3 and 16 hours of contact with the phosphate solution.

Table 7.9: Quantitative analysis results for the Cu18Zn after 1, 3 and 16hours of immersion in the neutral phosphate buffer solution. Standard deviations are reported in brackets.

Cu18Zn	1h			3h							
	%at	%at	%at	%at	%at	%at					
Cu(0)	9 (1)	Cu(0)	42 (7)	Cu tot	82 (1)	Cu(0)	0.9 (0.1)	Cu(0)	4 (1)	Cu tot	86 (2)
Cu(I)	6 (1)	Cu(I)	32 (15)			Cu(I)	9 (1)	Cu(I)	35 (3)		
Cu(II)	4 (2)	Cu(II)	18 (10)			Cu(II)	6 (1)	Cu(II)	45 (2)		
Zn(0)	2 (1)	Zn(0)	40 (11)	Zn tot	18 (1)	Zn(0)	0.5 (0.2)	Zn(0)	19 (5)	Zn tot	14 (2)
Zn(II)	2 (1)	Zn(II)	60 (11)			Zn(II)	3 (1)	Zn(II)	81 (5)		
O	32 (6)					O	30 (1)				
C	40 (9)					C	43 (1)				
P	5 (2)					P	8 (1)				
	16h										
	%at										
Cu(0)	0.14(0.01)	Cu(0)	1 (0.1)	Cu tot	90 (1)						
Cu(I)	1.8(0.5)	Cu(I)	12 (3)								
Cu(II)	13.8(0.5)	Cu(II)	88(3)								
Zn(0)	0.17(0.06)	Zn(0)	10 (2)	Zn tot	10 (1)						
Zn(II)	1.5(0.1)	Zn(II)	90(2)								
O	50.4(0.6)										
C	19.8(1.3)										
P	12.5(0.5)										



## Cu37Zn alloy exposed to buffer solutions

### High-resolution photoelectron and Auger signals

The high-resolution spectra of Cu37Zn acquired after 1, 3 and 16 hours of contact with the phosphate buffer solution are shown from figure 7.12 – 7.14. The related BE, KE and FWHM values were listed in Table 7.10.

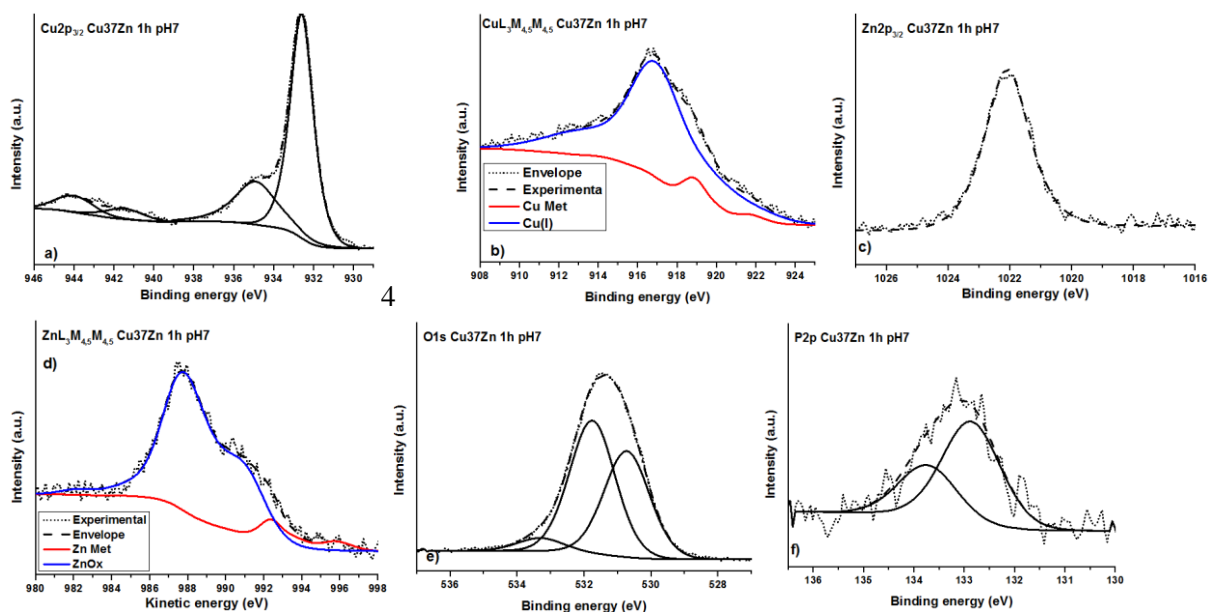


Figure 7. 12: Cu 2p<sub>3/2</sub> (a), Cu L<sub>3</sub>M<sub>45</sub>M<sub>45</sub> (b), Zn 2p<sub>3/2</sub> (c), Zn L<sub>3</sub>M<sub>45</sub>M<sub>45</sub> (d), O 1s (e), P 2p (f) signals for the Cu37Zn alloy after 1 hours of contact with the phosphate buffer solution.

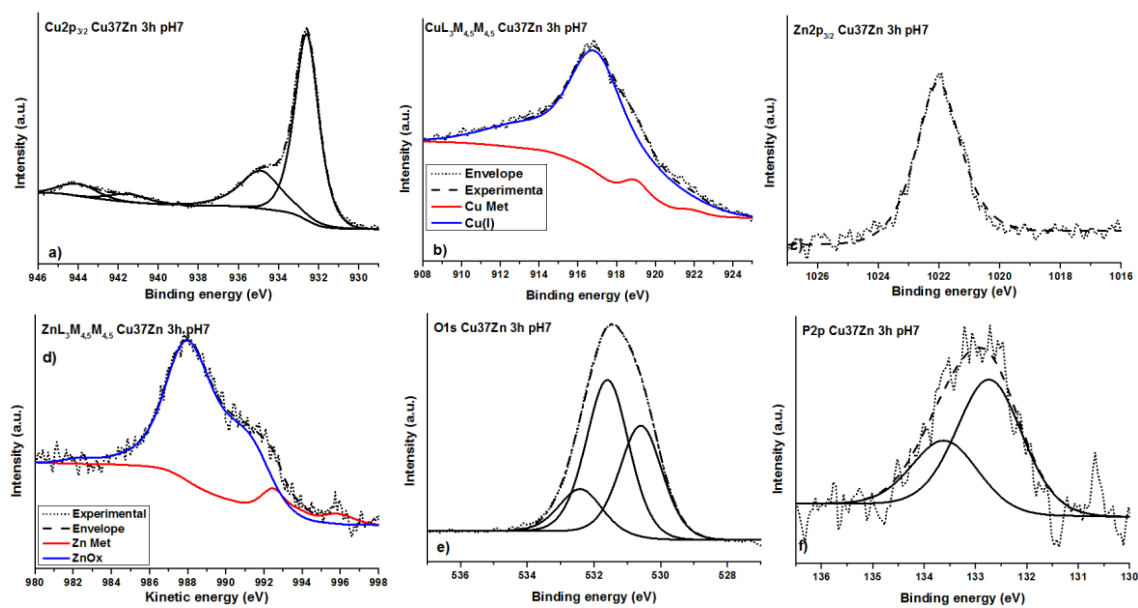


Figure 7. 13: Cu 2p<sub>3/2</sub> (a), Cu L<sub>3</sub>M<sub>45</sub>M<sub>45</sub> (b), Zn 2p<sub>3/2</sub> (c), Zn L<sub>3</sub>M<sub>45</sub>M<sub>45</sub> (d), O 1s (e), P 2p (f) signals for the Cu37Zn alloy after 3 hours of contact with the phosphate buffer solution.

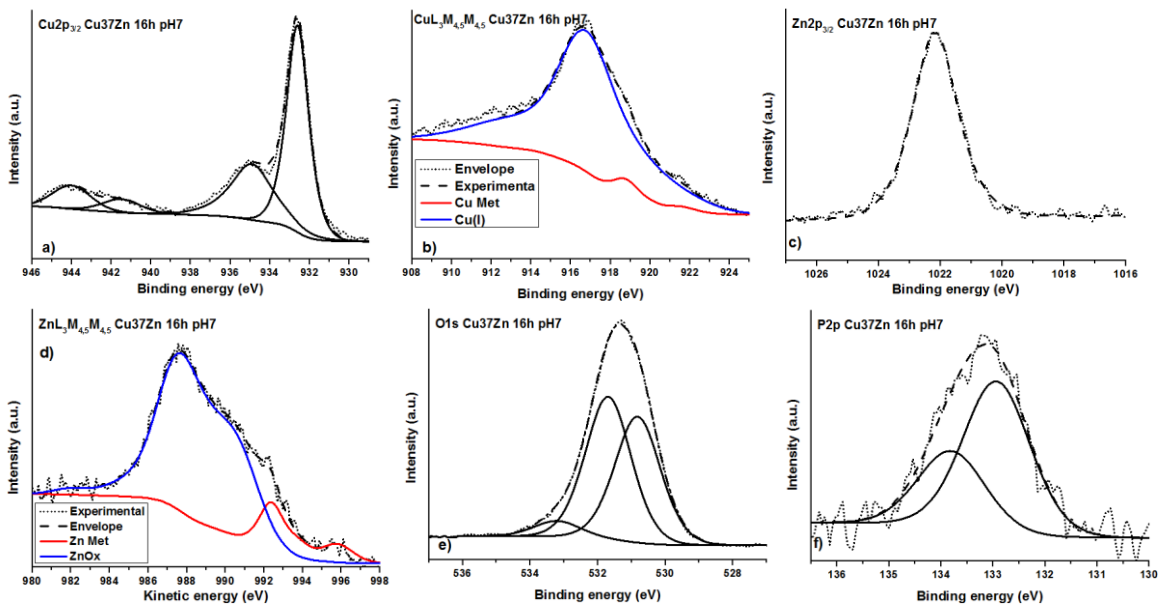


Figure 7. 14: Cu 2p<sub>3/2</sub> (a), Cu L<sub>3</sub>M<sub>45</sub>M<sub>45</sub> (b), Zn 2p<sub>3/2</sub> (c), Zn L<sub>3</sub>M<sub>45</sub>M<sub>45</sub> (d), O 1s (e), P 2p (f) signals for the Cu<sub>37</sub>Zn alloy after 16 hours of contact with the phosphate buffer solution.

Two components at 932.6 eV and 934.9 eV were detected in the Cu 2p<sub>3/2</sub> spectra after the curve fitting, together with the satellite structures due to Cu (II). The component at 934.9 eV can be ascribed to the presence of Cu(II) species whereas the component at BE 932.6 eV might be related to both metallic and Cu(I) species. The Cu L<sub>3</sub>M<sub>45</sub>M<sub>45</sub> spectra showed the presence of two different species. The KE of the the main components (<sup>1</sup>G) ae found to be 918.8 eV and 916.8 eV and are due to metallic copper and copper (I) oxide respectively. The results were in agreement to those obtained on pure copper and copper (I) oxide reported in Chapter 5.

The Zn 2p<sub>3/2</sub> photoelectron signal showed a single peak at about BE 1022.1 eV. As in the case of the Cu L<sub>3</sub>M<sub>45</sub>M<sub>45</sub> also the Zn L<sub>3</sub>M<sub>45</sub>M<sub>45</sub> Auger signal showed both the metallic and the oxidized Zn(II) components; their kinetic energies are 991.3 eV and 987.5 eV respectively. The former component is assigned to Zn (0) and the latter might be assigned to zinc orthophosphate according to literature [15], but the presence of ZnO cannot be ruled out.

The P 2p<sub>3/2</sub> signal was found at about BE 132.8 – 133.8 eV and could be assigned to the presence of zinc orthophosphate according to [17].

Table 7. 10a: Average binding energy (BE) and FWHM of the most intense peaks of the elements detected on the Cu37Zn samples after contact with the phosphate buffer solution. Standard deviations are given in parentheses.

Cu37Zn	1h pH7		3h pH7		16h pH7	
	BE (eV)	FWHM (eV)	BE (eV)	FWHM (eV)	BE (eV)	FWHM (eV)
<b>Cu 2p<sub>3/2</sub> Cu(0)</b>	932.5 (0.1)	1.4 (0.1)	932.6 (0.1)	1.5 (0.1)	932.6 (0.1)	1.3 (0.1)
<b>Cu 2p<sub>3/2</sub> Cu(I)</b>	932.5 (0.1)	1.4 (0.1)	932.6 (0.1)	1.5 (0.1)	932.6 (0.1)	1.3 (0.1)
<b>Cu 2p<sub>3/2</sub> Cu(II)</b>	934.9 (0.1)	2.5 (0.1)	934.9 (0.1)	2.4 (0.1)	934.9 (0.1)	2.5 (0.1)
<b>Sat 1</b>	944.1 (0.1)	2.2 (0.1)	944.0 (0.1)	2.2 (0.1)	944.0 (0.1)	2.3 (0.1)
<b>Sat 2</b>	941.8 (0.3)	2.2 (0.1)	941.5 (0.1)	2.2 (0.1)	941.5 (0.1)	2.3 (0.1)
<b>O 1s</b>	530.7 (0.1)	1.6 (0.1)	530.6 (0.1)	1.5 (0.1)	530.7 (0.1)	1.5 (0.1)
	531.7 (0.1)	1.6 (0.1)	531.6 (0.1)	1.5 (0.1)	531.7 (0.1)	1.5 (0.1)
	533.2 (0.2)	1.6 (0.1)	532.5 (0.2)	1.5 (0.1)	533.1 (0.2)	1.5 (0.1)
<b>P 2p</b>	133.0 (0.2)	1.5 (0.1)	132.8 (0.2)	1.5 (0.1)	133.0 (0.1)	1.5 (0.1)
	133.8 (0.2)	1.5 (0.1)	133.6 (0.1)	1.5 (0.1)	133.8 (0.1)	1.5 (0.1)
<b>Zn 2p<sub>3/2</sub> Cu(0)</b>	1022.1 (0.1)	1.7 (0.1)	1022.1 (0.1)	1.7 (0.1)	1022.2 (0.1)	1.7 (0.1)
<b>Zn 2p<sub>3/2</sub> Zn(II)</b>	1022.1 (0.1)	1.7 (0.1)	1022.1 (0.1)	1.7 (0.1)	1022.2 (0.1)	1.7 (0.1)

Table 10b: Average kinetic energy (KE) and FWHM of the most intense peaks of the elements detected on the Cu37Zn after contact with the phosphate buffer solution for 1, 3 and 16 hours. Standard deviations are given in parentheses.

Cu37Zn	1h pH7		3h pH7		16h pH7	
	KE (eV)	FWHM (eV)	KE (eV)	FWHM (eV)	KE (eV)	FWHM (eV)
<b>Cu L<sub>3</sub>M<sub>4,5</sub>M<sub>4,5</sub> met</b>	918.8 (0.2)	1.5 (0.1)	918.8 (0.1)	1.5 (0.1)	918.9 (0.2)	1.5 (0.1)
<b>Cu L<sub>3</sub>M<sub>4,5</sub>M<sub>4,5</sub> Ox</b>	916.8 (0.1)	2.8 (0.1)	916.9 (0.1)	3.0 (0.2)	916.9 (0.2)	2.9 (0.1)
	KE (eV)	FWHM (eV)	KE (eV)	FWHM (eV)	KE (eV)	FWHM (eV)
<b>Zn L<sub>3</sub>M<sub>4,5</sub>M<sub>4,5</sub> met</b>	992.3 (0.1)	1.6 (0.1)	992.4 (0.1)	1.6 (0.1)	992.3 (0.1)	1.6 (0.1)
<b>Zn L<sub>3</sub>M<sub>4,5</sub>M<sub>4,5</sub> Ox</b>	987.4 (0.2)	2.6 (0.1)	987.7 (0.2)	2.7 (0.1)	987.5 (0.1)	2.7 (0.1)

The apparent composition (at.%) vs emission angle obtained by the angle resolved data (Fig. 7.15) showed the presence of a contamination layer that covered the brass alloys for all the time of exposure; on the other hand it could be seen how after 1 hour of immersion the zinc content is in average close to the nominal composition, then after 3 hours the Zn content decreases.

This result is confirmed also by the quantitative analysis results obtained starting by standard mode data (Tab. 7.11). Zn depletion might be due to a preferential Zn removal from the surface by the dezincification process (Chapter 3); the resulting surface is enriched in Cu (I) and Cu (II).

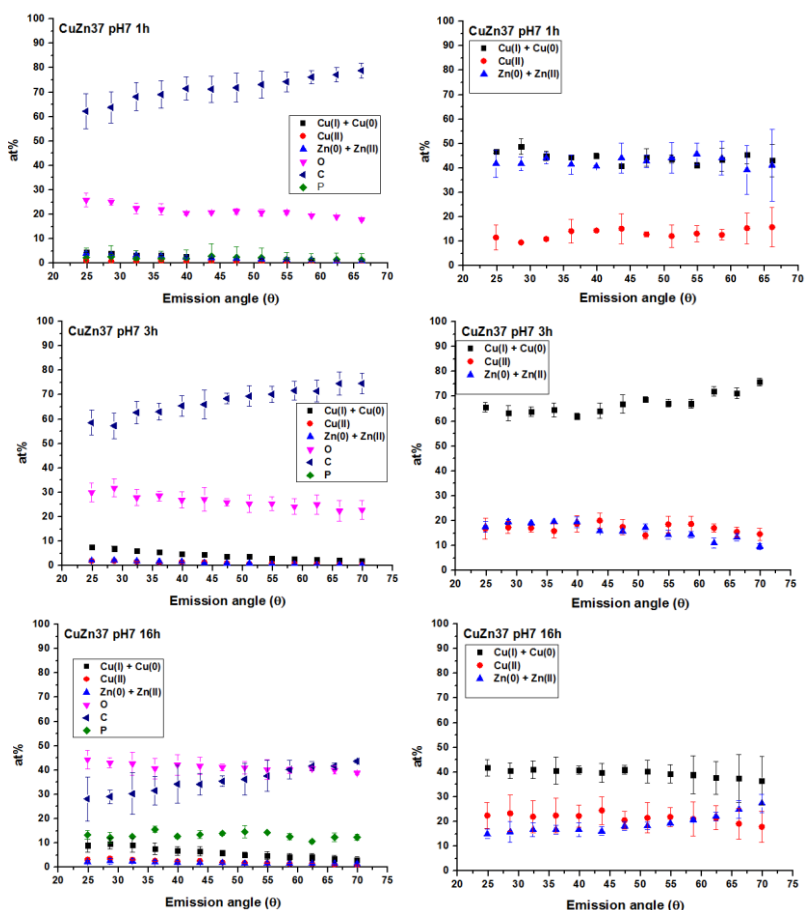


Figure 7. 15: Apparent composition (at.%) vs emission angle from ARXPS data for Cu<sub>37</sub>Zn after 1, 3 and 16 hours of contact with the phosphate solution.

Table 7. 11: Results of the quantitative analysis for the Cu<sub>37</sub>Zn after 1, 3 and 16 hours of immersion in neutral phosphate buffer solution. Standard deviations are reported in brackets.

Cu <sub>37</sub> Zn	1h			3h		
	%at	%at	%at	%at	%at	%at
<b>Cu(0)</b>	3 (1)	<b>Cu(0)</b> 33 (4)	<b>Cu tot</b> 60 (3)	<b>Cu(0)</b> 1 (0.4)	<b>Cu(0)</b> 14 (2)	<b>Cu tot</b> 77 (3)
<b>Cu(I)</b>	4 (1)	<b>Cu(I)</b> 40 (15)		<b>Cu(I)</b> 7 (1)	<b>Cu(I)</b> 59 (3)	
<b>Cu(II)</b>	3 (1)	<b>Cu(II)</b> 21 (4)		<b>Cu(II)</b> 3 (1)	<b>Cu(II)</b> 27 (4)	
<b>Zn(0)</b>	2 (1)	<b>Zn(0)</b> 28 (6)	<b>Zn tot</b> 40 (3)	<b>Zn(0)</b> 1 (0.2)	<b>Zn(0)</b> 28 (3)	<b>Zn tot</b> 23 (3)
<b>Zn(II)</b>	5 (1)	<b>Zn(II)</b> 72 (6)		<b>Zn(II)</b> 3 (1)	<b>Zn(II)</b> 72 (3)	
<b>O</b>	34 (2)			<b>O</b> 37 (1)		
<b>C</b>	44(2)			<b>C</b> 42 (1)		
<b>P</b>	7 (1)			<b>P</b> 6 (1)		
	16h					
	%at	%at	%at			
<b>Cu(0)</b>	0.6 (0.3)	<b>Cu(0)</b> 5 (2)	<b>Cu tot</b> 79 (1)			
<b>Cu(I)</b>	8 (1)	<b>Cu(I)</b> 59 (3)				
<b>Cu(II)</b>	4 (1)	<b>Cu(II)</b> 36 (3)				
<b>Zn(0)</b>	1.0 (0.1)	<b>Zn(0)</b> 31 (3)	<b>Zn tot</b> 21 (1)			
<b>Zn(II)</b>	2.2 (0.2)	<b>Zn(II)</b> 69 (3)				
<b>O</b>	44 (1)					
<b>C</b>	31 (1)					
<b>P</b>	9 (1)					

## Cu<sub>38</sub>Zn<sub>2</sub>Pb alloy exposed to buffer solutions

### High-resolution photoelectron and Auger signals

The high-resolution spectra of Cu<sub>38</sub>Zn<sub>2</sub>Pb acquired after 1, 3 and 16 hours of contact with the phosphate buffer solution are shown from figure 7.16 – 7.18. The related BE, KE and FWHM values are presented in Table 7.12.

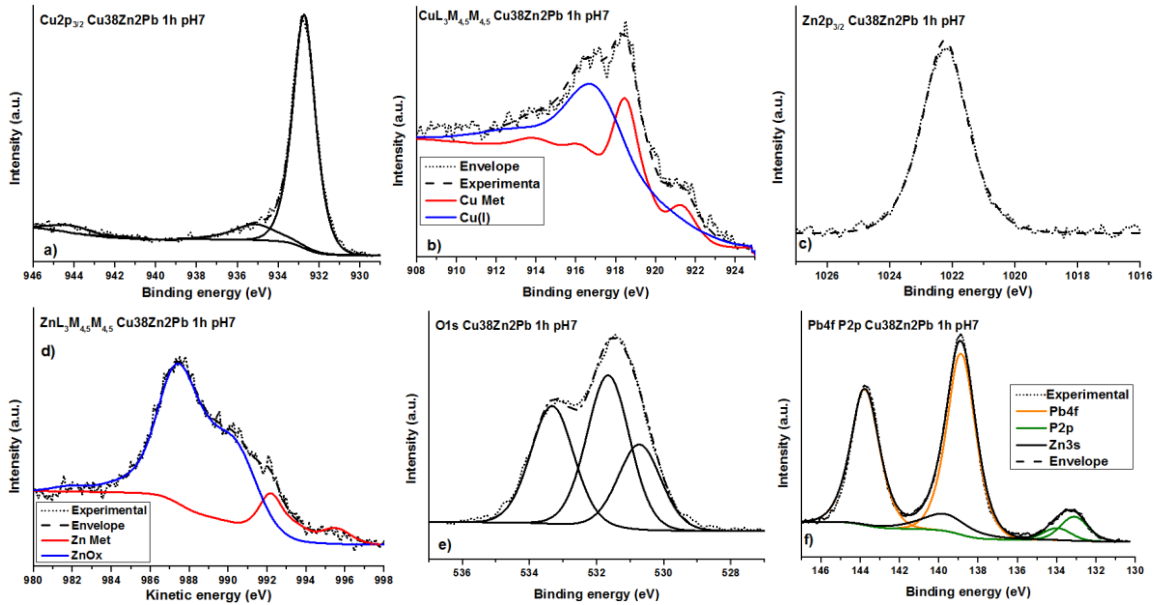


Figure 7. 16: Cu 2p<sub>3/2</sub> (a), Cu L<sub>3</sub>M<sub>45</sub>M<sub>45</sub> (b), Zn 2p<sub>3/2</sub> (c), Zn L<sub>3</sub>M<sub>45</sub>M<sub>45</sub> (d), O 1s (e), P 2p (f) signals for the Cu<sub>38</sub>Zn<sub>2</sub>Pb after 1 hours of contact with the phosphate buffer solution.

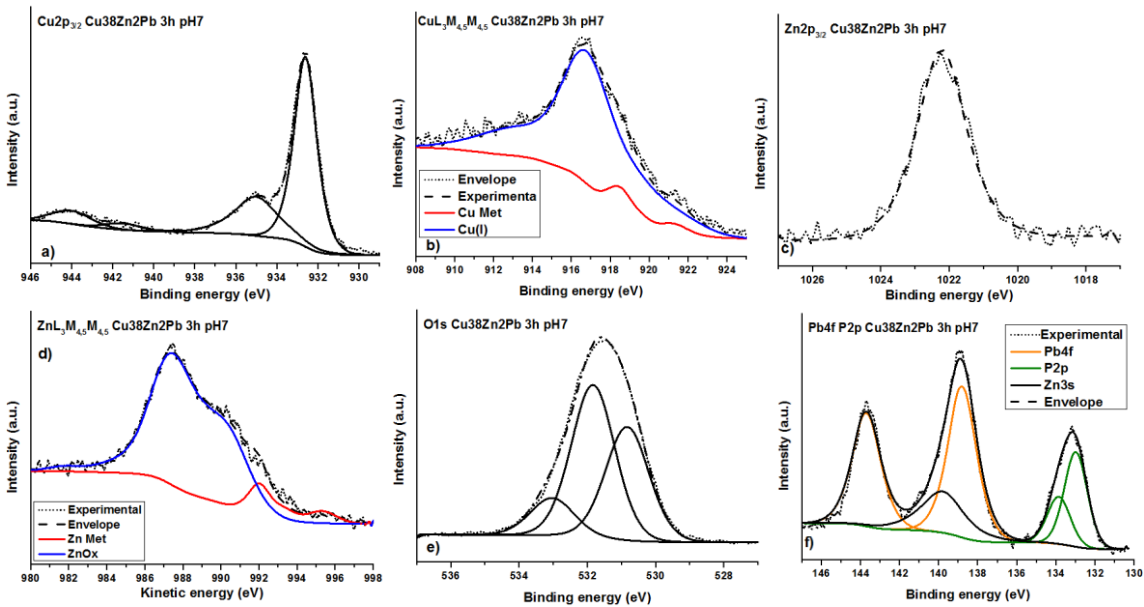


Figure 7. 17: Cu 2p<sub>3/2</sub> (a), Cu L<sub>3</sub>M<sub>45</sub>M<sub>45</sub> (b), Zn 2p<sub>3/2</sub> (c), Zn L<sub>3</sub>M<sub>45</sub>M<sub>45</sub> (d), O 1s (e), P 2p (f) signals for the Cu<sub>38</sub>Zn<sub>2</sub>Pb after 3 hours of contact with the phosphate buffer solution.

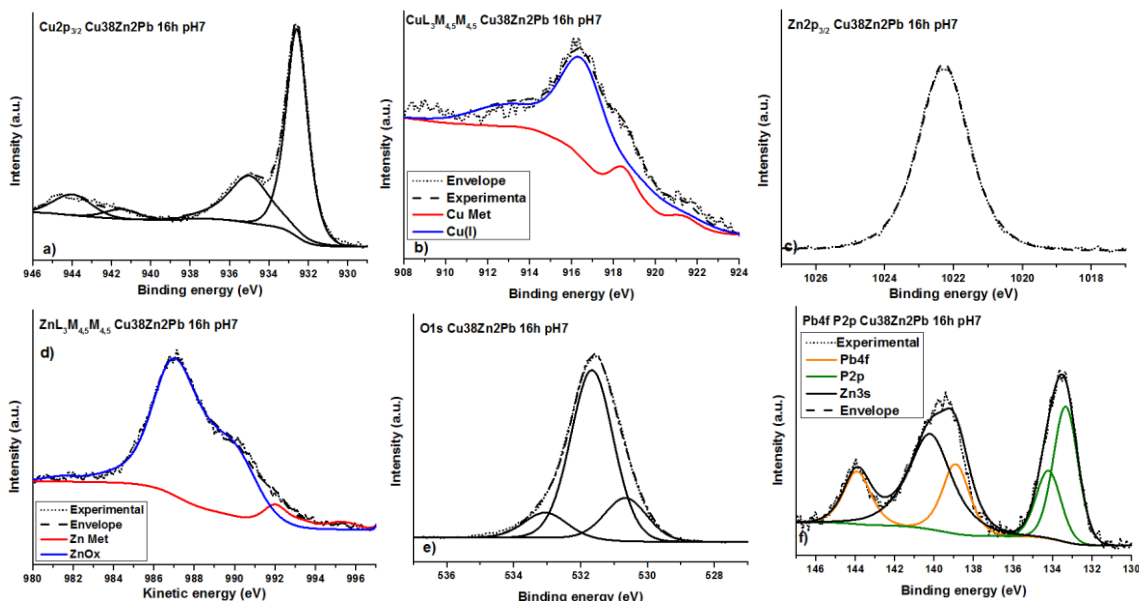


Figure 7. 18: Cu  $2p_{3/2}$  (a), Cu  $L_3M_{45}M_{45}$  (b), Zn  $2p_{3/2}$  (c), Zn  $L_3M_{45}M_{45}$  (d), O  $1s$  (e), P  $2p$  (f) signals for the Cu38Zn2Pb after 16 hours of contact with the phosphate buffer solution.

The Cu  $2p_{3/2}$  photoelectron signals for 1, 3 and 16 h of exposure to the pH7 solution showed two main signals: 1) one signal at BE 932.6 eV related to the presence of Cu(0) and Cu(I) and 2) the signal at about BE 935.0 eV due to the presence of Cu (II) together with the typical satellite structure. The presence of Cu(0) and Cu(I) could be established on the basis of curve fitting of the Cu  $L_3M_{45}M_{45}$  spectra: the two different species are present and their kinetic energy are 918.7 eV and 917.0 eV respectively. The results were in agreement with those obtained on pure copper, copper (I) oxide and with the results obtained on the mechanically polished brass alloys reported in Chapter 5.

The Zn  $2p_{3/2}$  showed the presence of a single peak at about BE 1022.1 – 1022.3 eV, whereas the related Zn  $L_3M_{45}M_{45}$  Auger signal showed the presence of both the metallic and the oxidized components. The oxidized component might be assigned to zinc orthophosphate [17].

The characteristic signal of Pb showed a well-separated spin orbit doublet having a FWHM of 1.7 eV each. The Pb 4f overlapped with the Zn 3s signal and on the lower BE side of the Pb  $4f_{7/2}$  the P 2p was also found. The BE of the Pb  $4f_{7/2}$ , the BE separation between the Pb  $4f_{7/2}$  and Pb  $4f_{5/2}$  and their area ratio (0.75) were kept constant. A symmetric peak for Zn 3s was also added; its BE was fixed at 139.8 eV and its area was 1/10 of the Zn  $2p_{3/2}$  peak as establish on pure Zn and on the Pb free alloys. Furthermore, P 2p signal was fitted taking into account the spin – orbit coupling with a doublet having one component at lower BE, assigned to the P  $2p_{3/2}$  signal, and one at higher BE, assigned to the P  $2p_{1/2}$  signal. The doublet was separated by 0.9 eV. The P  $2p_{3/2}$  signal was found at about 133.0 eV and it was likely assigned to the presence of phosphate group according to [17].

The Pb  $4f_{7/2}$  peak was found at about 138.8 eV (Table 5.7) and it might be due to PbO [18, 19].

Table 7. 12a: Average binding energy (BE) and FWHM of the most intense peaks of the elements detected on the Cu38Zn2Pb after exposure to the phosphate buffer solution. Standard deviations are given in parentheses.

Cu38Zn2Pb	1h pH7		3h pH7		16h pH7	
	BE (eV)	FWHM (eV)	BE (eV)	FWHM (eV)	BE (eV)	FWHM (eV)
<b>Cu 2p<sub>3/2</sub> Cu(0)</b>	932.7 (0.1)	1.4 (0.1)	932.6 (0.1)	1.4 (0.1)	932.6 (0.1)	1.4 (0.1)
<b>Cu 2p<sub>3/2</sub> Cu(I)</b>	932.7 (0.1)	1.4 (0.1)	932.6 (0.1)	1.4 (0.1)	932.6 (0.1)	1.4 (0.1)
<b>Cu 2p<sub>3/2</sub> Cu(II)</b>	935.1 (0.1)	2.5 (0.1)	935.0 (0.1)	2.5 (0.1)	935.0 (0.1)	2.5 (0.1)
<b>Sat 1</b>	944.1 (0.1)	2.2 (0.1)	944.0 (0.1)	2.2 (0.1)	944.0 (0.1)	2.2 (0.1)
<b>Sat 2</b>	941.6 (0.1)	2.0 (0.1)	941.5 (0.1)	2.0 (0.1)	941.5 (0.1)	2.0 (0.1)
<b>O 1s</b>	530.6 (0.1)	1.5 (0.1)	530.7 (0.1)	1.5 (0.1)	530.7 (0.1)	1.5 (0.1)
	531.5 (0.1)	1.5 (0.1)	531.8 (0.2)	1.5 (0.1)	531.7 (0.1)	1.5 (0.1)
	532.8 (0.1)	1.5 (0.1)	533.0 (0.3)	1.5 (0.1)	533.2 (0.1)	1.5 (0.1)
<b>Pb 4f</b>	138.6 (0.2)	1.7 (0.1)	138.7 (0.1)	1.7 (0.1)	139.1 (0.1)	1.7 (0.1)
	143.5 (0.2)	1.7 (0.1)	143.6 (0.1)	1.7 (0.1)	143.7 (0.1)	1.7 (0.1)
<b>P 2p</b>	132.9 (0.1)	1.5 (0.1)	132.9 (0.1)	1.5 (0.1)	133.0 (0.1)	1.5 (0.1)
	133.8 (0.1)	1.5 (0.1)	133.8 (0.1)	1.5 (0.1)	133.8 (0.1)	1.5 (0.1)
<b>Zn 2p<sub>3/2</sub> Cu(0)</b>	1022.0 (0.1)	1.7 (0.1)	1022.0 (0.1)	1.7 (0.1)	1022.3 (0.1)	1.7 (0.1)
<b>Zn 2p<sub>3/2</sub> Zn(II)</b>	1022.0 (0.1)	1.7 (0.1)	1022.0 (0.1)	1.7 (0.1)	1022.3 (0.1)	1.7 (0.1)

Table 12b: Average kinetic energy (KE) and FWHM of the most intense peaks of the elements detected on the Cu38Zn2Pb after exposure to the phosphate buffer solution for 1, 3 and 16 hours. Standard deviations are given in parentheses.

Cu38Zn2Pb	1h pH7		3h pH7		16h pH7	
	KE (eV)	FWHM (eV)	KE (eV)	FWHM (eV)	KE (eV)	FWHM (eV)
<b>Cu L<sub>3</sub>M<sub>4,5</sub>M<sub>4,5</sub> met</b>	918.6 (0.1)	1.5 (0.1)	918.7 (0.1)	1.5 (0.1)	918.8 (0.1)	1.5 (0.1)
<b>Cu L<sub>3</sub>M<sub>4,5</sub>M<sub>4,5</sub> Ox</b>	917.0 (0.1)	2.8 (0.1)	916.9 (0.1)	2.8 (0.1)	916.7 (0.1)	2.8 (0.1)
	KE (eV)	FWHM (eV)	KE (eV)	FWHM (eV)	KE (eV)	FWHM (eV)
<b>Zn L<sub>3</sub>M<sub>4,5</sub>M<sub>4,5</sub> met</b>	992.3 (0.1)	1.5 (0.1)	992.3 (0.2)	1.5 (0.1)	992.4 (0.1)	1.5 (0.1)
<b>Zn L<sub>3</sub>M<sub>4,5</sub>M<sub>4,5</sub> Ox</b>	987.7 (0.2)	2.4 (0.1)	987.8 (0.3)	2.4 (0.1)	987.2 (0.2)	2.4 (0.1)

The apparent composition (at.%) vs emission angle obtained by the angle resolved data (Fig. 7.19) recorded on the Cu38Zn2Pb samples showed the presence of an outer contamination layer. After 1 and 3 hours the zinc content is lower than the nominal composition and does not change with the emission angle. As in the case of Cu18Zn and Cu28Zn after 16 hours an increase of the zinc content was observed.

The results of the quantitative analysis on the Cu38Zn2Pb sample calculated from the standard mode XPS data (Table 7.13) showed that Zn content slightly decreases in the first three hours but the composition is still close to the one obtained on the mechanically polished brass reported in Chapter 5 (Table 5.15). The lead content is higher than the nominal one (2 wt.% = 0.6 at.% Pb) and lead is present only in the oxidized form.

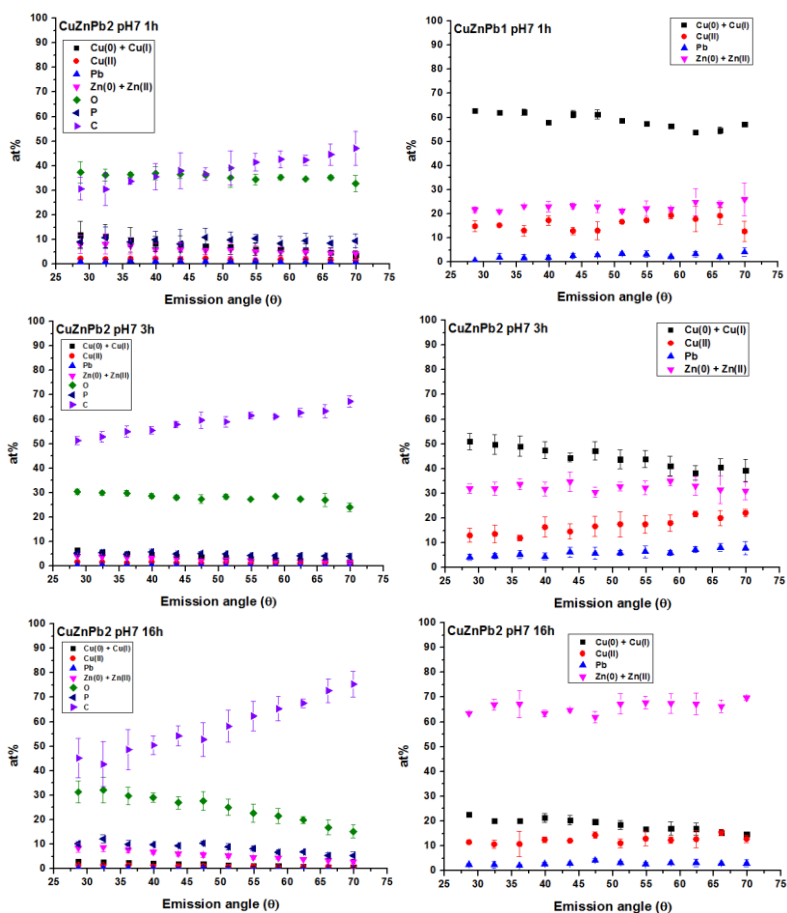


Figure 7. 19: Apparent composition (at.%) vs emission angle from ARXPS data for Cu<sub>38</sub>Zn<sub>2</sub>Pb after 1, 3 and 16 hours of contact with the phosphate solution.

Table 7. 13: Results of the quantitative analysis for the Cu<sub>38</sub>Zn<sub>2</sub>Pb after 1, 3 and 16 hours of immersion in neutral phosphate buffer solution. Standard deviations are reported in brackets.

Cu <sub>38</sub> Zn <sub>2</sub> Pb	1h					3h					
	%at		%at		%at	%at		%at		%at	
<b>Cu(0)</b>	4 (1)	<b>Cu(0)</b>	31 (2)	<b>Cu tot</b>	69 (3)	<b>Cu(0)</b>	2 (1)	<b>Cu(0)</b>	20	<b>Cu tot</b>	73 (4)
<b>Cu(I)</b>	8 (2)	<b>Cu(I)</b>	52 (2)			<b>Cu(I)</b>	6 (1)	<b>Cu(I)</b>	57		
<b>Cu(II)</b>	3 (1)	<b>Cu(II)</b>	17 (1)			<b>Cu(II)</b>	2.4 (0.3)	<b>Cu(II)</b>	23		
<b>Zn(0)</b>	3 (1)	<b>Zn(0)</b>	44 (7)	<b>Zn tot</b>	29 (3)	<b>Zn(0)</b>	2 (1)	<b>Zn(0)</b>	41	<b>Zn tot</b>	25 (8)
<b>Zn(II)</b>	4 (1)	<b>Zn(II)</b>	56 (7)			<b>Zn(II)</b>	2 (1)	<b>Zn(II)</b>	59		
<b>Pb Ox</b>	2 (1)	<b>Pb Ox</b>	100	<b>Pb tot</b>	2 (1)	<b>Pb Ox</b>	0.6 (0.1)	<b>Pb Ox</b>	100	<b>Pb tot</b>	2 (1)
<b>O</b>	34 (2)					<b>O</b>	32 (1)				
<b>C</b>	36 (5)					<b>C</b>	45 (2)				
<b>P</b>	7 (2)					<b>P</b>	7 (4)				
	16h										
	%at		%at		%at						
<b>Cu(0)</b>	2 (0.1)	<b>Cu(0)</b>	9 (1)	<b>Cu tot</b>	45 (2)						
<b>Cu(I)</b>	5 (1)	<b>Cu(I)</b>	48 (4)								
<b>Cu(II)</b>	5 (1)	<b>Cu(II)</b>	43 (4)								
<b>Zn(0)</b>	2 (1)	<b>Zn(0)</b>	14 (1)	<b>Zn tot</b>	54 (2)						
<b>Zn(II)</b>	11 (1)	<b>Zn(II)</b>	86 (1)								
<b>Pb Ox</b>	2 (1)	<b>Pb Ox</b>	100	<b>Pb tot</b>	1.1 (0.1)						
<b>O</b>	50										
<b>C</b>	18 (2)										
<b>P</b>	8 (1)										



### 7.3.3 Results of XPS – XAES surface analysis – artificial saliva solutions

Samples were analysed after mechanical polishing and after exposure to the saliva solution. The XPS results acquired on the brass alloys after mechanical polishing procedure were reported and discussed in Chapter 5. Here, the XPS-XAES results of the copper-zinc alloys exposed to artificial saliva solution up to 16 hours are shown. Results obtained on a low Zn alloy (Cu18Zn), a high Zn alloy (Cu37Zn) and a lead bearing alloy (Cu38Zn2Pb) are presented in detail. Results obtained on the other alloys are shown in appendix 1.

#### Cu18Zn alloy exposed to artificial saliva solutions

##### *High-resolution photoelectron and Auger signals*

The high-resolution spectra of Cu18Zn acquired after 1, 3 and 16 hours of contact with the artificial saliva solution are shown in Fig. 7.20 to 7.22. The BE, KE and FWHM mean values of the peaks are reported in Table 7.14

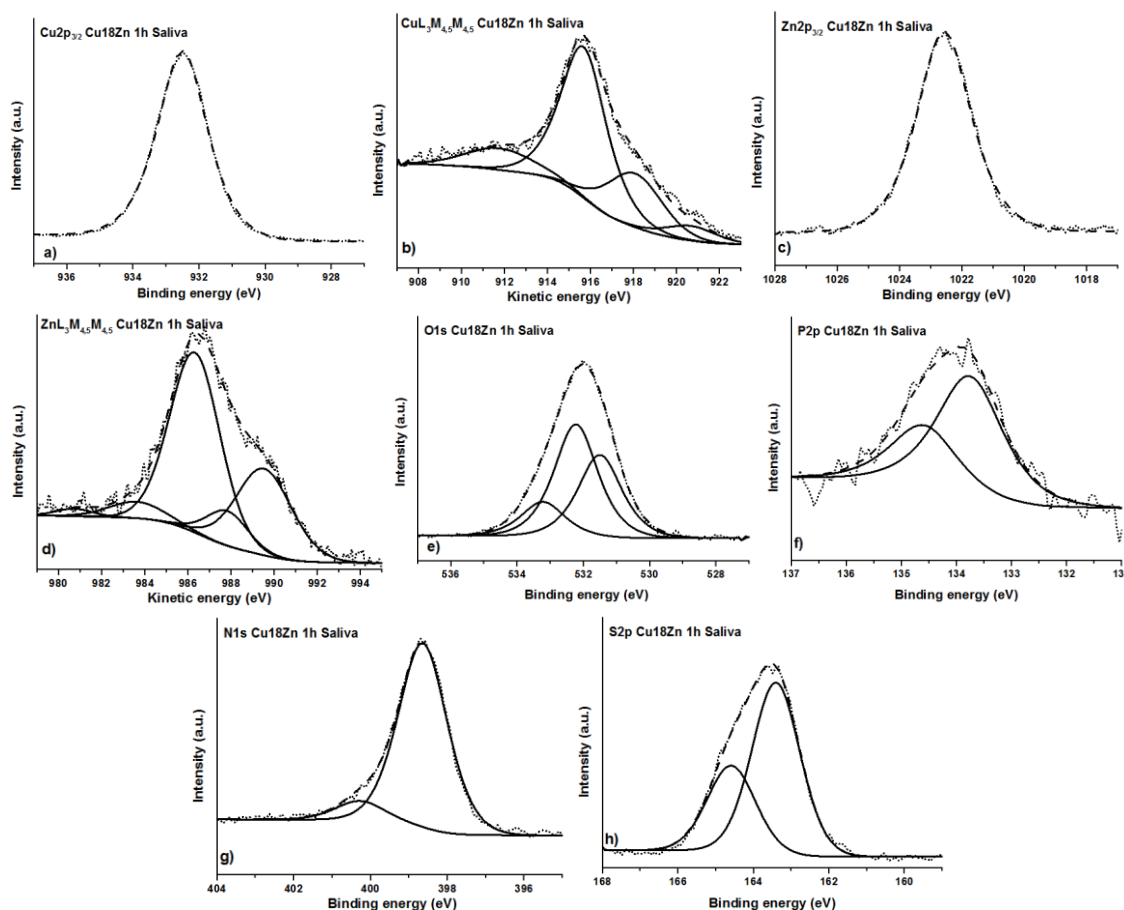


Figure 7. 20: High resolution spectra of Cu 2p<sub>3/2</sub> (a), Zn 2p<sub>3/2</sub> (b), O 1s (c), Cu L<sub>3</sub>M<sub>45</sub>M<sub>45</sub> (d), Zn L<sub>3</sub>M<sub>45</sub>M<sub>45</sub> (e), P 2p (f), N 1s (g), and S 2p (h) for the Cu18Zn after 1 hour of contact with the saliva solution.

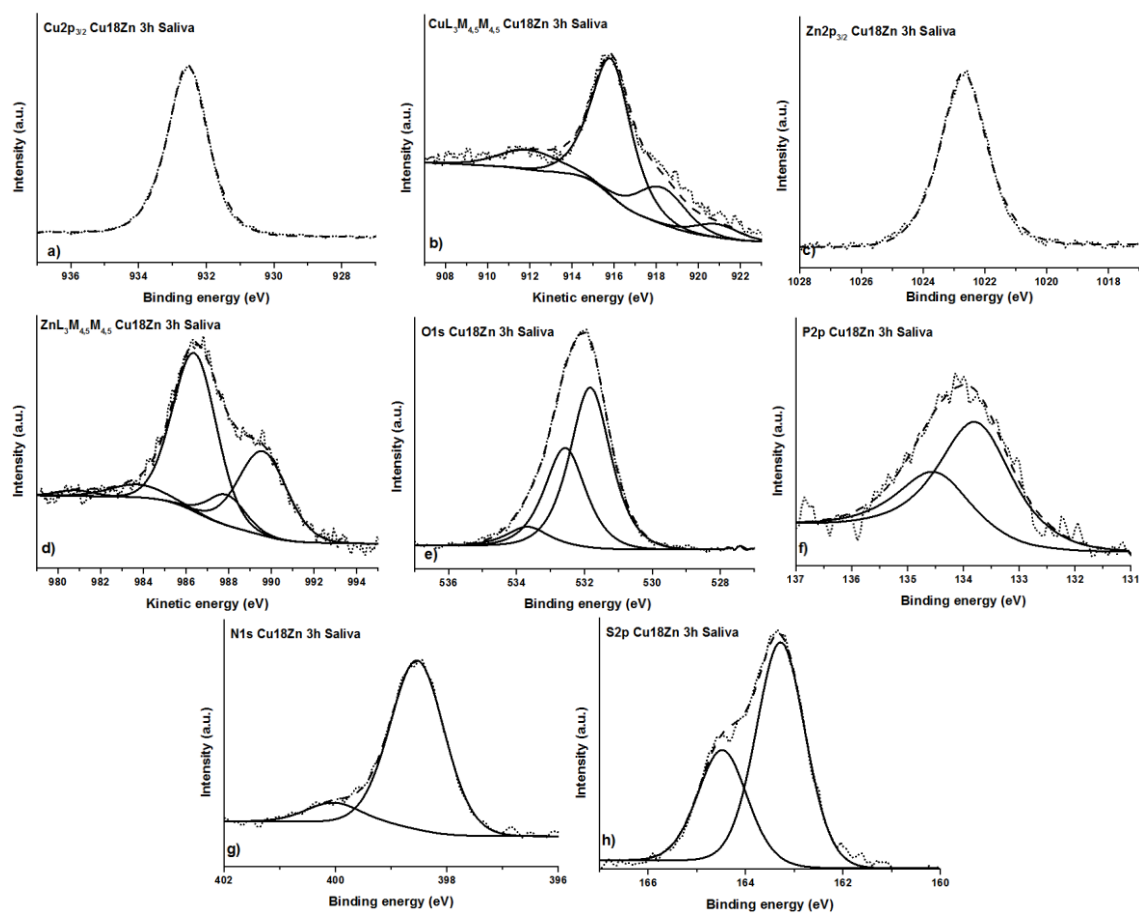


Figure 7. 21: High resolution spectra Cu  $2p_{3/2}$  (a), Zn  $2p_{3/2}$  (b), O 1s (c), Cu  $L_3M_{45}M_{45}$  (d), Zn  $L_3M_{45}M_{45}$  (e), P 2p (f), N 1s (g), and S 2p (h) for the Cu18Zn after 3 hours of contact with the saliva solution.

The Cu  $2p_{3/2}$  signal showed a single peak at 932.5 eV for both short and long contact times. The Cu  $L_3M_{45}M_{45}$  Auger signal exhibited a complex shape composed of four peaks associated to different final states of oxidized copper. No metallic component has been detected in the Auger spectrum even after 1 hour of exposure, hence the thickness of the film formed was greater than the sampling depth of the XPS. The kinetic energy of the main component of the Cu LMM signal was found to be 915.7 eV. This signal could be assigned to copper thiocyanate, CuSCN according to [20]. Moreover, this assignment was also confirmed by the presence of N 1s and S 2p and by their BE values. The N 1s spectra showed two components: 1) the most intense peak at about 398.5 eV might be due to nitrogen in  $SCN^-$  [20 - 22]; 2) the less intense component at about 399.9 eV is probably due to residual urea [23]. The S  $2p_{3/2}$  was found at 163.3 eV and its BE does not change upon exposure time. The position of the signal might be ascribed to a sulfur atom in  $^-S-CN$  [22]. The P 2p showed a well-separated spin orbit doublet; the energy separation between  $2p_{3/2}$  and  $2p_{1/2}$  is 1.2 eV.

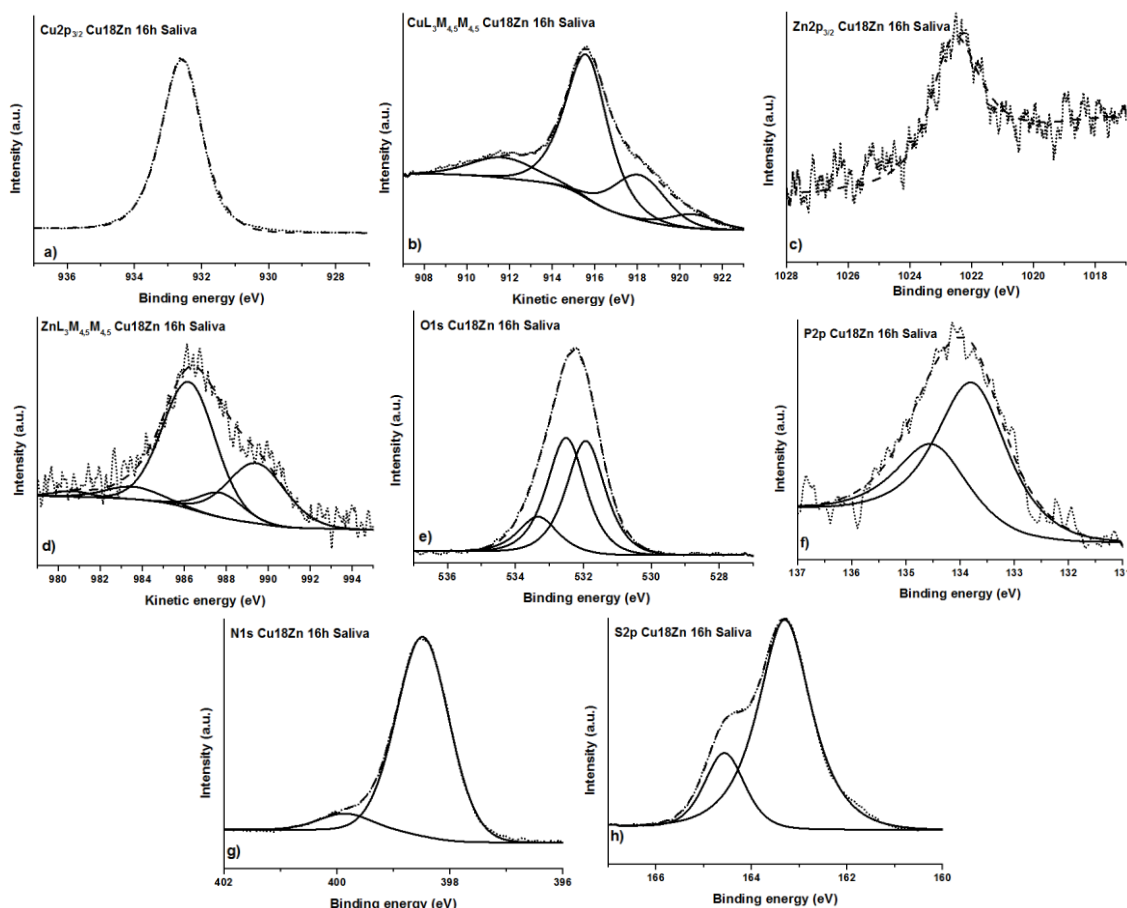


Figure 7. 22: High resolution spectra Cu  $2p_{3/2}$  (a), Zn  $2p_{3/2}$  (b), O  $1s$  (c), Cu  $L_3M_{45}M_{45}$  (d), Zn  $L_3M_{45}M_{45}$  (e), P  $2p$  (f), N  $1s$  (g), and S  $2p$  (h) for the Cu18Zn after 16 hours of contact with the saliva solution.

The Zn  $2p_{3/2}$  showed a single peak at about 1022.7 eV for each exposure time. The related Zn  $L_3M_{45}M_{45}$  Auger signal exhibited a complex shape with five components as a result of different final states; the main peak was located at KE = 986.4 eV. This could be assigned to the presence of oxidized zinc in the form of zinc orthophosphate according to literature [17, 24].

The P  $2p_{3/2}$  signal was found at 133.8 eV and it was likely assigned to the presence of phosphate group according to [17].

Quantitative analysis (Table 7.15) results showed an enrichment in zinc content compared to nominal composition that might be due to the precipitation of zinc – orthophosphate.

Table 7. 14: Average kinetic energy (KE) and FWHM of the most intense peaks of the elements detected on the Cu18Zn after contact with the saliva solution. Standard deviations are given in parentheses.

Cu18Zn	1h		3h		16h	
	BE (eV)	FWHM (eV)	BE (eV)	FWHM (eV)	BE (eV)	FWHM (eV)
<b>Cu</b>	932.5 (0.1)	1.4 (0.1)	932.6 (0.1)	1.4 (0.1)	932.6 (0.1)	1.4 (0.1)
<b>N 1s</b>	398.6 (0.1)	1.1 (0.1)	398.5 (0.1)	1.1 (0.1)	398.5 (0.1)	1.1 (0.1)
<b>N 1s</b>	399.9 (0.2)	1.1 (0.1)	400.1 (0.1)	1.1 (0.1)	399.9 (0.1)	1.1 (0.1)
<b>O 1</b>	531.7 (0.1)	1.6 (0.1)	531.8 (0.1)	1.5 (0.1)	532.0 (0.1)	1.3 (0.1)
<b>O 1s</b>	532.4 (0.2)	1.6 (0.1)	532.6 (0.1)	1.5 (0.1)	532.6 (0.1)	1.3 (0.1)
<b>O 1s</b>	533.4 (0.2)	1.6 (0.1)	533.6 (0.1)	1.5 (0.1)	533.4 (0.1)	1.3 (0.1)
<b>P 2p</b>	133.8 (0.1)	1.5 (0.1)	133.8 (0.1)	1.5 (0.1)	133.8 (0.1)	1.5 (0.1)
<b>P 2p</b>	134.6 (0.1)	1.5 (0.1)	134.6 (0.1)	1.5 (0.1)	134.6 (0.1)	1.5 (0.1)
<b>S 2p SCN</b>	163.3 (0.1)	1.5 (0.1)	163.2 (0.1)	1.5 (0.1)	163.3 (0.1)	1.5 (0.1)
<b>S 2p</b>	164.6 (0.1)	1.5 (0.1)	164.5 (0.1)	1.5 (0.1)	164.5 (0.1)	1.5 (0.1)
<b>Zn 2p</b>	1022.6 (0.1)	1.8 (0.1)	1022.8 (0.1)	1.8 (0.1)	1022.6 (0.1)	1.7 (0.1)
	<b>KE (eV)</b>	<b>FWHM (eV)</b>	<b>KE (eV)</b>	<b>FWHM (eV)</b>	<b>KE (eV)</b>	<b>FWHM (eV)</b>
<b>Cu L<sub>3</sub>M<sub>4,5</sub>M<sub>4,5</sub></b>	915.7 (0.1)	2.5 (0.1)	915.9 (0.1)	2.1 (0.1)	915.7 (0.1)	2.2 (0.1)
<b>Zn L<sub>3</sub>M<sub>4,5</sub>M<sub>4,5</sub></b>	986.3 (0.1)	2.7(0.1)	986.4 (0.1)	2.7 (0.1)	986.4 (0.2)	2.9 (0.1)

Table 7. 15: Results of the quantitative analysis (average at.%) for the Cu18Zn after 1, 3 and 16 hours of immersion in artificial saliva solution. Standard deviations are reported in brackets.

Cu18Zn	1h					3h					
	%at		%at		%at		%at		%at		
<b>C</b>	18 (1)					<b>C</b>	23 (1)				
<b>CuOx</b>	20 (1)	<b>CuOx</b>	24 (1)	<b>Cu tot</b>	73 (3)	<b>CuOx</b>	15 (2)	<b>CuOx</b>	19 (2)	<b>Cu tot</b>	66 (4)
<b>N</b>	15 (1)	<b>N</b>	18 (1)			<b>N</b>	11 (1)	<b>N</b>	14 (1)		
<b>O</b>	18 (2)	<b>O</b>	22 (1)			<b>O</b>	27 (2)	<b>O</b>	35 (3)		
<b>P</b>	3 (1)	<b>P</b>	4 (1)			<b>P</b>	4 (1)	<b>P</b>	5 (1)		
<b>S</b>	18 (1)	<b>S</b>	22 (1)			<b>S</b>	13 (1)	<b>S</b>	17 (1)		
<b>ZnOx</b>	7 (1)	<b>ZnOx</b>	9 (1)	<b>Zn tot</b>	27 (3)	<b>ZnOx</b>	7 (1)	<b>ZnOx</b>	10 (2)	<b>Zn tot</b>	34 (4)
	16h										
	%at		%at		%at						
<b>C</b>	32 (2)										
<b>CuOx</b>	16(2)	<b>CuOx</b>	24 (1)	<b>Cu tot</b>	75 (1)						
<b>N</b>	15 (1)	<b>N</b>	22 (1)								
<b>O</b>	13 (1)	<b>O</b>	19 (2)								
<b>P</b>		<b>P</b>									
<b>S</b>	20 (1)	<b>S</b>	27 (1)								
<b>ZnOx</b>	4 (1)	<b>ZnOx</b>	8 (1)	<b>Zn tot</b>	25 (1)						

## Cu37Zn alloy exposed to artificial saliva solutions

### High-resolution photoelectron and Auger signals

The high-resolution spectra of Cu37Zn acquired after 1, 3 and 16 hours of contact with the artificial saliva solution are shown in Fig. 7.23 to Fig. 7.25. The average BE, KE and FWHM values of the main peaks are given in Table 7.16.

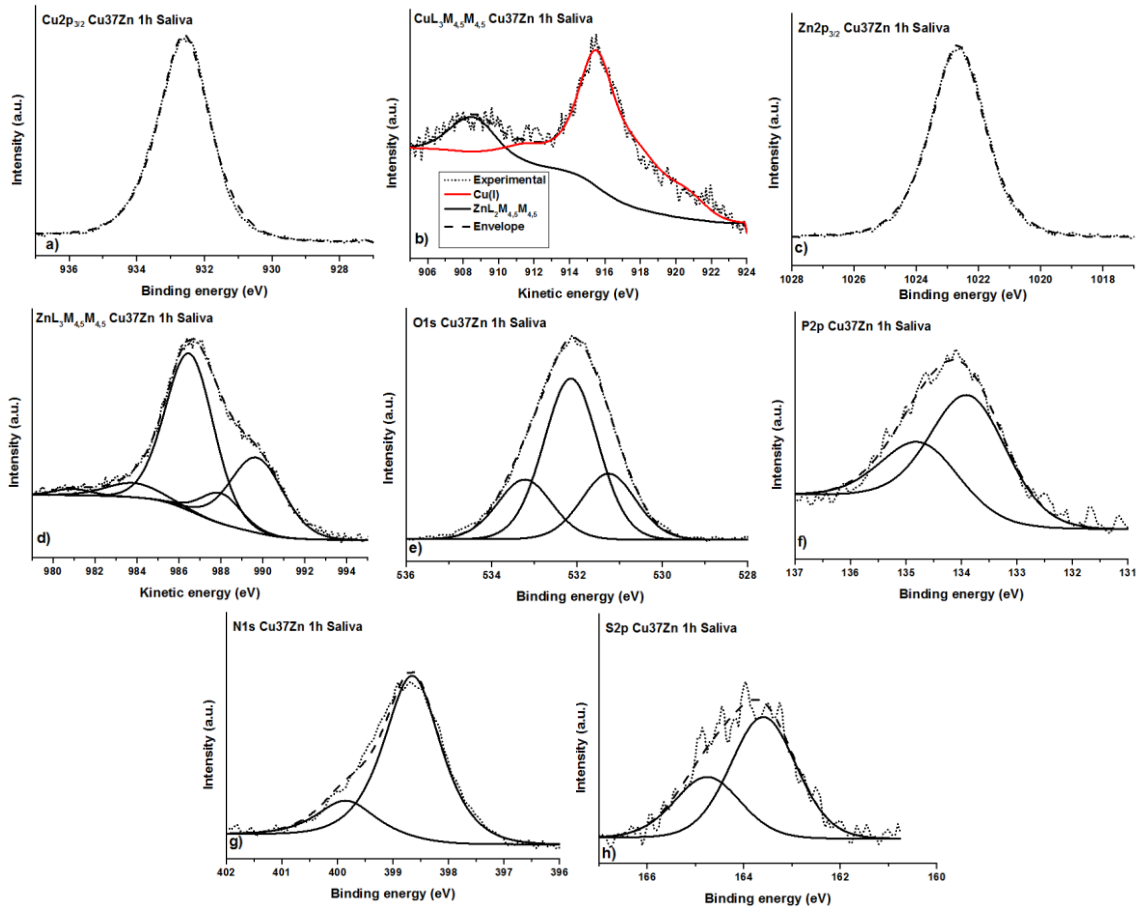


Figure 7. 23: Cu  $2p_{3/2}$  (a), Cu  $L_{31}M_{45}M_{45}$  (b), Zn  $2p_{3/2}$  (c), Zn  $L_{31}M_{45}M_{45}$  (b), O 1s (e), P 2p (f), N 1s (g) and S 2p (g) signals of the Cu37Zn sample after 1 hours of contact with the saliva solution.

The Cu  $2p_{3/2}$  showed also in this case a single peak at 932.6 eV for each time of contact and the relative Cu  $L_{31}M_{45}M_{45}$  Auger signal exhibited a complex shape showing four peak relative to the presence of oxidized copper. The main peak of the copper auger signals was found at about KE = 915.7 eV. This could be assigned to the presence of copper thiocyanate, CuSCN according to [20].

Cu  $L_{31}M_{45}M_{45}$  Auger peak overlaps with the Zn  $L_{2}M_{45}M_{45}$  (black line figures 7.23b – 7.25 b) on the high KE side of the main peak. The higher is the contact time the more visible is the superimposition. This could be explained as a result of the increasing of the zinc content in the film formed on the surface of the alloy.

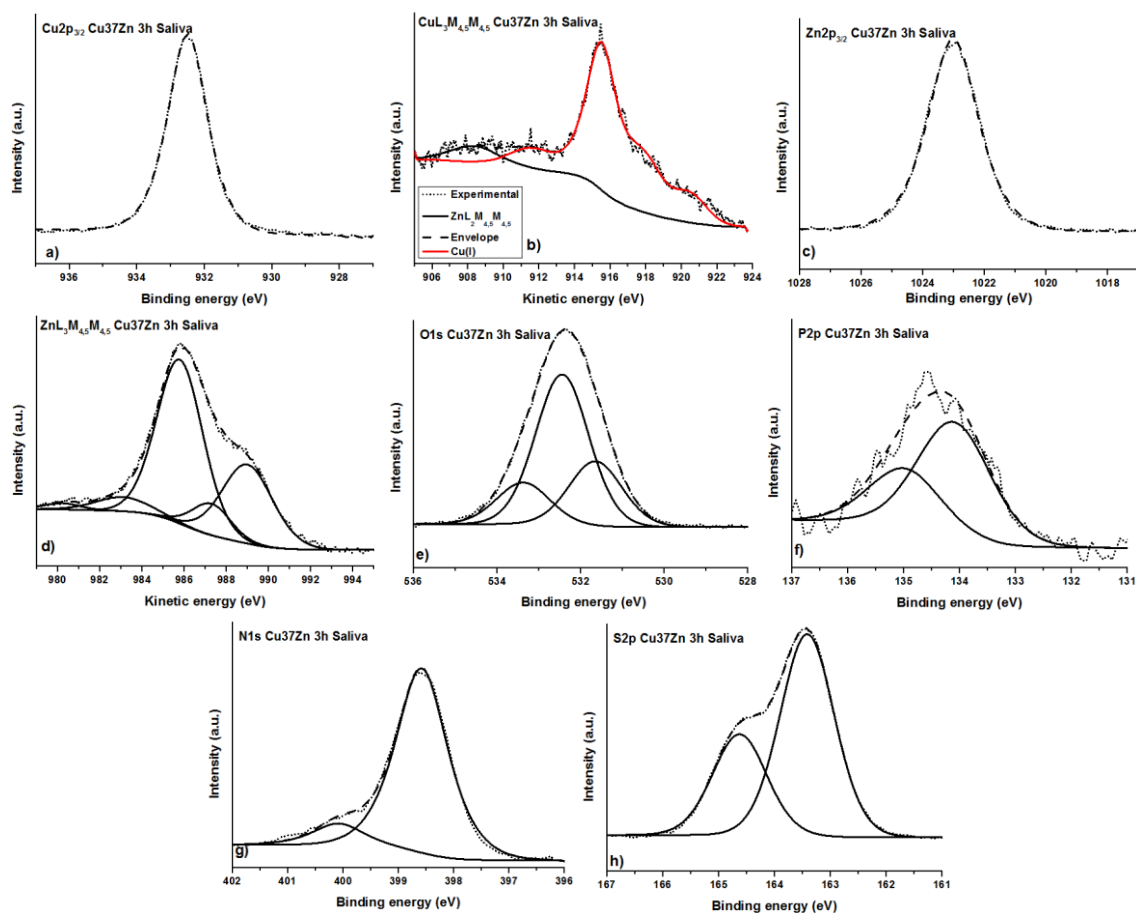


Figure 7. 24: Cu  $2p_{3/2}$  (a), Cu  $L_3M_{45}M_{45}$  (b), Zn  $2p_{3/2}$  (c), Zn  $L_3M_{45}M_{45}$  (b), O  $1s$  (e), P  $2p$  (f), N  $1s$  (g) and S  $2p$  (g) signals of the Cu37Zn sample after 3 hours of contact with the saliva solution.

Also in the case of the Cu37Zn in contact with the saliva solution the N, P and S were revealed. The N  $1s$  spectra showed two components, at 398.5 eV and 400 eV that can be assigned to  $SCN^-$  and residual urea [20 – 23]. The S  $2p$  was found at about 163.3 eV and it might be ascribed to  $^-SCN$  [22].

The Zn  $2p_{3/2}$  showed a single peak at about BE 1022.8 eV. The main signal related to the Zn  $L_3M_{45}M_{45}$  Auger signal peak was located at about KE 986.3 eV. This could be assigned to the presence of inc orthophosphate according to literature [17, 24], as also confirmed by P  $2p_{3/2}$  was found at BE 133.8 – 134.1 eV.

A marked Zn enrichment is observed for the sample exposed for 16 hours to artificial saliva (Table 7.17)

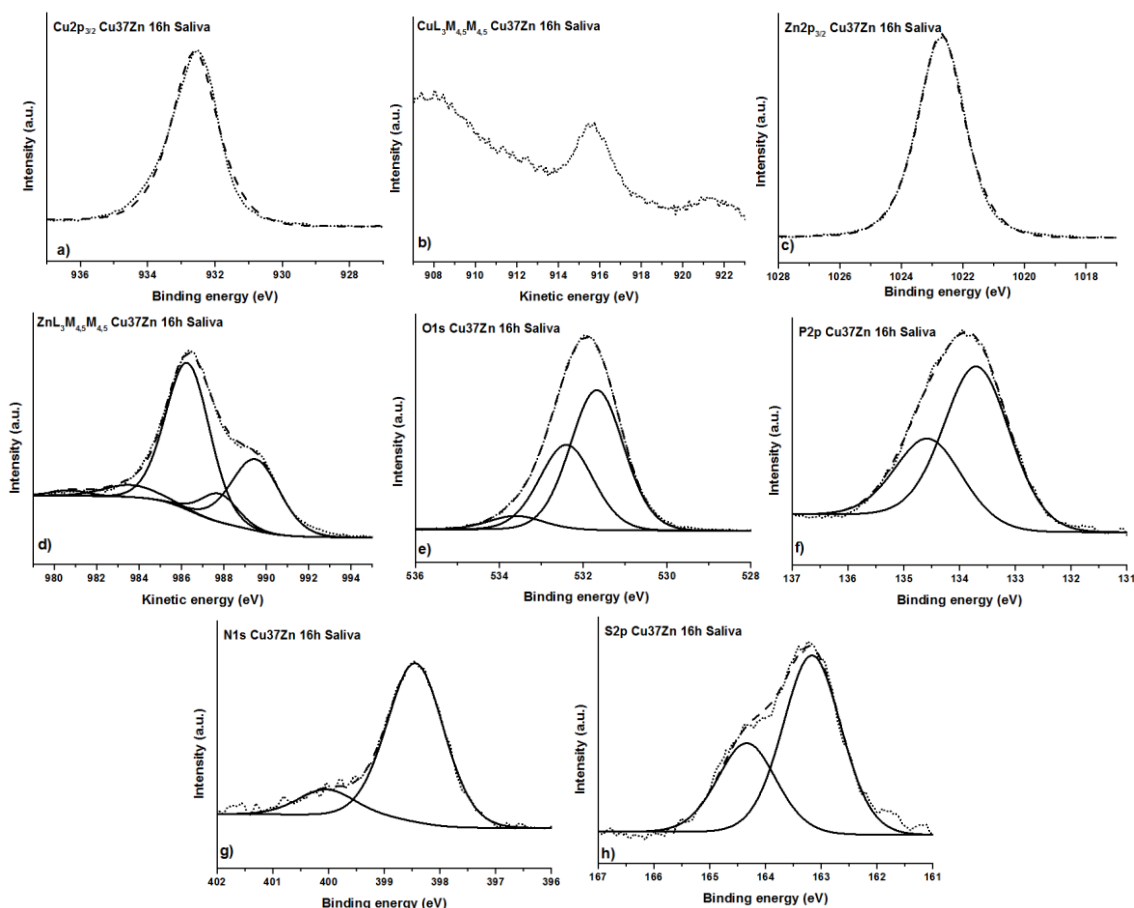


Figure 7. 25: Cu  $2p_{3/2}$  (a), Cu  $L_3M_{45}M_{45}$  (b), Zn  $2p_{3/2}$  (c), Zn  $L_3M_{45}M_{45}$  (b), O  $1s$  (e), P  $2p$  (f), N  $1s$  (g) and S  $2p$  (g) signals of the Cu37Zn sample after 16 hours of contact with the saliva solution.

Table 7. 16: Average kinetic energy (KE) and FWHM of the most intense peaks of the elements detected on the Cu37Zn after contact with the saliva solution. Standard deviations are given in parentheses.

	1h		3h		16h	
	BE (eV)	FWHM (eV)	BE (eV)	FWHM (eV)	BE (eV)	FWHM (eV)
<b>Cu 2p</b>	932.6 (0.1)	1.4 (0.1)	932.5 (0.1)	1.4 (0.1)	932.5 (0.1)	1.4 (0.1)
<b>N 1s</b>	398.6 (0.1)	1.5 (0.1)	398.5 (0.1)	1.5 (0.1)	398.5 (0.1)	1.5 (0.1)
<b>N 1s</b>	399.9 (0.2)	1.5 (0.1)	400.0 (0.1)	1.5 (0.1)	400.1 (0.1)	1.5 (0.1)
<b>O 1s</b>	531.1 (0.2)	1.5 (0.1)	532.1 (0.2)	1.5 (0.1)	532.4 (0.1)	1.5 (0.1)
<b>O 1s</b>	532.3 (0.2)	1.5 (0.1)	532.5 (0.2)	1.5 (0.1)	533.6 (0.1)	1.5 (0.1)
<b>O 1s</b>	533.3 (0.2)	1.5 (0.1)	533.0 (0.1)	1.5 (0.1)	531.7 (0.1)	1.5 (0.1)
<b>P 2p</b>	133.8 (0.2)	1.6 (0.1)	134.1 (0.2)	1.6 (0.1)	133.8 (0.1)	1.6 (0.1)
<b>P 2p</b>	135.1 (0.2)	1.6 (0.1)	134.9 (0.2)	1.6 (0.1)	134.6 (0.1)	1.6 (0.1)
<b>S 2p SCN</b>	163.3 (0.2)	1.5 (0.1)	163.3 (0.1)	1.5 (0.1)	163.2 (0.1)	1.5 (0.1)
<b>S 2p</b>	164.2 (0.2)	1.5 (0.1)	164.4 (0.1)	1.5 (0.1)	164.4 (0.1)	1.5 (0.1)
<b>Zn 2p</b>	1022.9 (0.2)	1.8 (0.1)	1022.8 (0.1)	1.8 (0.1)	1022.7 (0.1)	1.8 (0.1)
	<b>KE (eV)</b>	<b>FWHM (eV)</b>	<b>KE (eV)</b>	<b>FWHM (eV)</b>	<b>KE (eV)</b>	<b>FWHM (eV)</b>
<b>Cu <math>L_3M_{45}M_{45}</math></b>	915.7 (0.1)	2.4 (0.1)	915.5 (0.1)	2.2 (0.1)	915.5 (0.1)	-
<b>Zn <math>L_3M_{45}M_{45}</math></b>	986.3 (0.1)	2.5 (0.1)	986.2 (0.2)	2.5 (0.1)	986.3 (0.1)	2.5 (0.1)

Table 7. 17: Results of the quantitative analysis (average at.%) for the Cu<sub>37</sub>Zn after 1, 3 and 16 hours of immersion in artificial saliva solution. Standard deviations are reported in brackets

Cu <sub>37</sub> Zn	1h					3h					
	%at		%at		%at		%at		%at		
C	13 (1)					C	11 (3)				
CuOx	12 (1)	CuOx	13 (1)	Cu tot	43 (3)	CuOx	11 (3)	CuOx	13 (4)	Cu tot	50 (7)
N	9 (1)	N	10 (2)			N	22 (15)	N	25 (16)		
O	35 (1)	O	40 (4)			O	25 (2)	O	29 (3)		
P	6 (1)	P	7 (1)			P	6 (1)	P	6 (1)		
S	10 (1)	S	11 (1)			S	14 (6)	S	15 (7)		
ZnOx	16 (1)	ZnOx	18 (1)	Zn tot	57 (3)	ZnOx	11 (1)	ZnOx	12 (1)	Zn tot	50 (7)
	16h										
	%at		%at		%at						
C	35 (1)										
CuOx	4 (1)	CuOx	6 (1)	Cu tot	24 (1)						
N	3 (1)	N	5 (1)								
O	32 (3)	O	50 (1)								
P	8 (1)	P	13 (2)								
S	4 (1)	S	6 (1)								
ZnOx	13 (2)	ZnOx	20 (3)	Zn tot	76 (1)						

### Cu<sub>38</sub>Zn<sub>2</sub>Pb alloy exposed to artificial saliva solutions

#### *High-resolution photoelectron and Auger signals*

The high-resolution spectra of Cu<sub>38</sub>Zn<sub>2</sub>Pb alloy acquired after 1, 3 and 16 hours of contact with the artificial saliva solution are shown in Fig. 7.26 to 7.28. The BE, KE and FWHM average values of the peaks are summarized in Table 7.18.

The Cu 2p<sub>3/2</sub> showed also in this case only a single peak at 932.5 eV for each time of contact and the Cu L<sub>3</sub>M<sub>45</sub>M<sub>45</sub> Auger signal exhibited only the components ascribed to CuSCN [20].

The overlap of Cu L<sub>3</sub>M<sub>45</sub>M<sub>45</sub> and Zn L<sub>2</sub>M<sub>45</sub>M<sub>45</sub> is observed also for this sample. (figures 7.26b – 7.28b).

N due to CuSCN and residual urea, P due to phosphate and S ascribed to thiocyanate were revealed.

The Zn 2p<sub>3/2</sub> and Zn L<sub>3</sub>M<sub>45</sub>M<sub>45</sub> signals at BE and KE values typical for zinc orthophosphate are detected [17, 24], together with the phosphorus signals P 2p<sub>3/2</sub> due to phosphate.

Pb 4f<sub>7/2</sub> was found at about BE 138.8 eV and it can be assigned to lead oxides [18, 19].



Table 7. 18: Average kinetic energy (KE) and FWHM of the most intense peaks of the elements detected on the Cu38Zn2Pb after contact with the saliva solution. Standard deviations are given in parentheses.

CuZnPb2	1h		3h		16h	
	BE (eV)	FWHM (eV)	BE (eV)	FWHM (eV)	BE (eV)	FWHM (eV)
<b>Cu 2p</b>	932.5 (0.1)	1.4 (0.1)	932.5 (0.1)	1.4 (0.1)	932.5 (0.1)	1.5 (0.1)
<b>N 1s</b>	398.5 (0.1)	1.1 (0.1)	398.4 (0.1)	1.2 (0.1)	398.4 (0.1)	1.1 (0.1)
<b>N 1s</b>	399.7 (0.1)	1.1 (0.1)	400.3 (0.1)	1.2 (0.1)	400.0 (0.1)	1.1 (0.1)
<b>O 1s</b>	531.5 (0.1)	1.5 (0.1)	531.7 (0.1)	1.5 (0.1)	531.5 (0.1)	1.5 (0.1)
<b>O 1s</b>	532.3 (0.1)	1.5 (0.1)	532.6 (0.1)	1.5 (0.1)	532.2 (0.1)	1.5 (0.1)
<b>O 1s</b>	533.5 (0.1)	1.5 (0.1)	533.8 (0.1)	1.5 (0.1)	533.2 (0.1)	1.5 (0.1)
<b>Pb 4f</b>	138.8 (0.1)	1.7 (0.1)	138.6 (0.1)	1.6 (0.1)	138.8 (0.1)	1.6 (0.1)
<b>Pb 4f</b>	143.9 (0.1)	1.7 (0.1)	143.8 (0.1)	1.6 (0.1)	143.8 (0.1)	1.6 (0.1)
<b>P 2p</b>	133.9 (0.1)	1.5 (0.1)	134.2 (0.1)	1.5 (0.1)	133.8 (0.1)	1.5 (0.1)
<b>P 2p</b>	134.7 (0.1)	1.5 (0.1)	135.1 (0.1)	1.5 (0.1)	134.5 (0.1)	1.5 (0.1)
<b>S 2p SCN</b>	163.3 (0.1)	1.1 (0.1)	163.1 (0.1)	1.4 (0.1)	163.1 (0.1)	1.3 (0.1)
<b>S 2p</b>	164.5 (0.1)	1.1 (0.1)	164.3 (0.1)	1.4 (0.1)	164.3 (0.1)	1.3 (0.1)
<b>Zn 2p</b>	1022.7 (0.1)	1.8 (0.1)	1022.7 (0.1)	1.8 (0.1)	1022.6 (0.1)	1.8 (0.1)
	<b>KE (eV)</b>	<b>FWHM (eV)</b>	<b>KE (eV)</b>	<b>FWHM (eV)</b>	<b>KE (eV)</b>	<b>FWHM (eV)</b>
<b>Cu L<sub>3</sub>M<sub>4,5</sub>M<sub>4,5</sub></b>	915.6 (0.1)	2.1 (0.1)	915.8 (0.1)	2.1 (0.1)	915.7 (0.1)	2.5 (0.1)
<b>Zn L<sub>3</sub>M<sub>4,5</sub>M<sub>4,5</sub></b>	986.3 (0.1)	2.5 (0.1)	986.4 (0.1)	2.5 (0.1)	986.5 (0.1)	2.5 (0.1)

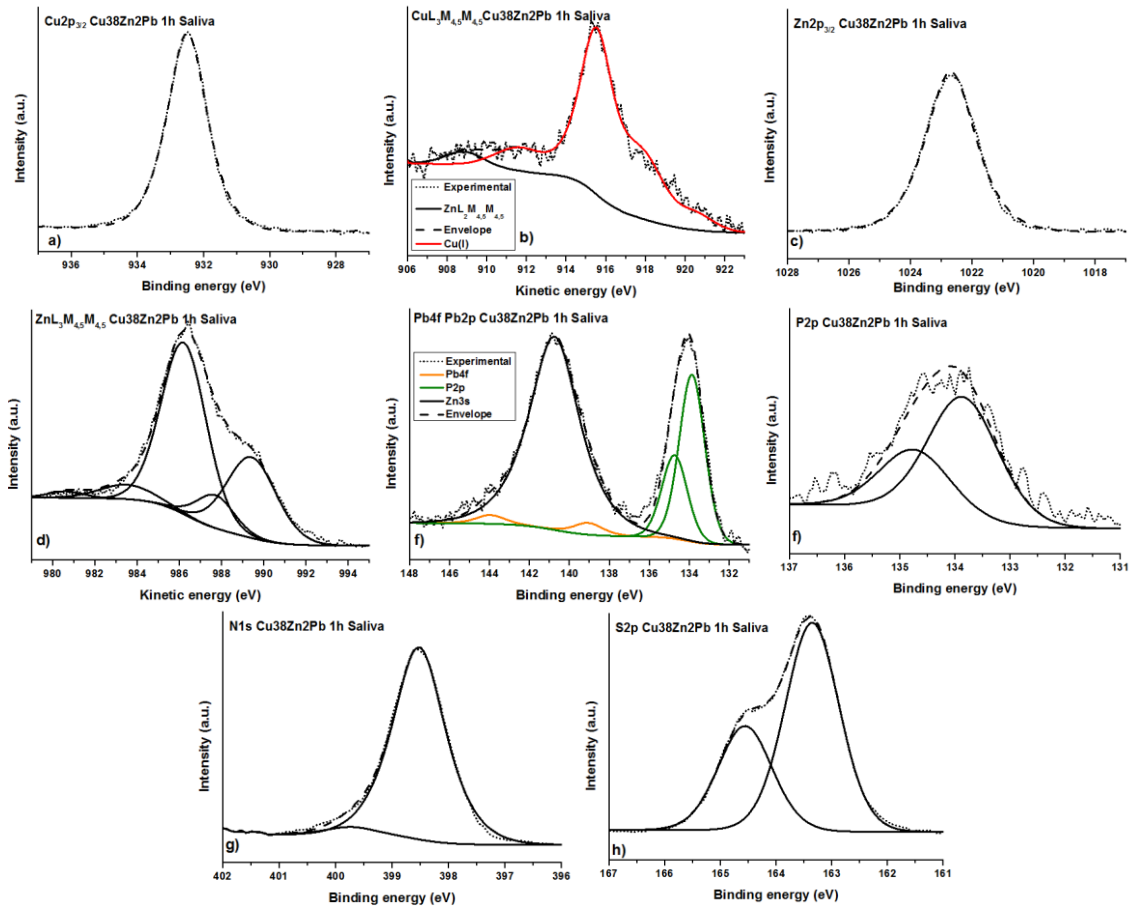


Figure 7. 26: The Cu 2p<sub>3/2</sub> (a), Cu L<sub>3</sub>M<sub>4,5</sub>M<sub>4,5</sub> (b), Zn 2p<sub>3/2</sub> (c), Zn L<sub>3</sub>M<sub>4,5</sub>M<sub>4,5</sub> (b), O 1s (e), Pb 4f together with P 2p (f), N 1s (g) and S 2p (g) for the Cu38Zn2Pb after 1 hours of contact with the saliva solution are shown.

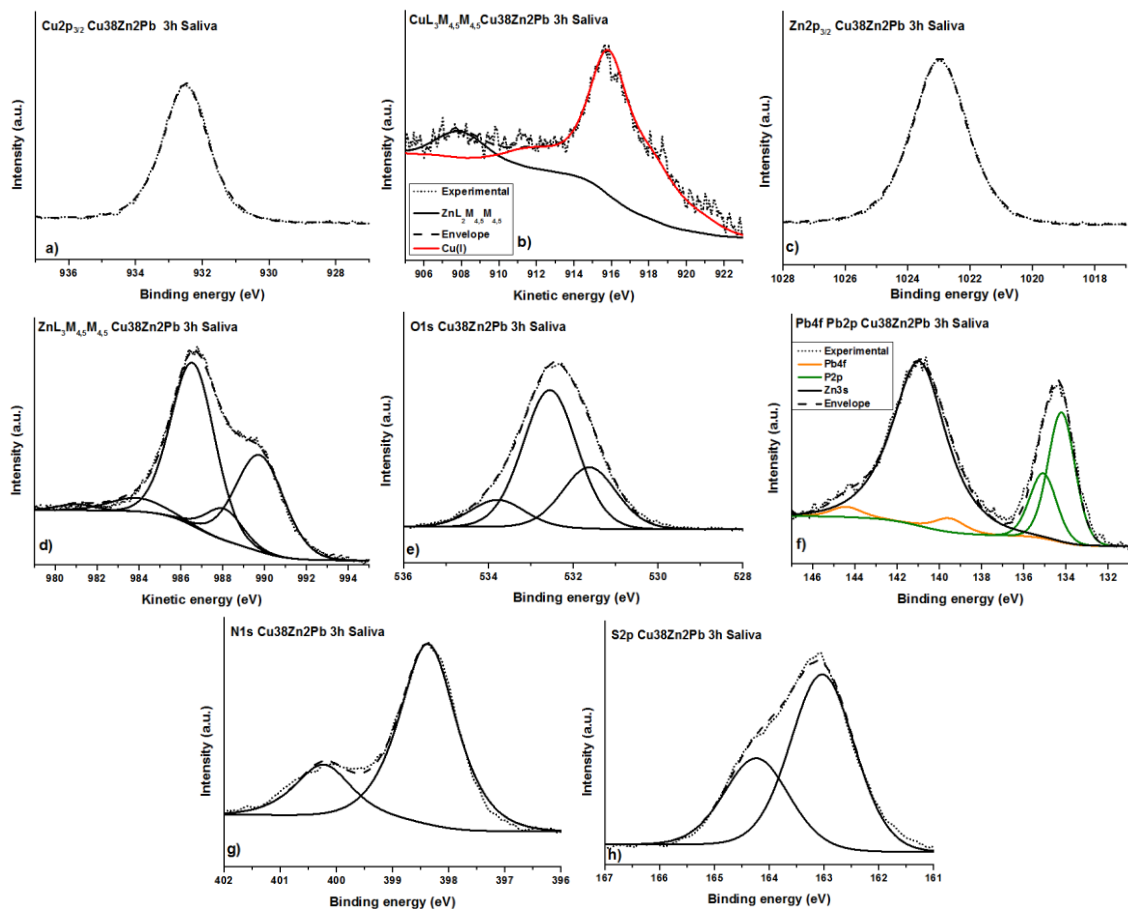


Figure 7. 27: Cu  $2p_{3/2}$  (a), Cu  $L_3M_{45}M_{45}$  (b), Zn  $2p_{3/2}$  (c), Zn  $L_3M_{45}M_{45}$  (b), O  $1s$  (e), Pb  $4f$  together with P  $2p$  (f), N  $1s$  (g) and S  $2p$  (g) signals of the Cu<sub>38</sub>Zn<sub>2</sub>Pb sample after 3 hours of contact with the saliva solution.

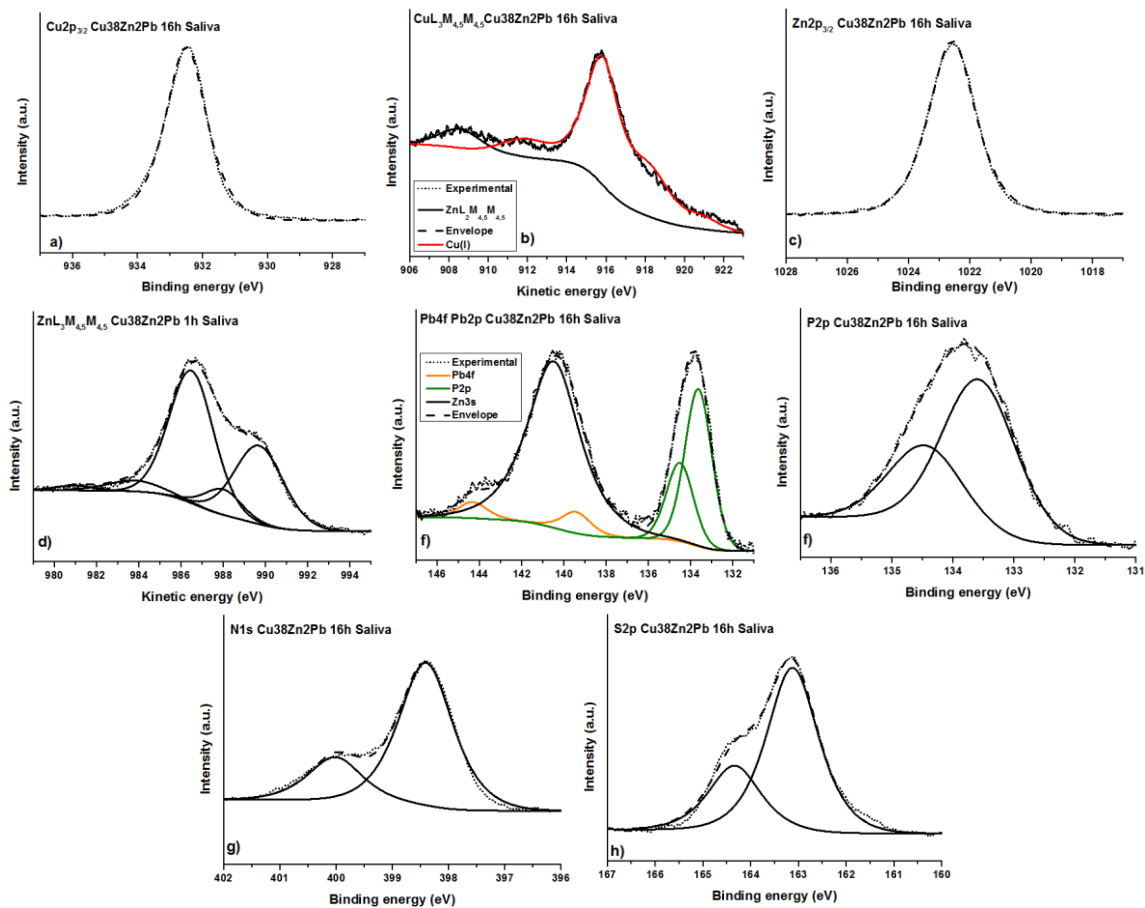


Figure 7. 28: Cu 2p<sub>3/2</sub> (a), Cu L<sub>3</sub>M<sub>45</sub>M<sub>45</sub> (b), Zn 2p<sub>3/2</sub> (c), Zn L<sub>3</sub>M<sub>45</sub>M<sub>45</sub> (b), O 1s (e), Pb 4f together with P 2p (f), N 1s (g) and S 2p (g) signals of the Cu<sub>38</sub>Zn<sub>2</sub>Pb sample after 16 hours of contact with the saliva solution.

Table 7. 19: Results of the quantitative analysis (average at.%) for the Cu18Zn after 1, 3 and 16hours of immersion in artificial saliva solution. Standard deviations are reported in brackets

	1h					3h					
	%at		%at		%at	%at		%at		%at	
<b>C</b>	8 (1)					<b>C</b>	21 (1)				
<b>CuOx</b>	13 (1)	<b>CuOx</b>	14 (1)	<b>Cu tot</b>	63 (1)	<b>CuOx</b>	5 (1)	<b>CuOx</b>	6 (1)	<b>Cu tot</b>	47 (7)
<b>N</b>	9 (1)	<b>N</b>	10 (1)			<b>N</b>	6 (1)	<b>N</b>	8 (1)		
<b>O</b>	44 (2)	<b>O</b>	47 (1)			<b>O</b>	52 (3)	<b>O</b>	66 (2)		
<b>PbOx</b>	0.01 (0.005)	<b>PbOx</b>	0.02 (0.005)	<b>Pb tot</b>	0.1 (0.05)	<b>PbOx</b>	0.05 (0.01)	<b>PbOx</b>	0.06 (0.01)	<b>Pb tot</b>	0.3 (0.1)
<b>P</b>	4	<b>P</b>	5			<b>P</b>	4 (1)	<b>P</b>	5 (1)		
<b>S</b>	15 (2)	<b>S</b>	16 (1)			<b>S</b>	7 (1)	<b>S</b>	9 (1)		
<b>ZnOx</b>	7 (1)	<b>ZnOx</b>	8 (1)	<b>Zn tot</b>	37 (1)	<b>ZnOx</b>	5 (1)	<b>ZnOx</b>	6 (1)	<b>Zn tot</b>	52 (7)
	16h										
	%at		%at		%at						
<b>C</b>	21 (3)										
<b>CuOx</b>	5 (1)	<b>CuOx</b>	6 (1)	<b>Cu tot</b>	47 (7)						
<b>N</b>	6 (1)	<b>N</b>	8 (1)								
<b>O</b>	52 (3)	<b>O</b>	66 (3)								
<b>PbOx</b>	0.03 (0.005)	<b>PbOx</b>	0.04 (0.01)	<b>Pb tot</b>	0.4 (0.05)						
<b>P</b>	4 (1)	<b>P</b>	5 (1)								
<b>S</b>	7 (1)	<b>S</b>	9 (1)								
<b>ZnOx</b>	5 (1)	<b>ZnOx</b>	6 (1)	<b>Zn tot</b>	52 (7)						

Unlike the case of the buffer solution where the metallic components are still detectable after 16 hours of exposure, No signals from the Cu (0) and Zn (0) were revealed, indicating that in saliva solution a thick film is formed on the surface.

In Figure 7.29 the Cu  $L_{3}M_{45}M_{45}$  and Zn  $L_{3}M_{45}M_{45}$  Auger peaks of Cu37Zn alloy in the mechanically polished state and after 16 hours of contact with the saliva solution and to the pH = 7 phosphate buffer solution are shown.

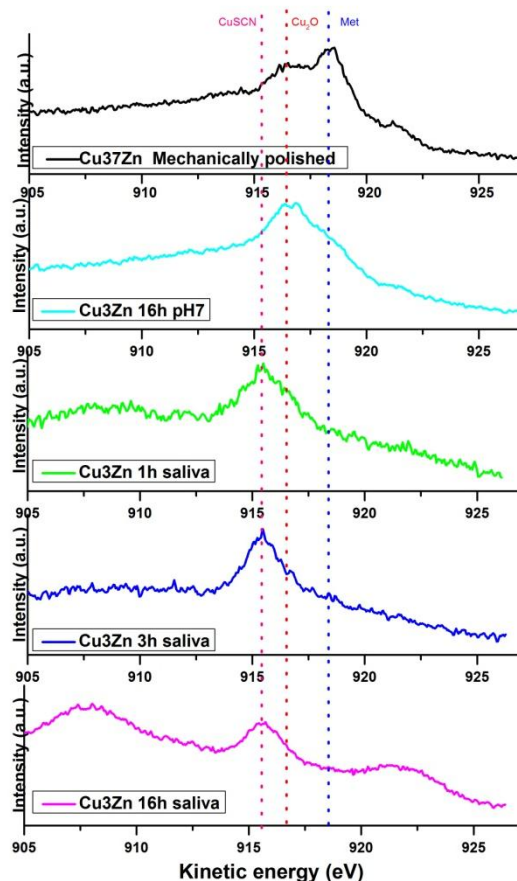


Figure 7. 29: Cu  $L_3M_{45}M_{45}$  Auger signals of Cu37Zn after mechanical polishing procedure after 16 hours of contact with the buffer solution and after 1, 3 and 16 h of contact with the saliva solution.

### 7.3.4 Scanning electron microscopy

The surface morphology of the brass alloy in contact with the aging solution was investigated by Scanning Electron Microscopy analysis. The surface of the brass samples was also observed before the contact with the solution to compare the images. As an example the SEM images acquired on the Cu18Zn (figure 7.30) before and after 16 hours of exposure to the buffer and the artificial saliva solutions are reported. The surface before the contact showed thin scratches due to the mechanical polishing and no particles were found on it. Some white spots probably due to a residue of the diamond paste used in the last step of the polishing procedure were observed. The diamond paste consists of diamond particles with an average size of 0.25  $\mu\text{m}$ .

After the contact with the buffer solution several black holes appeared at the surface of the alloy and they might be due to a localized corrosion or dezincification areas. The surface of the Cu18Zn after the exposure to the saliva solution was homogeneously covered by particles of about 200 nm and no scratches from the surface of the metal were detectable, on the contrary the scratches were still revealed after 16 hours of contact with the buffer solution.

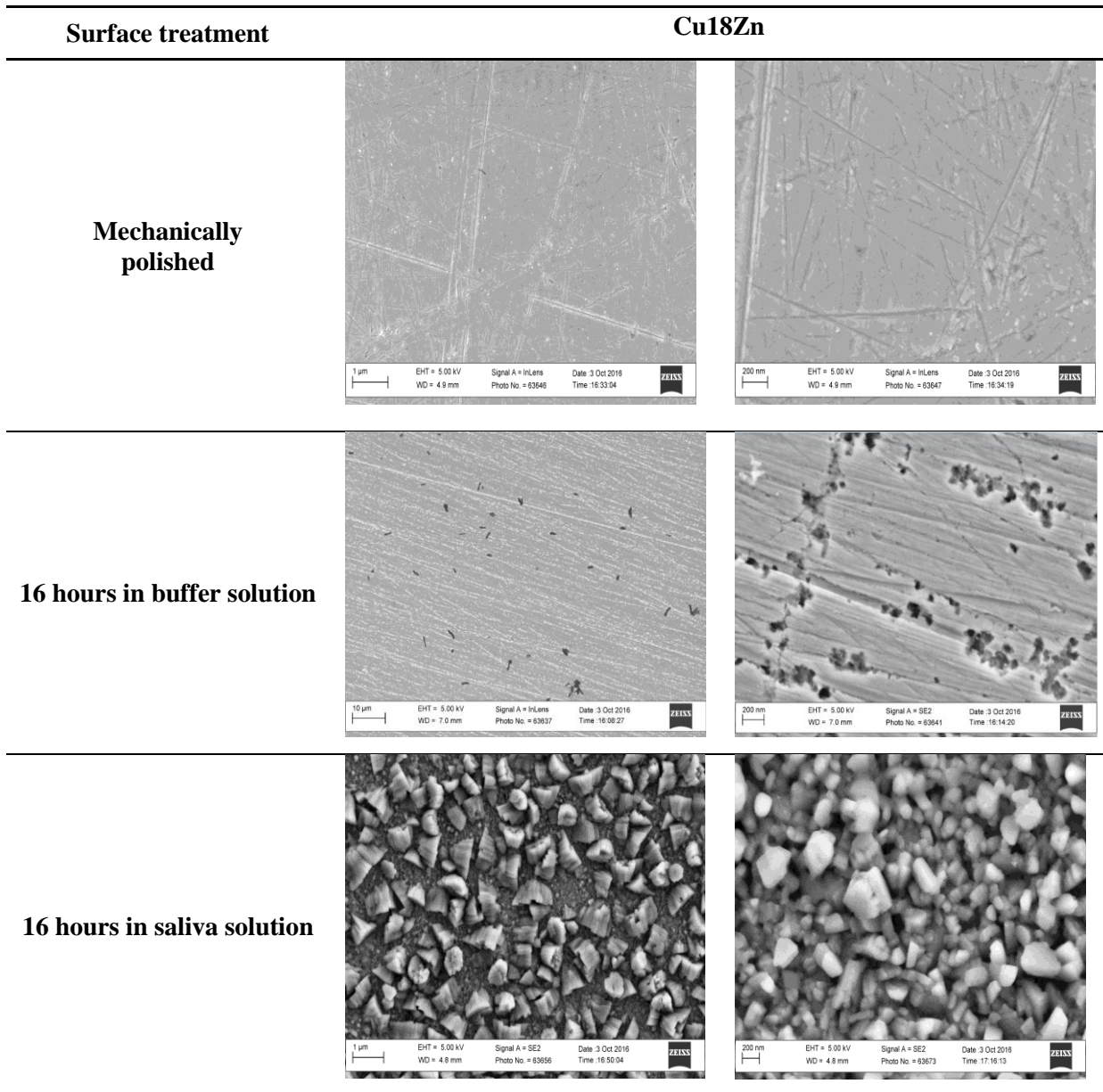


Figure 7. 30: SEM images acquired on the Cu18Zn alloy after the mechanical polishing procedure, after 16 hours of exposure to the phosphate buffer solution and to the artificial saliva solution.

The surface of the Cu37Zn was also investigated by SEM analysis and the images are shown in figure 7.31. As in the case of the Cu18Zn the surface before the contact showed slight scratches due to the grinding procedure and some white spots also were visible on the samples. After the immersion in the buffer solution pH7 the surface appeared different respect to the Cu18Zn. The black areas appeared as spots rather than holes and are clearly smaller than in the case of the Cu18Zn.

After 16 hours of exposure to the saliva solution, particles covered the surface, their size is similar compared to those found on the Cu18Zn but seemed more irregular. No scratches were observe and hence the particles layer was supposedly rather deep.

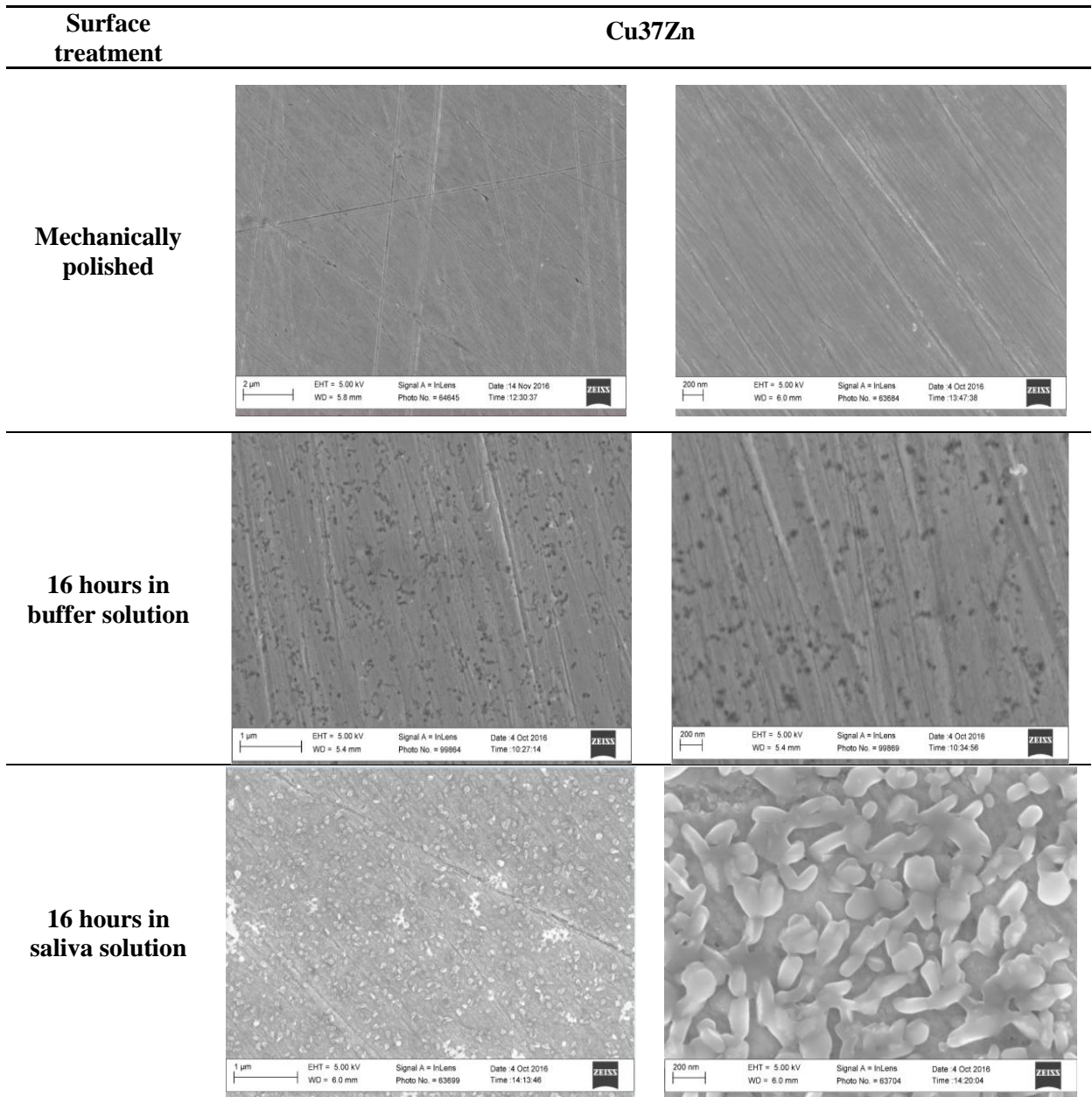


Figure 7. 31: SEM images acquired on the Cu37Zn alloy after the mechanical polishing, after 16 hours of exposure to the phosphate buffer solution and to the artificial saliva solution.

As for the Cu37Zn also for the Cu38Pb2 (figure 7.32) black spots appeared after 16 hours of exposure to the buffer solution. Particles of different size covered the surface and also in this case no scratches were visible after the immersion in saliva solution.

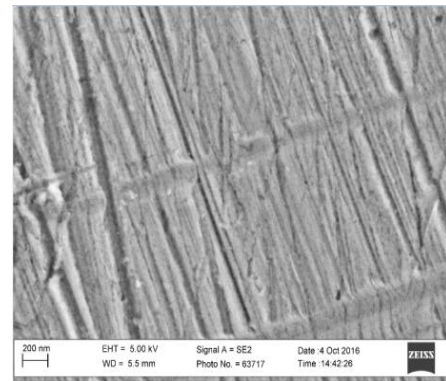
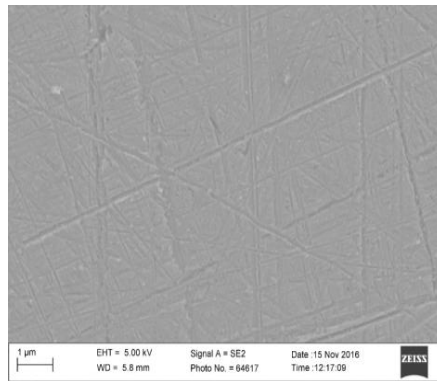
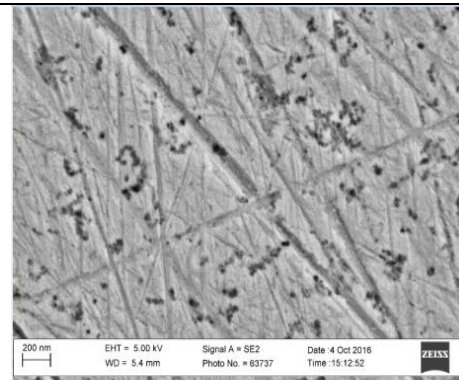
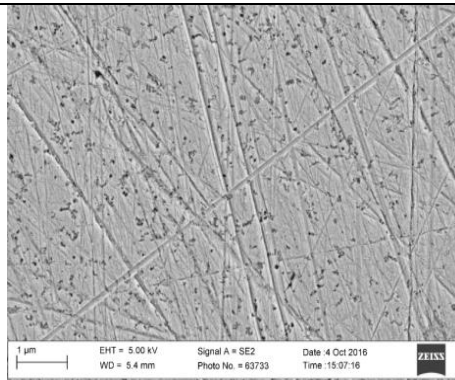
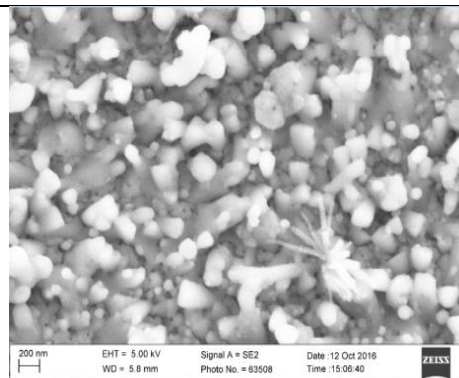
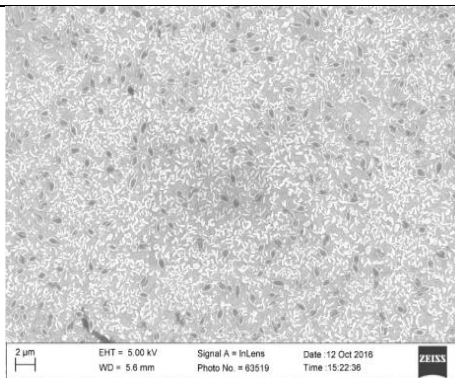
**Mechanically  
polished****16 hours in  
buffer solution****16 hours in saliva  
solution**

Figure 7. 32: SEM images acquired on the Cu<sub>38</sub>Zn<sub>2</sub>Pb alloy after the mechanical polishing, after 16 hours of exposure to the phosphate buffer solution and to the artificial saliva solution.

For comparison, also the SEM images of pure copper in contact with the saliva solution (Fig. 7.33) have been acquired: they show a surface covered by crystals that are bigger and less homogeneous in size and shape than in the case of copper – zinc alloys (Fig 7.30 – 7.32). This could be due to the absence of zinc phosphate in the surface film that might influence the growth of the particles.



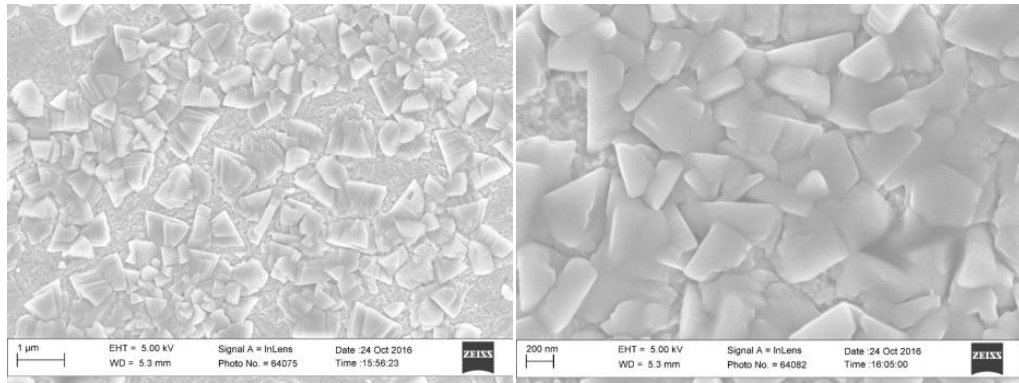


Figure 7. 33: SEM images acquired on the pure copper after contact with the saliva solution.

The surface morphology of Cu<sub>18</sub>Zn and Cu<sub>37</sub>Zn were also investigated after 16 hours of exposure to a pure KSCN solution; the concentration of the KSCN was the same as in saliva solution. The images are shown in figures 7.30 (Cu<sub>18</sub>Zn) and 7.31 (Cu<sub>37</sub>Zn). The particles that covered the surface were homogeneously distributed at the surface and no scratches were observed as in the case of the saliva solution, that supported the hypothesis of a thick layer. The crystals are different from the case of the saliva solution since they were bigger and had a less homogeneous size and shape distributions.

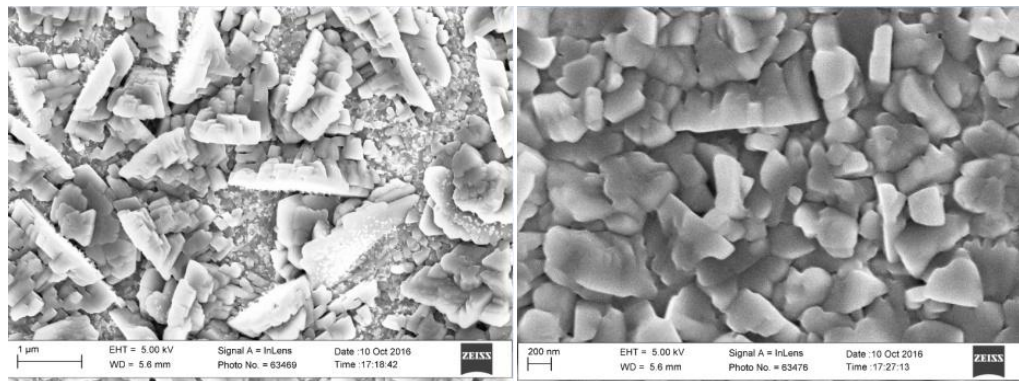


Figure 7. 34: SEM images acquired on the Cu<sub>18</sub>Zn alloy after the contact with the KSCN solution.

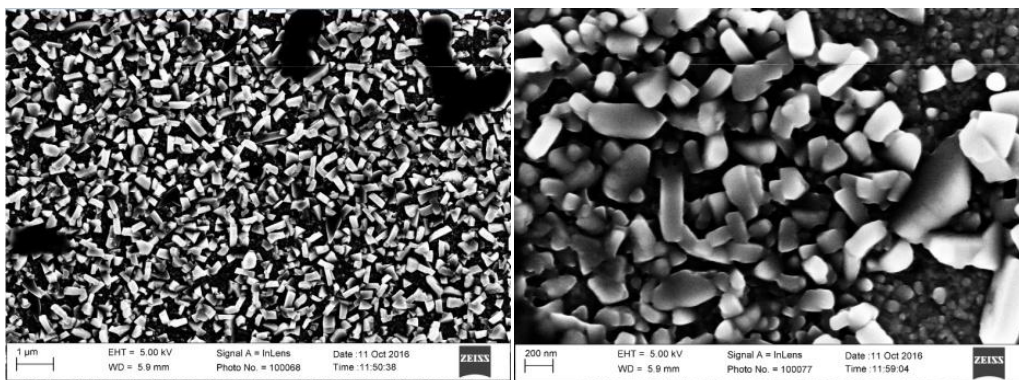


Figure 7. 35: SEM images acquired on the Cu<sub>37</sub>Zn alloy after the contact with the KSCN solution.

## 7.4 Discussion

### 7.4.1 Influence of the zinc content in brass alloys

The open circuit potentials immediately after immersion of the samples into the electrolyte ( $t_0$  Tables 7.1 and 7.2) were more positive in the case of pure copper than those measured for the brass alloys both in artificial saliva and in phosphate buffer solution. The small standard deviations indicate that the experimental procedure of sample preparation was controlled and reproducible.

The *steady-state open circuit potential* measured after 16 h of immersion in artificial saliva decreases with increasing zinc content (Fig. 7.36a). In the buffer solution pH 7 (Fig. 7.36b) the influence of the zinc content is much less pronounced, in agreement with literature [2] where similar results were observed for brass alloys with zinc content ranging from 5.5 to 38 % in 0.05 M  $\text{Na}_2\text{SO}_4$  solution.

With increasing zinc content in the alloy the *polarization resistance*  $R_p$  decreases slightly for the artificial saliva (Fig. 7.37a) and the buffer solution (Fig. 7.37b). Literature work reports a slight increase of the corrosion current density in 0.05 M  $\text{Na}_2\text{SO}_4$  from  $0.5 \mu\text{A}/\text{cm}^2$  for pure copper to  $2 \mu\text{A}/\text{cm}^2$  and for brass CuZn38 [2]. The results of this investigation (buffer solution pH 7, Fig. 7.36b) are in good agreement with the literature.

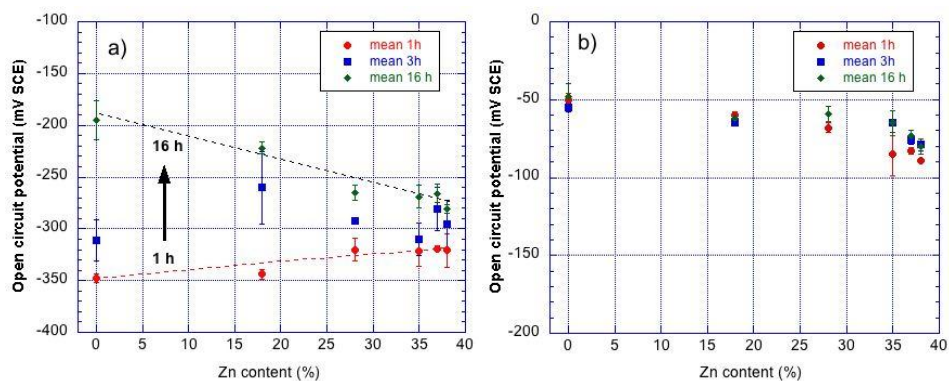


Figure 7. 36: Influence of the zinc content on the open circuit potentials measured after 1h, 3h and 16 h of immersion in a) artificial saliva, b) phosphate buffer

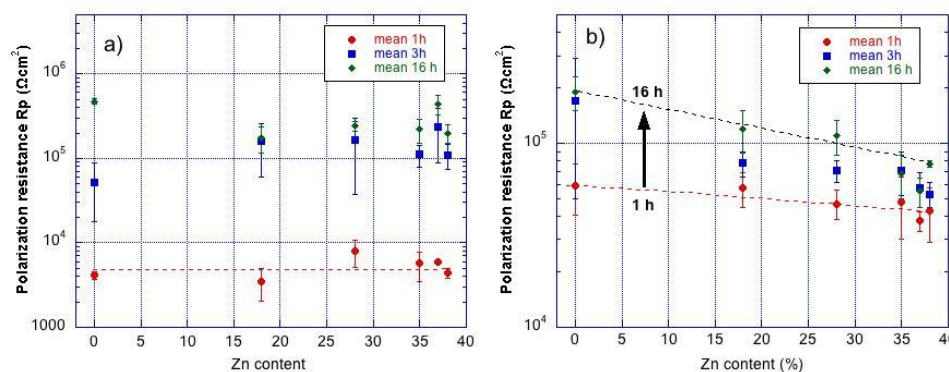


Figure 7. 37: Variation of the specific polarization resistance  $R_p$  with time of immersion for the different brass alloys in a) artificial saliva, b) phosphate buffer pH 7

The *surface films formed* in the two electrolytes are completely different:

In the *artificial saliva solution* a thick layer with many crystallites is formed for all the studied alloys as documented by the SEM images (Fig 7.30 – 7.32). In the X-ray induced Auger spectra of both Cu LMM and Zn LMM no signals from the metal could be detected for all the alloys, confirming a thick film. The binding energies of the elements composing the film remained constant (within  $\pm 0.1$  eV) irrespective of the zinc content in the alloy. The film composition instead was changing with the zinc content in the alloy. As is shown in Fig. 7.38a, a clear increase of the Zn (II) percentage and a decrease of the Cu (I) percentage in the film was found (Tables 7.15, 7.17, 7.19).

In the case of the alloys in contact with the phosphate buffer solution the oxide layer formed after the contact is very thin. The surface after the contact with the pH = 7 solution (Fig. 7.30 to 7.32) was similar to the surface of the mechanically polished samples, few scratches due to the mechanical polishing procedure were visible in both case and no crystals were found. In figure 7.38b is reported the Zn (II) and the Cu (I) %at in the buffer solution. Each samples showed a Zn( II) content always higher than the Cu (I) percentage in the film composition. Unlike the case of the saliva solution a slight increase of the Zn (II) percentage and a decrease of the Cu (I) percentage in the film was found (see also tables with the film composition). However, in each case the Cu(I) content is always the predominant specie respect to the Zn (II).

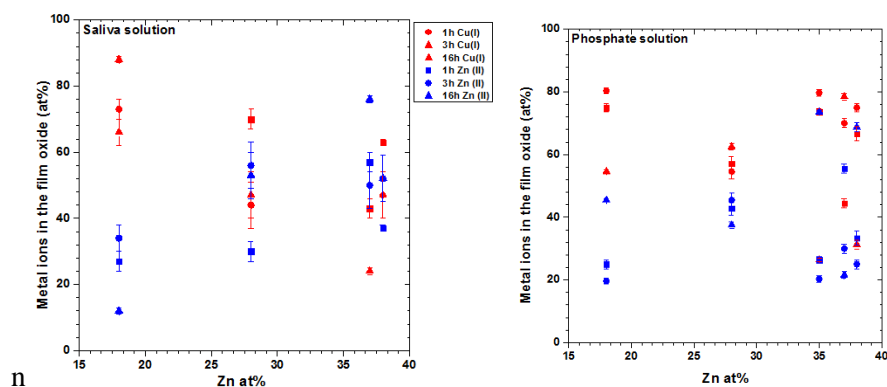


Figure 7. 38: Variation of the metal ion content in the surface film formed after exposure to the solutions. a) artificial saliva and b) phosphate buffer.

#### 7.4.2 Influence of exposure time

Prolonged exposure time leads to a progressive ennoblement of the OCP in artificial saliva (Fig. 7.1, 7.32a) and to a minor extent also in phosphate buffer pH 7 (Fig. 7.2, 7.32b). The same trend is reported in literature for brass alloys in Na<sub>2</sub>SO<sub>4</sub> solutions [2] and for brass in pH = 7 buffer solution [8]. The polarization resistance R<sub>p</sub> increases with exposure time for all alloys in artificial saliva, an increase by about a factor 50 – 100 was found following 16h exposure (Fig. 7.37). In phosphate buffer solution (Fig. 7.37b) the increase of R<sub>p</sub> was only a factor of 3 when examining the alloys with low Zn content and a factor of to 2 with high zinc-content alloys. This might be explained with the formation of a surface film different in the two electrolytes (see below).

### 7.4.3 Mechanism of brass dissolution – influence of surface films

Based on the plots  $\log R_p$  vs OCP (Fig. 7.39) more information on the rate-determining step governing the corrosion of copper and brass alloys in the two different neutral electrolytes here tested can be obtained. In the scatter plots, all individual points of the different alloys after different exposure times (1, 3 and 16 h) are shown; for each alloy 9 individual points (3 exposure times x 3 replica) are presented.

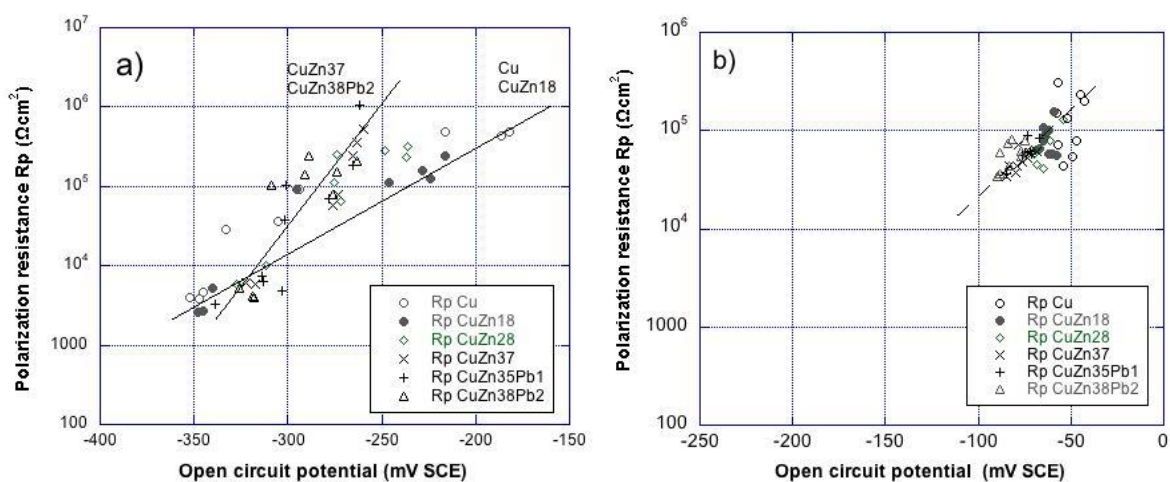


Figure 7. 39: Diagram  $\log R_p$  vs OCP for brass alloys (18 – 37 wt.% Zn) exposed for 1, 3 and 16 hours in a) artificial saliva, b) diluted buffer solution pH 7. Same potential axes are used in order to facilitate the comparison of the two sets of data.

#### *Artificial saliva solution*

For artificial saliva (Fig. 7.39a), the points group to different trend-lines: pure copper and Cu18Zn fall on a line with a slope of ca. 60 mV/dec whereas the zinc-rich alloys fall on a steeper trend-line with a slope of ca. 30 mV/dec. The brass alloy Cu28Zn is located between the two lines. A first information can be obtained from the graph (Fig. 7.39a): the dissolution of brass in artificial saliva is under anodic control (positive slope of  $\Delta \log R_p / \Delta OCP$ ). Moreover, as the slope varies with the zinc content, it can be concluded that the zinc content of the alloys influences the rate-determining step and – as seen above – the corrosion behaviour. The curve fitting of the X-ray induced Auger spectra Cu  $L_{3}M_{45}M_{45}$  and Zn  $L_{3}M_{45}M_{45}$  of Cu37Zn (Fig 7.23 – 7.25) substantiates this assumption since after 16 hours of exposure to the saliva solution no metallic component of both copper and zinc could be revealed leading to the conclusion that a thick film is formed on the surface. Based on the Wagner chemical state plot (Fig. 7.40), a two dimensional representation of XAES kinetic energy vs XPS binding energy of a given element [25, 26], zinc phosphate  $Zn_3(PO_4)_2$  and copper thiocyanate CuSCN are identified as main compounds of the protective film. The presence of zinc phosphate in the film might explain the influence of the zinc content. In addition, the formation of such a thick protective surface film might justify the marked increase of the polarization resistance  $R_p$  upon time in artificial saliva (Fig. 7.37a).

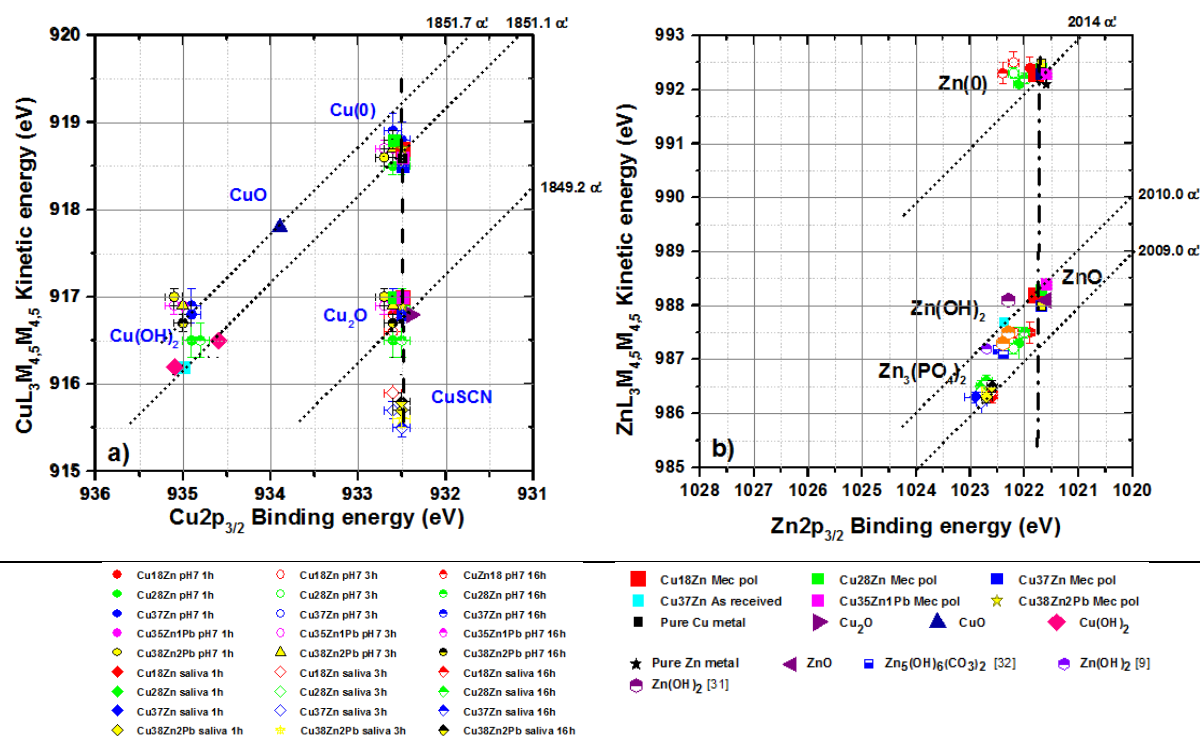


Figure 7.40: Wagner chemical state plots of copper (a) and zinc (b). The BE and KE of the photoelectron and Auger signals are compared with the literature.

#### Phosphate buffer solution

The same scatter plot,  $\log R_p$  vs OCP, for the alloys exposed to the buffer solution pH 7 is shown in Fig. 7.35b: the points of all the alloys, from pure copper to the CuZn38Pb2 brass alloy, are grouped in the diagram. It can be concluded that the zinc content in the alloy does not influence the rate-determining step in this case. The Auger spectra of the Cu37Zn alloy exposed for 16 h to the buffer solution (Fig 7.12 – 7.14) shown the presence of the copper and zinc metallic components located respectively at 918.5 (0.1) eV and 992.3 (0.1) eV. The detection of the metallic components from the substrate indicates that the thickness of the oxide layer formed at the surface is very thin: lower than the sampling depth which is estimated to be about 4 nm for Cu and Zn. The Wagner chemical state plot [25, 26] for copper and zinc (Fig. 7.40) provides evidence that the film is composed of ZnO and  $Cu_2O$  with a small amount of zinc phosphate. This thin film is rapidly formed, thus the time effect both on OCP (Fig. 7.2, 7.36b) and on the polarization resistance  $R_p$  (Fig. 7.37b) is less pronounced.

#### 7.4.4 Influence of the surface film

The differences in the ageing behaviour of brass alloys exposed to artificial saliva or the buffer solution are evidenced by the electrochemical results (OCP,  $R_p$ ). Additional information regarding the corrosion mechanism can be obtained from electrochemical impedance spectroscopy (EIS) in Chapter 7.3.2. The EIS spectra in both solution (Figures 7.4 – 7.6) show two time constants, associated to the resistance of the surface film,  $R_{film}$ , and to the charge transfer resistance,  $R_{ct}$ . The results from curve fitting show that in the buffer solution the film resistance  $R_{film}$  is found at 3 – 6  $k\Omega cm^2$  (Tables 7.5, 7.6) and it is not dependent on immersion time. The charge transfer resistance  $R_{ct}$  is in the order of 23

– 37  $\text{k}\Omega\text{cm}^2$  after 1 h of immersion and of 40 – 87  $\text{k}\Omega\text{cm}^2$  after 3h, indicating a slight decrease of the alloy dissolution rate. Brass samples immersed in the artificial saliva show lower charge transfer resistance values (7 – 18  $\text{k}\Omega\text{cm}^2$ , Table 7.6) but much higher film resistance values (26 – 60  $\text{k}\Omega\text{cm}^2$ ). This indicates that a protective surface film is formed in artificial saliva; on the contrary a thin and less protective film is formed in buffer solution at pH 7. XPS surface analysis results give an independent confirmation of this different rate controlling steps.

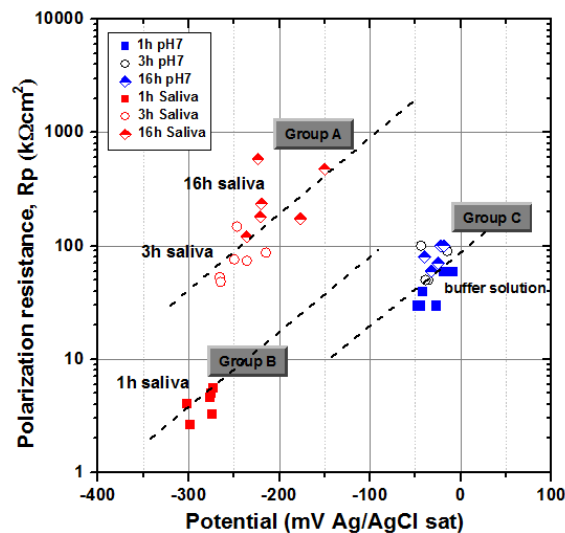


Figure 7. 41: Log ( $R_p$ ) vs OCP diagram as diagnostic plot showing the different evolution of brass alloys in artificial saliva and in buffer solution. Other data on brass wind instruments are reported in Chapter 6.

Combining all electrochemical data in a log  $R_p$  versus OCP plot (Fig. 7.41), three diagonal trend-lines (annotated group A, B and C) with different levels of the polarization resistance are plotted. The mechanically polished brass samples measured after 5 min of exposure to the solution (Chapter 6) are all similar with an OCP around -150 mV SCE and  $R_p$  values around 10  $\text{k}\Omega\text{cm}^2$ , thus the freshly polished surfaces showed a corrosion rate of about 20  $\mu\text{m}/\text{year}$ . The data obtained from the brass alloys immersed in buffer solution pH 7 after 1, 3 and 16 h of immersion are all located at about -60 mV SCE with a polarization resistance of about 5 – 10  $\text{k}\Omega\text{cm}^2$ ; slightly more positive OCP and higher  $R_p$  values correspond to longer immersion times. Brass samples immersed in artificial saliva show a clear time dependence and a shift from the trend line “group B” to the trend line “group A”, thus a change in corrosion behaviour due to the formation of a protective film between 1 and 3 hours of immersion. This protective film is becoming thicker and/or more compact in the time between 3 and 16 hours of immersion leading to more positive OCP and  $R_p$  values; the corrosion rate decreases but the corrosion mechanism does not change.

## 7.5 Conclusions

Based on the electrochemical and surface analytical results the following conclusions on the ageing of brass alloys in neutral electrolytes can be drawn:

- The corrosion rate determined from polarization resistance measurements of brass alloys with 18 – 38% of zinc exposed to artificial saliva (pH 7.4) is initially high (60  $\mu\text{m}/\text{year}$  after 1 hour) due to the aggressive electrolyte. It decreases markedly with prolonged exposure; after 16 h the corrosion rate is lower than 0.5  $\mu\text{m}/\text{year}$ . This is due to the formation of a thick protective film composed of  $\text{CuSCN}$  and  $\text{Zn}_3(\text{PO}_4)_2$  on the brass surface that hinders dissolution.
- The same alloys immersed in a diluted phosphate buffer (pH 7) show from the beginning a low corrosion rate; prolonged exposure to the solution had only a minor effect. The thin film composed of  $\text{Cu}_2\text{O}$ ,  $\text{ZnO}$  and a small amount of  $\text{Zn}_3(\text{PO}_4)_2$  is formed rapidly but does not evolve upon time, thus no protective film is formed.
- These different corrosion mechanisms are confirmed by the results of electrochemical impedance spectroscopy: in artificial saliva the resistive component associated to the thick film is high, in buffer solution the charge transfer resistance is much higher than the film resistance.
- Increasing zinc content in the alloy leads to less noble open circuit potentials and to higher corrosion rates, this effect is more pronounced in the phosphate buffer solution.
- The thickness and composition of the surface films formed in the two different electrolytes are essential for the interpretation of the electrochemical results.

## References

1. R. Procaccini, W.H. Schreiner, M. Vasquez, S. Ceré, *Applied Surface Science*, 268 (2013) 171 – 178
2. K.M. Ismail, R.M. Elsherif, W.A. Badawy, *Electrochimica Acta*, 49 (2004) 5151 – 5160
3. G. Kilinceker, M. Erbil, *Materials Chemistry and Physics*, 119 (2010) 30 – 39
4. W.A. Badawy and F.M. Al-Kharafi, *Corrosion – NACE*, 55 (1999) 268 – 277
5. J. Morales, G.T. Fernandez, P. Esparaza, S. Gonzalez, R.C. Salvarezza and A.J. Arvia, *Corrosion Science*, 37 (1995) 211 – 229
6. J. Morales, P. Esparaza, G.T. Fernandez, S. Gonzalez, J.E. Garcia, J. Caceres, R.C. Salvarezza and A.J. Arvia, *Corrosion Science*, 37 (1995) 231 – 239
7. M. Kabasakaloglu, T. Kiyak, O. Sendil, A. Asan, *Applied Surface Science*, 193 (2002) 167 – 174
8. W.A. Badawy, S.S. El-Egamy and A.S El-Azab, *Corrosion Science*, 37 (1995) 1969 – 1979
9. H.A. Abd El-Rahaman, *Materials and Corrosion*, 41 (1990) 635 – 639
10. M.B. Valcarce, S.R. De Sanchez, M. Vazquez, *Journal of Material Science*, 41 (2006) 1999 – 2007
11. L. Fuks, *Prediction and measurement of exhaled air effects in the pitch of wind instruments*, St. Albans, 1997
12. S. P. Humphrey, R. T. Williamson, *The Journal of Prosthetic Dentistry* 85 (2001) 162–169
13. S. Baliga, S. Muglikar, R. Kale, *Journal of Indian Society of Periodontology*, 17 (2013) 461–465.
14. G.Tani, F. Zucchi, *Minerva Stomatologica*, 16 (1967) 710 – 713
15. M.Stern, A.L.Geary, *Journal of the Chemical Society*, 104 (1957) 56 - 63
16. S. Palomba, Master thesis, University of Cagliari, 2015
17. E.C. Onyiriuka, *Journal of Non-Crystalline Solids* 163 (1993) 268-273
18. J.X.Wu, M.R.Ji, M.Galeotti, A.M.Giusti, G.Rovida, *Surface And Interface Analysis*, 22 (1994) 323-326
19. D. Atzei, B. Elsener, M. Fantauzzi, F. Brundu, A. Rossi, *Spectrochimica Acta Part B* 121 (2016) 38–46
20. Y. Itzhaik, T. Bendikov, D. Hines, P. V. Kamat, H. Cohen, G. Hodes, *Journal of Physical Chemistry C*, 120 (2016) 31 – 41
21. P. Pattanasattayavong, G.O.N. Ndjawa, K. Zhao, K. Wei Chou, N. Yaacobi-Gross, B. C. O'Regan, A. Amassian, T.D. Anthopoulos, *Chemical Communication*, 49 (2013) 4154—4156
22. D. Aldakov, C. Chappaz-Gillot, R. Salazar, V. Delaye, K. A. Welsby, V. Ivanova, P.R. Dunstan, *The Journal of Physical Chemistry C*, 118 (2014) 16095–16103
23. <https://srdata.nist.gov/xps/> (last access: 10-11-2016)



24. M. Crobu, A. Rossi, F. Mangolini, N. D. Spencer, *Analytical and Bioanalytical Chemistry* 403 (2012) 1415–1432
25. G. Moretti, *Journal of Electron Spectroscopy and Related Phenomena*, 95 (1998) 95-144
26. B. Elsener, M. Alter, T. Lombardo, M. Ledergerber, M. Wöhrle, F. Cocco, S. Palomba, M. Fantauzzi, A. Rossi, *Microchemical Journal*, 124 (2016) 757 – 764

# Chapter 8

## *Application of the in situ electrochemical sensor to monitor corrosion on ancient brass musical artifacts.*

*In this Chapter, an application of the electrochemical sensor that has been described in Chapter 6 is presented. The sensor was used on brass musical instruments of the 19<sup>th</sup> and early 20<sup>th</sup> centuries. Monitoring of the corrosion state of these historical brass wind instruments is essential to check the efficiency of preventive conservation protocol. In this Chapter, the results of open circuit potential (OCP) measurements and polarization resistance ( $R_p$ ) measurements are presented. The plot of ( $\log R_p$ ) vs open circuit potential (OCP) has been found to be a promising representation for diagnostic purpose. It allows assigning groups of OCP/ $R_p$  data obtained in the ancient brass instruments to different surface conditions as established by XPS and electrochemical measurements in controlled laboratory experiments.*

*Part of the work has been published in Microchemical Journal: B. Elsener, M. Alter, T. Lombardo, M. Ledergerber, M. Wörle, F. Cocco, M. Fantauzzi, S. Palomba, A. Rossi, Microchemical Journal 124 (2016) 757–764. The Journal has given the permission to reuse the paper in this thesis. The electrochemical measurements reported in this Chapter were carried out by myself at the laboratory of the Institute of Building Materials, ETH Zurich, (Switzerland) and at the laboratory of Electrochemistry and Surface analysis at the Department of Chemistry and Geological Science at the University of Cagliari, where I performed also the X-ray photoelectron spectroscopy experiments. Prof. A. Rossi, Prof. B. Elsener and Dr M. Fantauzzi supported the work with discussions and thorough revisions of the results.*

## 8.1 Introduction

In Chapter 6 the development of an electrochemical sensor has been described. The electrochemical sensor intends to understand the mechanism of corrosion of brass musical instruments of the 19<sup>th</sup> and 20<sup>th</sup> century and to monitor its evolution over time. Electrochemical techniques were used since the corrosion of metals is an electrochemical process, hence corrosion potential and polarization resistance measurements ( $R_p$ ) allow the calculation of the instantaneous corrosion rate. XPS surface analysis revealed that the sensor did not induce alteration of the surface composition of the brass reference alloys, thanks to the short time required to carry out the measurements and the very low corrosion rate in the pH = 7 phosphate buffer solution with  $10^{-3}$ M NaCl.

Based on the results reported in Chapter 6, the sensor has been used for testing and controlling the corrosion rate of historical brass wind instruments at critical points (tuning slides, mouthpiece) where corrosion due to condensed water and saliva is expected. Non-destructive techniques are very important tools for conservators to assess the conservation state of the artifacts by means of in-situ measurements, to obtain the important information on the corrosion state and rate and to control the efficiency of preventive conservation actions. In this work the small non-destructive electrochemical sensor for measurements in-situ is used to assess corrosion potentials and corrosion rate on different pieces of brass instruments.

## 8.2 Experimental

### 8.2.1 Materials

Brass model alloys used in this work are Cu18Zn, Cu28Zn, Cu37Zn, Cu35Zn1Pb and Cu38Zn2Pb (Chapter 4, Section 4.1.1). These model alloys were tested both in “as received” conditions and after mechanical polishing with diamond paste in ethanol and the results were reported in Chapter 6. In addition were tested in pH7 buffer solution and after contact with an artificial saliva solution and the results were reported and discussed in Chapter 7.







Moreover, measurements were also carried out on a brass mouthpiece of a historical instrument and on 5 pieces of a simple brass wind instrument (Bugle) from about 1920 that was destroyed (Table 8.1). These samples were analyzed by XRF and sample OO4 was analyzed by XPS.

Optical micrographies of the samples were acquired with an Axiolab A (Zeiss, Oberkochen, Germany, more details in Chapter 4, Section 4.3.1).

XRF measurements were performed directly on the historical samples using a hand-held EDXRF (SPECTRO xSORT EDXRF (Ametek Inc. PAR, USA) working under atmospheric pressure. More details about the instrument, the calibration and the data processing are given in Chapter 4, Section 4.4).

Moreover, surface composition of the OO4 samples (Table 8.1) was investigated by X-ray photoelectron spectroscopy (XPS). The instrument used was a Theta Probe (ThermoFisher, East Grinstead UK). Details about the instruments, the acquisition parameter and the data processing are reported in Chapter 4, Section 4.6.

Table 8. 1: Samples of historical brass musical instruments analyzed in this work.

Label	Part instrument	Condition
OO1		As received
OO2		As received
OO3		As received
OO4		As received
OO5		As received
OO6		As received

## 8.2.2 In-situ measurements with the sensor

The electrochemical measurements were carried out on samples listed in table 8.2 using the electrochemical sensor shown in Figure 6.1 (Chapter 6).

Table 8. 2: Composition of the reference and ancient brass samples obtained by XRF.

wt.%	Cu	Zn	Pb	Ni	Mn	As	Fe
OO1	67.3 (0.2)	32.3 (0.2)	0.5 (0.1)	0.017 (0.002)	0.024 (0.009)	0.05 (0.01)	-
OO2	67.3 (0.2)	32.1 (0.2)	0.5 (0.1)	-	0.027 (0.005)		-
OO3	67.4 (0.1)	32.2 (0.1)	0.4 (0.1)	-	0.031 (0.008)	0.03 (0.01)	-
OO4	67.6 (0.1)	31.7 (0.1)	0.5 (0.1)	-	-	-	-
OO6	67.6 (0.1)	31.8 (0.1)	0.5 (0.1)	0.019 (0.004)	0.016 (0.001)	0.04 (0.01)	0.018 (0.001)
Cu18Zn	84.3 (0.3)	15.6 (0.1)	-	-	-	-	-
Cu28Zn	71.5 (0.1)	28.5 (0.1)	-	-	-	-	-
Cu37Zn	64.4 (0.2)	35.6 (0.2)	-	-	-	-	-
Cu35Zn1Pb	65.2 (0.2)	33.7 (0.2)	0.8 (0.1)	-	-	-	-
Cu38Zn2Pb	60.4 (0.4)	37.8 (0.3)	1.7 (0.4)	-	-	-	-

## 8.2.3 Electrochemical measurements with the sensor

In this work, two electrochemical techniques were used: open-circuit (OCP) or corrosion potential measurement and linear polarization technique (LPR). The electrochemical measurements were performed with a VersaSTAT 4 Model 400 potentiostat/galvanostat (Ametek Inc. PAR, USA) under computer control (USB port, software Versa Studio v2). The potential difference between the standard reference electrode (Ag/AgCl sat.) and the AgCl electrode used in the sensor was measured before the tests. The sensor sponge had to be soaked before acquiring the data for about 15 minutes in the test solution to get a chloride concentration in the sponge before starting the measurements. The OCP was recorded for 5 minutes before starting the LPR measurements.

## 8.3 Results

### 8.3.1 X-ray fluorescence results

XRF results performed on the reference samples and ancient brass samples are reported in table 8.2. For the brass model alloys good agreement with the nominal wt.% composition was found and no other elements except those expected were detected.

All the ancient brass samples showed a similar copper and zinc content (about 67 wt.% Cu and 32 wt.% Zn). Together with copper and zinc also lead, nickel, manganese, arsenic and iron were detected. Lead was added to improve the machinability of the brasses during the manufacture and was found to be 0.5 wt.% for all the ancient samples. The presence of Ni, Mn, As and Fe could be due to impurities of the raw materials or to lacquering of the samples [1].

### 8.3.2 Optical microscopy (OM)

The samples from the historical brass instruments were observed by optical microscope. In this Chapter only the most significant micrographs are reported . The optical micrograph of the outer side of the samples showed the presence of remarkable areas of corrosion penetration into the brass (figure 8.1). For all the samples, dendritic structures were visible. The presence of dendrites clearly showed that the alloy during the production process solidified with segregation. In fact, the rate at which the metal is cooled influences the size of the dendrites [2]. The micrographs showed also cracks on the surface probably due to the production methods of the instrument.

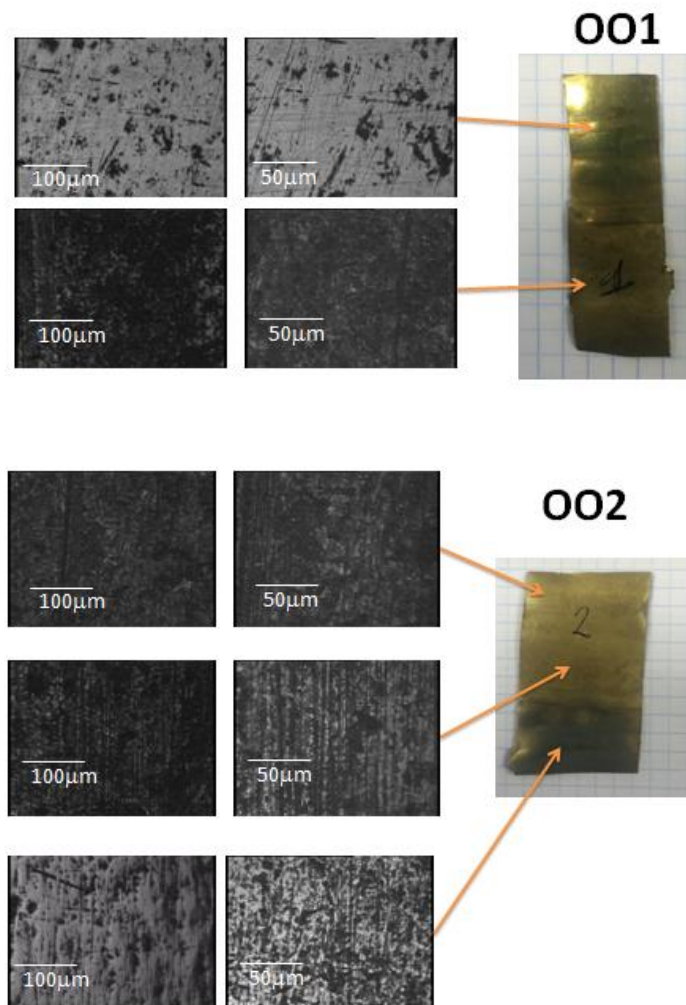


Figure 8. 1: Micrographs acquired under optical microscope (10x and 20x of magnification) of the OO1 and OO2 samples.

### 8.3.3 X-ray Photoelectron Spectroscopy analysis

XPS analysis was performed on the sample labeled OO4 in the as received state. The XPS survey spectra were acquired in order to identify all the elements present at the surface of the ancient brass alloy. Figure 8.2a shows the presence of the characteristic signals of copper, zinc and lead. Carbon and oxygen signals were also revealed due to the presence of a contamination layer and of oxidation products. Additionally, small amounts of other elements such as S, Cl and N were also revealed.

In figure 8.2 the high-resolution spectra of Cu  $2p_{3/2}$ , Zn  $2p_{3/2}$ , of the Auger signals Cu  $L_{3}M_{4,5}M_{4,5}$  and Zn  $L_{3}M_{4,5}M_{4,5}$  and of the Pb 4f are shown. The copper photoelectron signal after curve fitting procedure showed the presence of two main signals at 933.8 (0.1) eV and at 935.1 (0.1) eV. No signal of the metallic component of copper was detected indicating the presence of a thick contamination and oxide layer. The signal at 933.8 eV was assigned to CuO; together with the main signal the characteristic satellite structure at the higher BE side, assigned to the presence of Cu (II) species, is observed. Together with CuO also Cu(OH)<sub>2</sub> is detected at about 935.0 eV [3, 4]. Zn  $2p_{3/2}$  consists of a single peak at 1022.3 eV; this peak is assigned at ZnO and Zn(OH)<sub>2</sub> in agreement with [5]. The Pb 4f showed a well-separated spin orbit doublet; the Pb  $4f_{7/2}$  was found at 137.4 eV. The position of the signal might be due to the presence of PbO<sub>2</sub> [6].

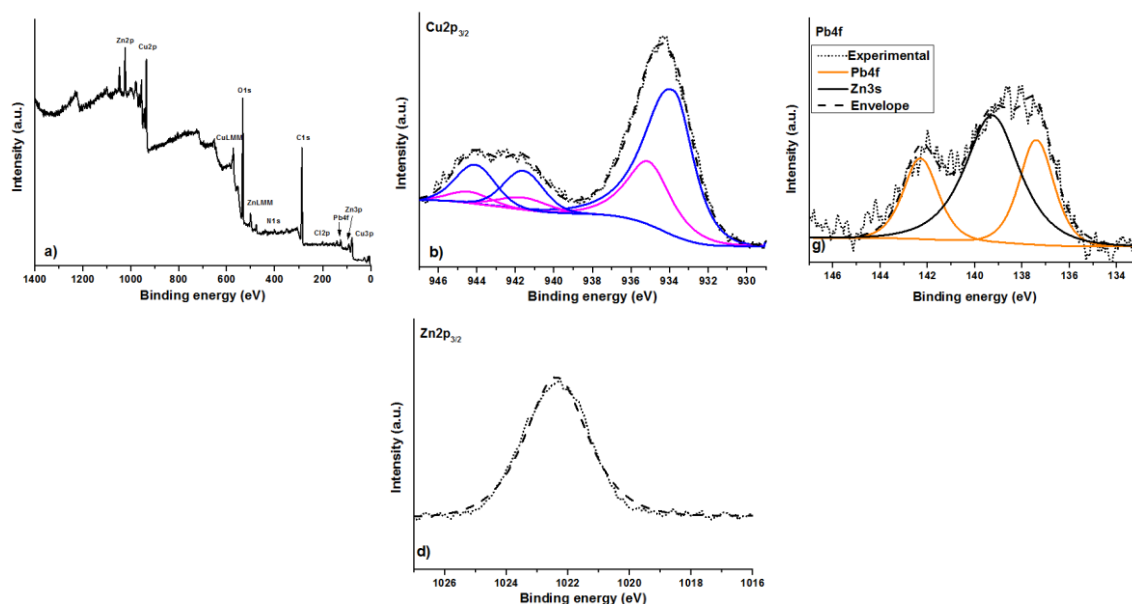


Figure 8. 2: Survey spectra, Cu  $2p_{3/2}$ , Zn  $2p_{3/2}$  and Pb 4f on OO4 ancient brass samples.

No curve fitting of the Auger signals was attempted due to the low intensity of both Cu LMM and Zn LMM.

The XPS results obtained on the as received brass model alloys are reported in Chapter 5. The results showed some differences respect to the ancient artifact. As well as the ancient sample, the brass model alloys showed the presence of a thick contamination and oxide layer since no metallic components of

copper and zinc were detected. The surface of the as received model alloys were found mainly composed by  $\text{Cu}_2\text{O}$  and  $\text{Cu}(\text{OH})_2$ ,  $\text{Zn}(\text{OH})_2$  and  $\text{ZnO}$ . Also in the case of the brass artefact  $\text{Zn}(\text{OH})_2$ ,  $\text{ZnO}$  and  $\text{Cu}(\text{OH})_2$ , were found but unlike the model alloys the component related to the  $\text{CuO}$  was detected [7].

### 8.3.4 Electrochemical measurements

Open-circuit potential were recorded on the samples listed in table 8.1 using the electrochemical sensor discussed in Chapter 6 and shown in Fig. 8.1. The OCP was measured for 5 minutes, afterwards the polarization resistance ( $R_p$ ) measurements were performed. The results of the  $R_p$  measurements on the ancient brass samples are summarized in table 8.3.

Table 8. 3: Polarization resistance  $R_p$  measured on ancient samples listed in tables 8.1.

Sample	$R_p$ ( $\text{k}\Omega\text{cm}^2$ )
OO1	200 – 500
OO2	350 – 390
OO3	400 – 450
OO4	350 – 400
OO5	600 – 740
OO6	600 – 1100

The polarization resistance measurements on brass artefacts could be possible only by the sensor since the shape of the instruments (mouthpiece) do not allow the measurements with a traditional electrochemical cell. The  $R_p$  results of the brass artifacts studied in the work with a thick oxide layer clearly showed an higher  $R_p$  values compared to the as received model brass alloys. Moreover the  $R_p$  values showed differences also within individual samples (three points per sample). For instance, the OO6 samples showed  $R_p$  ranging between 600 and 1100 $\text{k}\Omega\text{cm}^2$ . The mouthpiece (OO5) was characterized by  $R_p$  values in the range from 600 – 740  $\text{k}\Omega\text{cm}^2$ .

The OCP and  $R_p$  values of the brass model alloys in the as received state and after mechanically polishing procedure were reported in Chapter 6 (Table 7.5). The surface state of the brass model alloys could be differentiated on the basis of their  $R_p$  values: the freshly cleaned mechanically polished brass alloys were found at lower  $R_p$  ( $<15 \text{ k}\Omega\text{cm}^2$ ) values, the as received alloys showed higher  $R_p$  values (40 – 80  $\text{k}\Omega\text{cm}^2$ ). The  $R_p$  values of the ancient instruments are much higher, indicating a more protective oxide film on the surface.



## 8.4 Discussion

### 8.4.1 Electrochemical measurements - correlation between OCP and Rp

The electrochemical measurements allow determining the corrosion state and the instantaneous corrosion rate of an alloy in a given environment at the corrosion potential ( $E_{\text{corr}}$ ) defined by the electro-neutrality condition. The corrosion current density can be indirectly determined by the polarization resistance ( $R_p$ ) measurements.  $R_p$  is the inverse of the slope of the applied potential versus the current density diagram. The calculation of the corrosion current density needs the knowledge of the Tafel constants  $\beta_a$  and  $\beta_c$ . In fact, as reported in Chapters 3 and 7, the instantaneous corrosion rate  $i_{\text{corr}}$  can be determined from the measured specific polarization resistance,  $R_p$ , with the Stern-Geary equation (eq 6.2) [8]

$$i_{\text{corr}} = \frac{\beta_a \beta_c}{2.303 (\beta_a + \beta_c)} \cdot \frac{1}{R_p} = \frac{B}{R_p} \quad \text{eq 8. 1}$$

The function “product/sum” to calculate the constant B is not very sensitive to variations in anodic and cathodic Tafel slopes [9], so as the Tafel slopes are often not known, a value of 26 mV for B has been assumed in this work. The corrosion rate  $v_{\text{corr}}$  (in  $\mu\text{m}/\text{year}$ ) was calculated by Faraday's law.

The OCP/ $R_p$  values measured on the ancient brass artifacts are plotted in a log  $R_p$  vs potential diagram (Fig. 8.3) together with the results obtained on the as received and mechanically polished brass model alloys (Chapter 6) and the results from brass model alloys exposed to solutions (Chapter 7).

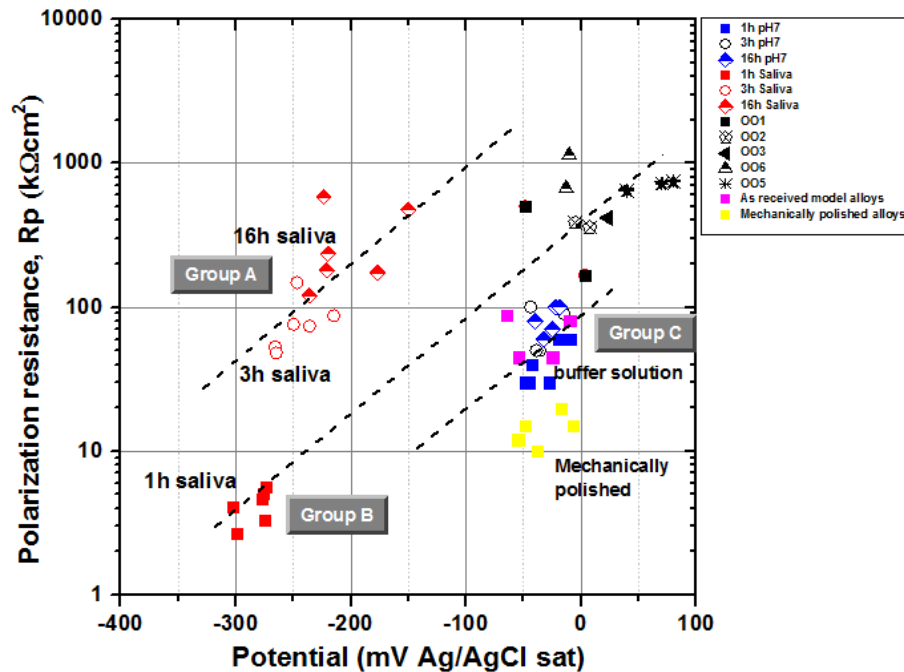


Figure 8. 3: Relation between specific polarization resistance  $R_p$  and open circuit potential of the samples reported in table 8.1. Data obtained brass model alloys immersed for 1, 3 and 16 h in artificial saliva in the pH = 7 buffer solution are included in the plot.

Three different groups of points are clearly visible in the log OCP/Rp diagram and are visualized by diagonal line. The group A with high to very high Rp values over the whole potential range is found for brass model alloys after 3 and 16 hours of the contact with the saliva solution. Brass samples immersed in artificial saliva show a clear time dependence and a shift from the trend line group B to the trend line group A, indicating a change in corrosion behaviour due to the formation of a protective film between 1 and 3 hours of immersion. This protective film becomes thicker and more compact between 3 and 16 hours of immersion leading to more positive OCP and Rp values; the corrosion rate decreases but the corrosion mechanism does not change. The group B shows Rp values at constant potential 10 times lower than group A.

A third group, labeled as Group C, can be found in the range of 50 – 100 kΩcm<sup>2</sup>, thus at quite low values of Rp. In this group, the brass samples immersed in the buffer solution pH7 for 1, 3 and 16 h are found; lower Rp values correspond to the mechanically polished brasses presenting a nearly bare surface related to higher oxygen reduction currents. The artifacts with a thicker oxide film were characterized by higher Rp values and they are found in the group B.

The three groups A, B and C can be described by different diagonal lines with slope ca. 150 mV per decade Rp. For a given (constant) environment characterized by pH value and oxygen content (in the sensor sponge), the surface state and the alloy composition give rise to systematic and correlated variations of both OCP and Rp showing that Rp increases with increasing OCP.

### **8.1.1. Correlation between OCP/Rp values and the surface film**

As shown in Figure 8.4, brass alloys with similar bulk compositions showed very different corrosion rates according to their surface state. In the potential range from -50 to +50 mV Ag/AgCl the highest corrosion current densities of 2 – 3 μA/cm<sup>2</sup> are found for the mechanically polished alloys where only a very thin surface film composed mainly of Cu<sub>2</sub>O and about 20 – 40% ZnO is present on the alloy.

At a similar potential the group of brass samples exposed to the phosphate buffer solution pH 7 for 1, 3 and 16 h is found with a clearly lower corrosion current density  $i_{\text{corr}}$  of 0.5 – 1 μA/cm<sup>2</sup>. The thickness of the surface film on these samples is in the order of a few nanometers and is composed to about 80% of Cu(I) and Cu(II) oxy-hydroxides, only about 20% of Zn (II) oxide was found (Chapter 7).

The samples of the ancient brass wind instrument showed much lower corrosion current densities with  $i_{\text{corr}}$  in the range of 0.02 – 0.1 μA/cm<sup>2</sup> at a similar corrosion potential. The surface of these old “as received” samples was covered by a thick contamination and oxide layer mainly composed of ZnO and Zn(OH)<sub>2</sub> and less CuO, no metallic component of Cu and Zn were revealed. The data points of the “as received” model alloys fall in a similar range as the samples exposed to the buffer solution, the surface film composition shows more Cu<sub>2</sub>O instead of CuO in the sample of the ancient instrument.

Mechanically polished alloys exposed for 1 h to the more aggressive artificial saliva solution show the most negative potentials and the highest corrosion current densities,  $i_{\text{corr}}$  in the range of  $5 - 8 \mu\text{A}/\text{cm}^2$ . After longer immersion time of 3 and 16 h the corrosion rate decreased due to the formation of a thicker surface film composed of  $\text{CuSCN}$  and  $\text{Zn}_3(\text{PO}_4)_2$  as reported in Chapter 7.

Based on these different data sets that combine results from electrochemical and XPS/XAES surface analysis the results from electrochemical measurements in the tuning slides (where XPS surface analysis is not possible) can tentatively be associated to a surface state.

### 8.4.2 Mechanistic interpretation

At the OCP or corrosion potential, the anodic current density (oxidation of metals) must be identical to the cathodic current density (oxygen reduction) and it is defined as the corrosion current density  $i_{\text{corr}}$  (Chapter 3) as reported in eq 8.2:

$$i_{\text{corr}} = |i_c| = i_a \quad \text{at OCP} \quad \text{eq 8. 2}$$

The variation of the corrosion current density  $i_{\text{corr}}$  with the potential (dotted lines in Fig. 8.4) is thus equal to the cathodic polarization curve and consequently to the kinetics of the cathodic oxygen reduction. The cathodic current density,  $i_c$ , can be written as function of the potential  $E$  [10]:

$$i_c = i_o \cdot \exp(-(E_o - E)/\beta_c) \quad \text{eq 8. 3}$$

$$\log(i_c) = \log(i_o) - (E_o - E)/\beta_c \quad \text{eq 8. 4}$$

in the diagram  $\log i_c$  vs  $E$  a line with negative slope  $\beta_c$  is found. The cathodic Tafel slope in this work is ca. 150 mV/dec (Fig. 8.4). If  $E$  is equal to the thermodynamic normal potential  $E_o$  (a function of pH), the cathodic current density corresponds to the exchange current density  $i_o$ .

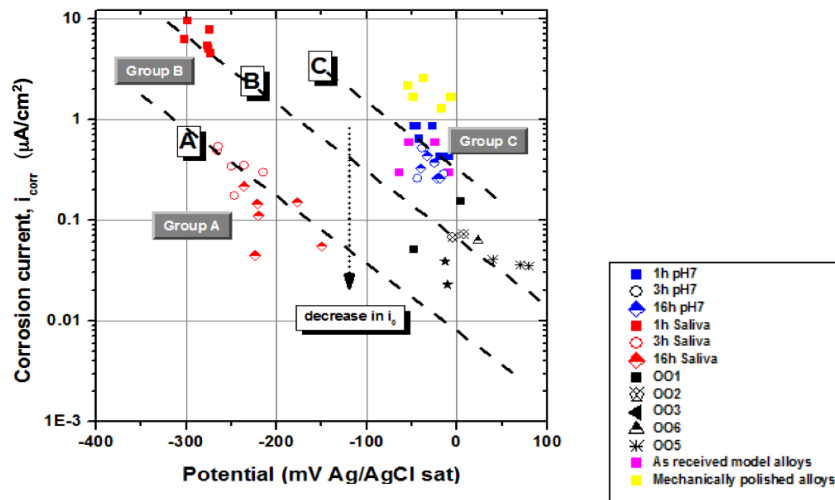


Figure 8. 4: Relation between open circuit potential and corrosion current of the samples reported in table 8.1. Data obtained on brass model alloys immersed for 1, 3 and 16 h in artificial saliva in pH = 7

buffer solution (Chapter 7) and data obtained on the as received and mechanically polished samples measured by the sensor (Chapter 6) are included in the plot.

The diagram in Figure 8.4 shows that the cathodic current density  $i_c$  measured at a constant potential  $E$  (e.g. + 50 mV) is very different for the lines A, B and C. The variation of the oxygen reduction current density at constant potential  $E$  can be explained by a different exchange current density  $i_o$  of the oxygen reduction (eq. 8.3). In the range of potentials where the cathodic oxygen reduction is under activation control, the Tafel slope reported was ca. 200 mV [11] in good agreement with the present results.

The oxygen reduction reaction proceeds through a chemical electrochemical (CE) mechanism where the redox couple  $\text{Cu}_2\text{O}/\text{CuO}$  plays a key role, thus the electron transfer reaction associated with the oxygen reduction is favored on a nearly bare surface and hindered on a surface with a thick oxide layer [12]. The reduction of the cathodic current density upon film formation was very marked on brass [13]. So the vertical displacement of the cathodic polarization curves found in this work (Fig. 8.4) is due to different exchange current densities,  $i_o$ . It can further be concluded that the lowest current densities correspond to thick films with a high ZnO content as found by XPS on the sample of the historic brass wind instrument.

### 8.4.3 Further application - inside the tuning slides

The sensor developed and discussed in Chapter 6 was also used to assess the corrosion state inside historical musical instruments and the first results were published in [12]. The measurements were performed at the critical parts of the instruments, especially the tuning slides, of four horns. The XRF composition of the alloy used for these instruments showed a copper content ranging between 65 – 69 wt.%, a zinc content ranging between 30 – 34 % wt, moreover Fe (0.03 – 0.05 % wt), Ni (0.1 – 0.22 wt.%) and Pb (0.1 – 0.5 wt.%) were revealed as in the case of the ancient brass analyzed in this Chapter. To carry out the measurements inside the tuning slides a tubular sensor was used. The sensor was mounted on a thin flexible tube that allowed to slightly inflate a small balloon mounted at the end of the tube and to press the sensor gently against the inside of the tuning slide. At the end of the measurement in each point the air pressure was released and the sensor was moved to the next measurement position without scratching the inside of the tuning slide. The results of the measurements inside the tuning slides were analyzed using the  $\log R_p/\text{OCP}$  diagram. As in the case of the ancient brass analyzed in this Chapter, the tuning slides fall in an area of the diagram characterized by very high  $R_p$  values from 200 to 1700  $\text{k}\Omega\text{cm}^2$ .

### 8.4.4 Instantaneous corrosion rate

The instantaneous corrosion rate was calculated for all the analyzed samples ( $\mu\text{m}/\text{year}$ ) from the measured  $R_p$  values. The results are shown in figure 8.5. The highest corrosion rates (ca. 40–50  $\mu\text{m}/\text{year}$ ) are found for mechanically polished samples and for samples that were 1 hour in contact with the artificial saliva (Chapter 7). For freshly polished brass alloys in contact with the sensor for 5

minutes, corrosion rates of 20–30  $\mu\text{m}/\text{year}$  were found. Thus, the mechanically polished surface state has the highest reactivity. Corrosion rates of the ancient brass artifact measured in this work were found in the range of 0.4 – 1  $\mu\text{m}/\text{year}$  (maximum 2  $\mu\text{m}/\text{y}$ ). Instead, the corrosion rates inside the tuning slides reported in the article [12] are in the range of 0.05 to 0.5  $\mu\text{m}/\text{year}$ , thus negligible also from the conservator point of view.

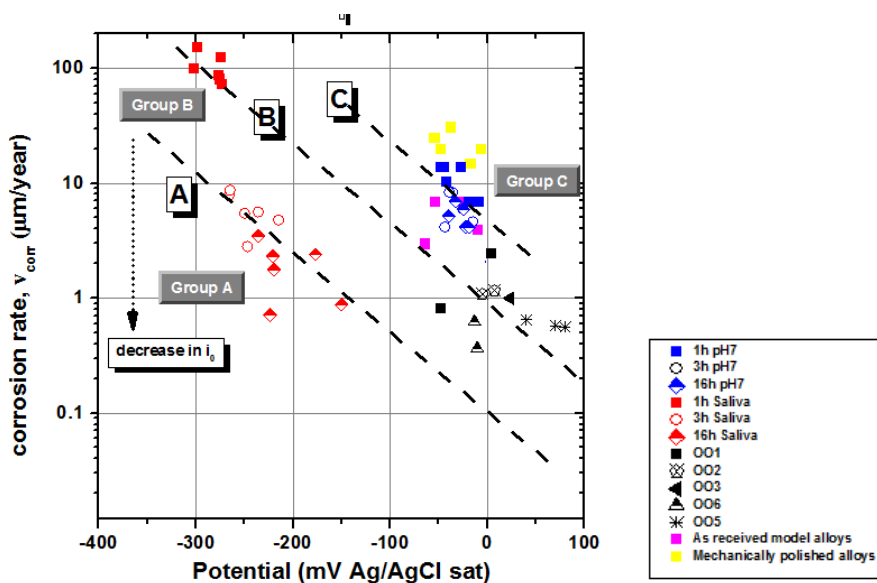


Figure 8.5: Relation between open circuit potential and corrosion rate of the samples reported in table 8.1. The data obtained on brass model alloys immersed for 1, 3 and 16 h in artificial saliva in the pH = 7 buffer solution (Chapter 7) and the data acquired on the as received and mechanically polished samples measured by the sensor (Chapter 6) are included in the plot.

## 8.5 Conclusions

The electrochemical sensor has proven to work well on samples from an ancient instrument and in historical brass instruments, especially inside the tuning slides, both for open circuit potential (OCP) and polarization resistance ( $R_p$ ) measurements.

A diagnostic representation “log  $R_p$  vs OCP” allows rationalize the measured OCP/ $R_p$  data in the context of electrochemical and XPS surface analytical results obtained in well controlled laboratory experiments. The instantaneous corrosion rate of the artifacts can be assessed by means of OCP/ $R_p$  in-situ measurements, the surface state can be estimated indirectly from the diagnostic plot.

The goal of this work was to monitor and understand corrosion inside ancient brass wind instruments of the 19<sup>th</sup> - 20<sup>th</sup> century; it was successfully achieved, together with the diagnosis of the degradation mechanism that affect the artifacts. The results obtained are very important for conservators for achieving the relevant information on the corrosion state and rate inside the instruments and to control

the efficiency of preventive conservation actions. The sensor and the procedure can in principle be applied to any metallic material.

## References

1. Hannes W. Vereecke, Bernadette Frühmann, and Manfred Schreiner, *Historic Brass Society Journal* 24 (2012) 61-77
2. D.A. Scott, *Metallography and Microstructure of Ancient and Historic Metals*, 1991 The J. Paul Getty Trust
3. S. K. Chawla, N. Sankarraman and J. H. Payer, *Journal of Electron Spectroscopy and Related Phenomena*, 61 (1992) 1–18
4. L. S. Dake, D. R. her and J. M. Zachara, *Surface And Interface Analysis*, 14 (1989) 71-75
5. T.L. Barr, J.J. Hackenberg, *J. Am. Chem. SOC.* 104 (1982) 5390-5394
6. L.R. Pederson, *J. Electron Spectrosc. Relat. Phenom.* 28 (1982) 203
7. S. K. Chawla, N. Sankarraman and J. H. Payer, *J. ElectronSpectrosc. Relat. Phenom.*, 61 (1992) 1–18
8. M. Stern, A. L. Geary, *J. El.chem. Soc.* 104 (1957) 56.
9. B. Elsener, *Corros. Sci.* 47 (2005) 3019–3033.
10. R.Winston Revie, Herbert H. Uhlig, *Corrosion and Corrosion Control — An Introduction to Corrosion Science and Engineering*, WILEY, 2008.
11. R. Procaccini, S. Ceré, M. Vazquez, *J. Appl. Electrochem.* 39 (2009) 177–184.
12. R. Procaccini, M. Vasquez, S. Ceré, *Electrochim. Acta* 54 (2009) 7324–7329.
13. B. Elsener, M. Alter, T. Lombardo, M. Ledergerber, M. Wörle, F. Cocco, M. Fantauzzi, S. Palomba, A. Rossi, *Microchemical Journal* 124 (2016) 757–764

# *Chapter 9*

## *Conclusions and Outlook*

*In the final Chapter of this thesis, the most important conclusions that can be drawn from this work are summarized. Furthermore, outlines directions for future research are reported.*



The goal of this thesis was to contribute to the understanding of the corrosion mechanism of brass alloys in neutral solutions by combining electrochemical and surface analytical investigations in the context of corrosion occurring inside historical brass wind instruments of the 19<sup>th</sup> and 20<sup>th</sup> centuries used for playing in historical informed musical practice.

## Conclusions

Surface analysis of the copper and zinc compounds present on the surface of brass alloys has been performed based on their x-ray induced Auger signals (XAES). The reference compounds showed multi-component spectra that could be described based on the theoretical approach reported in literature, predicting the differences in KE and intensity ratios between the components, thus defining a peak shape (envelope) for pure metal and oxides that could be used for curve-fitting in complex systems as e.g. a thin oxy-hydroxide film on brass. With the Wagner plot the chemical state of the compounds present at the surface was determined unambiguously. For the quantification, the XAES intensity  $I_{LMM}$  had to be transferred in an XPS intensity  $I_{2p}$ . Based on XAES and XPS measurements on standards an intensity ratio (corrected for attenuation length and transmission function)  $R = I_{2p}/I_{LMM}$  was calculated.  $R$  was found to be different not only for copper and for zinc but also different for metal and oxides and different for different XPS instruments. Thus a correction factor  $k = R_{ox}/R_{met}$  was defined and was independent of the instrument, being  $k = 1.5$  for copper and  $k = 0.8$  for zinc. This novel analytical strategy developed during this work allowed for the first time the simultaneous chemical state identification and full quantification of copper and zinc in complex, thin-layered systems of brass alloys.

Electrochemical techniques such as potential, polarization resistance and impedance (EIS) measurements were used to follow the ageing of brass model alloys in artificial saliva and a diluted phosphate buffer solution (pH 7). The results showed that in artificial saliva both the potential and the polarization resistance increased markedly and the EIS data indicated a resistive control by a surface film; in the phosphate buffer solution the effect of immersion time (ageing) was small and the EIS data indicated a charge transfer control. Thus high initial, but rapidly decreasing corrosion rates were found in artificial saliva (the most severe electrolyte that was expected inside the brass instruments). In the diluted buffer solution lower, over time quite constant corrosion rates were found. XPS/XAES analysis confirmed the formation of a thick, protective surface film composed of  $CuSCN$  and  $Zn_3(PO_4)_2$  in artificial saliva whereas a thin copper- and zinc oxi-hydroxide film was formed in the diluted buffer solution. Thus it was possible to correlate the electrochemical and corrosion data with the surface composition of the aged brass alloys.

A plot of logarithm of polarization resistance ( $R_p$ ) versus the open circuit potential (OCP) allowed rationalizing all the results obtained on the brass model alloys, brass from ancient instruments and brass alloys exposed to solutions. Knowing the surface state (composition, film thickness, oxidation

state) from the XPS/XAES surface analysis, the electrochemical results could be correlated to the surface state of the brass samples studied. The representation of the electrochemical results showing distinct groups of  $\log(R_p)$  vs OCP data can be used both for diagnostic purpose and for mechanistic interpretation.

A small, non-destructive and non-invasive electrochemical sensor for in-situ measurements that is able to measure the corrosion state (corrosion potential) and rate (polarization resistance) inside historical brass wind instruments was developed and tested during this work. The electrochemical sensor consisted of a combined Ag/AgCl solid-state reference electrode and a small platinum grid as counter electrode, both embedded in a thin sponge soaked with a diluted phosphate buffer solution, pH 7, with  $10^{-3}$  M chlorides. The test solution does not alter the surface composition as it was established by XPS/XAES analysis. In fact XPS surface analysis has shown that the sensor does not induce alteration of the surface composition of the brass model alloys thanks to the short time required to carry out the measurements and the very low corrosion rate in the test solution.

## **Outlook**

The novel analytical strategy has proven to be successful for the characterization of brass samples when two different chemical states (metal and oxide) of copper and zinc were simultaneously present. This procedure should be developed further to the situation when more species are present in a thin layer on the brass surface, e.g. metallic copper, copper oxide and copper sulfide.

The correlation between electrochemical and surface analytical results has been established in this work based on the brass model alloys exposed to artificial saliva solution and a phosphate buffer solution. It would be interesting to enlarge this database including other surface states (e.g. brass aged at the atmosphere, parts of tuning slides from dismantled instruments with naturally formed corrosion products, etc.). This would complete the diagnostic “ $\log R_p$  vs OCP” plot with other surface compositions.

The evaluation, if preventative measures (drying the instruments after playing) could reduce the ongoing corrosion in brass wind instruments to a negligible intensity, is ongoing. In addition to these experiments in real instruments, the environment inside brass wind instruments subject to wet/dry cycles could be simulated on samples of brass model alloys where XPS/XAES analysis is possible.

The results and conclusions of the thesis will be presented to musicians, scientists in charge of restoration of brass wind instruments and conservators. It is expected to give a contribution to answer the problem of historical informed musical practice “to play or not to play”.

# Appendix

## Appendix A – Chapter 7

In Appendix were reported the tables and the figures of Cu28Zn and Cu35Zn1Pb brass alloys after the contact with the phosphate pH7 and saliva solutions.

### Phosphate buffer solution

Cu28Zn

**Table A 1:** BE, KE and FWHM of the photoelectron and Auger signals detected at the surface of the Cu28Zn after contact with the phosphate buffer solution. Standard deviations are given in parentheses.

Cu28Zn	1h pH7		3h pH7		16h pH7	
	BE (eV)	FWHM (eV)	BE (eV)	FWHM (eV)	BE (eV)	FWHM (eV)
<b>Cu 2p<sub>3/2</sub> Cu(0)</b>	932.6 (0.1)	1.4 (0.1)	932.5 (0.1)	1.5 (0.1)	932.5 (0.1)	1.4 (0.1)
<b>Cu 2p<sub>3/2</sub> Cu(I)</b>	932.6 (0.1)	1.4 (0.1)	932.5 (0.1)	1.5 (0.1)	932.5 (0.1)	1.4 (0.1)
<b>Cu 2p<sub>3/2</sub> Cu(II)</b>	934.9 (0.1)	2.5 (0.1)	934.9 (0.1)	2.5 (0.1)	934.8 (0.1)	2.2 (0.1)
<b>Sat 1</b>	944.0 (0.1)	2.2 (0.1)	943.9 (0.1)	2.3 (0.1)	943.9 (0.1)	2.3 (0.1)
<b>Sat 2</b>	941.5 (0.1)	2.1 (0.1)	941.4 (0.1)	2.3 (0.1)	941.4 (0.1)	2.2 (0.1)
<b>O 1s</b>	530.8 (0.1)	1.6 (0.1)	530.7 (0.1)	1.6 (0.1)	530.8 (0.1)	1.6 (0.1)
	532.0 (0.2)	1.6 (0.1)	531.7 (0.1)	1.6 (0.1)	531.8 (0.1)	1.6 (0.1)
	533.5 (0.2)	1.6 (0.1)	533.1 (0.1)	1.6 (0.1)	533.2 (0.1)	1.6 (0.1)
<b>P 2p</b>	133.2 (0.1)	1.5 (0.2)	133.2 (0.2)	1.5 (0.1)	133.0 (0.2)	1.5 (0.1)
	134.1 (0.1)	1.5 (0.2)	134.0 (0.2)	1.5 (0.1)	133.8 (0.2)	1.5 (0.1)
<b>Zn 2p<sub>3/2</sub> Cu(0)</b>	1022.1 (0.1)	1.8 (0.1)	1022.2 (0.1)	1.8 (0.1)	1022.0 (0.1)	1.7 (0.1)
<b>Zn 2p<sub>3/2</sub> Zn(II)</b>	1022.1 (0.1)	1.8 (0.1)	1022.2 (0.1)	1.8 (0.1)	1022.0 (0.1)	1.7 (0.1)
	<b>KE (eV)</b>	<b>FWHM (eV)</b>	<b>KE (eV)</b>	<b>FWHM (eV)</b>	<b>KE (eV)</b>	<b>FWHM (eV)</b>
<b>Cu L<sub>3</sub>M<sub>4,5</sub>M<sub>4,5</sub>met</b>	918.5 (0.1)	1.5 (0.1)	918.6 (0.1)	1.5 (0.1)	918.5 (0.1)	1.5 (0.1)
<b>Cu L<sub>3</sub>M<sub>4,5</sub>M<sub>4,5</sub>Ox</b>	916.5 (0.2)	2.5 (0.1)	916.9 (0.2)	2.8 (0.1)	916.5(0.2)	2.7 (0.1)
	<b>KE (eV)</b>	<b>FWHM (eV)</b>	<b>KE (eV)</b>	<b>FWHM (eV)</b>	<b>KE (eV)</b>	<b>FWHM (eV)</b>
<b>Zn L<sub>3</sub>M<sub>4,5</sub>M<sub>4,5</sub>met</b>	992.1 (0.1)	1.6 (0.1)	992.3 (0.1)	1.6 (0.1)	992.2 (0.1)	1.6 (0.1)
<b>Zn L<sub>3</sub>M<sub>4,5</sub>M<sub>4,5</sub>Ox</b>	987.3 (0.3)	2.8 (0.2)	987.2 (0.1)	2.7 (0.1)	987.5 (0.1)	2.4 (0.1)

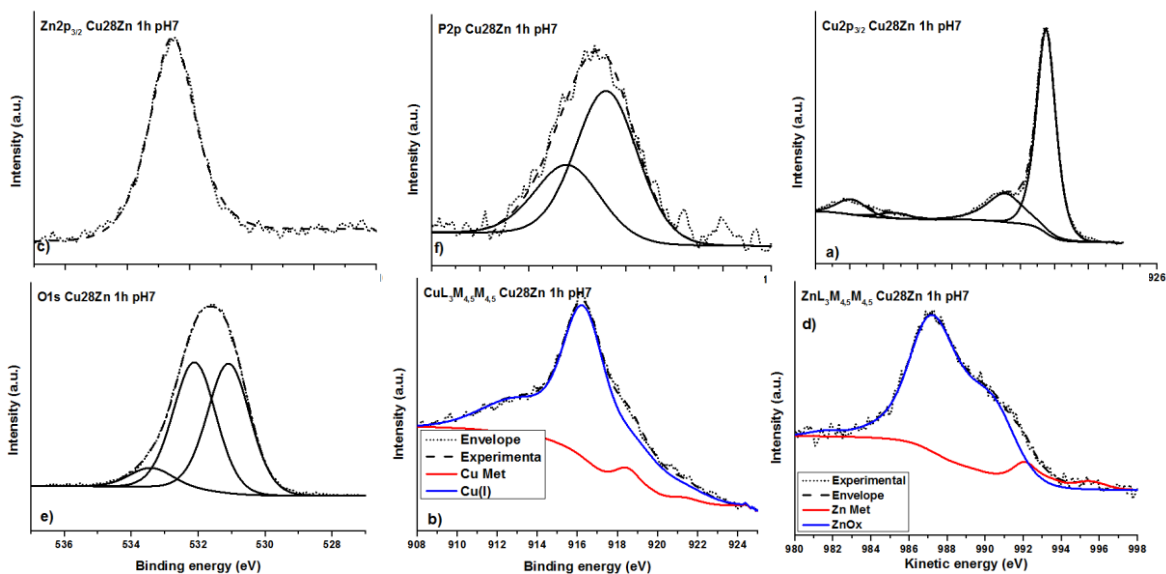


**Figure A 1:** Cu  $2p_{3/2}$  (a), Cu  $L_3M_{45}M_{45}$  (b), Zn  $2p_{3/2}$  (c), Zn  $L_3M_{45}M_{45}$  (d), O  $1s$  (e), P  $2p$  (f) signals for the Cu28Zn after 1 hours of exposure to the phosphate buffer solution.

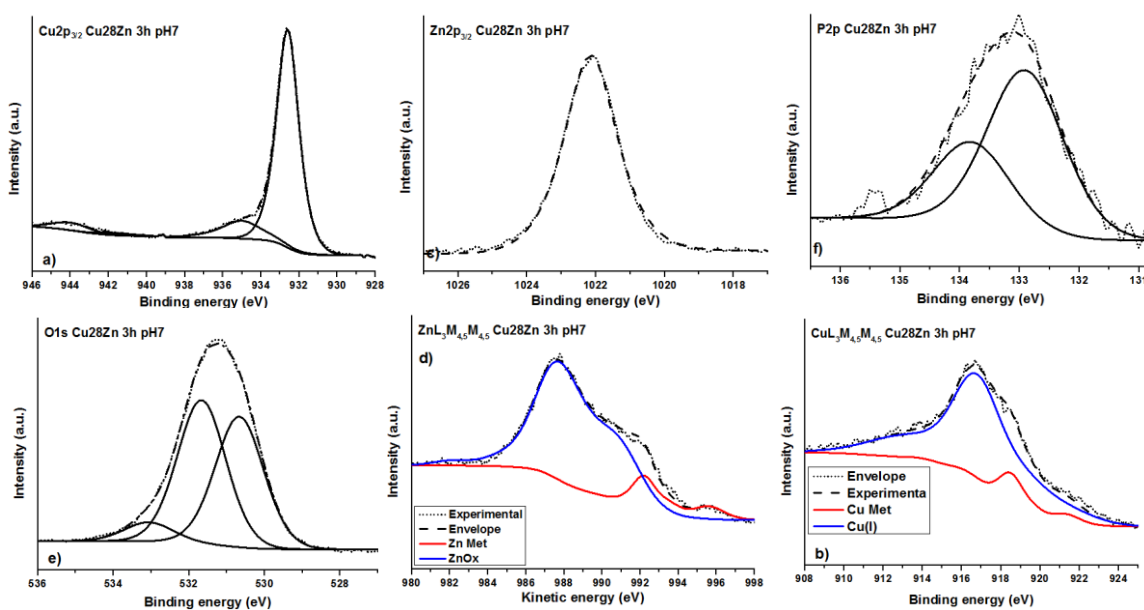


**Figure A 2:** Cu  $2p_{3/2}$  (a), Cu  $L_3M_{45}M_{45}$  (b), Zn  $2p_{3/2}$  (c), Zn  $L_3M_{45}M_{45}$  (d), O  $1s$  (e), P  $2p$  (f) signals for the Cu28Zn after 3 hours of contact with the phosphate buffer solution.

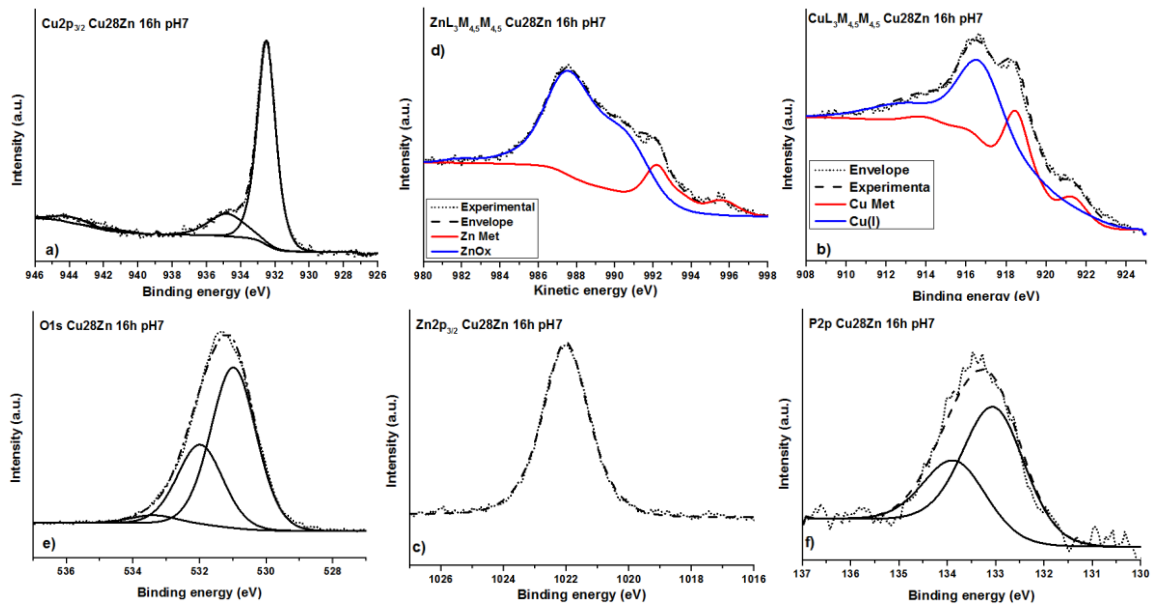


Figure A 3: Cu  $2p_{3/2}$  (a), Cu  $L_3M_{45}M_{45}$  (b), Zn  $2p_{3/2}$  (c), Zn  $L_3M_{45}M_{45}$  (d), O  $1s$  (e), P  $2p$  (f) signals for the Cu<sub>28</sub>Zn after 16 hours of contact with the phosphate buffer solution.

Table A 2: Results of the quantitative analysis for the Cu28Zn after 1, 3 and 16hours of immersion in neutral phosphate buffer solution. Standard deviations are reported in brackets.

Cu28Zn	1h				
	%at		%at		%at
<b>Cu(0)</b>	2 (1)	<b>Cu(0)</b>	20 (4)	<b>Cu tot</b>	71 (2)
<b>Cu(I)</b>	4 (1)	<b>Cu(I)</b>	36 (18)		
<b>Cu(II)</b>	3 (1)	<b>Cu(II)</b>	36 (9)		
<b>Zn(0)</b>	1.2 (0.1)	<b>Zn(0)</b>	34 (3)	<b>Zn tot</b>	29 (2)
<b>Zn(II)</b>	3 (2)	<b>Zn(II)</b>	66 (3)		
<b>O</b>	26 (1)				
<b>C</b>	57 (2)				
<b>P</b>	3 (1)				
	3h				
	%at		%at		%at
<b>Cu(0)</b>	0.9 (0.6)	<b>Cu(0)</b>	7 (3)	<b>Cu tot</b>	63 (5)
<b>Cu(I)</b>	6 (1)	<b>Cu(I)</b>	43 (22)		
<b>Cu(II)</b>	4 (1)	<b>Cu(II)</b>	40 (4)		
<b>Zn(0)</b>	1.3 (0.2)	<b>Zn(0)</b>	19 (3)	<b>Zn tot</b>	37 (5)
<b>Zn(II)</b>	5 (2)	<b>Zn(II)</b>	81 (3)		
<b>O</b>	38 (6)				
<b>C</b>	30 (10)				
<b>P</b>	7 (1)				
	16h				
	%at		%at		%at
<b>Cu(0)</b>	2 (1)	<b>Cu(0)</b>	33 (1)	<b>Cu tot</b>	68 (4)
<b>Cu(I)</b>	3 (1)	<b>Cu(I)</b>	46 (11)		
<b>Cu(II)</b>	0.9 (0.1)	<b>Cu(II)</b>	15 (3)		
<b>Zn(0)</b>	1.2 (0.1)	<b>Zn(0)</b>	39 (2)	<b>Zn tot</b>	32 (4)
<b>Zn(II)</b>	1.8 (0.1)	<b>Zn(II)</b>	61 (2)		
<b>O</b>	21 (2)				
<b>C</b>	66 (3)				
<b>P</b>	4 (1)				

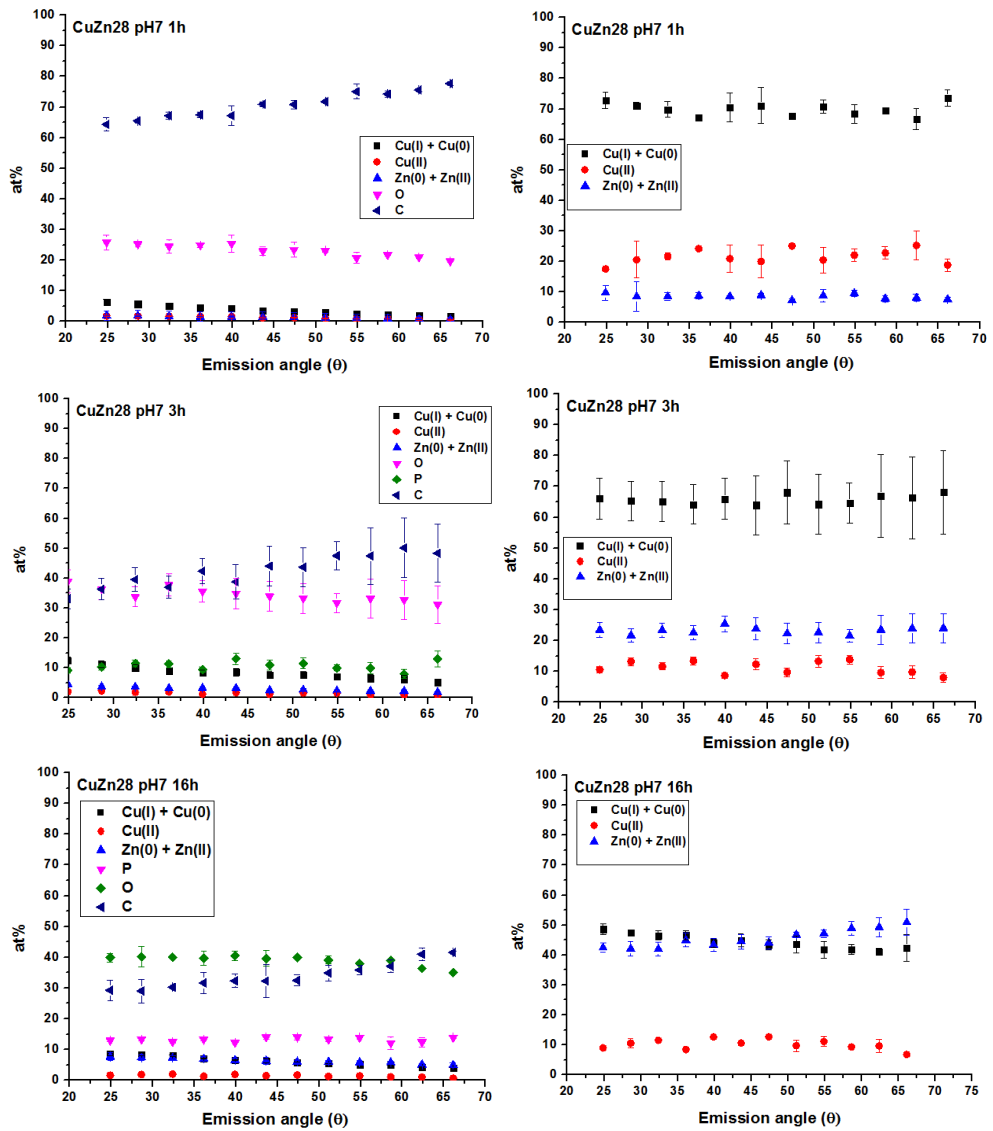


Figure A 4: Apparent composition (at.%) vs emission angle from ARXPS data for Cu<sub>28</sub>Zn after 1, 3 and 16 hours of contact with the phosphate solution.

## Cu35Zn1Pb

Table A 3: Average kinetic energy (KE) and FWHM of the most intense peaks of the elements detected on the Cu35Zn1Pb after contact with the phosphate buffer solution. Standard deviations are given in parentheses.

Cu35Zn1Pb	1h pH7		3h pH7		16h pH7	
	BE (eV)	FWHM (eV)	BE (eV)	FWHM (eV)	BE (eV)	FWHM (eV)
<b>Cu 2p<sub>3/2</sub> Cu(0)</b>	932.6 (0.1)	1.4 (0.1)	932.7 (0.1)	1.4 (0.1)	932.6 (0.1)	1.4 (0.1)
<b>Cu 2p<sub>3/2</sub> Cu(I)</b>	932.6 (0.1)	1.4 (0.1)	932.7 (0.1)	1.4 (0.1)	932.6 (0.1)	1.4 (0.1)
<b>Cu 2p<sub>3/2</sub> Cu(II)</b>	935.0 (0.1)	2.5 (0.1)	935.1 (0.1)	2.5 (0.1)	935.0 (0.1)	2.5 (0.1)
<b>Sat 1</b>	944.0 (0.1)	2.3 (0.1)	944.1 (0.1)	2.3 (0.1)	944.0 (0.1)	2.3 (0.1)
<b>Sat 2</b>	941.5 (0.1)	2.0 (0.1)	941.6 (0.1)	2.0 (0.1)	941.5 (0.1)	2.0 (0.1)
<b>O 1s</b>	530.8 (0.1)	1.5 (0.1)	530.7 (0.1)	1.5 (0.1)	530.7 (0.1)	1.5 (0.1)
	531.8 (0.1)	1.5 (0.1)	531.7 (0.1)	1.5 (0.1)	531.7 (0.1)	1.5 (0.1)
	533.0 (0.1)	1.5 (0.1)	533.2 (0.1)	1.5 (0.1)	533.1 (0.1)	1.5 (0.1)
<b>Pb 4f</b>	138.8 (0.1)	1.7 (0.1)	138.7 (0.1)	1.7 (0.1)	138.9 (0.1)	1.7 (0.1)
	143.7 (0.1)	1.7 (0.1)	143.6 (0.1)	1.7 (0.1)	144.1 (0.1)	1.7 (0.1)
<b>P 2p</b>	133.0 (0.1)	1.5 (0.1)	133.0 (0.2)	1.5 (0.1)	133.2 (0.1)	1.5 (0.1)
	133.8 (0.1)	1.5 (0.1)	133.8 (0.2)	1.5 (0.1)	134.1 (0.1)	1.5 (0.1)
<b>Zn 2p<sub>3/2</sub> Cu(0)</b>	1022.2 (0.1)	1.7 (0.1)	1022.1 (0.1)	1.7 (0.1)	1022.2 (0.1)	1.7 (0.1)
<b>Zn 2p<sub>3/2</sub> Zn(II)</b>	1022.2 (0.1)	1.7 (0.1)	1022.1 (0.1)	1.7 (0.1)	1022.2 (0.1)	1.7 (0.1)
	<b>KE (eV)</b>	<b>FWHM (eV)</b>	<b>KE (eV)</b>	<b>FWHM (eV)</b>	<b>KE (eV)</b>	<b>FWHM (eV)</b>
<b>Cu LMM met</b>	918.8 (0.1)	1.5 (0.1)	918.7 (0.1)	1.5 (0.1)	918.7 (0.1)	1.5 (0.1)
<b>Cu LMM Ox</b>	916.9 (0.1)	2.4 (0.1)	916.9 (0.1)	2.4 (0.1)	916.6 (0.1)	2.4 (0.1)
	<b>KE (eV)</b>	<b>FWHM (eV)</b>	<b>KE (eV)</b>	<b>FWHM (eV)</b>	<b>KE (eV)</b>	<b>FWHM (eV)</b>
<b>Zn LMM met</b>	992.3 (0.1)	1.5 (0.1)	992.3 (0.1)	1.5 (0.1)	992.2 (0.1)	1.5 (0.1)
<b>Zn LMM Ox</b>	987.4 (0.1)	2.4 (0.1)	987.8 (0.1)	2.4 (0.1)	987.2 (0.1)	2.4 (0.1)

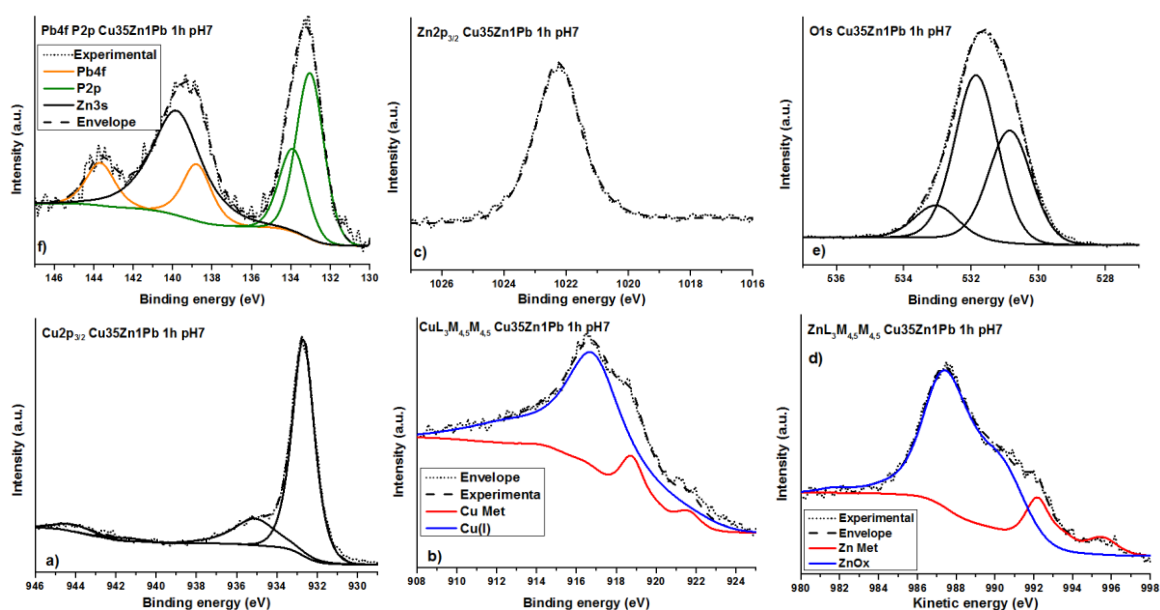


Figure A 5: Cu 2p<sub>3/2</sub> (a), Cu L<sub>3</sub>M<sub>45</sub>M<sub>45</sub> (b), Zn 2p<sub>3/2</sub> (c), Zn L<sub>3</sub>M<sub>45</sub>M<sub>45</sub> (d), O 1s (e), P 2p (f) signals for the Cu35Zn1Pb after 1 hours of contact with the phosphate buffer solution.



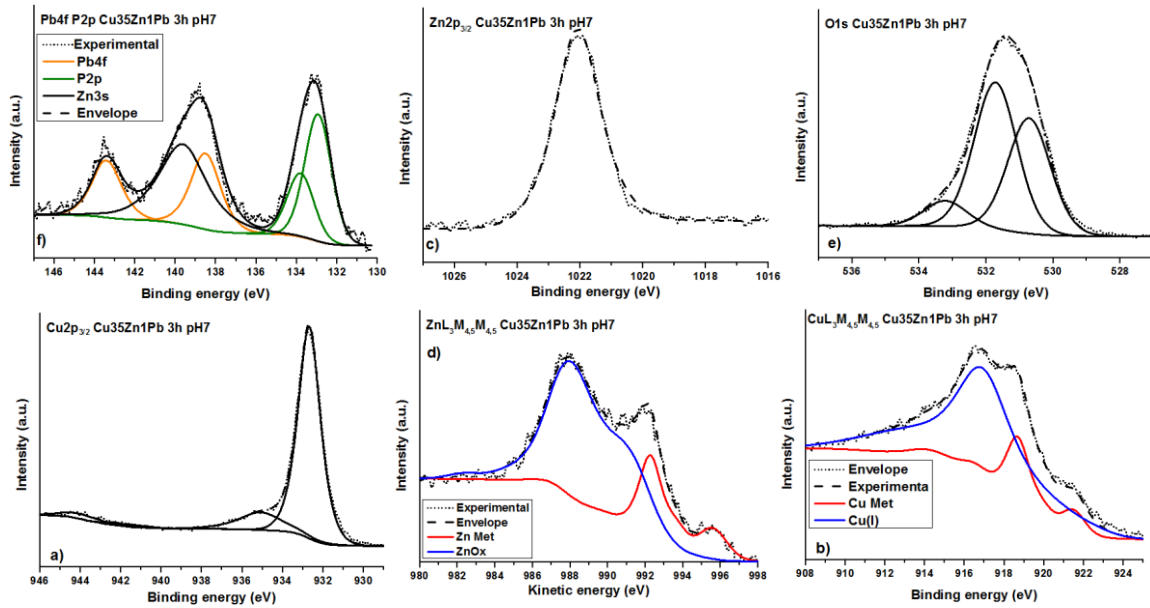


Figure A 6: Cu 2p<sub>3/2</sub> (a), Cu L<sub>3</sub>M<sub>45</sub>M<sub>45</sub> (b), Zn 2p<sub>3/2</sub> (c), Zn L<sub>3</sub>M<sub>45</sub>M<sub>45</sub> (d), O 1s (e), P 2p (f) signals for the Cu<sub>35</sub>Zn<sub>1</sub>Pb after 3 hours of contact with the phosphate buffer solution.

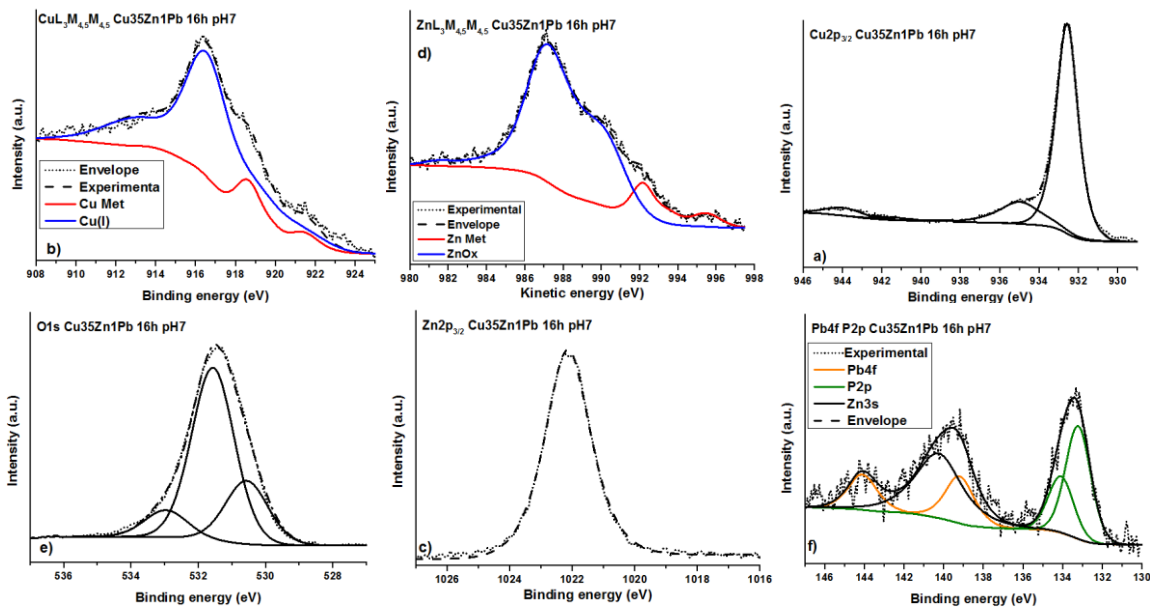


Figure A 7: Cu 2p<sub>3/2</sub> (a), Cu L<sub>3</sub>M<sub>45</sub>M<sub>45</sub> (b), Zn 2p<sub>3/2</sub> (c), Zn L<sub>3</sub>M<sub>45</sub>M<sub>45</sub> (d), O 1s (e), P 2p (f) signals for the Cu<sub>35</sub>Zn<sub>1</sub>Pb after 16 hours of contact with the phosphate buffer solution.

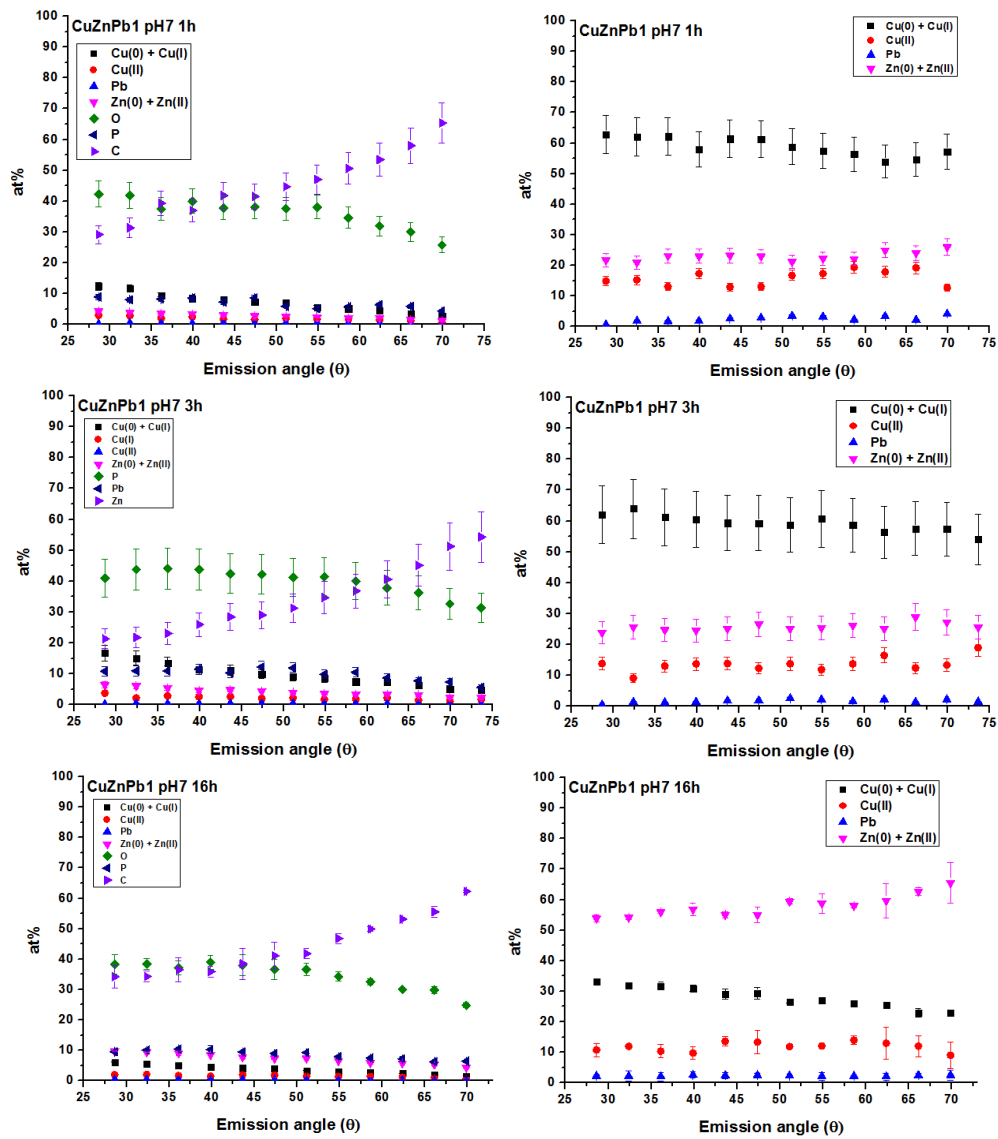


Figure A 8: Apparent composition (at.%) vs emission angle from ARXPS data for Cu<sub>35</sub>Zn<sub>1</sub>Pb after 1, 3 and 16 hours of contact with the phosphate solution.

Table A 4: Quantitative analysis results (average values) of the Cu<sub>35</sub>Zn<sub>1</sub>Pb after 1, 3 and 16 hours of immersion in the neutral phosphate buffer solution. Standard deviations are reported in brackets.

		<b>1h</b>			
<b>Pb1</b>	<b>%at</b>		<b>%at</b>		<b>%at</b>
<b>Cu(0)</b>	1.9 (0.2)	<b>Cu(0)</b>	16 (1)	<b>Cu tot</b>	75 (1)
<b>Cu(I)</b>	7 (1)	<b>Cu(I)</b>	61 (1)		
<b>Cu(II)</b>	2.6 (0.1)	<b>Cu(II)</b>	23 (1)		
<b>Zn(0)</b>	1.3 (0.1)	<b>Zn(0)</b>	34 (1)	<b>Zn tot</b>	24 (1)
<b>Zn(II)</b>	2.5 (0.2)	<b>Zn(II)</b>	66 (1)		
<b>Pb Ox</b>	0.2 (0.1)	<b>Pb Ox</b>	100	<b>Pb tot</b>	1.0 (0.1)
<b>O</b>	37 (1)				
<b>C</b>	40 (2)				
<b>P</b>	7 (1)				
		<b>3h</b>			
	<b>%at</b>		<b>%at</b>		<b>%at</b>
<b>Cu(0)</b>	4 (1)	<b>Cu(0)</b>	20 (1)	<b>Cu tot</b>	77 (1)
<b>Cu(I)</b>	11 (1)	<b>Cu(I)</b>	63 (1)		
<b>Cu(II)</b>	3 (1)	<b>Cu(II)</b>	18 (1)		
<b>Zn(0)</b>	2 (1)	<b>Zn(0)</b>	43 (1)	<b>Zn tot</b>	21 (1)
<b>Zn(II)</b>	2.8 (0.2)	<b>Zn(II)</b>	57 (1)		
<b>Pb Ox</b>	0.2 (0.1)	<b>Pb 4f</b>	100	<b>Pb tot</b>	1.1 (0.2)
<b>O</b>	39 (1)				
<b>C</b>	31 (1)				
<b>P</b>	7 (1)				
		<b>16h</b>			
	<b>%at</b>		<b>%at</b>		<b>%at</b>
<b>Cu(0)</b>	0.5 (0.2)	<b>Cu(0)</b>	6 (2)	<b>Cu tot</b>	42 (1)
<b>Cu(I)</b>	3.4 (0.6)	<b>Cu(I)</b>	46 (5)		
<b>Cu(II)</b>	3.5 (0.4)	<b>Cu(II)</b>	48 (8)		
<b>Zn(0)</b>	0.9 (0.2)	<b>Zn(0)</b>	9 (1)	<b>Zn tot</b>	58 (1)
<b>Zn(II)</b>	9.5(0.2)	<b>Zn(II)</b>	91 (1)		
<b>Pb Ox</b>	0.1(0.02)	<b>Pb Ox</b>	100	<b>Pb tot</b>	0.4 (0.2)
<b>O</b>	42 (1)				
<b>C</b>	30 (1)				
<b>P</b>	11 (1)				

**Cu28Zn**

Table A 5: Average kinetic energy (KE) and FWHM of the most intense peaks of the elements detected on the Cu28Zn after exposure to the saliva solution. Standard deviations are given in parentheses.

Cu28Zn	1h		3h		16h	
	BE (eV)	FWHM (eV)	BE (eV)	FWHM (eV)	BE (eV)	FWHM (eV)
<b>Cu</b>	932.6 (0.1)	1.4 (0.1)	932.6 (0.1)	1.4 (0.1)	932.6 (0.1)	1.5 (0.1)
<b>N 1s</b>	398.7 (0.1)	1.5 (0.1)	398.5 (0.1)	1.1 (0.1)	398.4 (0.1)	1.1 (0.1)
<b>N NCS</b>	400.1 (0.1)	1.5 (0.1)	399.9 (0.1)	1.1 (0.1)	399.7 (0.1)	1.1 (0.1)
<b>O 1</b>	531.6 (0.1)	1.5 (0.1)	531.8 (0.1)	1.5 (0.1)	531.4 (0.1)	1.6 (0.1)
<b>O 1s</b>	532.5 (0.1)	1.5 (0.1)	532.5 (0.1)	1.5 (0.1)	533.2 (0.1)	1.6 (0.1)
<b>O 1s</b>	533.5 (0.2)	1.5 (0.1)	533.7 (0.1)	1.5 (0.1)	531.9 (0.1)	1.6 (0.1)
<b>P 2p</b>	134.0 (0.1)	1.6 (0.1)	133.8 (0.1)	1.4 (0.1)	133.8 (0.1)	1.4 (0.1)
<b>P 2p</b>	134.8 (0.1)	1.6 (0.1)	134.7 (0.1)	1.4 (0.1)	134.3 (0.1)	1.4 (0.1)
<b>S 2p SCN</b>	163.5 (0.1)	1.5 (0.1)	163.3 (0.1)	1.2 (0.1)	163.2 (0.1)	1.2 (0.1)
<b>S 2p</b>	164.7 (0.1)	1.5 (0.1)	164.6 (0.1)	1.2 (0.1)	164.4 (0.1)	1.2 (0.1)
<b>Zn 2p</b>	1022.8 (0.1)	2.1 (0.1)	1022.8 (0.1)	1.8 (0.1)	1022.7 (0.1)	1.8 (0.1)
	<b>KE (eV)</b>	<b>FWHM (eV)</b>	<b>KE (eV)</b>	<b>FWHM (eV)</b>	<b>KE (eV)</b>	<b>FWHM (eV)</b>
<b>Cu LMM</b>	915.7 (0.1)	2.3 (0.1)	915.7 (0.1)	2.0 (0.1)	915.8 (0.1)	2.0 (0.1)
<b>Zn LMM</b>	986.5 (0.1)	2.6 (0.1)	986.4 (0.1)	2.4 (0.1)	986.6 (0.1)	2.4 (0.1)

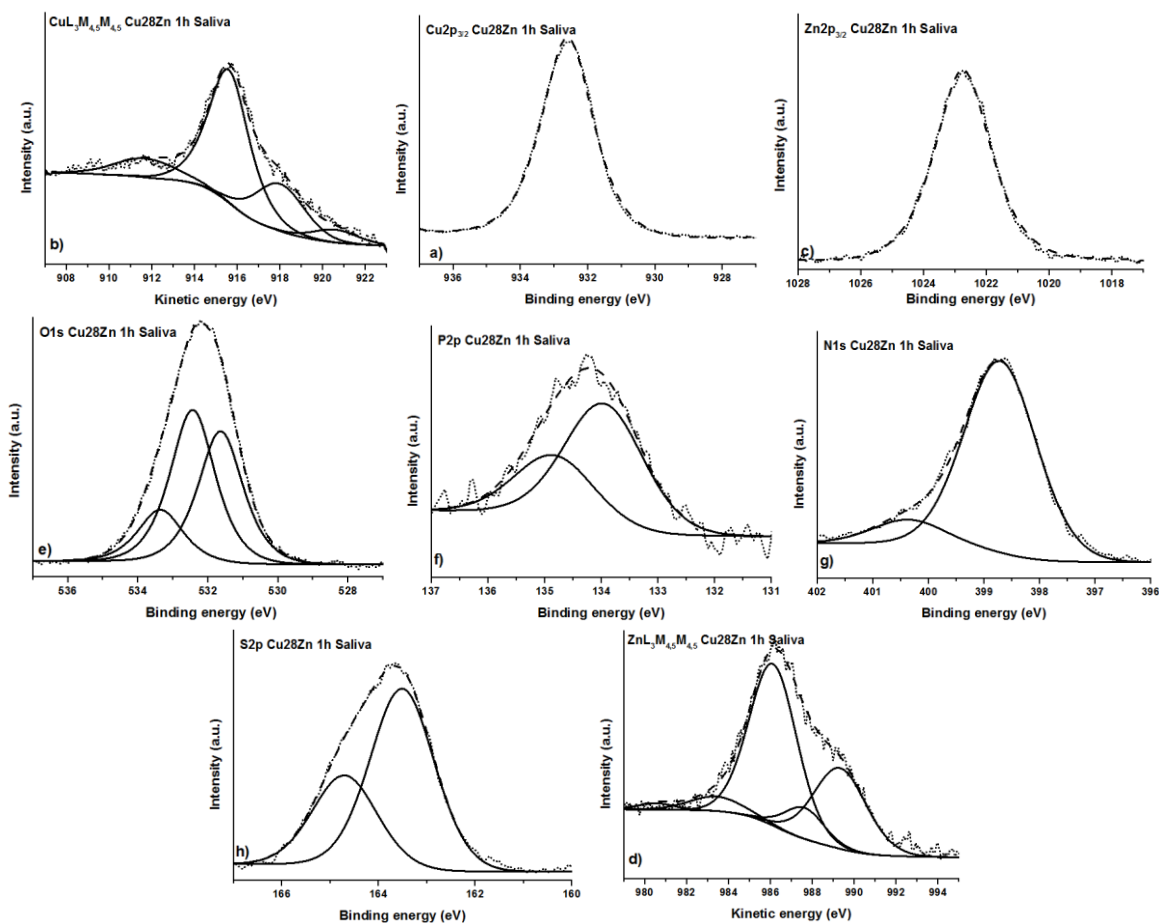


Figure A 9: High resolution spectra of Cu  $2p_{3/2}$  (a), Zn  $2p_{3/2}$  (b), O 1s (c), Cu  $L_3M_{45}M_{45}$  (d), Zn  $L_3M_{45}M_{45}$  (e), P 2p (f), N 1s (g), and S 2p (h) for the Cu28Zn after 1 hour of contact with the saliva solution.

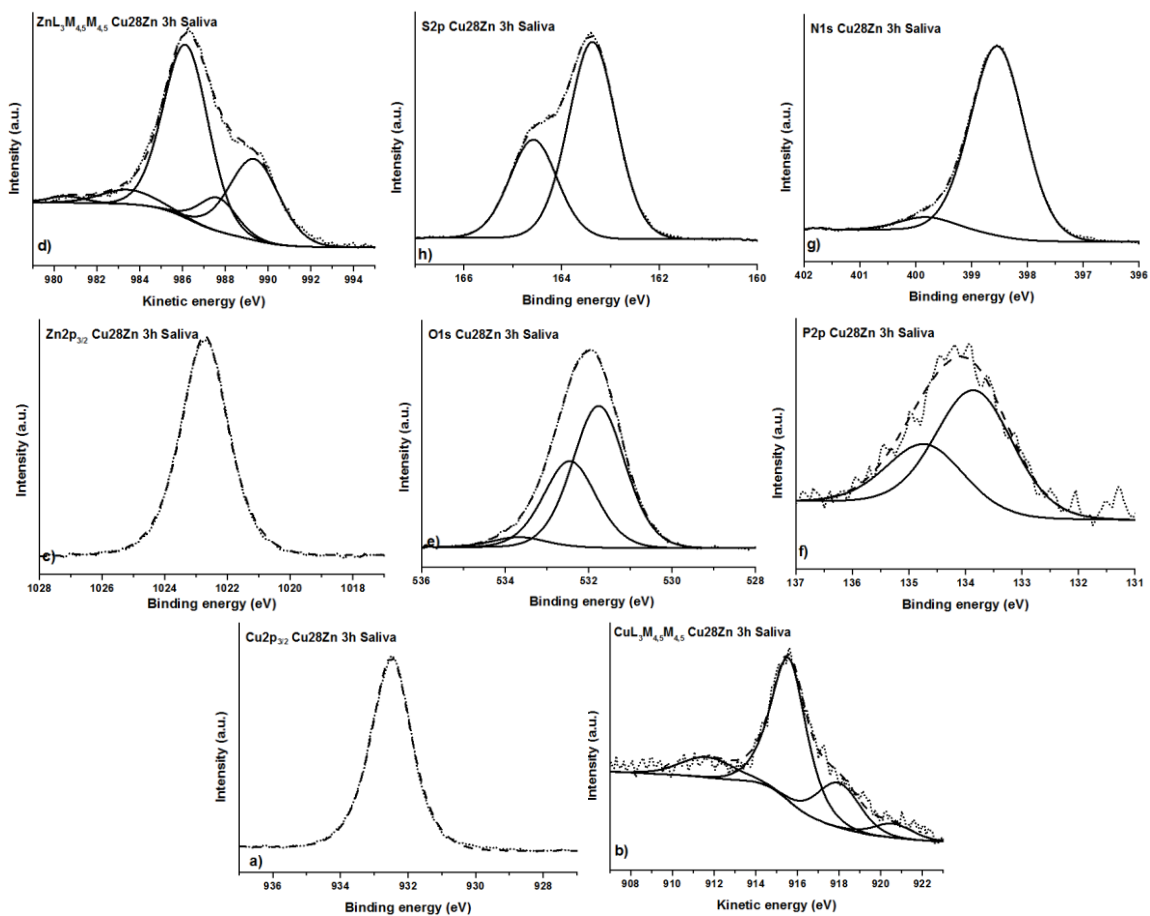


Figure A 10: High resolution spectra of Cu  $2p_{3/2}$  (a), Zn  $2p_{3/2}$  (b), O 1s (c), Cu  $L_3M_{45}M_{45}$  (d), Zn  $L_3M_{45}M_{45}$  (e), P 2p (f), N 1s (g), and S 2p (h) for the Cu28Zn after 3 hour of contact with the saliva solution.

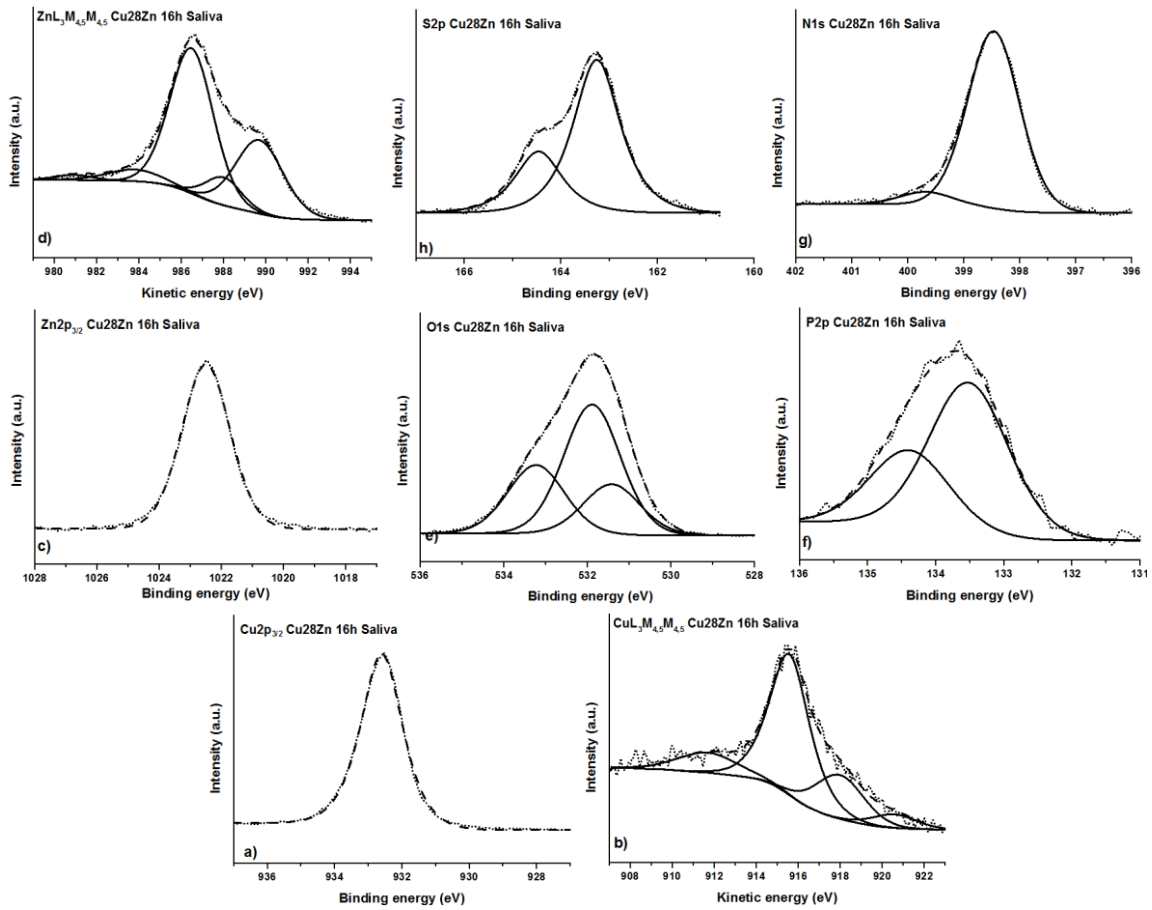


Figure A 11: High resolution spectra of Cu 2p<sub>3/2</sub> (a), Zn 2p<sub>3/2</sub> (b), O 1s (c), Cu L<sub>3</sub>M<sub>45</sub>M<sub>45</sub> (d), Zn L<sub>3</sub>M<sub>45</sub>M<sub>45</sub> (e), P 2p (f), N 1s (g), and S 2p (h) for the Cu<sub>28</sub>Zn after 16 hour of contact with the saliva solution.

Table A 6: Quantitative analysis results (average values) of the Cu28Zn after 1, 3 and 16 hours of immersion in the artificial saliva solution. Standard deviations are reported in brackets.

<b>Cu28Zn</b>	<b>1h</b>				
	<b>%at</b>		<b>%at</b>		<b>%at</b>
<b>C</b>	18 (3)				
<b>CuOx</b>	19 (1)	<b>CuOx</b>	23 (1)	<b>Cu tot</b>	70 (3)
<b>N</b>	13 (1)	<b>N</b>	16 (1)		
<b>O</b>	22 (1)	<b>O</b>	27 (1)		
<b>P</b>	4 (1)	<b>P</b>	5 (1)		
<b>S</b>	16 (2)	<b>S</b>	19 (1)		
<b>ZnOx</b>	8 (1)	<b>ZnOx</b>	10 (1)	<b>Zn tot</b>	30 (3)
	<b>3h</b>				
	<b>%at</b>		<b>%at</b>		<b>%at</b>
<b>C</b>	11 (1)				
<b>CuOx</b>	12 (6)	<b>CuOx</b>	13 (3)	<b>Cu tot</b>	44 (7)
<b>N</b>	8 (3)	<b>N</b>	9 (2)		
<b>O</b>	32 (5)	<b>O</b>	36 (7)		
<b>P</b>	8 (2)	<b>P</b>	9 (2)		
<b>S</b>	14 (3)	<b>S</b>	16 (2)		
<b>ZnOx</b>	14 (3)	<b>ZnOx</b>	16 (2)	<b>Zn tot</b>	56 (7)
	<b>16h</b>				
	<b>%at</b>		<b>%at</b>		<b>%at</b>
<b>C</b>	51 (4)				
<b>CuOx</b>	6 (1)	<b>CuOx</b>	12 (2)	<b>Cu tot</b>	47 (7)
<b>N</b>	4 (1)	<b>N</b>	8 (1)		
<b>O</b>	22 (3)	<b>O</b>	45 (2)		
<b>P</b>	4 (1)	<b>P</b>	9 (1)		
<b>S</b>	6 (1)	<b>S</b>	12 (2)		
<b>ZnOx</b>	7 (1)	<b>ZnOx</b>	14 (2)	<b>Zn tot</b>	53 (7)

# *Acknowledgments*

Here I am at the end of my doctoral studies. I would like to express my gratitude to all of the people that supported me and contributed to the progress of the project.

First, I would like to express my sincere gratitude to my advisor Prof. Antonella Rossi for providing me with the opportunity to work within this interesting and motivating project and for supporting me in these past three years. I am very grateful for her patience, passion and for transferring to me the enthusiasm for science.

I am also deeply indebted to Professor Bernhard Elsener I felt very lucky to have the opportunity to work under his patient supervision. I am very grateful of all his contributions making my doctoral experience productive and stimulating. Professors Bernhard Elsener and Antonella Rossi helped me in all the time of the research project. This thesis could not have been completed without their thoughtful guidance, meticulous attention and enormous support in learning the basis of corrosion.

My research would have been impossible without the aid and support of my former bachelor and master thesis co-supervisor, the researcher of the group, my officemate as well as my dearest friend Dr. Marzia Fantauzzi that always managed to make me feel special if it is not. These past 3 years have been an amazing experience and I am very indebted to Marzia, not only for her incredible academic support, but also for her friendship. She is one of the most intelligent, wise, competent, clever and ironic people I have ever known. I cannot explain the importance you have had in my working life and beyond.

I want to express my gratitude to Professor N.D. Spencer for giving me the opportunity to work in his research group, the Laboratory for Surface Science and Technology (LSST), at ETH Zurich. I am very honored of having had the opportunity to participate at extremely motivating and fascinating group meetings about surface and material sciences. In particular, I would like to thank Josephine Baer for her support in the administrative issues and for her kind patience.

I am especially thankful to Cristiana Passiu who helped me in the SEM and AFM characterization of the brass alloys. Her help was precious. I am very grateful to her for the support that she gave me during my permanence in Zurich.

I am thankful to all the colleagues at the LSST group, especially to Rebecca, Alok, Yvonne, Josephine, Fabiana, Rok, Andrea, Clement and Maura for their constant kindness and patience even if my English was not particularly fluent ☺ especially at the beginning of my traineeship. Many thanks



to Fabiana, she is always smiling and she has able to make the atmosphere more pleasant even if you have to spend hours cleaning brass alloys 😊.

I would like to thank Prof. Francesco Caruso and Dr. Filippo Mangolini for having accepted to be the external reviewers of the thesis.

I also would like to thank Professor Carla Cannas, for all the fruitful scientific discussions, for her academic support but also for her friendship that made these years enjoyable.

I wish to thanks all my beloved colleagues with whom I have shared the best coffee breaks moments, some moments deep anxious but also of big excitement. Their presence was very important during my doctoral studies.

A warm word for my colleagues and great friends since the first year at the University: Mercedes, Claudio e Alessandro who have always been great sources of support even when things would get a bit discouraging.

Many thank to Laura Brundu, a great colleague, friend and officemate for her precious support.

Special thanks go to Dr. Andrea Ardu for the inspiring scientific discussions but also for all jokes.

I thank all the former and current members of the Surface Analysis, Electrochemistry and Corrosion group for the nice working atmosphere and inspiring discussions.

Last but not least, my warmest thanks go to Mum, Dad and Marta for the almost unbelievable support throughout these last months and my life in general. I wish to express my gratefulness to Mauro for his continued support and encouragement especially in these past three years. They are the most important people in my life and I dedicate this thesis to them.

# Curriculum vitae

## Federica Cocco

### Personal information

**Home address:** Via Santa Barbara, 11 Loc. Solanas – Sinnai (CA) 09048

**Nationality:** Italian

**Date and place of birth:** 22/01/1986 Cagliari

**Gender:** Female

**Languages:** Italian (Native speaker), English (FCE level), Spanish (A2 level)

**e-mail:** cocco.federica86@gmail.com

### Education and training

---

1/1/2014 – to date	PhD in Chemical Sciences and Technologies at the Department of Chemical and Geological Sciences at the Università degli Studi di Cagliari
1/1/2015 to 1/09/2015	Training at the Laboratory for Surface Science and Technology (LSST), Department of Materials, ETH Zurich, Zurich, Switzerland.
22 – 26/09/2014	National school of Analytical Chemistry for PhD students, Roma 22 – 26/09/2014
5/12/2013	Master Degree in Chemical Sciences at the Università degli Studi di Cagliari - <i>Electrochemical behaviour and XPS / XAES characterization of brass musical instruments of the XIX century</i> 110/110 e lode
19/12/2010	Bachelor degree in Chemistry at the Università degli Studi di Cagliari <i>Arsenic removal by interaction with gypsum</i> 101/110

---

### Teaching and Supervising Experience

---

May 2016 (20 hours)	Lab assistant within the project “Progetto Alternanza Scuola Lavoro” at the Department of Chemical and Geological Sciences at the Università degli Studi di Cagliari
April – June 2016 (40 hours)	Lab assistant within the course Chimica Analitica I e Laboratorio, Prof. D. Atzei
February – April 2014 (40 hours)	Lab assistant within the project “Piano Lauree Scientifiche”, Prof. A. Rossi, Università degli Studi di Cagliari

---

### Teaching school

---

2014	Scuola nazionale di didattica chimica e ricerca educativa “Ulterico Segre” VI edizione – 2014, Rende (CS) 12 – 15 Settembre
------	---

---

## Publications

---

- 2016 F. Cocco, M. Fantauzzi, B. Elsener, A. Rossi, Dissolution of brass alloys naturally aged in neutral solutions – an electrochemical and surface analytical study, *RSC Advances* 6 (2016) 90654 - 90665
- 
- 2016 B. Elsener, F. Cocco, M. Fantauzzi, S. Palomba, A. Rossi, Determination of the corrosion rate inside historical brass wind instruments – Proof of concept, *Materials and Corrosion* 2016 DOI: 10.1002/maco.201608996
- 
- 2016 B. Elsener, M. Alter, T. Lombardo, M. Ledergerber, M. Wörle, F. Cocco, S. Palomba, M. Fantauzzi, A. Rossi, A non-destructive in-situ approach to monitor corrosion inside historical brass wind instruments, *Microchemical Journal* 124 (2016) 757 - 764
- 
- 2016 F. Cocco, B. Elsener, M. Fantauzzi, D. Atzei, A. Rossi, Nanosized surface films on brass alloys by XPS and XAES, *RSC Advanced* 6 (2016) 31277 - 31289
- 

## Oral Presentations

---

- 2016 F.Cocco, B.Elsener, M.Fantauzzi, A.Rossi, Characterization of brass alloys aged at open circuit potential in neutral solutions by XPS and XAES, XXVI Congresso di Chimica Analitica della Società Chimica Italiana, Giardini Naxos – 18 – 22 Settembre 2016
- 
- 2016 F. Cocco, B. Elsener, M. Fantauzzi, S. Palomba, A. Rossi, Characterization of brass alloys aged at open circuit potential in neutral solution, Incontro di Spettroscopia Analitica ISA2016, 29 Maggio – 1 Giugno 2016
- 
- 2015 F.Cocco, B.Elsener, M.Fantauzzi, A.Rossi, Misure elettrochimiche per determinazione dello stato di corrosione di leghe ottone utilizzati per strumenti d'epoca, Giornate Nazionali sulla Corrosione e Protezione, Ferrara 15 – 17 Giugno 2015
- 
- 2014 F.Cocco, B.Elsener, M.Fantauzzi, A.Rossi, XPS and XAES characterisation of natural patinas on brasses, ISA 2014 Incontro di Spettroscopia Analitica, Ravenna (RA) 5 – 6 June 2014
- 

## Poster Presentations

---

- 2016 F. Cocco, Silvia Palomba, Marzia Fantauzzi, Bernhard Elsener, Antonella Rossi, Breathing new life into historical brass wind instruments – the role of XPS surface analysis, Sustainability In Cultural Heritage, SICHPIN 2010/2011 Conference 2016, 11-12 Gennaio 2016, CNR, Roma
- 
- 2015 F.Cocco, B.Elsener, M.Fantauzzi, A.Rossi, Non-destructive XPS surface analysis in cultural heritage – surface composition of ancient brass instruments, Technart 2015 Non-destructive and microanalytical techniques in art and cultural heritage, Catania 27 – 30 Aprile 2015
- 
- 2014 F.Cocco, B.Elsener, M.Fantauzzi, A.Rossi, Surface cleaning of brasses for musical instruments: an XPS study, XXV Congresso Nazionale della Società Chimica Italiana SCI 2014, Arcavacata di Rende (CS) 07 – 12 September 2014
- 
- 2013 M.Fantauzzi, F.Cocco, B.Elsener, A.Rossi, Brass musical instrument of the 19th and early 20th centuries: an XPS and XAES investigation, 15th
-

---

European Conference of Application of Surface and Interface Analysis, 13  
– 18 October 2013, Pula (CA) (ISBN: 978-88-907670-0-5)

---

---

## Awards

---

2016 Italian Chemical Society (SCI) Fellowship to present my research at the XXVI Congresso di Chimica Analitica della Società Chimica Italiana, Giardini Naxos – 18 – 22 Settembre 2016.

---

2015 Globusdoc Fellowship for the trainship at the ETH Zurich (Switzerland) – 6 months

---

2015 The results of the research were mentioned among the outstanding research topics of TechnArt conference 2015 by the magazine C&EN, A Taste Of Artful Science dedicated to the most TechnArt conference celebrates how science is providing answers to important questions about our most precious pieces of cultural heritage, 93 (2015) 38-39  
<http://cen.acs.org/articles/93/i21/Taste-Artful-Science.html>

---